In situ Optical Microscopic Examination Techniques of Thermally Induced Displacive Transformations

Marton Benke[1,a], Valeria Mertinger[2,b]

[1]Hungarian Academy of Sciences-University of Miskolc Materials Science Research Group, University of Miskolc, Miskolc-Egyetemvaros, Hungary

[2]Institute of Physical Metallurgy, Metalforming and Nanotechnology, University of Miskolc, Miskolc-Egyetemvaros, Hungary

[a]fembenke@uni-miskolc.hu, [b]femvali@uni-miskolc.hu,

Keywords: martensitic transformation, relief, in situ optical microscopy

Abstract. The mechanical (reversible deformation, stress-strain diagrams, etc.) and thermal (transformation temperatures, hysteresis) characteristics of the thermoelastic martensitic transformations are in the focus of many manuscripts, however, other aspects of the transformations are given less attention. The relief formation accompanied with displacive transformations ensures the possibility of the direct observation of the mechanism and physical metallurgical characteristics of the martensite↔austenite transformations. The authors of the present manuscript applied the in situ optical microscopy method successfully using self-developed examination techniques and self-made heating stages to characterize the thermally induced displacive transformations in shape memory alloys (SMAs) and TWIP steels.

Introduction

The displacive solid state transformations can be characterized by a deformation that brings the parent lattice into the product lattice. The shape change of the parent lattice generates mechanical stresses in both phases which can be minimized by introducing either slip planes or twin boundaries. However, the stress introduced by the transformation is not completely eliminated by these mechanisms. As the parent/product interface reaches the free surface, the stress is relieved by the macroscopic displacement of the surface. This displacement forms topological features on the surface, which are called reliefs. Martensitic transformations are the most widely known examples for displacive transformations [1-6]. Optical microscopy is a respective method to study relief structures. However, conventional sample preparation cannot be used where the contrast is assured by the different etching behavior of the different phases and the phase boundaries. The relief structure can only be examined if it is formed on a smooth parent surface. The in situ observation of the relief formation during transformation provides direct information about the characteristics of the transformation. Some physical metallurgical characteristics of the displacive transformations such as shape change, martensite variant nucleation sites during consecutive cycles, shear band formations, elastic/plastic deformations accompanied with the transformations can only be directly observed using in situ optical microscopy. In situ optical microscopy was successfully used by Tong et al. to study the thermoelastic martensitic transformation (TMT) of an AgCd shape memory alloy (SMA) [7]. Brinson et al. investigated the stress induced TMT in TiNi alloys using in situ optical microscopy [8] and Jiang et al. used in situ TEM for the examination of the same alloy [9]. In situ optical microscopy was also used to study crystallization processes [10, 11] and oxidation processes [12]. Bainitic reactions were observed to occur in many Cu based SMAs: in CuAlNiMnTi SMAs in refs. [13-16], CuZnAl alloys in refs. [17-19], in CuAlNiMn and CuAlNiMnFe alloys in refs. [20, 21]. The bainitic reaction strongly affects the characteristics of the TMT (transformation temperatures, transformable volume) and thus, the shape memory effect (SME). Furthermore, in many cases it destroys the SME in the first heating cycle. Thus, the characterization of the bainitic reaction is of great importance in Cu-based SMAs. The bainitic reactions of Cu based SMAs are also accompanied with visible relief formations, therefore in situ optical microcopy is a suitable method to examine them. The authors of the present manuscript

applied the in situ optical microscopy method successfully using self-developed examination techniques and self-made heating stages to characterize the thermally induced ε↔γ transformations of FeMnCr steels showing twinning induced plasticity (TWIP), the thermally induced TMTs and the bainitic reactions in Cu based SMAs [22,23]. All of the examined transformations are thermally induced. There are heating stages for optical microscopes available on the market, but they are not designed for relief change examinations of martensitic transformations (MTs). There are some issues that need to be dealt with during in situ optical microscopic examinations of MTs. The developed techniques face these difficulties and provide suitable methods for the examinations of MTs. The aim of the present manuscript is to give detailed descriptions of the examination methods and give an overview of the different types of relief formations.

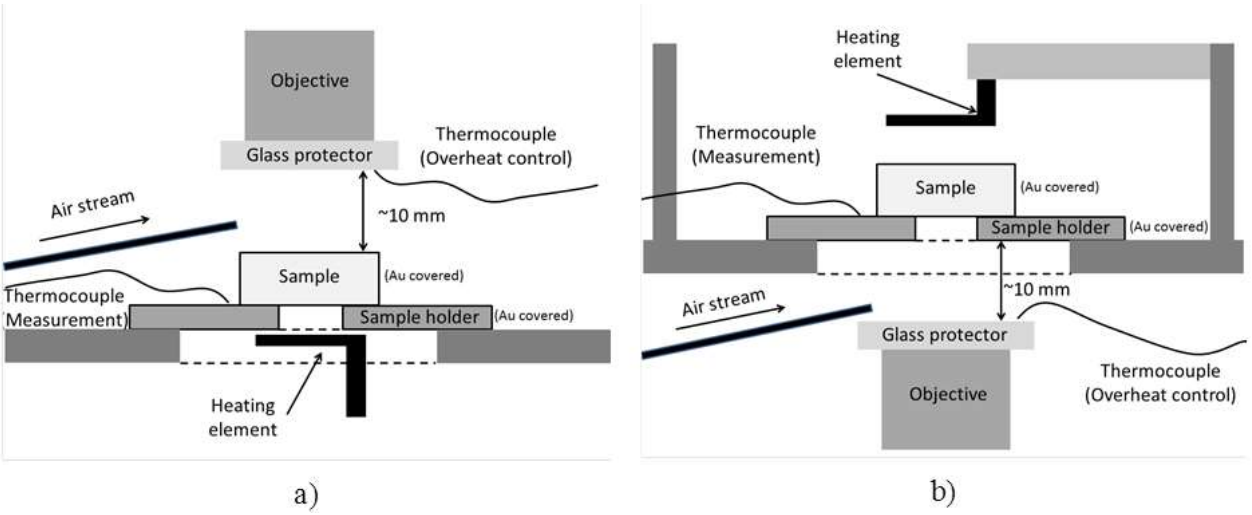

Fig. 1 Microscope modes a) normal set-up b) inverse set up

Built experimental set up

Imaging system and microscope set-up

The surface relief accompanied with a displacive transformation is a 3 dimensional topological feature. The differential image contrast (DIC) imaging technique is one of the most sensitive techniques for such topological features. A Zeiss Axio Imager m1M optical microscope with DIC imaging and Zeiss AxioCam ERc 5c was used for the in situ optical examinations. The magnification of the 10X objective was found to be enough for the examinations. Its focal distance is ~10 mm. The images were captured with 10 fps frequency. The images and the thermovoltage data were collected, synchronized and stored by Labview software.

There were two types of examination set-ups used during the examinations. The first one was the normal arrangement (Fig. 1 a). In this set-up the sample was held by its bottom surface while the upper surface was examined. The advantage of this set-up was that the forming martensite variants did not lift the sample. This method was used during the cyclic examination of the TMT in the CuAlNi alloy (Fig. 4). The disadvantage of this set-up was that due to the small sample size it was not possible to set the examined surface parallel to the focal plane and thus, not all the examined area was in focus. Furthermore, as the sample expanded upwards during heating, it moved out from the focal distance.

The second arrangement was the inverse arrangement. In this set-up the sample was held by the bottom surface, which was also examined. The advantage of this set-up was that the whole examined area was in focus and the sample could freely expand upwards during heating while the examined surface was kept at the focal distance (Fig. 1 b). The disadvantage of this arrangement was that in some cases the formed martensite variant was so large that the relief lifted the sample and moved it aside. This method was used for the examinations of the TMT in CuAlNi alloy (Fig. 3), the bainitic reaction in a CuAlNiMn alloy (Fig. 5) and the examination of the ε martensite→γ transformation of FeMnCr TWIP steels (Fig. 6).

Sample preparation

Conventional sample preparation (polishing and etching) could not be used to monitor the relief formation because of two reasons. First of all, etching gives contrast to a smooth surface based on the different etching behavior of the different phases and interfaces. This contrasting method would characterize the phase transformation, but not the relief formation. Secondly, the in situ observation requires in situ etching. This is not possible to carry out since the TMTs in SMAs are much faster than etching processes.

Fig. 2 shows the three different types of relief formations. During the first method, the sample in its austenitic (A) state was polished to get a smooth surface. Martensite (M) variants grew from the smooth austenite surface during the forward (austenite→martensite) transformation. During the martensitic reverse transformation (martensite→austenite) the variants grew back into the smooth austentite surface (Fig. 2 a). This preparation method was used to examine the TMT in the CuAlNi and CuAlNiMn alloys. See example at Fig. 3.

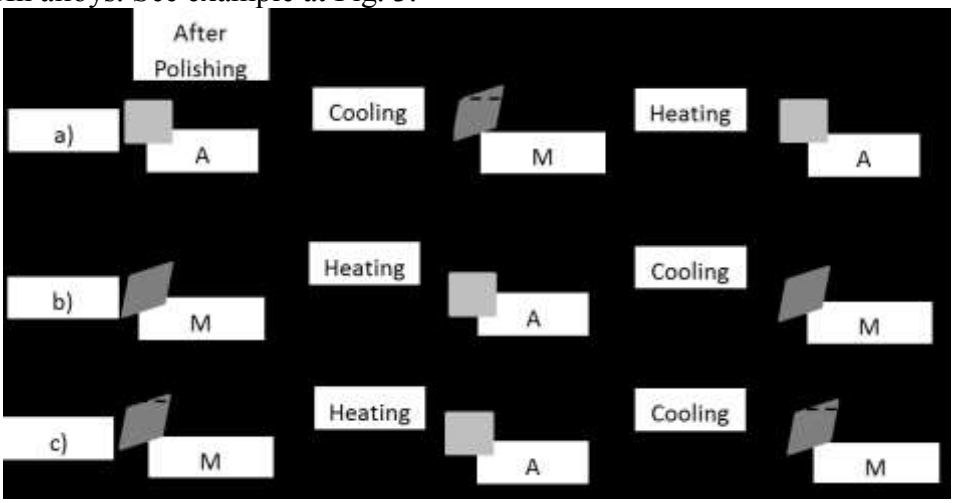

Fig. 2 Sample polishing methods for relief change observations [23]. The small filled quadrangles represent the microscopic shape changes of the martensite↔austenite transformations, while the big blank multiangulars represents the macroscopic shape change of sample. A-austenite, M-martensite

For the second method the sample was in its martensitic state during the polishing. Thus, starting from a smooth martensitic surface a hill-valley topologic formation formed during the martensite→austenite reverse transformation due to the shape change (Fig. 2 b). The topological feature that formed during these examinations is called "inverse relief" in order to distinguish it from the relief formation, which is related to martensite formation, in general. The inverse relief disappeared during the austenite→martensite forward transformation. This sample preparation was used for the examination of the ε martensite→γ transformation of FeMnCr TWIP steels (Fig. 6).

The third type of sample preparation is a mixture of the previous two. During this preparation method the sample was in its martensitic state, but the surface was not polished to a completely smooth surface. Thus, some of the relief of the initial martensite structure was preserved. During the martensite→austenite reverse transformation an inverse relief formed, while new relief formed during the consecutive cooling run (Fig. 2 c). Using this method it was possible to compare the martensite variant structures formed in the consecutive thermal cycles to the initial variant structure during the cyclic TMT examinations of the CuAlNi alloy (Fig. 4) Furthermore, using this method it was possible to compare the relief formed by the bainitic reaction to the relief of the TMT in the CuAlNiMn alloy (Fig. 5). For simplicity and to quicken sample changing, the developed examination techniques were developed as open air techniques. To avoid the samples from oxidation, they were coated with Au layer with a BIO-RAD Scanning Electron Microscope Coating System (2.2 KV, 12 mA, 2 X 30 s). To avoid any previously observed oxidation reaction between the covered sample and the steel sample holder, the holder was also covered with Au.

Results

Thermoelastic martensitic transformations in CuAlNi and CuAlNiMn alloys

Fig. 3 a-e show consecutive images taken from the heating of the quenched Cu-10.2Al-4.92Ni-4.12Mn (w/w%) sample. It can be seen how the martensite variants grow back into the smooth austenite surface during the reverse martensitic transformation. The shape change can be observed by the aid of the scratches in the middle of the images. It can be seen that the scratches have zig-zag type as they pass through different martensite variants, while they become straight as the variants disappear. Such scratches that demonstrate the shape change are called "fiducial lines". Fig. 4 a-c show images of the Cu-12.7Al-4.5Ni sample taken after different thermal cycles. The inverse relief of the first martensite variant structure remains visible due to the applied sample preparation. It can be seen that different martensite variant structures formed in every consecutive cycle.

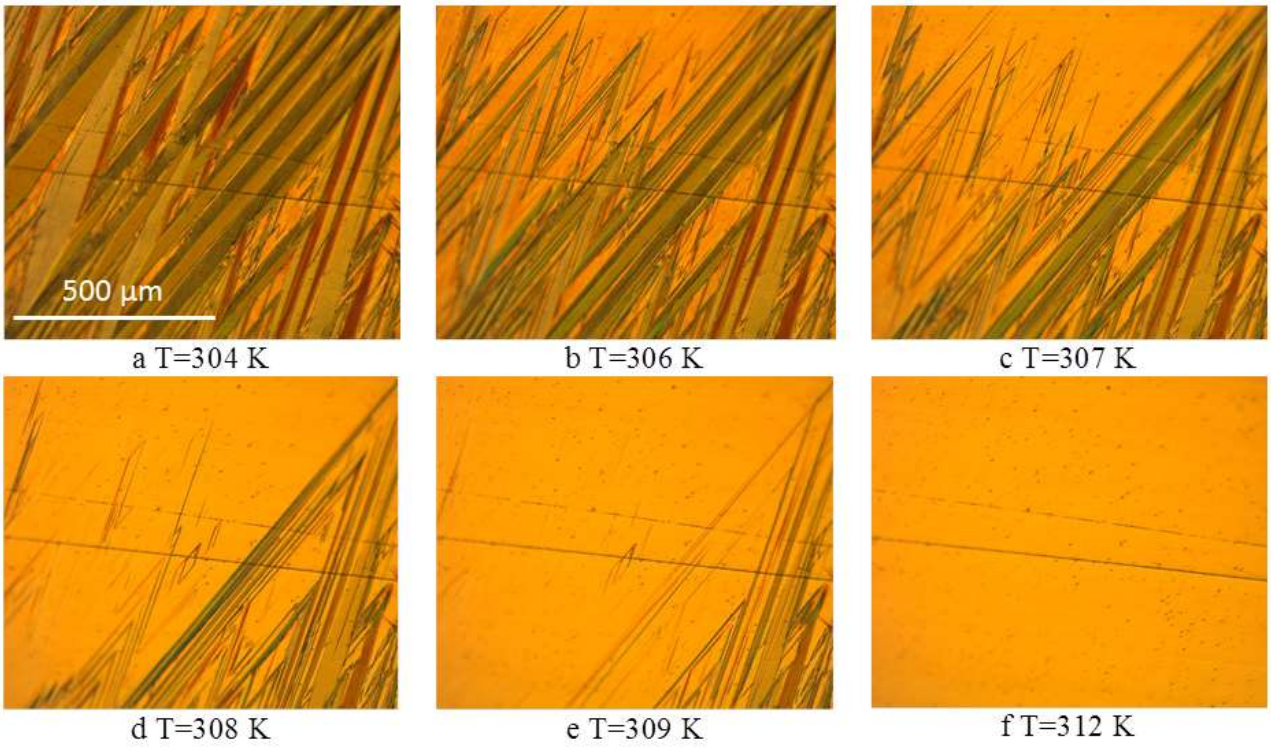

Fig. 3 Thermoelastic reverse martensitic transformation in a CuAlNiMn alloy

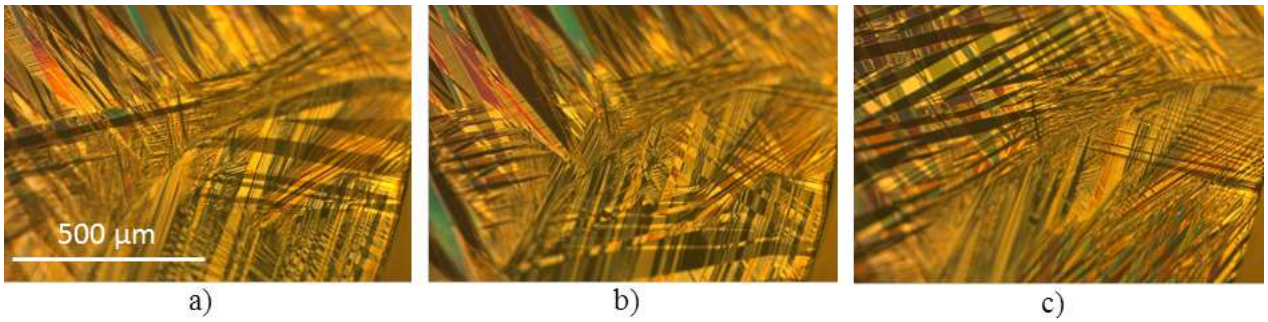

Fig. 4 Martensite variant structures in a CuAlNi alloy a) initial b) after the 1st cycle c) after the 4th cycle

Bainitic reaction in a CuAlNiMn alloy

The relief formation accompanied with the austenite→bainite reaction in the Cu-10.2Al-4.92Ni-4.12Mn alloy can be observed in Fig. 5 a-c. The inverse relief formed during the martensite→austenite reverse transformation is also visible due to the applied sample preparation. It

can be seen that the relief accompanied with the bainitic reaction is much finer compared to the inverse relief formed during the martensite→austenite thermoelastic reverse transformation.

ε→γ transformation in TWIP steel

The inverse relief formation during the ε→γ transformation in a Fe-0.08C-21.03Mn-6.53Cr TWIP steel can be seen in Fig. 6. The smooth surface of the ε+γ structure turns into an inverse relief as the ε phase transforms to γ phase.

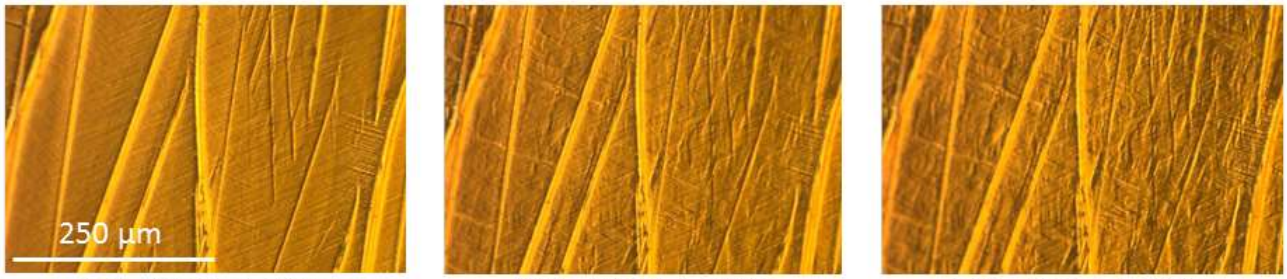

a) T= 523K, t=152 s b) T= 537K, t=180 s c) T= 541K, t=200 s

Fig. 5 Bainitic reaction in a CuAlNiMn alloy

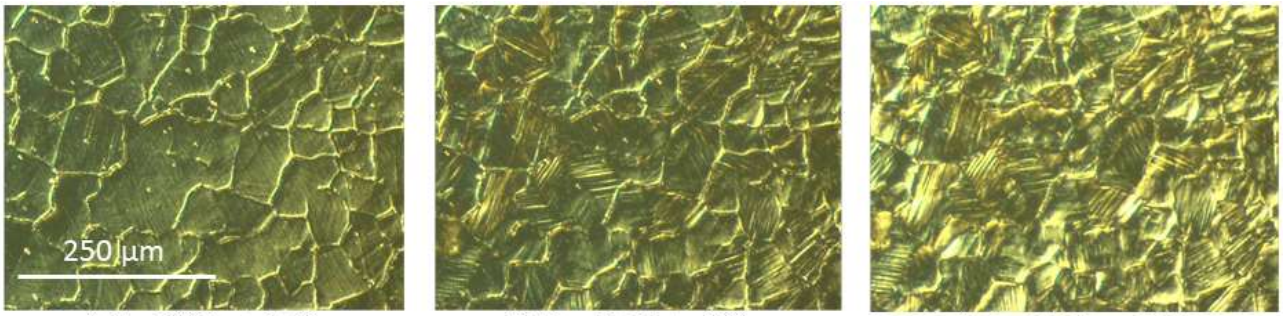

a) T= 480K, t=170 s b) T= 481K, t=190 s c) T= 490K, t=220 s

Fig. 6 ε→γ transformation in a FeMnCr TWIP steel

Summary

A detailed description of the developed sample preparation methods and examination techniques for in situ optical microscopic examinations of thermally induced displacive transformations were given. It was proved through our results on Cu based shape memory alloys and TWIP steels that the developed sample preparation and examination techniques are useful for the observation of relief changes accompanied with the thermally induced displacive transformations. It was shown that the proper selection of the different sample preparation methods and examination set-ups gave direct information about the mechanisms of the examined processes.

Acknowledgement

This work has been carried out as part of the OTKA K 84065 and the TÁMOP-4.2.1.B-10/2/KONV-2010-0001 projects within the framework of the New Hungarian Development Plan. The realization of this project is supported by the European Union, co-financed by the European Social Fund.

References

[1] J. D. Verhoeven: Fundamentals of Physical Metallurgy, John Wiley & Sons Inc, 1975.
[2] H. K. D. H. Bhadeshia, R. W. K. Honeycombe, Steels Microstructure and Properties, Butterworth-Heinemann, 2006.
[3] H. Funakabo, Shape Memory Alloys, Gordon and Breach, 1987.

[4] K. Otsuka and C. M. Waymann, Shape Memory Materials, Cambridge University Press, 1998.
[5] K. Otsuka and X. Ren, Recent developments in the research of shape memory alloys, Intermetallics 7 (1999) 511-528.
[6] V. Brailovski, S. Prokoshkin, P. Terriault and F. Trochou, Shape Memory Alloys: Fundamentals, Modeling and Applications, École de Technologie Supérieure 2003.
[7] H. C. Tong, C. M. Wayman, Characteristic temperatures and other properties of thermoelastic martensites, Acta Metallurgica Vol. 22 (1974) 687-696.
[8] L. C. Brinson, I. Schmidt and R. Lammering, Stress-induced transformation behavior of a polycrystalline NiTi shape memory alloy: micro and macromechanical investigations via in situ optical microscopy, Journal of the Mechanics and Physics of Solids 52 (2004) 1549-1571.
[9] X. Jiang, M. Hida, Y. Takemoto, A. Sakakibara, H. Yasuda and H. Mori, In situ observation of stress-induced martensitic transformation and plastic deformation in TiNi alloy", Materials Science and Engineering A238 (1997) 303-308.
[10] A. Bluma, T. Höpfner, G. Rudolph, P. Lindner, S. Beutel, B. Hitzmann, T. Scheper, Adaption of in-situ Microscopy for crystallization process, J. Cryt. Growth 311 (2009) 4193-4198.
[11] M.-Y. Lee, G. M. Parkinson, Growth rates of gibbsite single crystals determined using in situ optical microscopy, J. Cryst Growth 198/199 (1999) 270-274.
[12] S. Gangireddy, S. N. Karlsdottir, S. J. Norton, J. C. Tucker, J. W. Halloran, In situ microscopy observation of liquid flow, zirconia growth, and CO bubble formation during high temperature oxidation of zirconium diboride-silicon carbide, J. Eur. Ceram. Soc. 30 (2010) 2365-2374.
[13] W. H. Zou, H. Y. Peng, R. Wang, J. Gui, D. Z. Yang, Heating effects on fine structure of a Cu-Al-Ni-Mn-Ti shape memory alloy, Acta Mater. Vol. 43 (1995) 3009-3016.
[14] Z. G. Wei, H. Y. Peng, D. Z. Yang, C. Y. Chung, J. K. L. Lai, Reverse transformations in CuAlNiMnTi alloy at elevated temperatures, Acta Mater. Vol. 44 (1996) 1189-1199.
[15] W. Zou, J. Gui, R. Wang, C. Tang, M. Xiang, D. Zhang, Baintic precipitation and its effect on the martensitic transformation in the Cu-Al-Ni-Mn-Ti Shape-Memory alloy, J. Mater. Sci. 32 (1997) 5279-5286.
[16] E. Hornbogen, V. Mertinger, J. Spielfeld, Ausageing and ausforming of a copper based shape memory alloy with high transformation temperatures, Z. Metallkd. 90 (1999) 5 318-322.
[17] L. G. Bujoreanu, S. Stanciu, P. Barsanescu, N. M. Lohan, Study of the transitory formation of α1 bainite, as a precorsor of α-phase in tempered SMAs, A.T.O.M. IV, Vol. 7297 (2009) 72970B 1-6.
[18] K. Takezawa, S. Sato, Composition dependence of bainite morphology in Cu-Zn-Al alloys, Mater. Trans. JIM, Vol. 33 (1992) 102-109.
[19] K. Marukawa, M. Tabuchi, Analysis of the transformation strain of bainites in Cu-Zn-Al alloys by utilizing interference fringes in TEM images, Mater. Trans.Vol. 44 (2003) 1774-1782.
[20] M. Benke, V. Mertinger, P. Pekker, Investigation of the bainitic reaction in a CuAlNiMnFe shape memory alloy, J. Min. Metall., Sect. B-Metall., 49 (1), B (2013) 43-47.
[21] M. Benke, V. Mertinger, P. Barkoczy, Investigation of the kinetic of a bainitic reaction upon heating in a CuAlNiMn and a CuAlNiMnFe shape memory alloy, Mat. Sci. For. Vol. 752 (2013) 3-9.
[22] M. Benke, V. Mertinger, In situ optical microscope examinations of the ε↔γ transformations in FeMn(Cr) austenitic steels during thermal cycling, Mat. Sci. For. Vol. 738-739 (2013) 257-261.
[23] M. Benke, V. Mertinger, In situ optical microscope study of the thermally induced displacive transformations in CuAlNi based shape memory alloys, submitted to J. Materi. Eng. Perform. (2014)

Effect of high energy Ar-ion milling on surface of quenched low-carbon low-alloyed steel

Tibor Berecz[1,a], Szilvia Kalácska[2,b], Gábor Varga[2,c], Zoltán Dankházi[2,d], Károly Havancsák[2,e]

[1] Budapest University of Technology and Economics, Department of Materials Science and Engineering

1111 Budapest, Bertalan Lajos utca 7., Hungary

[2] Eötvös Loránd University, Department of Materials Physics

1117 Budapest, Pázmány Péter sétány 1/a.

a: berecz@eik.bme.hu (corresponding author); b: kalacska@metal.elte.hu;

c: bagoj@caesar.elte.hu; d: z.dankhazi@szft.elte.hu; e: hkaroly@caesar.elte.hu

Keywords: Specimen preparation, Ion milling, SEM, EBSD.

Abstract. Surface preparation for electron backscatter diffraction (EBSD) measurements requires a lot of time and experience. We chose a lath martensitic iron based alloy to demonstrate the efficiency of ion polishing techniques. The average image quality (IQ) values from the EBSD measurements were assigned to be the characteristic parameter for surface goodness. The ideal ion sputtering time and the angle of incidence were determined, and the corresponding inverse pole figure (IPF) and IQ maps were compared to the mechanical polishing treatment.

Introduction

Transmission electron microscopy (TEM) and scanning electron microscopy (SEM) play a key role in the experimental research work of materials science and solid state physics. At the same time, however to a different extent, both methods request demanding sample preparation. The traditional sample preparation techniques, such as mechanical or electro-polishing methods can hardly satisfy all demands, and they are usually time consuming treatments. The mechanical surface treatment has another drawback; after grinding and polishing an amorphous layer of 1-100 nm thickness remains on the surface. The name of this amorphous layer is the Beilby layer [1]. The removal of this layer is difficult or needs long time careful mechanical treatments.

These are the reasons that in the last decades a new promising technique has been spreading. This new method is based upon the ion milling, the physical basic of which is the sputtering of atoms. Different ion beam methods have been used in the last decades for TEM lamella thinning or to prepare flat sample surface and cross sectional specimens for SEM measurements. These methods use either low energy (0,1-2 keV) or relatively high energy (2-10 keV) ions of inert gases (e.g. Ar^+, Kr^+) or some ions of metallic origin, as for instance Ga^+ ions in the focused ion beam (FIB) technique. Ion milling is the erosion of solid surfaces due to ion bombardment. During ion milling the incident ions transfer energy to the atoms of the target through collisions. If the target atoms gain sufficient energy (more than the surface binding energy) then they escape from the surface. The rate of this erosion depends mainly on the material of the target (*via* surface binding energy) and the energy density given to the surface target atoms. This energy density depends on the mass, the energy, and the direction of the incident ion beam [2, 3].

The electron backscatter diffraction (EBSD) is an optional application in scanning electron microscopy to characterize the grain parameters, the texture and phase features of a polycrystalline material. In an EBSD measurement the SEM sample is tilted at ~70°. The result of a diffraction measurement is the so called Kikuchi pattern detected by a special detector containing a high resolution fluorescent screen and a CCD camera behind it. The Kikuchi pattern contains Kikuchi

bands, construction of which characterizes the crystal structure and the orientation of that grain the electron beam spot right hits. [4]

The EBSD technique is a remarkably useful and versatile tool in the hands of materials scientist; however it needs a careful sample surface preparation. Perhaps one of the most promising methods for satisfying the high surface quality demand of the EBSD is the ion milling procedure. The main benefit of the ion milling technique is that it is less sensitive to the microstructure and chemical composition of the sample. The method can be easily automated and moreover it can be characterized by some exact parameters. The apparent disadvantage of this method is that the ion milling devices are relatively expensive apparatuses, and since this is a new method of the last decades, we have no broad experiences on it yet.

The purpose of this paper is to apply the Ar-ion milling method for the complex, so called lath martensitic microstructure of a quenched commercial low-carbon low-alloyed steel. The lath martensite morphology exhibits a characteristic multilevel microstructure. A parent austenite grain consists of several packets (the group of laths with the same habit plane). Each packet is divided into parallel blocks and a block is further subdivided into laths. The size of individual martensite laths is very small; therefore they cannot be seen by optical microscopes. There are high angle boundaries between the blocks and packets, while low angle (about 5-10°) boundaries between the single laths. [5, 6] The lath martensite have high industrial significance due to its high strength and toughness. Because of these properties the mechanical surface preparation hardly satisfies the severe requirements of EBSD quality. In this paper we demonstrate the advantages of the Ar ion polishing method in case of samples from martensitic steel material.

Experiment

For the present study we chose an iron based alloy containing Ni, Mn, Si and C. The exact alloying element contents are presented in Table 1. The steel composition went through austenitization, then it was aged at 1100 °C and finally, quenched in ice cold (0 °C) water. The lath martensitic structure formed during the quenching. Hardness measurements were taken on the sample, which concluded a relatively low hardness value (295 HV) as a result of the small carbon presence in the alloy.

Alloying elements	C	Si	Mn	Ni
Content (%)	0.15	0.35	1.10	5.00

Table 1: Alloying contents of the steel sample (beside Fe).

Before the EBSD measurements the cast sample was polished using a traditional surface preparation method. The finest polishing step contained colloidal silica particles of 0.02 μm average size, and the final treatment was applied for approximately 20 minutes. Although the surface preparation was so careful and exhaustive, the resulting EBSD maps were not clear and detailed enough to be useful for a lath martensitic structure investigation, and this is why we chose this kind of material to observe the effects of ion polishing treatment.

The cast was cut into smaller pieces for ion polishing time and incidence angle measurements. The smaller samples were then prepared with an SC-1000 SEMPrep instrument made by Technoorg Linda Ltd. Co., which uses high energy (10 keV) Ar ions for ion milling [7]. The angle of ion beam incidence varied relative to the surface of the samples while the specimens were rotated in the milling device. In a separate measurement different sputtering times were chosen over the same marked area to find the optimal milling time for EBSD mapping.

The changes were observed using a FEI Quanta 3D dual beam SEM at Eötvös Loránd University, equipped with an EDAX type EBSD system and an OIM Analysis 5.3 software configuration [8]. The quality of the measured surface was characterized by the image quality (IQ) parameter, which refers to the quality of a diffraction pattern. During an EBSD scanning, the

detector collects the Kikuchi patterns in each measurement point, then the software computes the corresponding IQ value. With these IQ values we can create an IQ map showing the quality of the surface by a grayscale visualization. Dark points refer to low IQ values, points with high IQ values get bright color. When a grain boundary is being illuminated by the electron beam, diffraction patterns from grains with different orientations overlap in the Kikuchi pattern, so the IQ number is going to be low.

The IQ values were averaged over the scanned area, so we assigned one number to each surface. The IQ parameter strongly depends on the type of the examined material and the surface preparation. In our case specimens were cut from the same material, so the average IQ values are only related to the surface preparation. The EBSD scans covered a 100 μm × 100 μm area with 0.2 μm step size on a hexagonal grid.

Results and discussion

The high energy Ar-ion milling effects on average IQ depending on incidence angle and sputtering time are shown in Fig. 1 and Fig. 2, respectively. The highest average IQ can be achieved in about 24 minutes sputtering time using 7° incidence angle. Fig. 1 and Fig. 2 also show that short and long exposure time, as well as low and high incidence angle lower the average IQ.

During the measurements of the ion beam incidence angle versus IQ dependence numerous samples were made with the same mechanical polishing preparation. Ion polishing with different angles was applied independently on each piece of sample. Because of the varying areas which were scanned the initial IQ values have wide distribution. This effect causes relatively high inaccuracy in IQ measurement at small angles. This phenomenon comes from the fact that different areas have different surface morphologies and grain distribution. Knowing the small differences in the scanned regions and bearing in mind that small angles have little effect on the surface polishing we started the measurement at 2°, as it can be seen in Fig. 1. This figure also shows the magnitude of error. The fitted curve is just for illustrating the change in average IQ values. Decreasing of IQ at higher angles can be explained with the channeling effect, inhomogeneous sputtering and surface roughness.

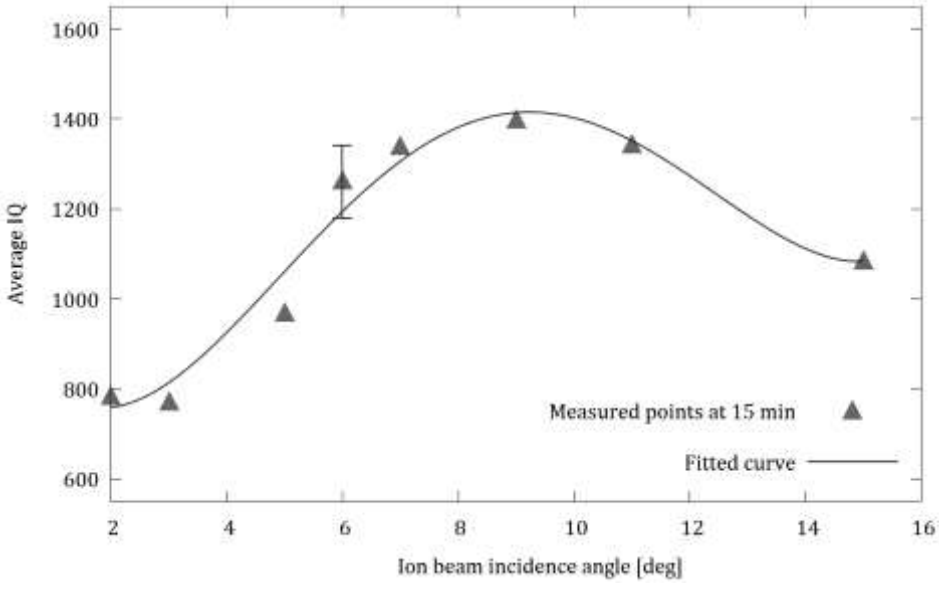

Fig. 1. Effect of incidence angle of ion beam on the average IQ.

Fig. 2. shows the average IQ versus ion milling time dependence. For this measurement only one sample was prepared with the same method as before, and the area was marked with two FIB milled sign. This way always the same area was mapped in the same position so the magnitude of the average IQ error could be reduced. The fitted curve in Fig. 2 reveals that average IQ increases

(nearly linearly) with increasing sputtering time, because the ion beam removes the outer amorphous layer proportional to the elapsed time. After a given sputtering time the average IQ reaches a maximum and subsequently does show a kind of overexposure. The reasons of the deterioration in the surface quality are the same as in case of angle dependence.

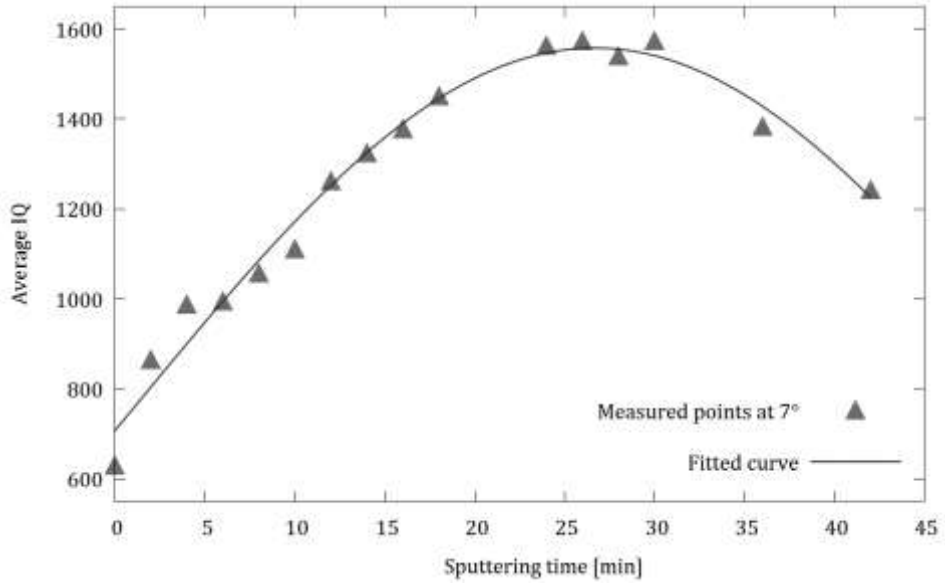

Fig. 2. Effect of sputtering time on the average IQ.

Fig. 3 a) and b) compare SEM images of mechanically polished surface before and after ion milling. The initial surface after mechanical polishing is very smooth. An area with some initial imperfections has been selected to illustrate their later evolution. The smoothness is the result of the so called smeared, or ironed out, amorphous outer layer. Upon multiple short-time application of the ion milling process the smooth surface became slightly rougher and the surface irregularities became larger due to sputtering.

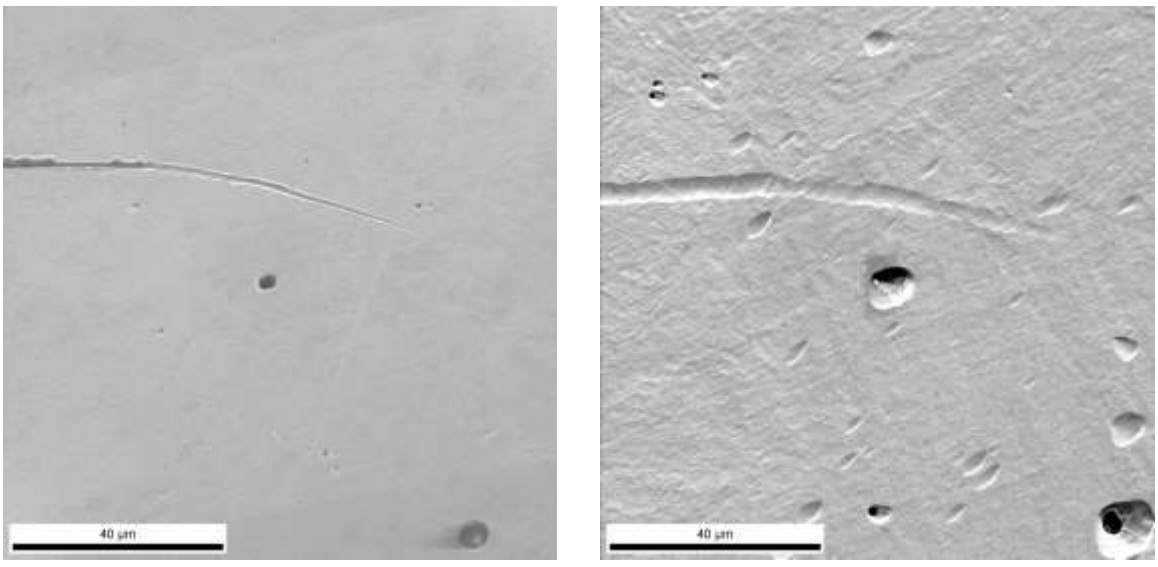

a) b)

Fig. 3. a) SEM image of the ion untreated surface. b) SEM image of the surface milled for 30 min by 7° incidence angle ion beam.

Fig. 4 a) and b) show IQ maps of the mechanically polished surface before and after ion milling. Scratches and inclusions are apparent on the IQ map of the mechanically polished sample. The local IQ values are very low everywhere on the scanned surface due to presence of the amorphous outer

layer. After ion milling the IQ map spectacularly shows the multilevel lath martensitic microstructure, such as packets, blocks, single laths, and the fine grain boundaries separating them.

This IQ map shows that single crystallites (so called laths) can have high IQ values: usually the larger a lath is the higher will be its average IQ value. IQ values of grain boundaries are usually much lower than those of the lath's and therefore they reduce the average IQ of the whole scanned area. It also can be seen that the slight increase in surface roughness caused by the ion milling negligibly affects the IQ values, since the Kikuchi lines originating from the individual eroded, slightly tilted microscopic surface elements are still easy to process and to qualify with the IQ figure.

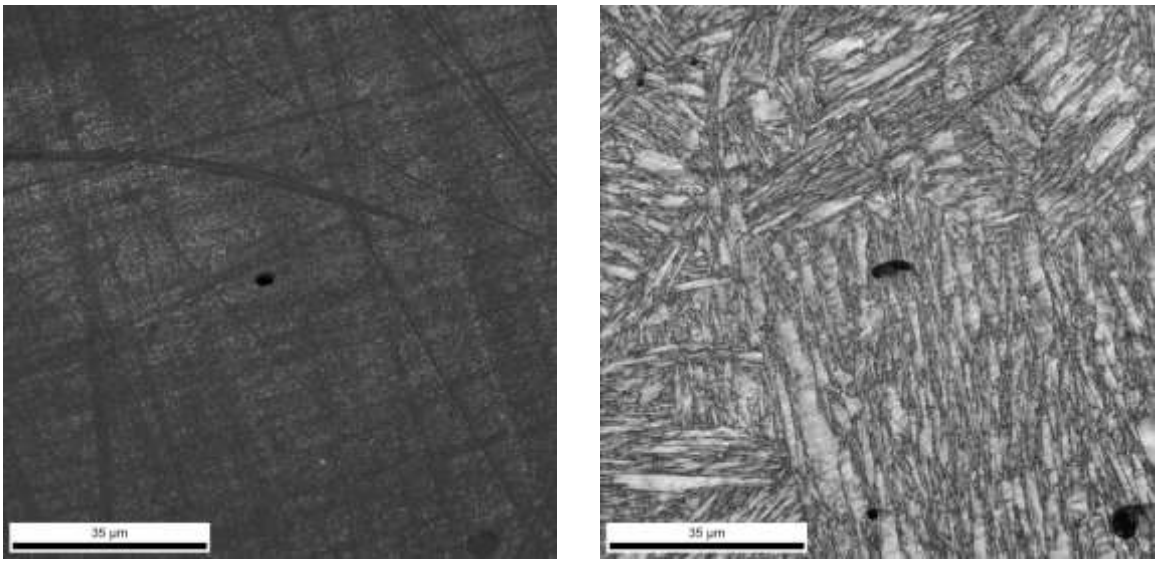

a) b)

Fig. 4. a) IQ map of the ion untreated surface. b) IQ map of the surface milled for 30 min by 7° incidence angle ion beam.

The high quality of the Kikuchi lines suggests, because they arise in the upper 50 nm layer, that the outer amorphous layer was almost perfectly removed by the properly selected ion milling parameters.

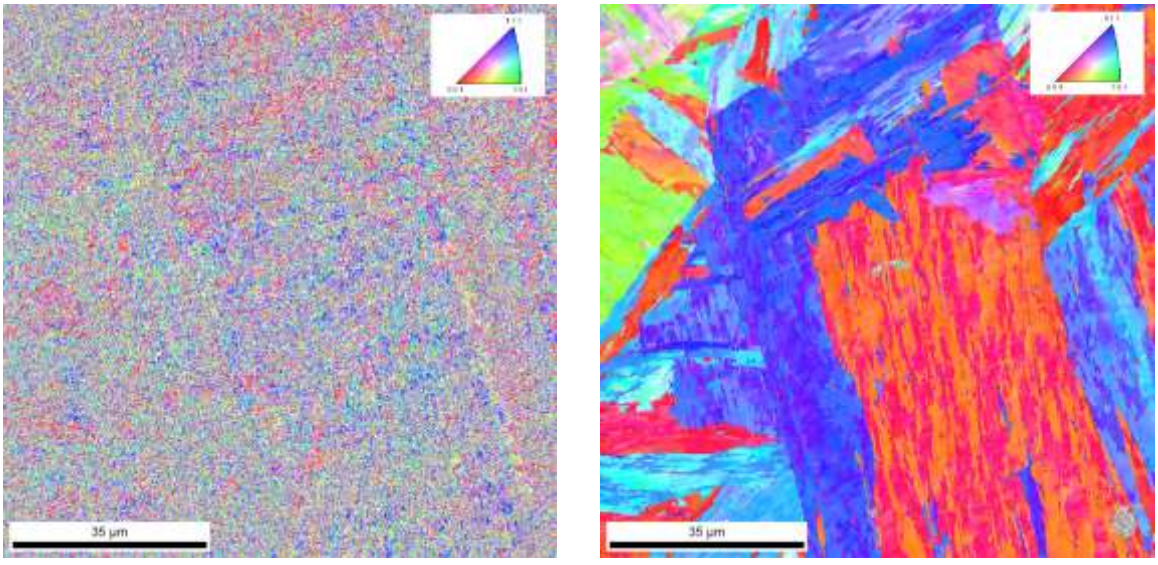

a) b)

Fig. 5. a) IPF map of the ion untreated surface. b) IPF map of the surface milled for 30 min by 7° incidence angle ion beam.

Fig. 5 a) and b) show inverse pole figure (IPF) maps before and after ion milling. An EBSD IPF map shows the orientation of a crystallite in a given point, determined from the Kikuchi pattern. The different orientations are represented with different colors. Details of the microstructure are not recognizable before ion milling (Fig. 5 a), similarly to the case of IQ maps. However after ion milling (Fig. 5 b) different areas can be seen on the IPF map with different and coherent orientation. The IPF map reveals the small differences between the orientation of the adjacent laths, as the adjacent light and navy blue, respectively the red and orange areas illustrate.

Summary and conclusions

High energy (10 keV) Ar-ion milling is a useful tool to prepare quenched low-carbon low-alloy steel samples for EBSD examination despite of the high density of dislocations in the martensitic crystal. For the high quality EBSD pattern the previously polished surface of the steel samples should be ion milled for 24...30 minutes by a 10 keV Ar-ion beam at ~7° angle of incidence.

The milling time to achieve the best surface quality seems to be longer compared to other softer materials, which are 7 min. in case of Cu and Fe, 6 min. in case Al and Ni milled also by Ar ion beam of 10 keV [9]. The reason for this difference is certainly that the martensitic steel has extremely high strength and toughness. During this relatively long milling time the surface smoothness of the steel material seemingly decreases and the size of pits and other surface roughness increase, however these do not affect the quality of the EBSD pattern.

SEM/EBSD is an effective tool to study the multilevel microstructure of low-carbon low-alloyed lath martensitic steel. In case of high quality EBSD pattern the IQ map looks like a conventional SEM image, nevertheless it can characterize the fine structure of the near surface region.

Acknowledgement

This work was supplied by the Hungarian Scientific Research Fund (OTKA PD 101028).

This work is connected to the scientific program of the "Development of quality-oriented and harmonized R+D+I strategy and functional model at BME" project. This project is supported by the New Hungary Development Plan (Project ID: TÁMOP-4.2.1/B-09/1/KMR-2010-0002).

References

[1] G. Beilby, Aggregation and Flow of Solids, Macmillan, London, 1921.
[2] V. S. Smentkowski, Trends in sputtering, Progress in Surface Science 64 (2000) 1-58.
[3] P. Sigmund, Theory of sputtering. I. Sputtering yield of amorphous and polycrystalline targets, Physical Reviews 184 (1969) 383-416.
[4] Z. Gaál, P. J. Szabó, J. Ginsztler, Evolution of special grain boundaries in austenitic steels, Materials Science Forum 589 (2008) 19-24.
[5] Hiromoto Kitahara, Rintaro Ueji, Nobuhiro Tsuji, Yoritoshi Minamino, Crystallographic features of lath martensite in low-carbon steel, Acta Materialia 54 (2006) 1279–1288.
[6] S. Morito, H. Tanaka, R. Konishi, T. Furuhara, T. Maki, The morphology and crystallography of lath martensite in Fe-C alloys, Acta Materialia 51 (2003) 1789–1799.
[7] Information on SC-1000 SEM sample preparation system: http://www.technoorg.hu
[8] Information on FEI Quanta 3D dual beam SEM: http://sem.elte.hu
[9] Z. Dankházi, Sz. Kalácska, A. Baris, G. Varga, Zs. Radi, K. Havancsák, EBSD sample preparation: high energy Ar ion milling, to be published.

Examination of thermodynamic realignments of metals and metal-alloys, by DMTA technique

Béres Gábor, Dugár Zsolt, Kis Dávid, Hansághy Pál

6000 Kecskemét, Izsáki út 10. Hungary

e-mail: gabberix@freemail.hu

Keywords: DMTA, recrystallization, DSC, hardness analyze, tin-bronzes, brasses, viscoelastic

Abstract.
The researcher work pushes the borders of the application of a high efficiency equipment, in the matter of metals. With this equipment, which already testified in the compound industry, a flasher query of some metal-related technological parameters could be easily available. Towards the searching, we shaped different compound copper-alloy samples, in different states, and accordingly we monitored the realignments. Following the shaping, the DMTA detected such microscopic transformations (as we expected), according to heating rate, whereby we could determine the specialities of the transformations. In order to monitor the effect of the work hardening, we applied two different shaping grade: 50% and 75%. The heat treatment already took place in the DMTA, using 3 K/min heating rate. The specimens were loaded by inflection in the 2-point bending support with constant frequency and amplitude.
Our current object was the monitoring of the recrystallization, and the investigation of the influential factors of this process, but other transitions were also regarded. Those measurements' results, that the DMTA presented, had been compared with DSC and hardness analysis, whereby we try to conclude to the utility of DMTA, in matter of metal alloys.

Introduction

The researcher team examines both the industrial metals (principally) as well as the high-tech materials and special metals (for example shape memory alloys) with DMTA equipment. Our main object is the monitoring of the recrystallization, in case of copper alloys and the investigation of the influential factors of this process. The measurements' results, that the DMTA presented, had been compared with DSC and hardness analyses.
The literature research added up to that, we are not the first to examine metals with DMTA. But other (particularly Asian) researchers usually take into consideration the copper as alloying element or as compound, not as all-metal. For example Tang et al. examined the structure of copper electropolyurushiol film. The EPU-Cu2+ film was characterized by dynamic mechanical thermal analysis, but the Cu2+ content in the coordination polymer is only 8.63 %, as compound [5]. There are still many events, when the copper gives the base for surface treatment. Loo et al. investigated N,N-dimethylthioacetamide adsorbed on Ag and Cu electrode surfaces. The comparison was made by vibration analysis of DMTA [6].
In contrast with them, we would like to write up the measurement method, whereby the properties of the industrial material itself, would be easier defined.
The DSC detected the convection, due to energy release or energy attenuation. The DMTA is able to load mechanical stress, next to heating [1]. Therefore it can determine the changes of the mechanical properties, otherwise than DSC. Furthermore, it is a very precise instrument. The exact temperature monitoring with hardness analyses are difficult because of the variation of the furnaces' constant temperature [2].
In case of a visco-elastic material the σ bending stress is delayed to the deformation with delta angle (figure 1). In case of clearly viscous materials, like the water, the delay is 90°. Because the copper alloys are elastic materials, the σ bending stress and the deformation should have be in the same phase [1].

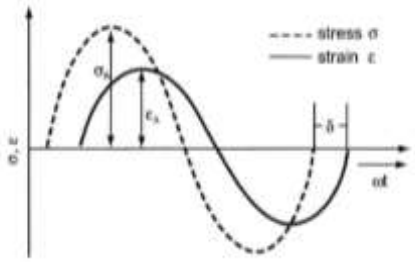

Fig. 1. DMTA curve

In the curves of the DMTA, the loss factor appeared. It means that in certain cases, the investigated copper alloys also can show similar properties than visco-elastic materials.

Method

Samples

The baseline was four different compound copper alloy ingots. The rolling was started from 15 mm thickness, on 500°C. This relatively low temperature ensured the avoidance of the oxidation. Samples were manufactured from all of the ingots on 2 mm and on 4 mm thickness. Next to four different compositions, it means eight pieces of samples. All of the samples were softened one hour. After that, all of the samples were rolled to 1 mm thickness, on room temperature. Based on this I made two different shaping grades. In case of the initial 4 mm thickness samples, the deformation grade became 75%. In case of the initial 2 mm thickness samples, the deformation grade became 50%. It is well known, that the temperature of the recrystalliaztion is depend on the structure, and the shaping grade of the material [4]. In this way I tried to monitor both the effect of the shaping and the composition during the searching.

I selected such copper alloys, which processing is done by forming. It was necessary because of the recrystallization. The mark of the samples originated from University of Miskolc. The determination of the exact composition was done by spectrometer:

- sample 31 (sample 10): 58,8 % Cu 40,9 % Zn
- sample 24: 61,3 % Cu 26,8 % Zn > 5 % Ni
- sample 21: 91,5 % Cu 6,19 % Sn
- sample 23: 95,8 % Cu 3,70 % Sn

At first sight, the samples can be partition into two groups:

- the first two samples are brasses: (31, 24)
- the last two samples are tin-bronzes: (21, 23)

Examining brasses, in case of the sample 24 the average Zn content is lower than 30%, and the average Ni content is more than 5%. Based on this, the sample 24 belongs to formed brasses. The sample 31 may seem rigid alloy because of the high Zn content. However, in the lack of other elements, it also can be organized to the group of formed brasses [3].

In case of the tin-bronzes, the average Sn content is between 2% and 14%, and there are no casting type elements. So these samples belong to the group of formed tin-bronzes [3].

Preparation

I applied two point bending method. The measurement frequency was 5 Hz, the amplitude of the elongation was 10 μm. The measurements were carried out in air. The DMTA provided the heating of the samples with 3 K/min heating rate. The DSC samples were manufactured by cutting. The cutting made the samples' structure formed, therefore some DSC measurements failed. Furthermore I had to clear the samples in alcohol. The hardness analyses were done by Instron Wolpert 2100B Vickers hardness tester. The samples were heated from room temperature to 500°C. The frequency of the measures was increased between 400°C and 500°C, for more precise results. Five parallel measurements were done in all temperatures. The edge values were left and the middle three values' average was taken.

Results

In case of copper alloys, the peak of the loss factor is around at 0,1 and 0,2 on the DMTA curves. The value is smaller than polymers by one decimal digit. The value of the loss factor is usually about at 1,5 at polymers.

Sample 21 (tin-bronze)

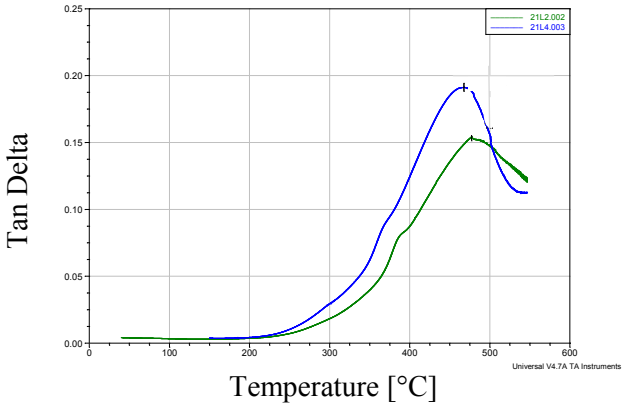

Fig. 2. DMTA curve of sample 21, tanδ highlighted: 50% (green) and 75% (blue) shaped

The transitions are well visible in both diagrams. The blue curve shows the 75%, the green curve shows the 50% deformed sample. The main peaks around 470°C, refer to the β-β' transitions. The temperature of β-β' transition is as lower as the deformation higher. It is also true for the recrystallization. The bigger deformation grade gives the bigger area under the curve. The recrystallization starts at around 400°C, according to the hardness analyze (figure 3). The smaller, tanδ peaks would refer to it (figure 2).

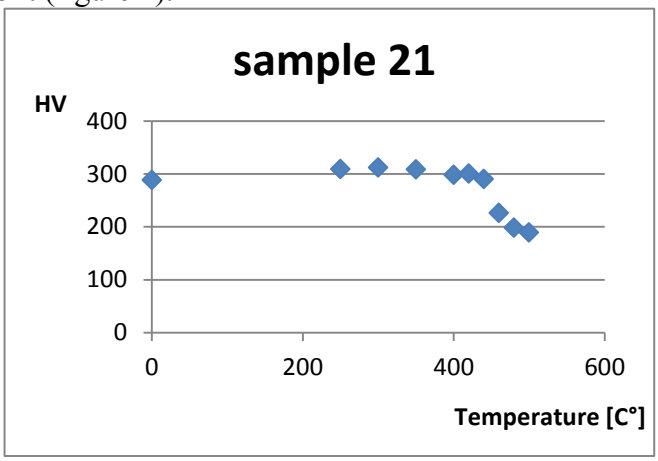

Fig. 3. Hardness analyze result of sample 21

Sample 23 (tin-bronze)

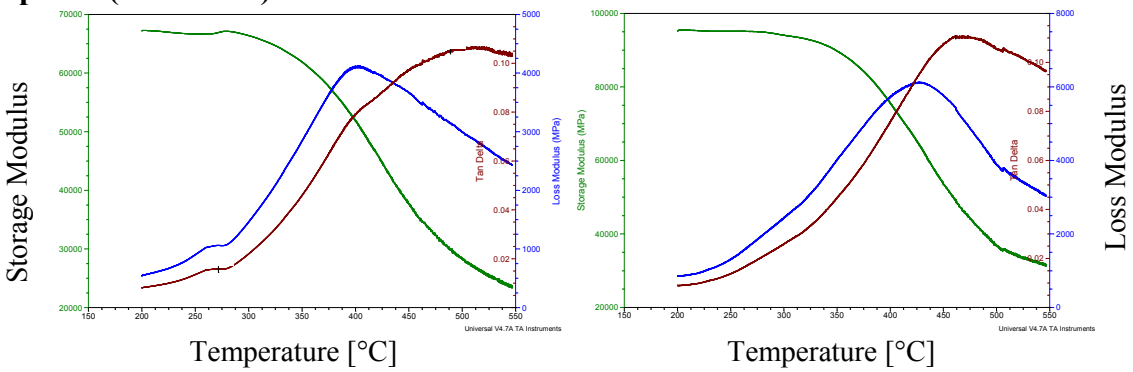

Fig. 4. DMTA curve of sample 23, 50% (left) and 75% (right) shaped

The β-β' transitions are clear in both cases. Unfortunately the recrystallization is not visible in the curves. On the left side of figure 4, a little peak can be seen roughly on 400°C, which refer to it. It is

justified by the DSC curve on figure 5. The recycling is also clear, in lower temperature range, at 271°C. The curve of the 75% deformed sample (right) is flat until it reaches the β-β' transformation point. The reason for this believed, that too small grains grown up during to the recrystallization, which can't display the transition. The temperature of β-β' transition is also as lower as the deformation higher again.

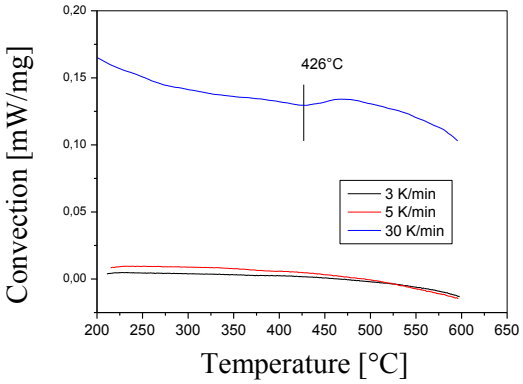

Fig. 5. DSC curve of sample 23

Sample 10 (brass)

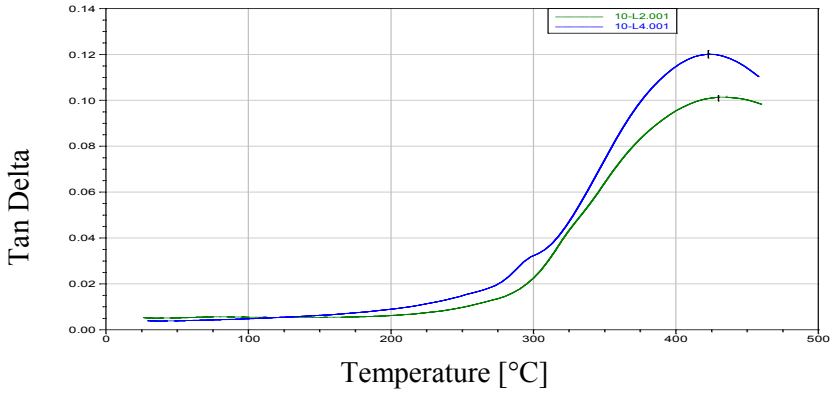

Fig. 6. DMTA curves of sample 10, tanδ highlighted: 50% (green) and 75% (blue) shaped

Based on the results, I conclude that the recrystallization takes place at around 300°C, lower than tin-bronzes. It can be clearly seen in case of 75% deformed samples, but no peaks appeared on 50% shaped sample's curve. The β-β' transitions are also visible, as in the previous cases.
The diagram clarifies well the discrepancy between the effects of the shaping grade. The biggest area under the curve, and the lower temperature of β-β' transition belongs to the biggest deformation, which is shown by the blue curve.

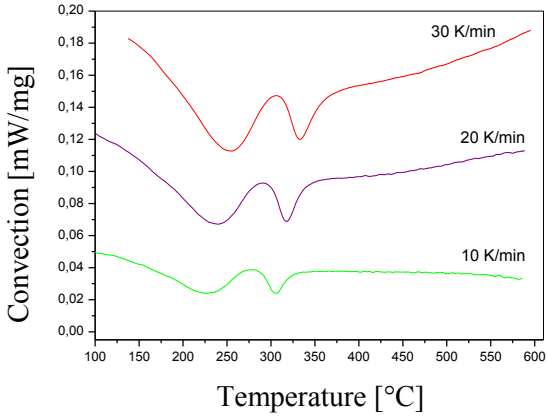

Fig. 7. DSC curve of sample 10

The place of the DSC peaks was changed by the heating rate. But it still can be seen, that the recrystallization happened around 300°C as the DMTA and hardness analyze (figure 8) show.

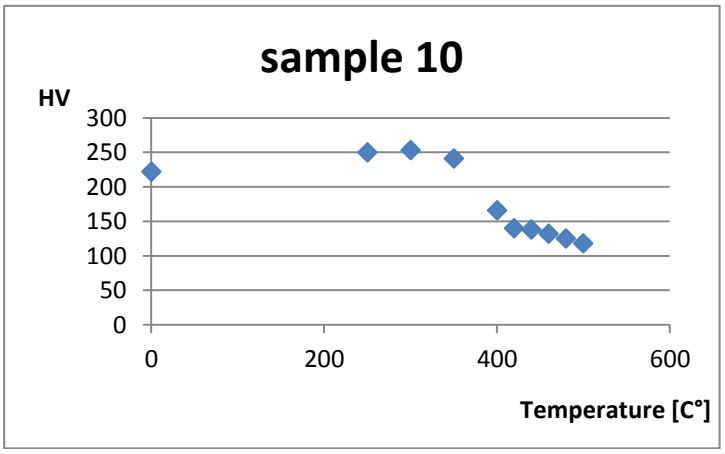

Fig. 8. Hardness analyze result of sample 10

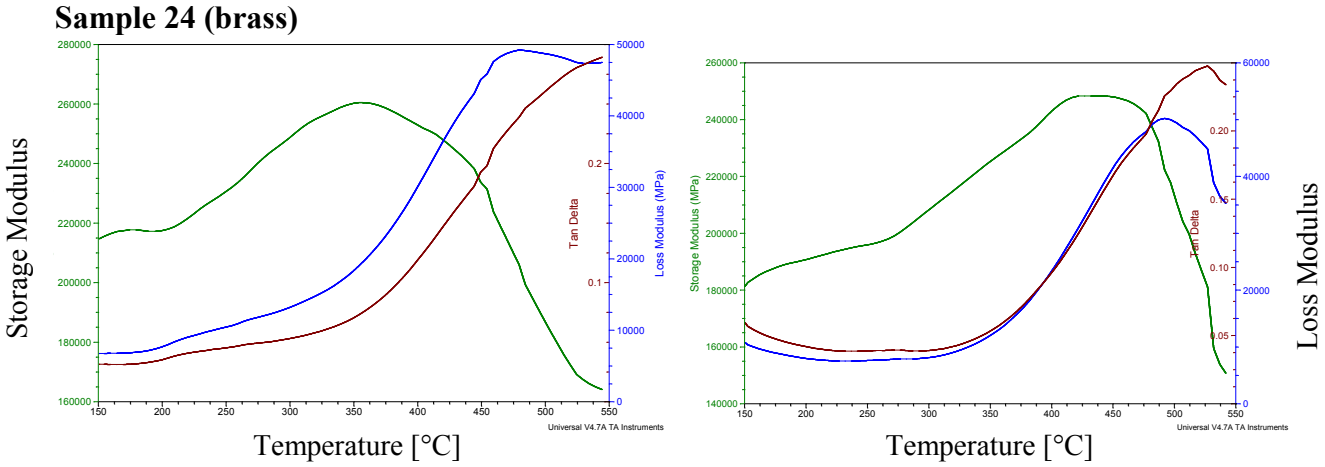

Fig. 9. DMTA curve of sample 24, 75% (left) and 50% shaped

In case of 75% deformed sample, the β-β' transition took place such high temperature, that was outside the boundaries of the measuring. There is an uncertainty at around 450°C, which is maybe not enough to declare the recrystallization, but according to the DSC (figure 10 left) and the hardness analyze (figure 10 right) it should be there. In lower temperature range, between 200°C and 250°C, the recycling appeared.

In case of the 50% deformed samples, only the β-β' transformation can be seen. This is already the second event of brasses, when the recrystallization does not appear at lower deformation grade. Furthermore it should be mentioned that the highest loss factor values are shown by the DMTA curve of sample 24. Both curves' peaks transcend the 0,2 tanδ value, the more deformed sample better, the less deformed sample less. Based on this it is observed, that this sample is the most elastic.

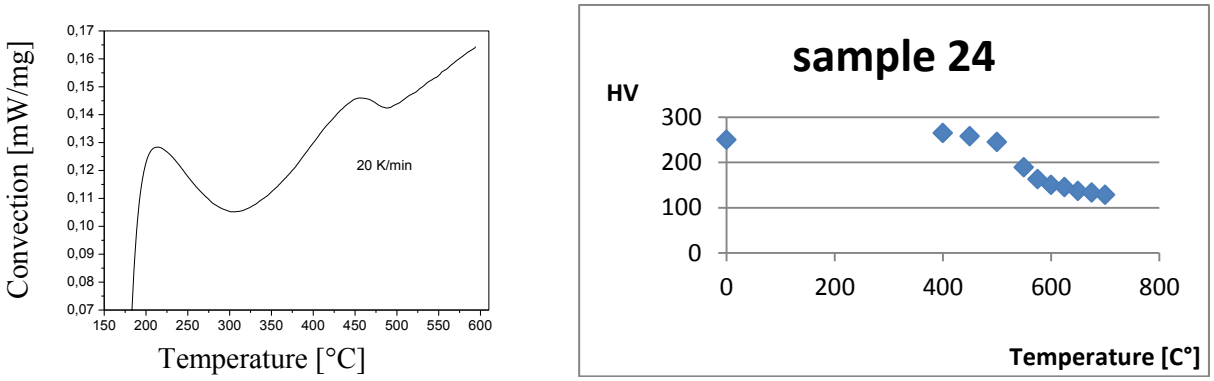

Fig. 10. DSC curve (left) and hardness analyze result (right) of sample 24

Left, on the DSC figure, the first peak refers to the recycling, the next one, around 450°C refers to the recrystallization. The end of the process is not in the figure, as in the case of DMTA.

Conclusion

Realignments of copper alloys were investigated in different circumstances. To reveal the transformations we applied DMTA, DSC equipments, and hardness analysis. Transitions have been demonstrated in several cases. β-β' transition is always visible, expect only in one or two times. In case of brasses, the presence of the recrystallization depends on the shaping grade. It is never appeared under 75% deformation. The recycling is visible in more cases in lower temperature ranges.

Based on the results, we succeeded in demonstrating the appearance of the loss factor, with this new measurement process. Furthermore, it is observed, that the thermo-dynamic measurement process is a suitable method for monitoring realignments.

Acknowledgement

The research work presented in this paper/study/etc. was carried out as part of the TÁMOP-4.2.2.A-11/1/KONV-2012-0029 project in the framework of the New Széchenyi Plan. The realization of this project is supported by the European Union, and co-financed by the European Social Fund.

References

[1] Joel R. Fried: Polymer Science and Technology
[2] Raymond A. Higgins: Engineering Metallurgy, Applied Physical Metallurgy, Hodder Headline Group 1993.
[3] ASM Metals Handbook Desk Edition 2001. Volume 2: Properties and Selection: Nonferrous Alloys andSpecial-Purpose Materials
[4] William F. Hosford:, Robert M. Caddel: Metal Forming, Mehanics and Metallurgy, Cambridge University Press 2007.
[5] Tang, JY; Zhang, WG; Shen, GC; Gao, F: Coordination structure of copper electropolyurushiol film and its catalytic performance for methyl methacrylate, Chinese Journal of Catalysis Volume: 22 Issue: 2 Pages: 119-123, mar. 2001
[6] Loo, BH; Lee, YG; Kato, T : Raman-Spectra os N,N-Dimethylthioacetamide Adsorbed on Silver and Copper Electrode Surfaces, Bulletion of the Chemical Society of Japan Volume: 64 Issue: 10 Pages: 3126-3128, oct. 1991

A method for the determination of ferrite grains with a surface normal close to the (111) orientation in cold rolled steel samples with color etching and optical microscopy

Attila Bonyár[1, a], Péter J. Szabó[2]

[1] Budapest University of Technology and Economics, Department of Electronics Technology, H-1111 Budapest, Egry József street 8., Hungary

[2] Budapest University of Technology and Economics, Department of Materials Science and Engineering, H-1111 Budapest, Bertalan Lajos street 7., Hungary

[a]bonyar@ett.bme.hu

Keywords: optical microscopy, electron back scattering diffraction (EBSD), color etching, steel.

Abstract. Cold rolled steel specimens were investigated by color etching. We proved that in this sample ferrite grains with a surface normal close to the (111) orientation are etched with the slowest speed with Beraha-I type color etchant, and that after a sufficient over-etching these specific grains could be distinguished based on this feature. It was demonstrated, that it is possible to stop the color etching in a phase when only grains with (111) orientation show color due to the layer interference, while all the other grains are dull gray due to a thick and transparent layer. This observation was utilized to develop a method to identify and quantify ferrite grains with (111) orientation in cold rolled steel samples with the application of color etching, optical microscopy and digital image post-processing.

Introduction

During a traditional metallographic investigation, the grains are made visible by etching. Two main types of etching are applied: 1) the corrosive chemical etching, when an etchant removes the top layer of the metal in a selective way, and 2) the so-called color etching, when a thin film is deposited on the top of the metal, causing light interference between the reflections from the metal surface and from the layer surface [1]. Chemical etching is orientation sensitive, which means that grains having different crystallographic orientations are etched differently in depth. This phenomena is frequently used in anisotropic etching of silicon single crystal wafers [2], but was also observed in the case of quartz wafers [3], and other applications. Orientation dependent topography formation has also been reported for mechanical polishing [4] and FIB-cutting [5]. The orientation dependence of the color etching was observed qualitatively by Ray et.al. [6]. Quantitative orientation dependence was shown by Szabo et. al. [7], where the correlation between color shade and the crystal orientation was determined.

The thickness of the interfering layer after color etching is depending on the etching time and the etching speed of the grains, which was proven to be crystal orientation sensitive in our previous works [8, 9]. Depending on the thickness of the formed interfering layer the grains will either be colored – standard procedure with small or moderate etching time, where the thickness of the film and thus the color of the grain correlate to the crystallographic orientation – or by elongating the etching time to 7 minutes, the film atop the over-etched surface becomes transparent. In the case of the standard procedure it is very hard to directly and precisely relate the color to the crystal orientation, since as the thickness of the interfering layer increases the color changes cyclically – which means that one grain changes color several times as the etching progresses – and also abruptly. This cyclic change in the color means, that it is possible – after a given etching time – that grains with different orientations will have the same color. This explains the parallel lines, which Szabó and Kardos observed while investigating the correlation between the color shade and the orientation in their work [7].

In this work we prove that by stopping the etching process close to the borderline of over-etching it is possible to selectively color the grains which are etched with the slowest speed. In this case only these specific, slowly etched grains will have interference color, as the thickness of the interfering layer above all the other grains will pass the transparency borderline. Since by increasing the etching time we increase the differences between the thicknesses of the interfering layers above the grains, it is much easier to reproducibly reach this phase of the etching process, compared to the standard color etching procedure, where the changes in the color are abrupt. In other words, by working on the borderline of over-etching we are less sensitive to the variations in the etching parameters (precise etching time, temperature etc.), which increase the stability and reproducibility of the procedure.

Hereby we demonstrate that in the case of a cold rolled steel sample the grains which are close to the (111) orientation are etched with the slowest speed, and that this fact can be used to design a method to determine the relative frequency of these grains in the sample by utilizing only color etching, optical microscopy and digital image post-processing. Several metal processing technologies require or favor textured microstructures. For example the deep drawability of the cold rolled steel sheets are depending on the frequency of grains close to the (111) orientation, when the plane of the sheet is perpendicular to the drawing direction. Several groups are working on the development of the sheet processing technologies (rolling, annealing) to improve the frequency of (111) grains in the steel sheet prior to deep drawing [10, 11]. Our method, which enables the determination of this frequency without the need of expensive equipment (transmission electron microscope (TEM) or a scanning electron microscope with electron back scattering diffraction extension (SEM-EBSD)) and elaborate sample preparation could be a valuable tool for researchers working in this area.

Materials and Methods

The alloying elements of the cold rolled steel specimen are given in Table 1. The chemical composition of the Beraha-I etchant is: 3 g $K_2S_2O_5$, 10g $Na_2S_2O_3$ in 100 ml distilled water.

C	Mn	Si	S	P	Cu	Cr	Ni	Al	Mo	Ti	Nb	V
0.06	0.68	0.008	0.006	0.012	0.05	0.09	0.04	0.06	0.001	0.001	0.021	0.002

Table 1. The alloying elements of the steel in wt%

In order to investigate the connection between the striping of the grains and their orientation the following experiments were done. First, EBSD measurements were performed on the sample surface with a Philips XL-30 scanning electron microscope and an EDAX-TSL automated EBSD-system. As a positioning marker, a micro-Vickers hardness indent was used. Consecutively, after a traditional preparation technique (grinding, polishing) the specimen was immersed into Beraha-I color etchant, which was stirred above the sample during the whole etching process, which lasted for 2.5 minutes for standard color etching and 7 minutes for over-etching. After investigating the sample with optical microscope, the surface of the specimen was cleaned by removing the interfering layer by rinsing it into 0.5 % sulfuric acid for 3 s. Finally contact mode AFM images were taken with a Bruker diInnova scanning probe microscope (SPM) with Veeco MSCT-AUNM-10 probes. For data evaluation the Gwyddion 2.27 software was used.

Results and Discussion

Figure 1 presents an EBSD inverse pole figure map and an optical micrograph of the sample. The EBSD measurement was done directly prior to the color etching. The optical micrograph illustrates the so called borderline state of over-etching. In this case only some of the grains have interference color, while others are gray due to the too thick and thus transparent layer. On the right image we highlighted the grains which still show color and it is clear that they are close to the [111]

orientation (see top left insert). This means that, the layer which causes the color interference is the thinnest above these grains, and based on our previous works [9], this means that they are etched with the slowest speed.

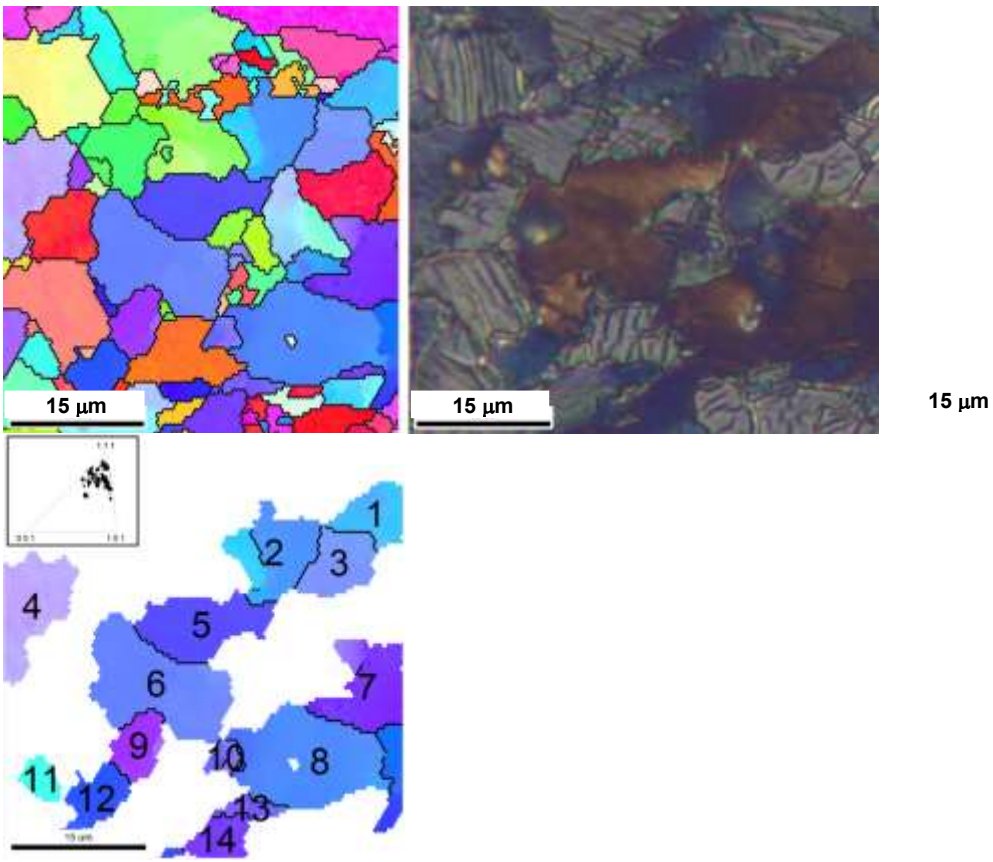

Figure 1. Inverse pole figure of the cold rolled steel specimen (left); optical micrograph of the same area of the specimen after color etching (middle); inverse pole figure of the specimen highlighting the grains which have an orientation close to [111] (right).

The AFM image presented on Figure 2 also confirms this statement. Note that the area of interest is the same on the images of Fig. 1 and 2. On the cross-sectional profile it can be clearly seen, that the height difference of the grains, which was measured after removing the interfering layer by rinsing in mild sulphuric acid for 2 second – which is supposedly does not etch the steel any further – is significant. Based on the interference criteria, this 0.5 µm difference is enough to cause the thicker layer to be transparent, while the thinner is still capable of interference.

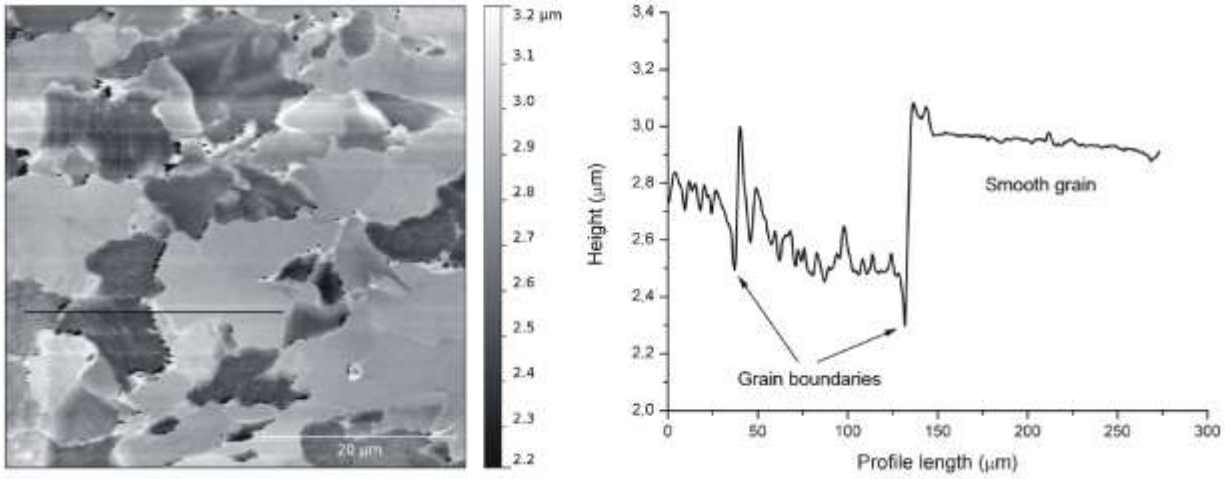

Figure 2. Contact mode AFM image (left) and cross-sectional profile (right) of the same specimen after the removal of the interference layer with mild sulphuric acid.

It is also interesting to note, that the surface of the higher grains – which are close to the (111) orientation – are smooth, while all the other grains have striped patterns. These patterns can clearly be seen on the optical microscopy images as well (Fig 1, 3, 4), and the AFM image confirms that this pattern is located directly on the surface of the grains, and not in the interfering layer, since the latter was completely removed prior to the AFM measurements. The exact causes behind this phenomenon are currently under investigation; hereby we only want to note, that the lack of stripped pattern on the grains close to the (111) orientation also enables another way to selectively distinguish them from the other grains with digital image processing.

Our currently proposed method however utilizes only the differences in the orientation dependent etching speed of the grains. Figure 3 illustrates the main steps of the method. First the cold rolled steel sample was over-etched with Beraha-I type reagent for 7 minutes. The optical micrograph of Fig. 3 shows, that in this phase only the grains close to the (111) orientation show distinctive interference color, which is blue. Note, that the blue color of the (111) grains in Fig. 3 is a bit different from the color in Fig. 1, which is between brown and blue. In this phase of over-etching colors change rapidly before graying due to the too thick layer, so the precise control of etching time and also temperature is required to end up with a desired color. It is still true, that the (111) grains lose color last due to the slowest etching speed in this direction, however the possibility of small variations in their color needs to be considered – and thus the subsequent image processing adapted accordingly – if the etching parameters are not controlled precisely.

To identify these blue grains on the image, the gray scaled red channel (which is complementary to blue color) was selected from the RGB system (Fig. 3/B). We investigated the B and G channels and also other color systems (CMY, Lab) as well, but found that the R channel has the best contrast for the detection of the blue grains of the image. The next phase of the detection is the binarization of the image based on a pre-defined threshold. The gray scaled image of Fig. 3/B is transformed to the black and white image of Fig. 3/C by selecting the threshold on a scale of 256. As you can see on Fig. 3/C the binarized image contains several features, which are considered noise, such as the striped pattern on the other grains. To selectively filter the grains which are close to the (111) direction several established grain detection algorithms – such as the watershed, for example – could be used [12]. In our case a simple cyclic "erode-dilate" type MATLAB algorithm was used. On the final image of Fig. 3/D the black/total pixel ratio is equal to the ratio of the grains with (111) orientation in the sample, which was 29 % for this example.

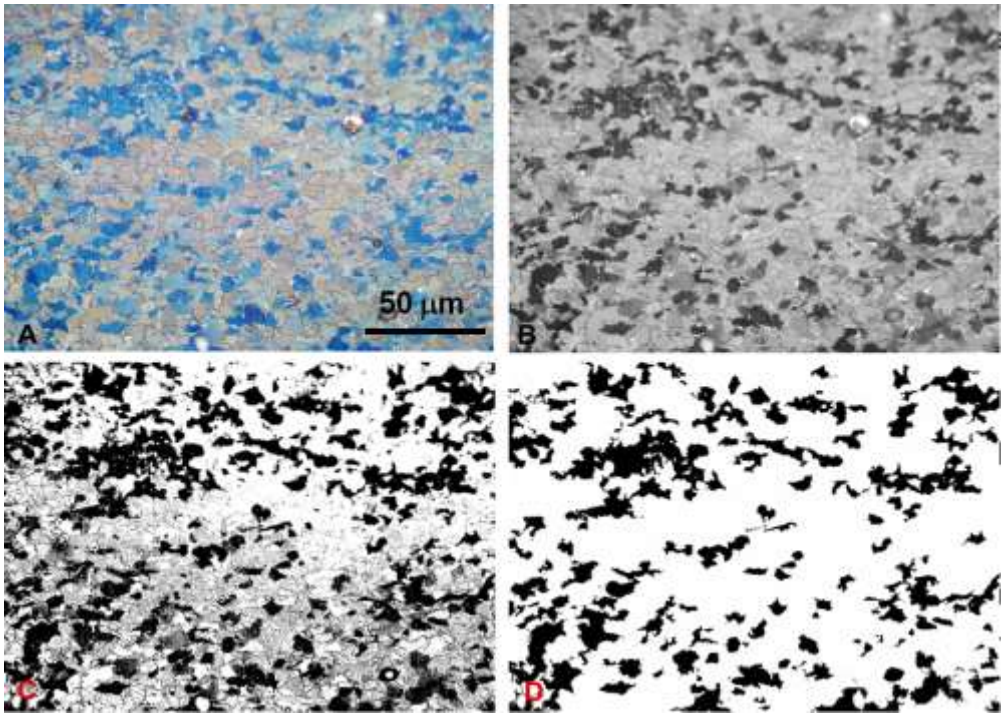

Figure 3. The original optical micrograph after color etching for 7 minutes; B) gray scale image from the red channel of the original micrograph; C) binarized image after tresholding; D) after the application of grain segmentation (filtering).

We have to note that the selection of the threshold value is a critical step of the image processing. The effect of different binarization thresholds is illustrated on Fig. 4. The smaller the threshold of binarization is (on a range of 256) the stricter is the selection of the grains. In this example the threshold was varied between 70 and 100 and it can be seen, that in the case of the higher threshold more grains are selected – and some of them are not considered to be entirely blue on the original image. The black/total pixel ratio is 21 %, 27 % and 35 % for Fig. 4/B/C/D respectively. The selection of the appropriate threshold is the task of the user and is depending on the desired application. As can be seen on the EBSD inverse pole figure of Fig. 1, based on the angle between the grain surface normal and the (111) direction the grain orientations have a distribution, in other words some of them are closer to (111) than the others. We could say that, by lowering the binarization threshold only the grains closest to the (111) orientation are selected, while a higher threshold enables a wider selection of the grains.

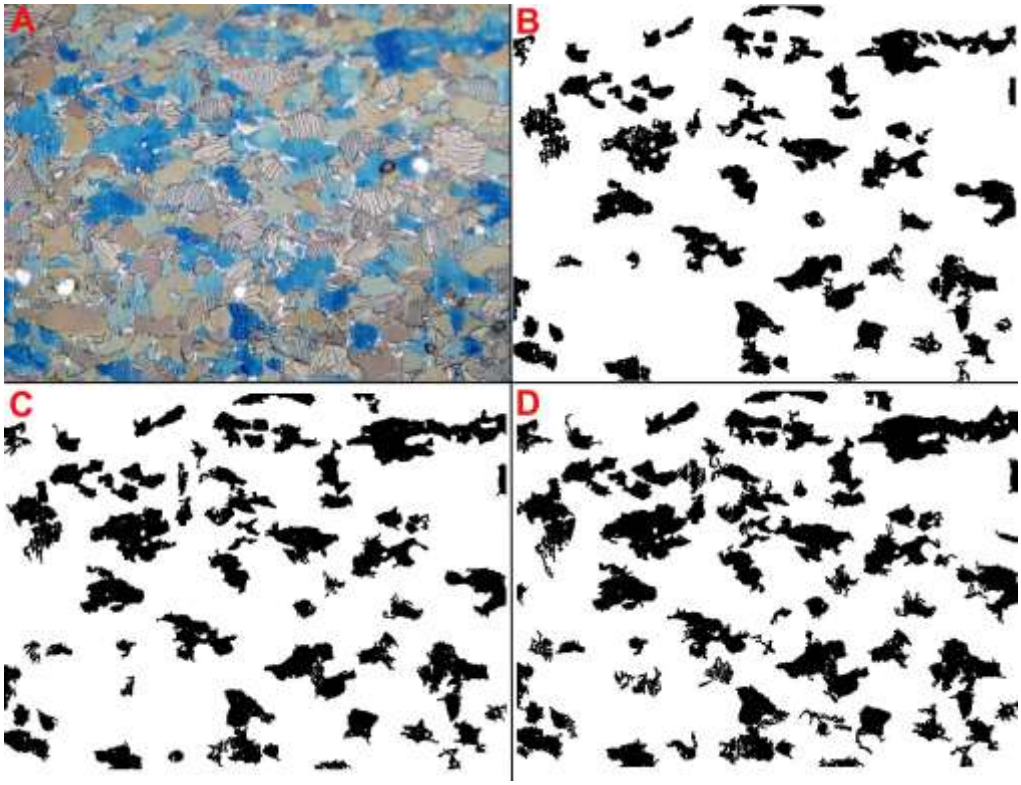

Figure 4. A) the original optical micrograph after color etching for 7 minutes; B-D) the application of different binarization tresholds (70, 85, 100) on a scale of 256.

Conclusions

A method to identify and quantify the number of grains which are close to the (111) orientation in a cold rolled steel sample was presented. The method is based on color etching with Beraha-I type reagent, optical microscopy and image processing, and does not require expensive equipment (such as TEM, EBSD) or elaborate sample preparation. The exact mechanism behind the etching with Beraha-I was described, along with two possibilities to distinguish the (111) grains: 1) the lack of a striped pattern, which always occur after a given etching time; and 2) and a distinguished color after over-etching, due to the slowest etching speed in this direction. An effective image processing method for the identification of the grains based on the latter property was proposed and demonstrated for blue (111) grains.

Acknowledgement

This research was supported by the European Union and the State of Hungary, co-financed by the European Social Fund in the framework of TÁMOP 4.2.4. A/2-11-1-2012-0001 'National Excellence Program'.

References

[1] G. Vander Voort, Metallography. Principles and Practice. McGraw-Hill Book Co., New York, ASM International, Materials Park, Ohio, 1984.

[2] K. Sato, M. Shikida, Y. Matsushima, T. Yamashiro, K. Asaumi, Y. Iriye, M. Yamamoto, Characterization of orientation dependent etching properties of single-crystal silicon: Effect of KOH concentration, Sensors and Actuators A 64 (1998) 87-93.

[3] T. Ueda, F. Kohsaka, T. Iino, D. Yamazaki, Theory to predict etching shapes in quartz and application to design devices, Trans. Soc. Instrument Control Eng. 23 (1987) 1233-1238.

[4] H. Zhu, Chemical Mechanical Polishing (CMP) Anisotropy in Sapphire, Applied Surface Science 236 (2004) 120-130.

[5] M. Lenius, R. Kree, C. A. Volkert, Influence of crystal orientation on pattern formation of focused-ion-beam milled Cu surfaces.Phys. Rev. B 84 (2011) 035451.

[6] A. Ray, S. K. Dhua, Microstructural manifestations in color: Some applications for steels. Mater. Char. 37 (1996) 1-8.

[7] P. J. Szabó, I. Kardos, Correlation between grain orientation and the shade of color etching, Mater. Char. 61 (2010) 814-817.

[8] P. J. Szabó, A. Bonyár, Effect of grain orientation on chemical etching, Micron 43 (2011) 349-351.

[9] A. Bonyár, P. J. Szabó, Correlation between the grain orientation dependence of color etching and chemical etching, Microscopy and Microanalysis, DOI 10.1017/S1431927612013554

[10] Y. Liu, J. Sun, L. Zhou, Y. Tu, F. Xing, Y. Guo, Q. Tong, Experiment investigation of deep-drawing sheet texture evolution, Journal of Materials Processing Technology 140/1 (2003) 509-513.

[11] Y. Yazawa, Y. Ozaki, Y. Kato, O. Furukimi, Development of ferritic stainless steel sheets with excellent deep drawability by {1 1 1} recrystallization texture control, JSAE Review 24/4 (2003) 483-488.

[12] M. Frucci, G. S. di Baja, From segmentation to binarization of gray-level images, Journal of Pattern Recognition Research 1 (2008) 1-13.

Innovative Residual Stress Measurements by X-Ray Diffraction

David Cseh[1,a], Valeria Mertinger[1,b] and Marton Benke[2,c]
[1]Institute of Physical Metallurgy, Metalforming and Nanotechnology, University of Miskolc, Miskolc-Egyetemvaros, Hungary
[2]MTA-ME Materials Science Research Group, University of Miskolc, Miskolc-Egyetemvaros, Hungary
[a]cseh88david@gmail.com (corresponding author),[b]femvali@uni-miskolc.hu, [c]fembenke@uni-miskolc.hu

Keywords: X-Ray diffraction, residual stress, $\sin^2\psi$ method, non-destructive measurements, stress tensor

Abstract

An innovative X-ray diffractometer especially designed for residual stress measurements was deployed at the Institute of Physical Metallurgy, Metalforming and Nanotechnology of the University of Miskolc. The advantages of the equipment over the traditional X-ray diffraction stress measuring methods are presented through our experiences on industrial components with varying sizes, geometries and measurement requirements. The microstructural limitations of the X-ray diffraction based residual stress measurement method are also discussed.

Introduction

The technical residual stresses have increasing importance nowadays. Residual stresses can be classified by their extent. 1st order or macroscopic stresses are in the range of the component size; 2nd order or microscopic stresses vary between individual grains and 3rd order or submicroscopic stresses vary within the grain. Technological stresses are typically 1st order stresses. The designed residual stresses can be really beneficial in some cases of applications. The intentionally generated compressive residual stress convincingly improves the fatigue performance of the material or a machine element [1,2,3,4]. On the other hand, residual stresses can also be harmful [5,6]. In general, a residual stress is called harmful if it works in the same direction as the dangerous external stress. The relevance of the residual stress demands the ability of their accurate measurements.
The 1st order or macroscopic stresses influence a series of characteristics of the material such as microstructure, magnetic behaviour and optical properties in case of transparent materials. Due to these effects several methods are used to described the residual state usually in metallic alloys for example electron, X-ray or neutron diffraction, Barkhausen noise, ultrasonic, hole drilling and other destructive methods. The Almen test is also very popular in the industrial practice. Among these techniques only the diffraction methods give truly quantitative results. It is evident what kind of influence does the residual stress have on the lattice parameter of an elastic material [7,8]. The compressive residual stress reduces the interplanar distance while the tensile does the opposite. The different diffraction methods are sensitive to these changes. The residual stress measurement by X-ray, as all of the other diffraction measurements is based on the Bragg's law (1).

$$n\lambda = 2dsin\theta \tag{1}$$

This equation gives the diffraction angle (θ) where the diffracted X-ray photons meet in the same phase for a given wave length (λ) and a lattice plane distance (d). (n is integer.) The diffraction angle appears as a peak on the recorded interference function. The diffraction angle of a stressed material is shifted compared to the relaxed value. The lattice parameter change is the source of this phenomenon which is generated by the residual stress. Assuming linear elastic distortions, the related normal stresses can be calculated by equation (2) [9].

$$\sigma = \frac{d_\psi - d_0}{d_0} * \frac{E}{(1+\nu)\sin^2\psi} \tag{2}$$

where d_0 and d_ψ are the lattice plane distances of the strained (stressed) material in the normal and in the tilted position defined by the angle ψ, respectively. E (Young modulus) and ν (Poisson number) are the elastic parameters of the material. The X-ray diffraction technique is a reliable method for stress measurements. However, the residual stress state of a component can be measured accurately only if the true stress state is not affected by sample cutting. This requirement demands a special equipment and measurement method [9,10**Hiba! A hivatkozási forrás nem található.**. 0

Experimental

The present manuscript gives on overview on the measurement possibilities by an innovative equipment of the Institute of Physical Metallurgy, Metalforming and Nanotechnology at the University of Miskolc. The equipment is a Stresstech Xstress 3000 G3R type X-ray diffractometer developed especially for non-destructive residual stress measurements. The presented diffractometer has a remarkable innovation compared to the traditional ones. In the case of traditional diffractometers the sample is tilted (ψ) by precision mechanics. The revolutionary construction of the G3R tilts the device instead of the specimen, which allows measurements without sample cutting, so the true stress state of the component is unaffected. Furthermore, there are no sample size and weight limits for the measurements.
Generally, the diffractometer is used in a radiation protection cabin (Fig. 1 a, b). In this case the measuring unit (X-ray tube, goniometer, detectors and the stepper motors with the tensor measuring arc) stand on three adjustable legs with magnetic anchoring. This configuration can be used without the safety cabin as a table top device. For such measurements a photocell controlled safety gate is connected into the safety circuit to ensure the radiation protection. To avoid height limitation, the device can be installed to a floor stand which ensures 6 orders of freedom to position the incidental beam path (in zero tilting position) perpendicular to the surface of any point. This is a huge benefit in cases of complicated sample geometries.

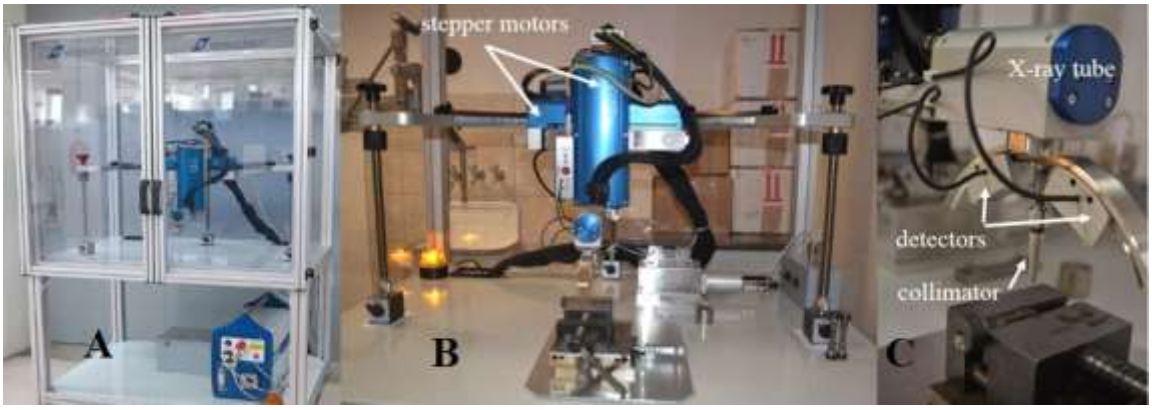

Fig. 1. a) The Stresstech Xstress 3000 G3R diffractometer b) the diffractometer in the radiation protection cabin c) the X-ray tube, collimator and detectors

Depending on the position of the tilting axle relative to the plane of the incident and diffracted beam the diffractometer can operate in both ψ and ω modes. The mode can be chosen depending on the specimen geometry. The equipment is a low power device operating with 8 mA current and 30 kV voltage. Only one plane series distance is measured by the two line detectors placed on the two sides of the collimator (Fig. 1 c). The equipment can be used with different X-ray tubes Cr, Co, Mo to provide sufficiently high Bragg angles, i.e. accuracy for the $(d_\psi - d_0)/d_0$ measurement for different materials. The measurement point is marked with a laser pointer to provide precision sample positioning. The focus distance setting is also unique. Before the measurement the surface of the sample is touched by the collimator. After that the equipment is lifted to the calibrated measurement distance.

The equipment meets the requirements of the regarding Machinery and Low Voltage directives and applies the following standards: SFS-EN ISO 12100-1, 12100-2, 13857, 60204-1.

Results

Measurements on small radius fillets

The applicability of the equipment is shown through some of our measurement experiences. At first, measurement in a fillet with a small radius (2 mm) is presented. The objective was to measure the tangential residual stress developed by low plasticity burnishing in the fillet of a knuckle (Fig. 2 a, b). The difficulty of measurements in fillets with such small radius is that a collimator is required with a diameter that the following equation stands:

$$d \leq 0{,}4r \tag{3}$$

where d is the width of the irradiated area (i.e. the diameter of the collimator) and r is the radius of the fillet. This restriction is given by the EN 15305 standard. For the 2 mm fillet and 0.5 mm collimator eq. 3 stands ($0.5 \leq 0.5 * 2$). Applying larger collimator false data will be measured because of multiple reasons. For instance, using the 3 mm diameter collimator a misfit (~0.67 mm) exists between the end of the collimator and the measurement point as the collimator touches the fillet (Fig. 2 c). Since the working distance is measured from the point of contact, the actual distance between the measurement point and the end of the collimator will be larger than the calibrated value. The deviation of the actual distance from the calibrated distance is called "defocusing error" since the measurement point is out of the focal distance (the focus circle). The magnitude of the defocusing error was measured on stress-free reference sample by removing the reference from the calibrated working distance manually. The results are shown in Fig. 3. The scatter of each measurement point is also indicated. The error caused by the defocusing is additive and is a linear function of the magnitude of defocusing. It can be seen in Fig. 3 that a ~0.8 mm defocusing results a ~100 MPa error.

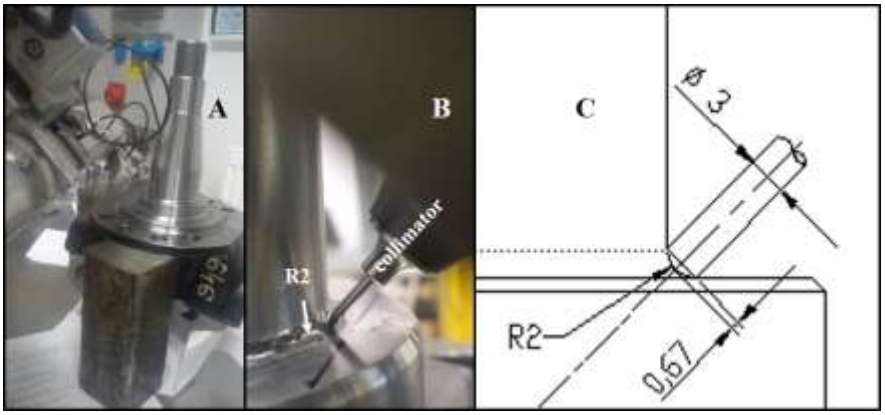

Fig. 1. a) Measuremet in the fillet of the knuckle b) using correct collimator size and c) the scheme of the measurment with incorrect collimator size

X-ray diffraction techniques of Bragg-Brentano geometry require flat sample surface that is, a fillet with infinite radius. If the surface is curved, that is, the radius of the fillet is finite, and the beam width is sufficiently low, the curvature of the sample surface is negligible. Therefore, for small fillet radius the beam width must be decreased as much as possible. This is another reason to use the smallest collimator size possible for the given problem. Another difficulty of measurement in such small radius fillet is that the collimator must be positioned precisely to the measurement point.

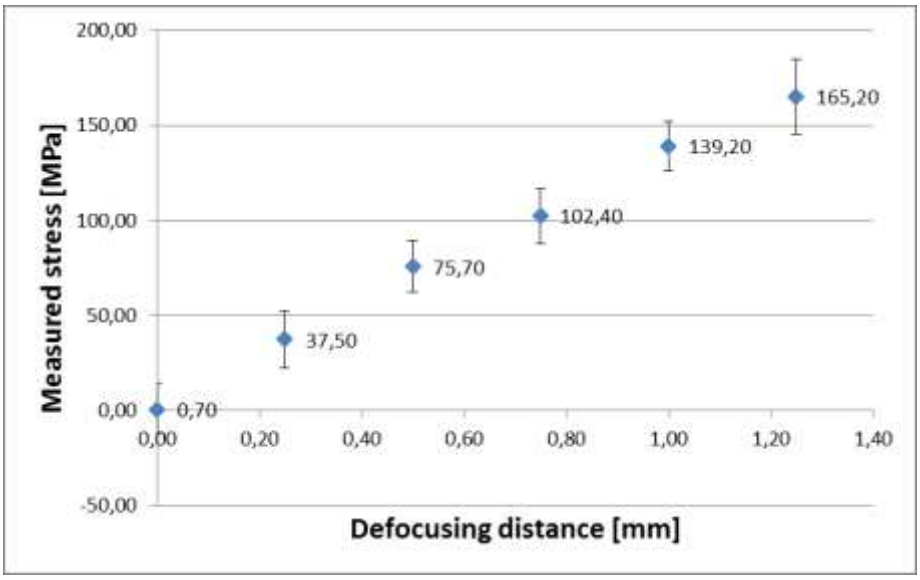

Fig. 2. The defocusing error as a function of defocusing distance

On-site measurements

The G3R X-ray diffractometer is portable with an internal cooling system and a 220V power supply need. Consequently, it is suitable for on-site measurements. An obvious benefit of the portable feature is presented by the measurement of a large machine components in Fig. 3

Fig. 3 a), b) Measurements on larege machine components in industrial environment

Depth profile measurements

The measurement of stress profiles along depth is commonly desired for surface hardened components. Due to the precision working distance setting the G3R is highly applicable for measuring residual stress depth profiles. For such examinations a Struers mobile electrolytic polishing and etching equipment is used to remove the surface layers of the material. A Mitutoyo displacement gauge is used for the depth measurements with a μm accuracy. Fig. Fig. 4.shows the measured residual stress profile along depth of a shoot peened gear wheel. The maximum of the residual stress (in absolute value) is in the 0.07 mm depth. This sub-surface maximum of the stress profile is a common phenomenon in the case of shoot peened samples.

Tensor measurements

The equipment can be rotated in the -45° - +45° range on its holder arc (Fig. 6). This ensures a 90° interval of different measurement directions. Performing measurements in at least 3 rotations the calculation of the stress tensor is possible.

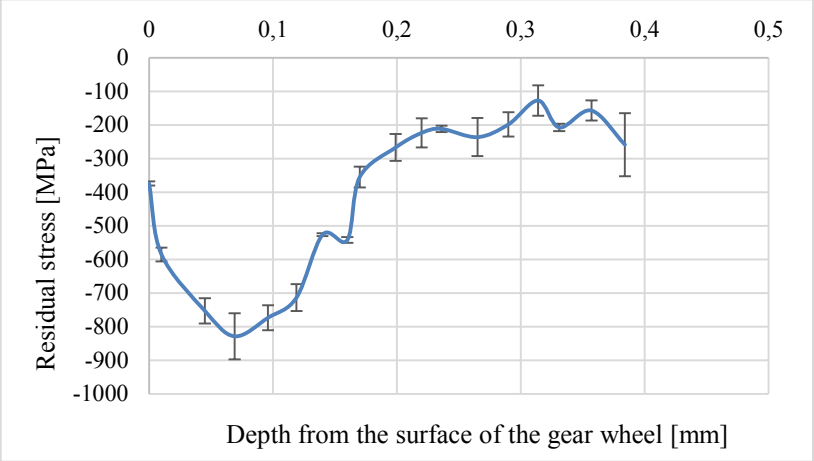

Fig. 4. Residual stress profile along depth of a shoot peened gear wheel

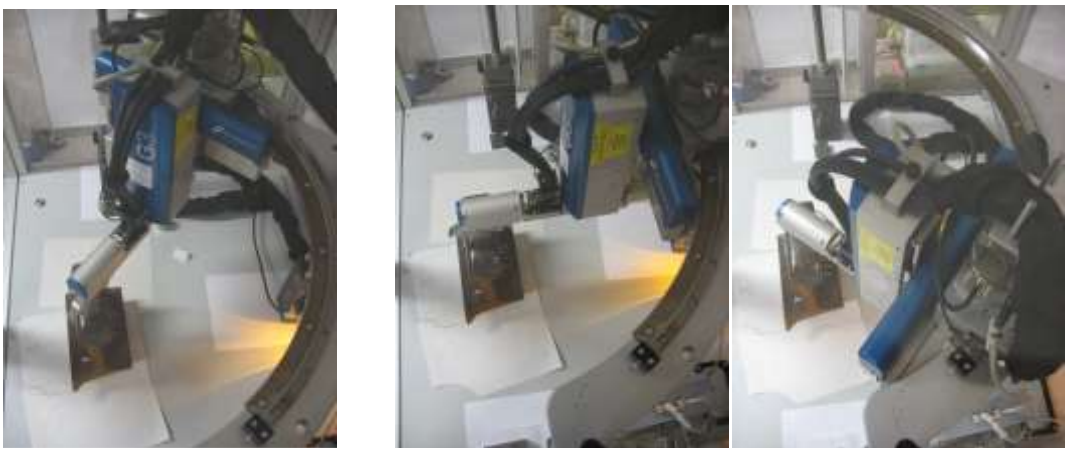

Fig. 6. Tensor measurement

Microstructural effects

X-ray diffraction techniques require fine grained, isotropic samples. These requirements are fulfilled for fine grained powders. For this reason these techniques are often referred to as powder diffraction. However, for some bulk metallic materials these requirements are not always fulfilled. For such materials the reflections become distorted and the measurement cannot be performed. The distorting effects of an oriented, coarse grained microstructure are presented through the reflections of die cast aluminium components. For comparison, Fig. 7 a shows the reflections of a fine grained, isotropic steel component detected by the two line detectors. The peaks are smooth, having shapes close to a Lorentz function. As for the die cast aluminium, the peaks are ragged (Fig. 7 b), furthermore, the intensities detected by the two detectors differ notably (Fig. 7 c). Both effects are caused by the microstructure of the die cast aluminium. The ragged reflections are due to the small number of grains that contribute to the peak (Fig. 7 b), while the differing intensity of the two detection directions is caused by the texture of the component (Fig. 7 c).

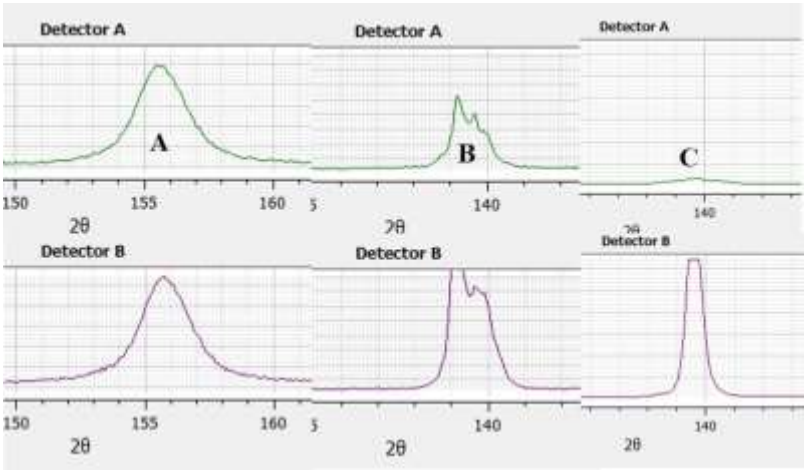

Fig. 7. Diffractions peaks a) fine grained, isotropic sample b) coarse grained sample c) textured microstructure

Summary

The advantages of the innovative Stresstech G3R X-ray diffractometer and related techniques are the following compared to traditional X-ray diffraction stress measurement techniques. Measurements can be performed without sample cutting, thus, the true stress state of the component can be measured and the measurement is completely non-destructive. Measurements can be performed on small radius geometries with sufficient accuracy. On-site measurements can be carried out even in industrial environment. Depth profiles can also be measured if step by step surface removal is allowed. Furthermore, the stress tensor can be measured if it is required. Besides these advantages the measurements can still be limited by microstructural effects such as coarse grain structure or texture.

Acknowledgements

This work has been carried out as part of the TÁMOP-4.2.1.B-10/2/KONV-2010-0001 project within the framework of the New Hungarian Development Plan. The realization of this project is supported by the European Union, co-financed by the European Social Fund.

References

[1] Handbook of Residual Stress and Deformation of Steel, ASM International, USA 2008, pp. 347-358
[2] E. Macherauch, V. Hauk, Residual stess in Scinence Technology Vol 2, (1987), pp. 697.
[3] K. A. Soady, B.G. Mellor, J. Shackleton, A. Morris, P.A.S. Reed, The effect of shot peening on notched low cycle fatigue, Mat. Sci .Eng. A 528 (2011) 8579-8588.
[4] D.Cseh, V.Mertinger, J.Lukács, Residual Stress Evolution During Fatigue Test of a Shoot Peened Steel Sample, Materials Science Forum Vol. 752 (2013) pp. 95-104.
[5] Cast Irons ASM Specialty Handbook, ASM International USA 1996, pp.339-341.
[6] Heat treating ASM Handbook Vol. 4, ASM International USA 1991, pp. 606-607.
[7] G. S. Schajer Practical residual stress measurement methods, John Wiley (2013) 140-161.
[8] P.J.Withers, H.Bhadeshia, Residual Sress Part1- Measurement techniques, Mat Sci and Technology Vol17, (2001) pp. 355-365.
[9] A. D. Krawitz: Introduction to diffraction in materials science and engineering, John Wiley (2001) 119-143, 278-318.
[10] Dr Bárczy, Dr Fuchs Erik: Metallográfia I, Tankönyvkiadó, Budapest 1981, pp.119-12

EBSD sample preparation: high energy Ar ion milling

Zoltán Dankházi[1,a], Szilvia Kalácska[1,b], Adrienn Baris[1,c], Gábor Varga[1,d], Zsolt Radi[2,e], Károly Havancsák[3,f]

[1] Eötvös Loránd University, Department of Materials Physics

Hungary, 1117 Budapest, Pázmány Péter sétány 1/a.

[2] Technoorg Linda LTD. CO.

Hungary, 1044 Budapest, Ipari Park utca 10.

[3] Eötvös Loránd University, Faculty of Science Research and Instrument Core Facility

Hungary, 1117 Budapest, Pázmány Péter sétány 1/a.

a: z.dankhazi@szft.elte.hu; b: kalacska@metal.elte.hu; c: adrienn.baris@gmail.com
d: bagoj@caesar.elte.hu; e: info@technoorg.hu; f: hkaroly@caesar.elte.hu

Keywords: EBSD, sample preparation, ion milling, SEM.

Abstract. Surface quality development on series of metal samples was investigated using a new Ar ion milling apparatus. The surface quality of samples was characterized by the image quality (IQ) parameter of the electron backscatter diffraction (EBSD) measurement. Ar ion polishing recipes have provided to prepare a surface appropriate for high quality EBSD mapping. The initial surfaces of samples were roughly grinded and polished. High quality surface smoothness could be achieved during the subsequent Ar ion polishing treatment. The optimal angles of Ar ion incidence and the polishing times were determined for several materials.

Introduction

EBSD is a versatile tool providing grain size determination, orientation mapping, phase identification and 3D mapping. Since the EBSD information comes from a few tens of nanometers of the specimen surface regions the most critical issue of the EBSD measurement is the surface quality. The surface should be perfectly clean, free of amorphous or deformed surface layer and moreover it should be flat because of the shadowing effect. Lack of these factors can result either no or faded diffraction pattern.

As it is known, the usual mechanical grinding and polishing create an amorphous layer of (1 — 100) nm thickness on the surface; the so called Beilby layer [1]. Furthermore, diamond polishing is not recommended, because it can deform the grains on the surface. Both induce the diffuseness of the diffraction patterns. The commonly suggested colloidal silica polishment continues for hours and can embed residual polishing material in the surface grains. Electro-polishing of the surface can also be tried, but this is a difficult and complex procedure, nevertheless in some cases it cannot lead to the desired result.

In the last decades a new surface milling method is spreading. This is based on energetic ion beam milling; the underlying physical process is the sputtering. One direction of this method is the focused ion beam technique (FIB) with ion energies up to 30 keV. The other direction uses near parallel inert gas (usually Ar) ion beams with energy up to 10 keV. In this paper we present a newly developed Ar ion sample milling apparatus and show how advantageously it can be utilized to produce high quality sample surface.

This new apparatus is the SC-1000 SEMPrep sample preparation device [2] designed by Technoorg Linda Ltd. Co., Hungary. The milling apparatus has two Ar ion guns, a high-energy (E_{max} = 10 keV) one for rapid milling, as well as a low-energy (E_{max} = 2 keV) ion gun for gentle surface polishing and cleaning (Fig. 1a.). Moreover, this device is capable for cross-sectional sample preparation by slope cutting for traditional SEM and EBSD measurements (Fig**. 1**b.). In this apparatus the sample can be rotated or oscillated using different tilting angles. In this paper first of

all we concentrate on the surface cleaning capabilities of the device, but the advantage of the slope cutting will be shown in one example. The details of the slope cutting-capabilities of the SC-1000 SEMPrep apparatus will be discussed in another report.

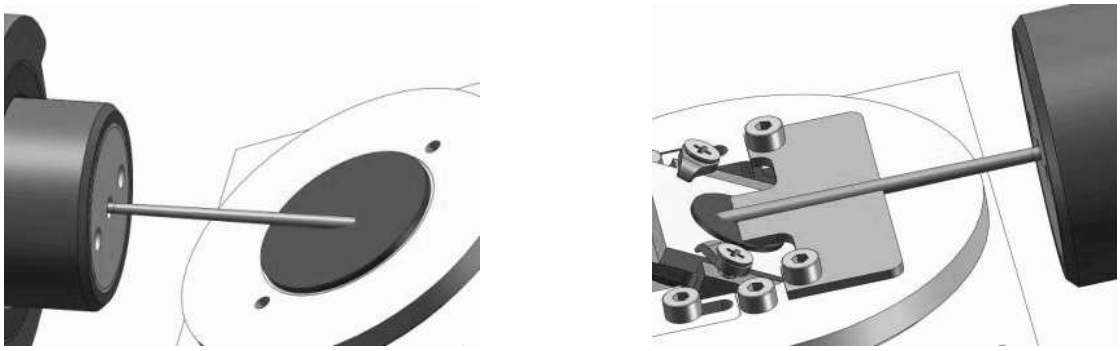

a. **b**.

Fig. 1. Scheme of the two operation modes in SEMPrep:
low angle surface polishing (a) and ion beam slope cut (b).

Experiment

In the framework of cooperation between Eötvös University and Technoorg Linda Co. Ltd. sample preparation protocols are specified in the university SEM laboratory [3]. A FEI "Quanta 3D FEG" SEM and its EDAX EBSD device was used to study the surface quality effects of ion milling.

EBSD provides information on surface microstructure. To optimize backscattered electron yield the sample has to be tilted.

Elastically backscattered electrons from a crystalline sample produce a diffraction pattern (Kikuchi pattern) which is detected by a fluorescent screen, and the pattern is recorded by the high speed CCD camera [4]. The Kikuchi pattern shows bands corresponding to Bragg reflection directions according to a family of the grain lattice planes where the electron beam spot is directed to. To define the quality of a Kikuchi pattern the system calculates the image quality value (IQ) as the intensity sum of the indexed Kikuchi bands. There is direct relation between the Kikuchi pattern and the IQ: the blurrier or vaguer the bands are, the smaller the IQ is. No upper limit can be determined for this value. Since we get an image quality from every point, we can map it just like a SEM image: pixels with brightness according to the IQ at the point. An image quality map is shown in Fig. 2a. with the corresponding SEM image (Fig. 2b.). We used the average IQ parameter corresponding to the whole image for the classification of the surface quality.

The link between the IQ and the diffraction pattern is direct, but the relation of the IQ to the material itself is complex. It depends on many factors: the crystal orientation, the conditions of the measurement (contrast, brightness etc.), the strains in the material and naturally the quality of the surface are the most important. To be careful we kept all possible conditions constant during the measurements, so the image quality will give us information on the quality of the surface. The EBSD measurement conditions were the following: 70° sample tilt, 20 kV accelerating voltage and 4 nA sample current for the SEM electron beam.

Since the resulting IQ values are not comparable for different samples, the same sample was used for one series of measurement. To eliminate the orientation dependence of the band intensities (consequently the IQ) large area (more than 25 grains) was measured to have reliable IQ average. The EBSD measurement step interval between points was chosen to have the same number of measured points for all samples. To ensure the exactly same position of the scanning area small markers were milled with FIB outside of the interesting region. These markers were used to reposition the sample after Ar ion polishing. The same series of measurements were performed on copper, aluminum, silver, iron, nickel and steel samples.

The used Al, Cu and Fe samples were technical material. The Al sample was $AlMg_{1.5}Si_{0.5}$ alloy with 0.3 % Mn and Fe contamination. The Cu was electrical wire of 3 mm diameter with 0.1 % impurity Ni content. The Ni and Ag samples were annealed GoodFellow high purity (99.0 %) materials. The steel sample ($Fe_{93,4}C_{0,15}Si_{0,35}Mn_{1,1}Ni_5$) was austenitezed and aged at 1100 °C then quenched in icy (0 °C) water having multilevel lath martensitic microstructure **Hiba! A hivatkozási forrás nem található.**.

The first step of the surface treatment was a quick mechanical grinding and polishing, not preparing a high quality surface, but removing the rough bumpiness, to ensure a clean and uniform surface to start Ar ion milling. The steps of the mechanical treatment were as follows: series of grinding paper 600-, 1200-, 2500- and 4000-grit; and 1 μm average particle size alumina paste for the finishing step.

The EBSD mapping was begun on the raw surfaces to determine the initial average IQ value. The-Ar ion milling system has four relevant adjustable parameters: accelerating voltage, time of ion bombardment, angle of beam incidence and sample movement. Since ion polishing leaves marks on the sample showing the direction of incidence the samples were rotated around the axis perpendicular to the surface. In all cases the accelerating voltages was of 10 keV, while the time- and incident angle dependence is the subject of this work.

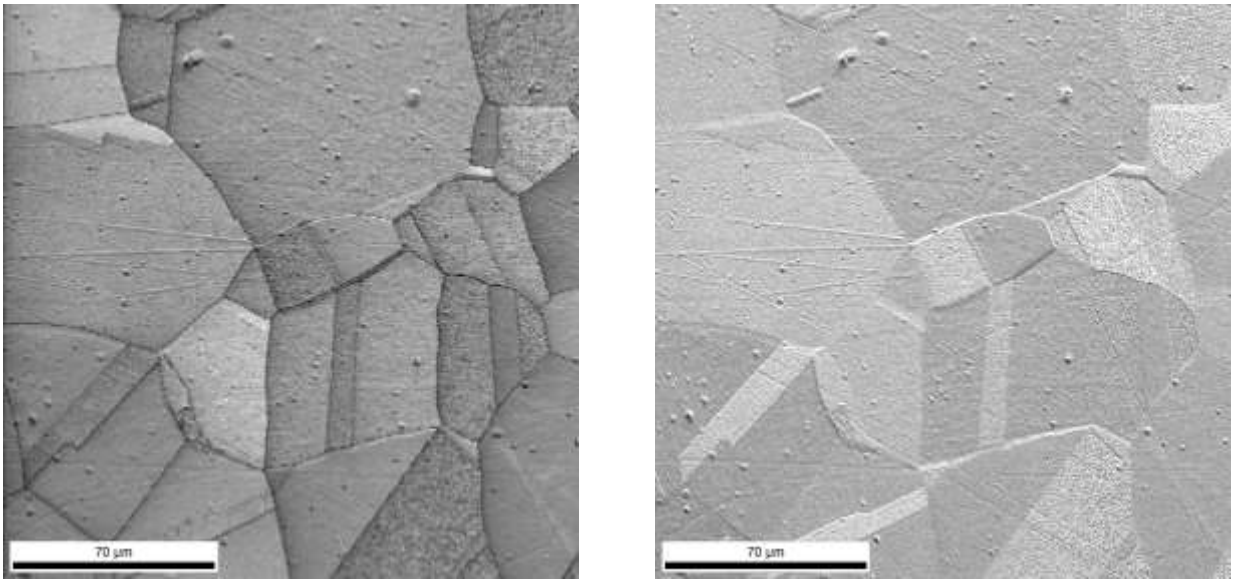

a. **b**.

Fig. 2. Image quality (IQ) map (a) and the corresponding SEM image (b) of a nickel sample.

Results and discussion

The aim of the present work was to elaborate protocols, how to obtain high quality surfaces by Ar ion polishing using the SC-1000 SEMPrep apparatus. The primary issue is that in what angle and how long we have to mill the sample to create an EBSD quality surface using the high-energy (10 keV) Ar ion beam. As a first step Ar ion treatment was performed where the incident beam angle was changed relatively to the sample surface. At each angle the polishing treatment was followed by EBSD measurement. The EBSD program calculates the IQ parameter in each measurement point. After each completed EBSD measurement the average IQ values were calculated over the whole area. In Fig. **3**. the average IQ value can be seen as a function of angle of Ar ion beam incidence measured on a Cu sample. Since the points were measured on different samples, to decrease the deviation due to distinct initial IQ, these initial values were subtracted from the respective IQ calculated after polishing.

The time value of this isochronous curve was determined prior to the measurements so that the polishing should not take too long, and at the same time not too short to prevent the accurate measurement. The milling time of this curve in each point was 6 min. Fig. 3. shows the resulting curve for Cu, but very similar curves were obtained for aluminum, silver, nickel and iron. The curve following a nearly linear initial rise saturates and then it begins to decline. The rising part is related to the reduction in the thickness of the deformed (amorphous) surface layer. The saturation indicates that the deformed surface layer has been stripped due to the Ar ion polishing. Decrease after saturation can be regarded as the consequence of the inhomogeneity of the Ar ion polishment, which is partly due to the orientation dependence of the sputtering, and partly to the initial surface

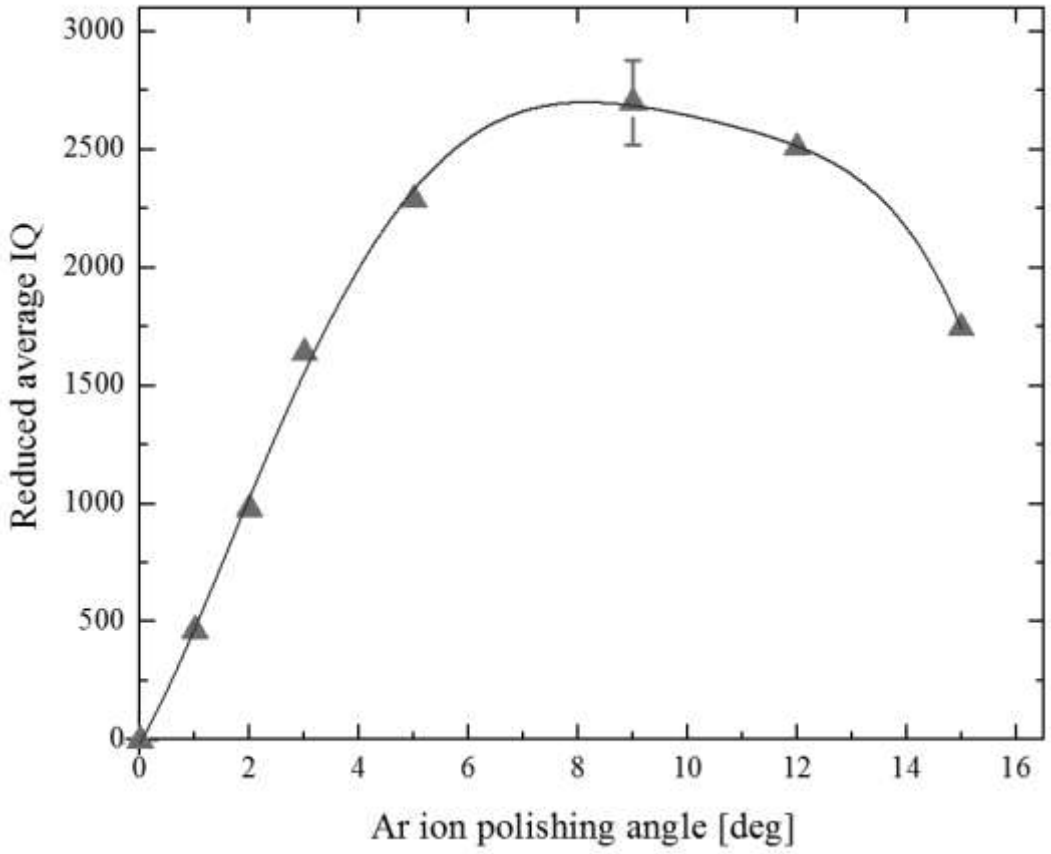

Fig. 3. Effect of ion beam incidence angle on the background subtracted average IQ of copper.

irregularities having different milling speeds. Consequently, after a relatively long processing time surface coarsening can be observed and for some materials even cratering starts. The ideal Ar ion polishing angle was determined from the curve in Fig. 3. and 6-8 degree was obtained. This value proved to be suitable for other materials as well, as it listed in Table **1**a.

sample	Al	Cu	Ni	Fe	steel
angle (deg)	7	8	8	6	8

a.

sample	Al	Cu	Ni	Fe	steel
time (min)	6	7	6	7	26

b.

Table 1. Ideal angle (a) and time (b) values to prepare high quality EBSD surface for various materials.

The second step was the determination of the ideal time of milling at the optimal angle found previously. The time dependence of the average IQ values can be seen in Fig. 4. measured on a similar Cu sample. In order to assure the accuracy each point were measured on the same sample and even at the same area of that. As a result of the careful measuring procedure the uncertainty of the measurement was not larger than 2%. As it can be seen in Fig. 4. after a relatively rapid growth saturation occurs in IQ. The saturation is again the sign of the removal of the amorphous and/or deformed layer. However, coarsening occurs in the saturation region due to the Ar bombardment, although if the surface roughness is not too large, the EBSD measurements practically are not sensitive to these surface irregularities. After a long time milling the IQ trend begins to decline but this is not shown in the figure. Thus if we want to have a good quality surface smoothness then the Ar ion milling should be completed at the beginning of the IQ saturation. In case of Cu the proposed milling time is between 6-8 minutes.
Table **1**b. shows the ideal time values for various materials.

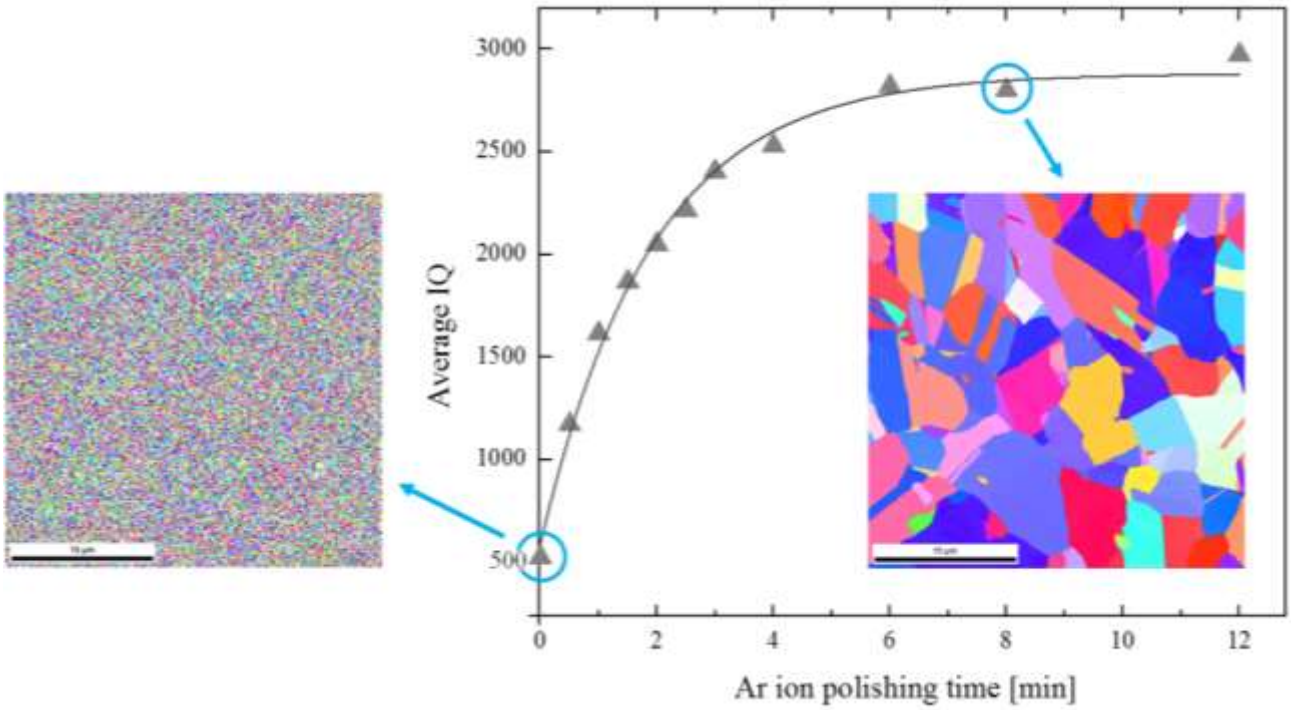

Fig. 4. Effect of ion milling duration on the average IQ with the corresponding inverse pole figure (IPF) maps on copper sample.

The texture analysis by EBSD measurement of geological materials is of great importance. According to our experience, the geological materials can easily form a relatively thick amorphous surface layer during mechanical polishing, and afterwards it is difficult to remove this layer by the Ar ion polishing. In this case it is favorable to use the slope cutting capability of the SEMPrep apparatus. As an example a slope cutting experiment was accomplished on limestone at 30° sample tilt with high energy Ar ion beam of 10 keV. The maximum cut depth of 200 µm was achieved in 2 hours. The whole area and a part of the new cut surface can be seen in Fig. 5a. and Fig**. 5**b., respectively.
After forming this new surface the low energy (2 keV) Ar ion gun was used at 5° relatively to the new surface for 1 hour. During this cleaning process the sample was oscillated between ± 30° limiting angles. The resulting inverse pole figure orientation map can be seen in Fig. 5c. Without the cleaning step the Kikuchi images were blurred. The possible reason of this blurring is the surface backsputtering. During this type of high energy milling huge amount of particles (atoms and ions) are produced and they deposit over the cut area even during the milling process. The

backsputtered material form thin amorphous layer which can be cleaned by the low energy Ar ion beam.

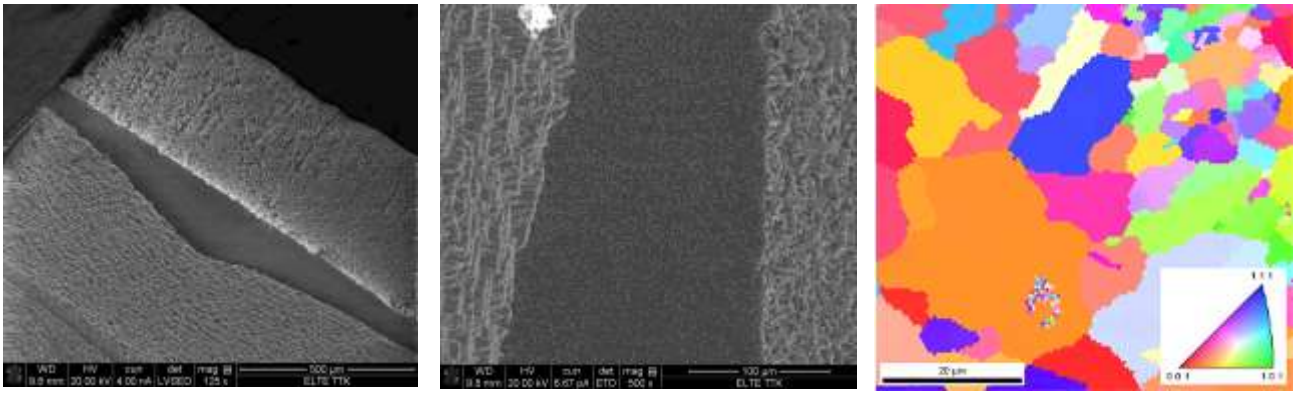

a b c

Fig. 5. SEMPrep slope cut – limestone SEM image of the whole milled area (a), part of the central region (b) and inverse pole figure after 2 keV Ar ion final polishing (c).

Summary

It has been shown that starting with roughly polished initial surfaces the SC-1000 SEMPrep apparatus is capable to prepare a high quality surface appropriate for high resolution EBSD mapping. The preparation time is much less and the Kikuchi pattern quality of the sample is higher comparing to traditional polishing methods. The optimal parameters for several materials are determined and summarized in Table 1.

References

[1] G. Beilby, Aggregation and Flow of Solids, Macmillan, London, (1921).

[2] Information on http://www.technoorg.hu/uploads/semprep.pdf

[3] Information on http://sem.elte.hu

[4] T. Berecz, Sz. Kalácska, G. Varga, Z. Dankházi, K. Havancsák, Effect of high energy Ar-ion milling on surface of quenched low carbon low-alloyed steel, published in this issue.

[5] J. Goldstein, D. Newbury, D. Joy, Ch. Lyman, P. Echlin, E. Lifshin, L. Sawer and J. Michael, Scanning Electron Microscopy and X-Ray Microanalysis, Springer (2007), ISBN: 978-0-306-47292-3.

Cold Rolling Effect on Microstructure and Mechanical Properties of Low Carbon Al-Killed Steels

Enikő-Réka[1,a] Fábián, Áron Kótai [2,b]

[1,2] Budapest University of Technology and Economics
Department of Materials Science and Engineering
H-1111 Budapest, XI. Bertalan L. u. 7. Build. MT
[a] fabianr@eik.bme.hu [b] aron.kotai@gmail.com

Keywords: LC enamel-grade steel, deformation, microstructure, orientation.

Abstract
It have been studied the cold rolling effects on the microstructure of samples prepared from Al-killed low carbon steel sheets with high coiling temperatures. The microstructure of the hot rolled steels sheet is formed from ferrite and large carbides when the coiling temperature is high. The cold rolling affects the steel mechanical and electrochemical properties due to microstructural changes. We have studied the microstructure by optical microscope and scanning electron microscope. Low angles grain boundaries and the texture of samples were studied by EBSD method.

Introduction

The unalloyed low carbon steel sheet after the hot rolling can be coiled at different temperatures depending on the application. In recent years there has been a steady increase of interest from the automotive industry in isotropic steel product; i.e. steel products with a minimum of variation of mechanical properties, most noticeably drawability, in the plane of the sheet. In enamelling industry the steels near the good drawability need correspondent hydrogen permeability in special at enamelling by wet process.
Texture is an important parameter of steel sheets as it induces plastic anisotropy that can be beneficial to drawability of steels [1, 2, and 3]. The anisotropy is conveniently measured in terms of r_m-value that is the ratio of true width strain to true thickness strain determined through standard tensile tests. r_m-value varies essentially with respect to rolling direction of the sample. Thus, an average of the r-values is taken as r_m, which is expressed through the expression $-(r_0+ 2r_{45}+ r_{90})/4)-$ termed as 'normal anisotropy'- where the subscripts 0, 45 and 90 refer to the tensile specimens with parallel to, 45° and 90° to the rolling direction of the steel sheet. Isotropic steels have r_m -value around 1, while steels suitable for deep drawing applications should have r_m -value 1.8 [4]. High r_m-values correlate well with good deep drawability [2]. Good drawability also diminishes the edge splitting tendency during hole-expansion tests [5]. To ensure satisfactory drawability in these steels, i.e. to increase the depth of drawing and avoid the crack during deep drawing process and at the same time to make the edge on the top of a drawn cup smooth without the phenomenon of earing, the deep drawing sheet is required to possess high plastic anisotropy r_m and low normal anisotropy, Δr. It has been demonstrated that high r_m values are displayed by materials which have a high proportion of crystallographic texture oriented with their {111} planes parallel to the sheet plane [6] (henceforth abbreviated as $\langle 111 \rangle \parallel$ ND), i.e. by materials which possess a strong {111} type texture (or γ-fibre texture) [7]. Other texture components, such as the {001}, have been found to be detrimental to the drawability. According to the work reported by Daniel and Jonas [8], the most desired texture components to obtain good drawability properties are {111}<110> and {111}<112>, and the most undesired ones will be {110}<001> and {001}<110>.
In other words, to maximize r_m -value and minimize Δr-value, {111}<112> and {111}<110> components of γ-fibre are the ideal crystallographic textures for deep drawing steel, because the correct texture gives the proper orientation of slip system so that the strength in the thickness direction is greater than that in the plane of the sheet. If {100} plane parallels rolling plane, the

strength is the lowest in the thickness direction of sheet. In practice, the intensity ratio of the above two components, I(111)/I(100), is found to be linearly related to r_m as it was determined by Held [9]. The strength of ⟨111⟩ ‖ ND texture is influenced by chemistry and the prior technological processing steps, such as hot rolling, cold rolling and annealing [10, 11, 12 and 13].
The aluminium-killed low carbon steel sheets (LC steels) manufactured for enamelling are coiled at high temperature. These steels after pickling are cold rolled and annealed. DC04EK grade steel is intended principally for 2 coats/ 1 fire enamelling process after only degreasing. This grade is suitable for deep drawing and, after degreasing, suited to 2 coats / 1 fire enamelling by wet/ powder or wet/wet process. It also offers an excellent resistance to fish scales defect. The susceptibility to fish-scale formation in case of the cold rolled Al-killed low carbon enamel grade steel sheets is characterized by the hydrogen permeability [14]. That is why hydrogen permeation test has been used for long time to estimate the hydrogen absorption capability of steel sheets used for double surface enamelling. In order to eliminate fish-scaling of enamelled unalloyed steel products, the normalized hydrogen permeation time of the sheet (T_H *value*) has to be high: $T_H = t_0/d^2 \geq 6.7$, where t_0 is the hydrogen permeation time [min], d is the steel sheet thickness [mm]. The T_H value of the low carbon unalloyed steel depends from the microstructure of the steel [15, 16, 17].
Iron texture has influence on the hydrogen diffusion also [18]. The diffusion of hydrogen into iron subsurface has a much lower barrier on the (100) plane of iron) than on the (110) plane.
Verdeja et al [19] have postulated that the presence of a {110} - {332} texture, when these planes lie parallel to the rolling plane is expected to reduce the sensitivity to hydrogen induced cracks of ferritic-pearlitic steels, while the presence of a {001}-{113}-{112} planes lying parallel to the rolling plane will produce the opposite effect.
At hot rolled LC steels T_H *values* are very low (T_H<1), but the T_H value increases exponential with the deformation ratio during cold rolling process [15, 16]. After annealing of DC04EK steels the T_H value is a magnitude order higher as at hot rolled LC steel [17]. At extra deep drawing steel (EDD steel) r_m value increases with cold reduction till r_m~1.8 [12], after annealing the r_m value depend on the coiling temperature of hot rolled steel, on the thickness reduction, and on the annealing method (batch annealing, continuous annealing ($1.3 < r_m < 2$ [20], at IF steel r_m value is higher than 1.4, sometimes $r_m > 2$ depending on microalloying elements [21, 22].

Materials and testing

During the experiment there were examined properties of specimens taken out from hot rolled unalloyed, aluminium-killed, low carbon steel sheet after several cold rolling levels. The chemical composition of the steel is given in Table 1**.**

Table 1. The chemical composition of the examined steel

Chemical composition [%]										
C	**Mn**	**Si**	**P**	**S**	**Cu**	**Ni**	**Cr**	**Al**	**N**	**Fe**
0.031	0.21	0.011	0.009	0.011	0.04	0.034	0.044	0.045	0.004	rest

The examined steel sheet was elaborated in LD steel converter, followed by continuous casting, hot rolling and pickling. The coiling temperature strip was 730 ±15°C. Several samples from the hot rolled, non alloyed, Al-killed low carbon strip were cold rolled in laboratory condition by duo rolling mill (rolls diameters are 206 mm) for detailed study of cold rolling effect on microstructure.
The microstructures of the samples were studied on longitudinal, transversal cross sections and parallel to the surface of the sheet by an Olympus PMG3 microscope.
Electron backscatter diffraction (EBSD) was used to determine the individual grain orientations, low and high angle grain boundaries and characteristic fibres of the rolling structure at samples prepared parallel with rolling plane. An EDAX-TSL orientation imaging microscopy (OIM) system was used which was mounted on a Philips XL-30 scanning electron microscope. The acceleration voltage was 25 kV. Orientation image maps were constructed from about 30 000 pixels.

Results and discussion

The microstructure of the hot rolled EK2 sheet was formed from ferrite (98±1%) and coarse carbides and a few pearlite (2±1%). The non ferrous inclusions were 0 and 1 grade of oxides. The carbides and pearlite were located at boundaries of the equiaxed ferrite grains (Fig. 1a., Fig. 3a and Fig. 6a.). In the microstructure no significant changing was observed up to 30% reduction of thickness by optical microscope, but already a few cracks in some of the carbides (Fig. 3a.) it could be discern after ε=12%. A moderate ferrite grain elongation in rolling direction were observed by optical microscope after ε=30%. The ferrite grains elongation became characteristic at ε≈60% thickness reduction. Shear bands in ferrite grains have became visible by the optical microscope (Fig 1) on the samples taken out in rolling direction after heavy reduction of thickness (at samples with deformation level ε >60%).

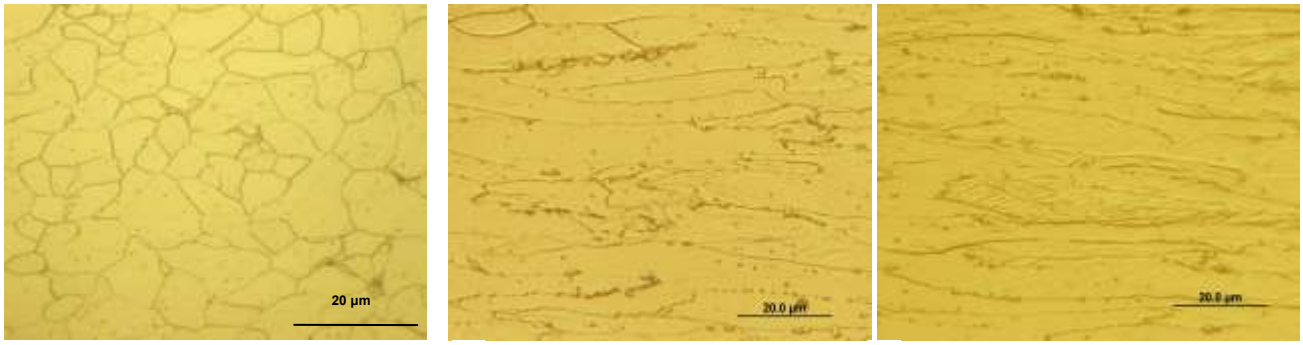

a) b) c)

Fig. 1. Microstructure of the samples in rolling direction a) hot rolled samples, b) ε=62% c) ε=71%

Numerous fragmented carbides and microcavities between them were observed after 37% of reduction of thickness. Each of coarse carbide has become fragmented after heavy reductions (ε≈50%). The proportion of fragmented carbides as compared to initial carbides content as function of deformation is presented at Fig. 2. (R_{fr}=number of fragmented carbides/ number of total carbides).

The groups of fragmented carbides became elongated in the rolling direction. Cavities appeared between the carbides fragments are growing due to cold rolling. After high deformation level by cold rolling the broken carbides fragments become apart from each other. When the carbides are getting further apart, the cavities are disappear (Fig.3.).

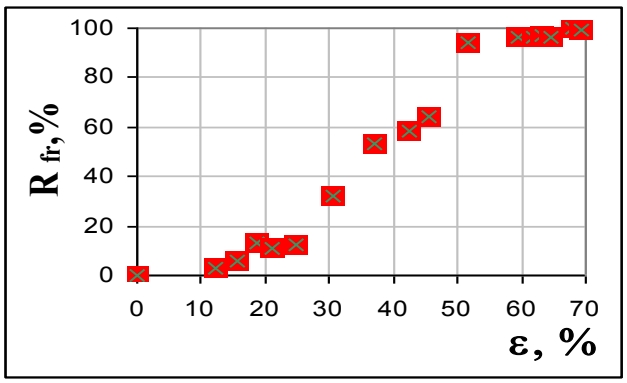

Fig. 2.The ratio of (fragmented carbides)/ (total carbides) as the function of deformation

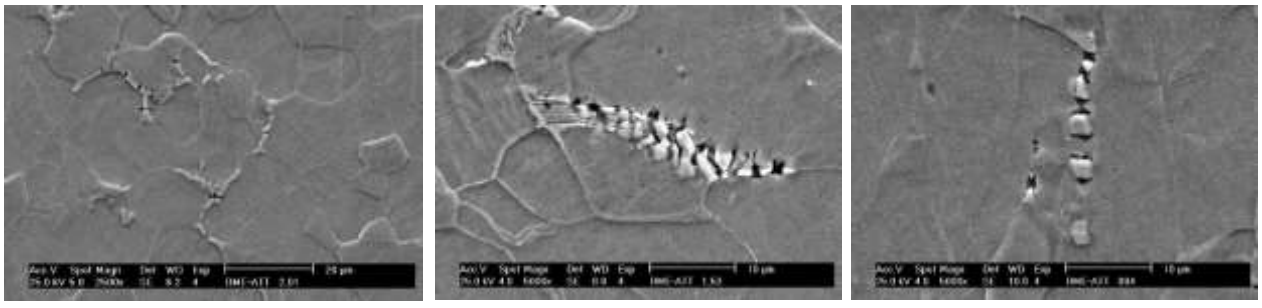

a). b) c)

Fig 3. SEM images nearby carbides fragments after different deformation levels at the samples parallel whit rolling plan a) ε=12.3%, b) ε= 30%, c) ε=60%

We made electron backscatter diffraction (EBSD) measurements on the samples which are parallel with the rolling plane.
In grain boundaries map (Fig. 4.a) it can be seen that the equiaxed ferrite grains are characterised by high angled grain boundaries (GB >10°). In this work high angle grain boundaries (GB >10°) are thick and black, the grain boundaries with angles between 5°and 10° ($5°<LGB_I<10°$) are red, the low angles boundaries with the angles under 5° ($2°<LGB_{II}<5°$) are thin and green.

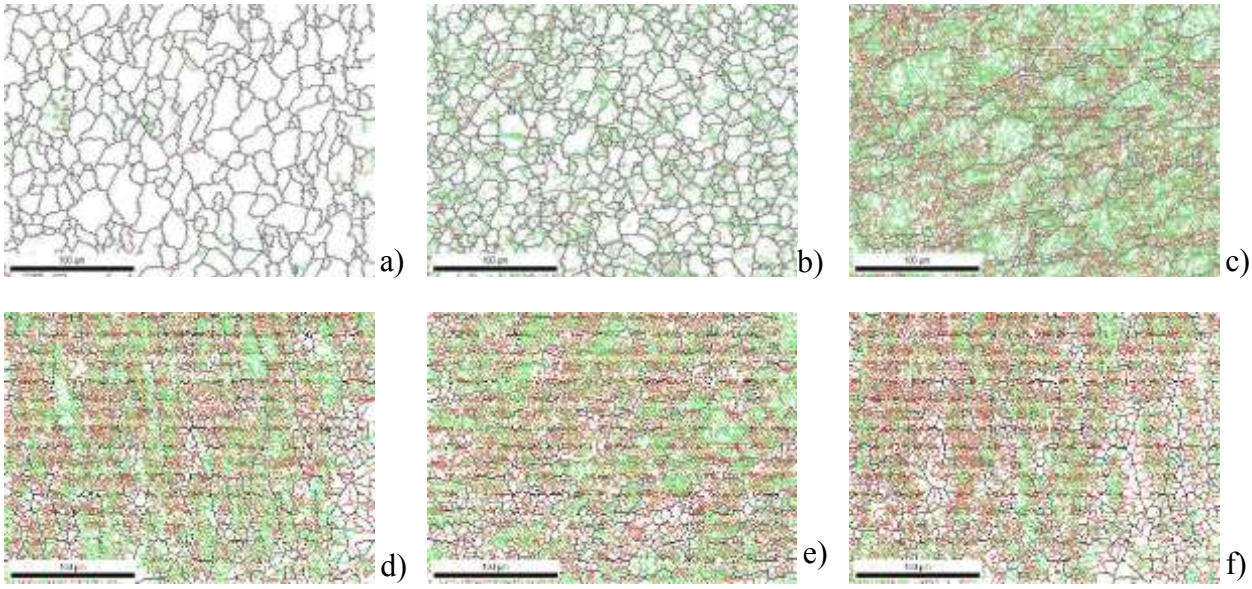

Fig. 4. Grain boundaries maps after different deformation level
a) ε = 0% b) ε = 16% c) ε = 44% d) ε =58.6% e)ε =63.6% f)ε =70.8%

In grain boundaries maps we can see that the quantity of the low angles grain boundaries in the ferrite grains are insignificant at the hot rolled specimens as it was expected. Low angles boundaries, LBG_{II} appear inside of ferrite grains during cold rolling. Quantities of LGB_{II} increase very quickly at the beginning of the process. Half of the grain boundaries are the type LGB_{II} when the deformation level is 25 %< ε<50%. The quantity of grain boundaries with grain angles between 5°-10° (type LGB_I) increase monotone applying the usually deformation levels (Fig. 5).

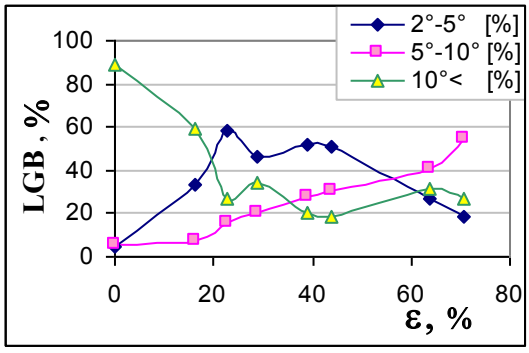

Fig. 5. Grain boundaries distribution at different deformation levels

Microscopically observations and the grain boundaries maps are in good correlations with the image quality maps (Fig. 6.). In image quality map (IQ map) dark areas represent areas of poor diffraction, which can be due to strain or overlapping/poor patterns at grain boundaries. In the Fig. 6. it can be seen that after hot rolling the ferrite grains are light, there is no strain; but the carbides are dark. By cold rolling of hot rolled low carbon Al-killed unalloyed steel the strain increase in the sheets.

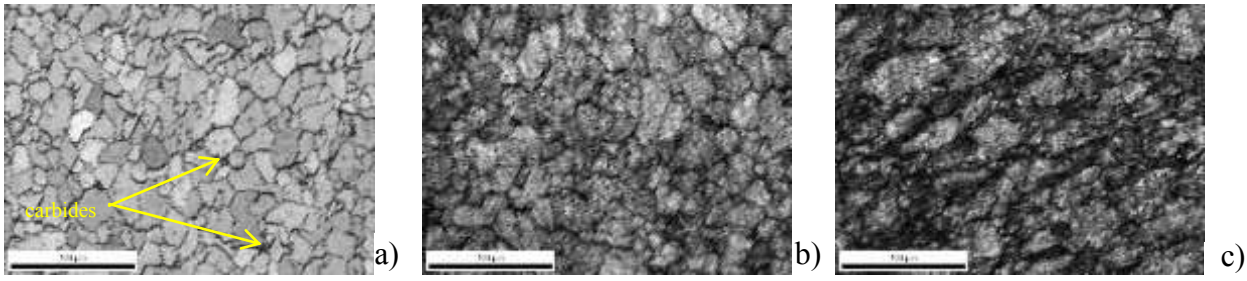

Fig. 6. Image quality maps after different deformation levels. a) ε = 0 %, b) ε= 23%, c) ε =44%

Orientation studies showed that at hot rolled steel the ferrite grains are randomly oriented. For this reason hot rolled LC steel has no good deep drawability, and has low T_H value [23]. As it can be seen in Fig. 7 the amount of the crystallographic texture ⟨111⟩ ‖ ND increased with deformation degree. This phenomenon is more visible in inverse pole figure (Fig. 8.). At samples, where the fragmentation of the carbides become very intensive and between the carbides fragments were observed microcavities, the intensity of ⟨111⟩ ‖ ND texture decreased comparing with the preceding deformation level. The fragmented carbides had become characteristic for the microstructure at ε≈50%. After this reduction level ⟨111⟩ ‖ ND texture increases again, this is favourable for deep drawability.

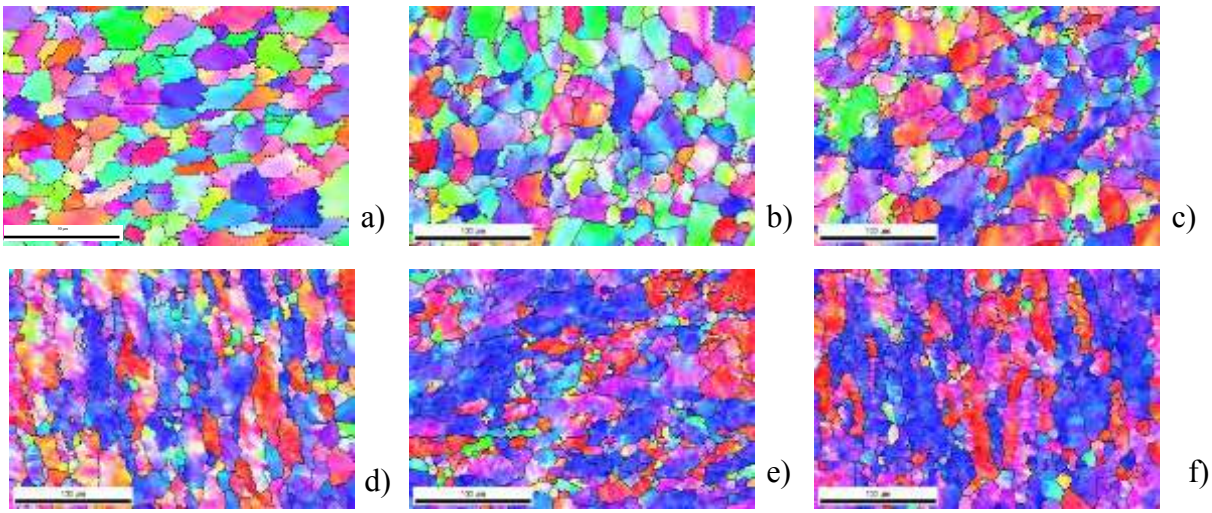

Fig. 7. Orientation maps of strip EK2 after several cold rolling degree. The crystallographic texture with {111} orientations are blue, with {100} orientations are red and with {110} orientations are green.
a) ε= 0% b) ε = 22.8% c) ε = 38.9% d) ε = 58.6% e) ε = 63.6% f) ε = 70.8%

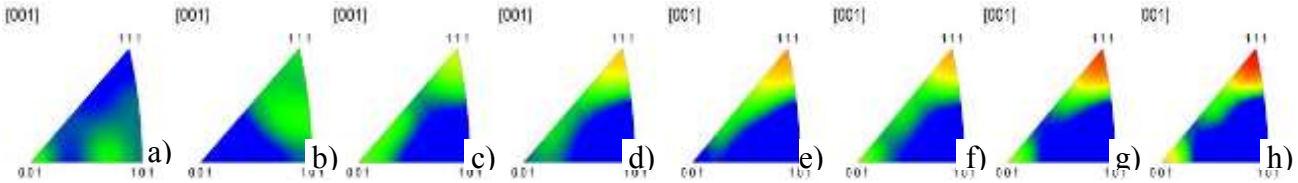

Fig. 8. Inverse pole figures a) ε= 0% b) ε = 22.8% c) ε = 28.9% d) ε = 38.9%
e) ε= 43.9 % f) ε= 58.6% g) ε =63.6% h) ε = 70.8%

The microstructures of annealed samples were studied also. Orientation map of cold rolled and in industrial condition batch annealed LC steel sheet is presented at Fig. 9. The ⟨111⟩ ‖ ND texture is dominant after annealing.

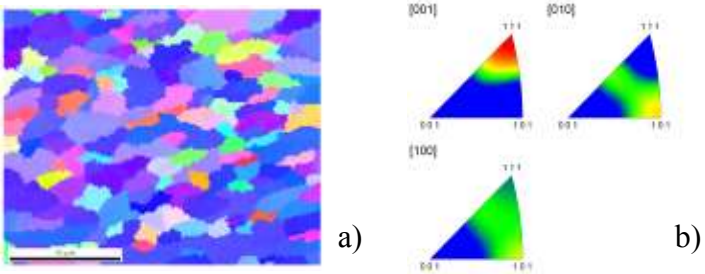

Fig. 9. Texture of cold rolled and batch annealed LC steel

Conclusions

When the coiling temperature of the hot rolled LC steels sheet is high, the microstructure is formed from ferrite and large carbides. Due to the cold rolling the large carbides are cracks and breaks in microstructure. While carbides are fracturing, micro cavities are forming between the carbides. After high deformation by cold rolling, the broken carbide parts become apart from each other, the

cavities are growing but when the carbides are getting further apart, the cavities are disappear. During to the cold rolling, the ferrite crystallites became elongate. Shear bands are visible by light microscope after 60% thickness reduction.
The quantity of low angles grain boundaries are increasing at the beginning of the cold deformation. After ε=25% deformation the high angles grain boundaries are about the whole grain boundaries quarters, which do not change after higher deformation level.
During the orientation measurements we found that the hot rolled steel has isotropic microstructure, but due to cold rolling, a high proportion of crystallographic texture oriented with their {111} planes parallel to the sheet plane. The <111>∥ND texture increased, remained dominant after batch annealing also, which is preferred for drawability.

Acknowledgments
This work is connected to the scientific program of the "Development of quality-oriented and harmonized R+D+I strategy and functional model at BME" project. This project is supported by the New Hungary Development Plan (Project ID: TÁMOP-4.2.1/B-09/1/KMR-2010-0002).

References
[1] Hosford W. F. and Backholen W.A. Fundamentals of Deformation Processing, Syracuse Press, New York, 1964, p. 259.
[2] Lankford W. T., Snyder S. C. and Bauscher J. A.. Trans. AS1/I, Vol. 42, (1950) pp.1197—1232.
[3] Yoshicla K. at. (1974): Deep Drawing Research Group, Proc. 8th Biennial IDDIG Congr. Gothenburg, 1974, pp. 258—268
[4] Holie S. Mater. Sci .Technol., Vol 16, (2000). pp. 1079-1093.
[5] Klein A. J. and Hitchler, E. W. Met. Eng. Q., Vol. 13. (1973)., pp. 25—27.
[6] Whiteley R. L. and Wise D. E Flat rolled products III, Interscience, New York, 1962., pp. 47-63.
[7] Kestens L., Jonas J. J., Van Houtte P. and Aernoudt E. (1996). Textures and Microstructures, Vol. 26-27, pp. 321-335.
[8] D. Daniel and J. J. Jonas: Metall. Trans. A., 1990, 21, 331-342.
[9] Held J. F. Mechanical Working and Steel Processing IV, ed. D. A. Edgecombe, American Institute of Mining, Metallurgical and Petroleum Engineers, New York, ,1965, p. 3.
[10] Perera M., Saimoto S. and Boyd D.. Interstitial Free Steel Sheet: Processing, Fabrication and Properties, eds. L. E. Collins and D.L. Baragar; Ottawa, CIM/ICM, 1991, pp. 55 -64.
[11] Wilshynsky-Dresler D. O., Matlock D. K. and Krauss G. (1995): ISS Mech. Work. Steel Process. Conf., 1995, 33, pp. 927 – 940.
[12] Kumkum Banerjee Physical Metallurgy and Drawability of Extra Deep Drawing and Interstitial Free Steels, Recristalization book edited by Krzysztof Sztwiertnia, ISBN 978-953-51-0122-2, 2012 under DOI: 10.5772/35073 pp. 168, 141-142, 175
[13] Tsunoyama K.. Phys. Stat. Sol. (A), Vol. 167, No. 427, (1998), pp. 427-433.
[14] Information on http://www.arcelormittal.com/fce/repository/Brochures/Enamelledsteel_brochure_FR.pdf
[15] E. R. Fábián: Materials Science Forum, 659:. (2010), pp. 7-12
[16] E. R. Fábián, L. Dévényi, Materials Science Forum Vols. 537-538 (2007) pp. 33-40
[17] E. R. Fábián, B. Verő, and L. Dévényi: Materials Science Forum 473-474 (2005) pp. 201-206,]
[18] D. E. Jiang and Emily A. Carter: Physical Review B, 70, 2004, 064102-5
[19] J.I. Verdeja, J. Asensio, and J.A. Pero-Sanz: Mater. Charact. 2003, vol. 50, pp. 81–86.
[20] G Beranger, G Henry and G Sanz. 1996. The book of Steel, Springer-Verlag, 2-85206-981-18 USA, (1994), pp. 935-951.
[21] Mendoza R. , Alanis M. , Aramburo G. , Serrania F. and Juárez-Islas J. A. Mater. Sci. Eng. A, Vol. 368 (2004) pp. 249–254.
[22] H.Kang, C. I. Garcia, K. Chin and A. J DeArdo. ISIJ Int., Vol. 47 No. 3, . (2007)pp. 486–492.
[23] E.R. Fábián., P.J. Szabó: Materials Science Forum, Vol. 659: (2010), pp. 301-306

Residual Stress in Plain Carbon Steel Induced by Laser Hardening

A. Filep[1,a], M. Benke[2,b], V. Mertinger[1,c], G. Buza[3,d]

[1]Institute of Physical Metallurgy, Metalforming and Nanotechnology, University of Miskolc, 3515 Miskolc-Egyetemváros, Hungary

[2]MTA-ME Materials Science Research Group, University of Miskolc, Miskolc-Egyetemváros, Hungary

[3]Bay Zoltán Applied Research Nonprofit Ltd., Department of Laser technology, 1116 Budapest, Fehérvári út 130., Hungary

[a]adam9032@gmail.com (corresponding author), [b]fembenke@uni-miskolc.hu, [c]femvali@uni-miskolc.hu, [d]gabor.buza@bayzoltan.hu

Keywords: laser hardening, residual stress measurement, X-ray diffraction

Abstract. Technological residual stresses have great importance in the manufacturing processes and the lifetime of components. The residual stresses formed by quenching can be very diverse because of its multiple sources. Alternative quenching processes such as laser hardening have a great potential for different applications. The direction of heat transfer during laser hardening is the opposite compared to conventional quenching. This further increases the complexity of the developed stress state. The residual stress profile and the microstructure formed by laser hardening treatment are investigated in the present manuscript.

Introduction

Among the various steel technological processes the heat treating has the greatest interest and impact on the control of deformation and residual stress. Among the heat treating processes the quenching is one of the most important due to the fact that residual stress can be attributed to three different causes: differential shrinkage due to thermal gradients, volume changes due to phase transformations, different shrinkages due to the different expansion coefficients of present phases (austenite and martensite) [1,2]. The thermal gradient effects can be controlled by applying proper geometries and quenching media. In general, the greater the quenching intensity, the grater the propensity for distortion, and results in increased thermal stress. Thus, applying martempering instead of direct quenching can also be very helpful [3]. When austenite transforms to martensite the volume increases and this volume change causes stresses that are constrained within the strength of the material and residual stresses are created. Each one of these phenomena is well known, but the situation is more complex because all the three events occur simultaneously. If composition and/or heating, cooling inhomogenity occur, the process is further complicated. Large heating inhomogenity can form when high energy density heating methods are applied, for example during induction, flame, electron beam or laser hardening. In all these cases heat is generated in the surface layer of the work piece [4-8]. Laser heat treatment can be considered a versatile, flexible, high density heating and a very clean technology. Deficiencies of laser hardening are very low energy efficiency and the relatively high cost. Laser hardening is important for the following specific applications: hardening of small product of intricate shapes, hardening of small internal surfaces, hardening of parts where the acceptable distortion is very limited. The main difference between the laser and the conventional quenching treatments is the direction of the heat transfer. During the laser surface hardening the heat is transferred from the surface into the bulk, while in case of conventional hardening it is transferred from the surface into the quenchant. X-ray diffraction is an appropriate tool to obtain quantitative data about residual stresses [7,9]. The aim of the present work is to demonstrate the stress distribution determined by X-ray diffraction methods on a laser treated flat surface of plain carbon steel.

Experimental

Discs with thickness of 22 mm were sawed from hot-rolled plain carbon steel rods (carbon concentration 0,45 wt%) with diameter of 120 mm. Laser hardened bands with 20 mm width were produced on the disc with a 5 kW nominal maximal power CO2 laser equipment with 100% laser power and 400 mm/min feed rate. Sprayed graphite was used as absorber before the laser treatment. The surface residual stress measurements were performed on the discs without sample cutting with a Stresstech Xstress G3R X-ray diffractometer. 1 mm spot size and 5 tilting angles in the -45° – 45° interval were used. The ferrite/martensite {211} reflections were measured. The stresses were calculated by the $\sin^2\psi$ method using Young's modulus of 211 000 MPa and Poisson ratio of 0.3. Both normal and shear stresses were measured. The stress values were measured in two directions: perpendicular to the length of the hardened band (traverse direction, TD) and parallel with the hardened band (feed direction, FD). The stress state of the disc was determined as the average of seven measurements along the centerline of the disc. The stress profile formed by the laser hardening was measured as a function of distance from the centerline of the hardened band. Fig. 1. shows the measurement points of the laser beam treated disc.
Samples were cut from the disc for the further examinations. Fig. 2. shows the locations of sample removals for the phase analysis, microstructure examinations and hardness measurements.

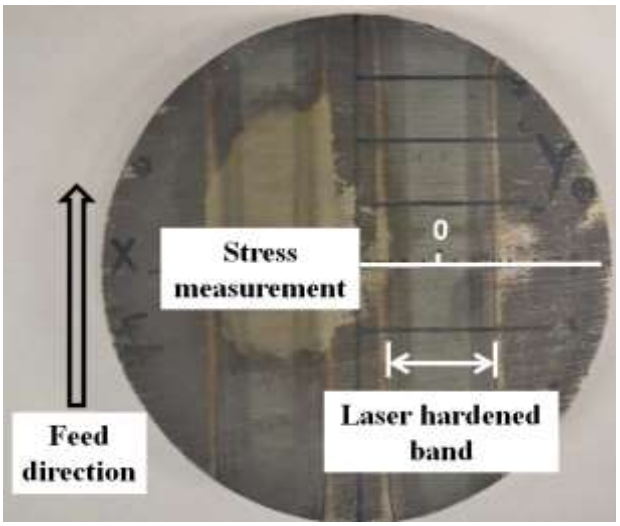

Figure 1. Locations of the residual stress measurements

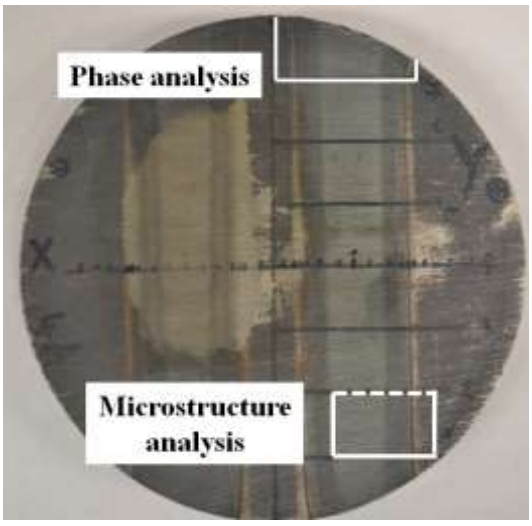

Figure 2. Locations of sample removals for the examinations

Phase analysis was performed with a Bruker D8 Advance X-ray diffractometer using CoKα radiation. Diffraction patterns were measured in two states of the disc: after removing the graphite absorber by simple washing and after mechanically polishing the surface. Standard metallographic preparation was used for the microstructure examinations. Optical microscope examinations were carried out using a Zeiss Axio Imager M1m microscope. The Vickers hardness measurements were performed with an Instron Wilson-Wolpert Tukon 2100B equipment using 10 N loading force. The hardness traverse was measured as the function of the distance from the surface. The consecutive indentation points were shifted with 50 µm downwards and with 250 µm right relative to the previous one to increase the resolution of the depth profile. After five measurements the indentation was performed right below the first one. Thus, five parallel rows contained the measurement points (Fig. 3.).

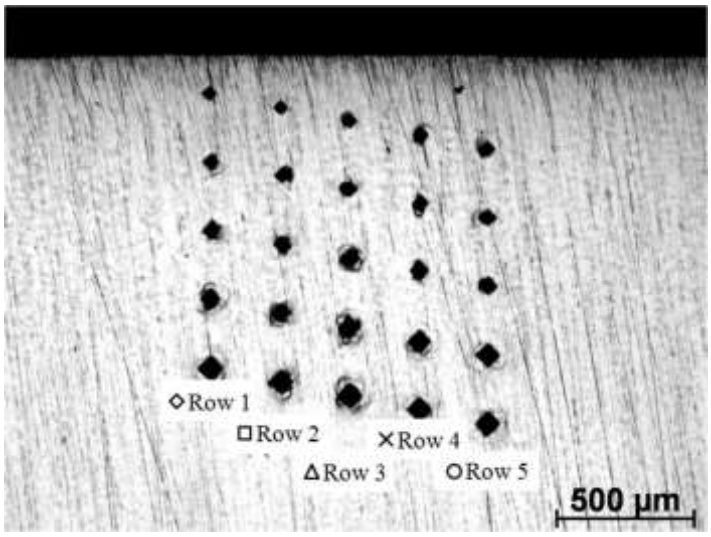

Figure 3. The indentation points of the hardness measurements

Results

Fig. 4. shows the normal (a) and shear stress values (b) formed during the laser hardening in the TD. The scatter of the measurements is also indicated. The average of the stress values prior to the laser treatment are indicated with the dashed lines.

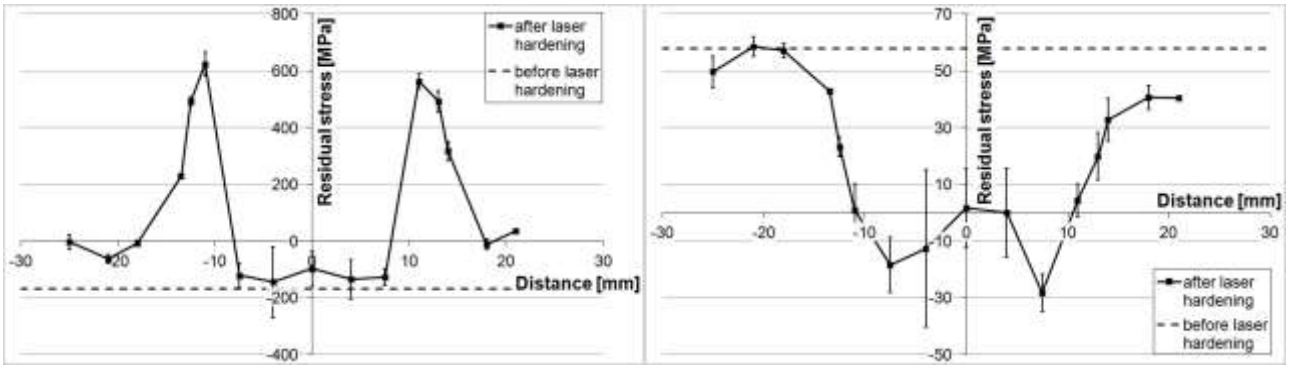

a) b)

Figure 4. The a) normal and b) shear stress profiles measured in the traverse direction (TD)

It can be seen that an initial compressive stress of ~ -180 MPa and shear stress of ~ 60 MPa was in the disc prior to the laser treatment. After the laser hardening a plateau formed in the middle region with normal stress values of ~ - 100 MPa. This region is the hardened band. At the edge of the hardened band tensile stress of 600 MPa is formed, which gradually decreases and converges to the initial stress state of the disc. The shear stress is 0 MPa within the hardened band while it reaches the initial values outside the hardened band. Fig. 5. shows the normal (a) and shear stress values (b) formed during the laser hardening in the FD. The average of the stress values prior to the laser treatment is also indicated.

The initial compressive stresses are somewhat larger in the FD being ~ -300 MPa, than was in the TD. The initial shear stresses in the FD are negligible. The normal stress profile in FD is similar to the profile in the TD. The stress values are somewhat smaller in the absolute sense, being around -50 MPa in the hardened band and ~ 500 MPa at the margin of the hardened band. The shear stress values are around 0 MPa in the whole profile.

Fig. 6. shows the diffraction patterns obtained from the same area after cleaning and surface polishing.

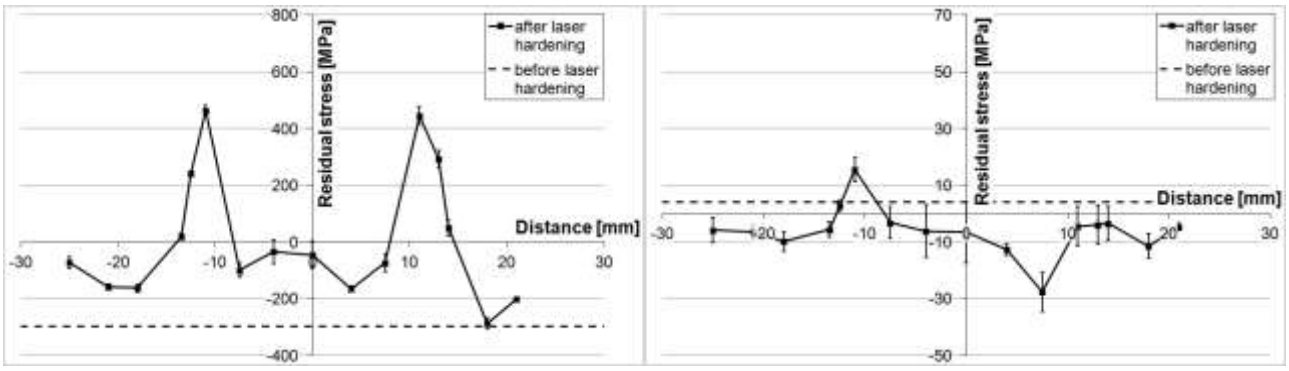

Figure 5. The a) normal and b) shear stress profiles measured in the feed direction (FD)

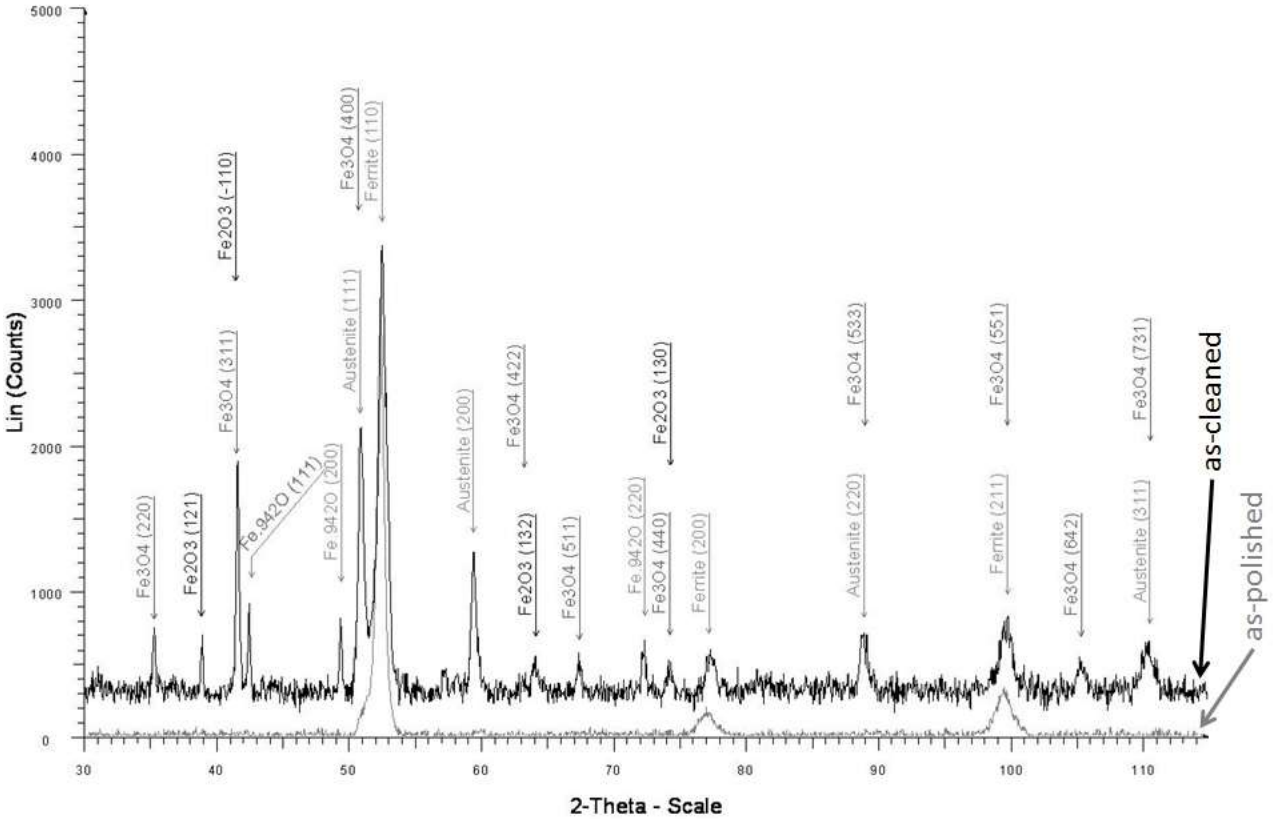

Figure 6. X-ray diffraction patterns of the treated surface in the as-cleaned and as-polished state of the same area.

Besides reflections of the ferrite/martensite phases, iron-oxides and a large amount of retained austenite were observed at the surface of the laser treated disc. The quantitative analysis of the retained austenite was not carried out since all peaks of austenite except for one overlapped with another peak. After polishing the surface, only the ferrite/martensite phases were present.

Fig. 7 shows the cross section of the disc before the laser treatment. The microstructure consisted of rows of ferrite and pearlite (Fig. 7. a). The martensite is shown with higher resolution in Fig. 7. b. Fig. 8. shows the microstructure of the laser hardened band in the cross section of the sample.

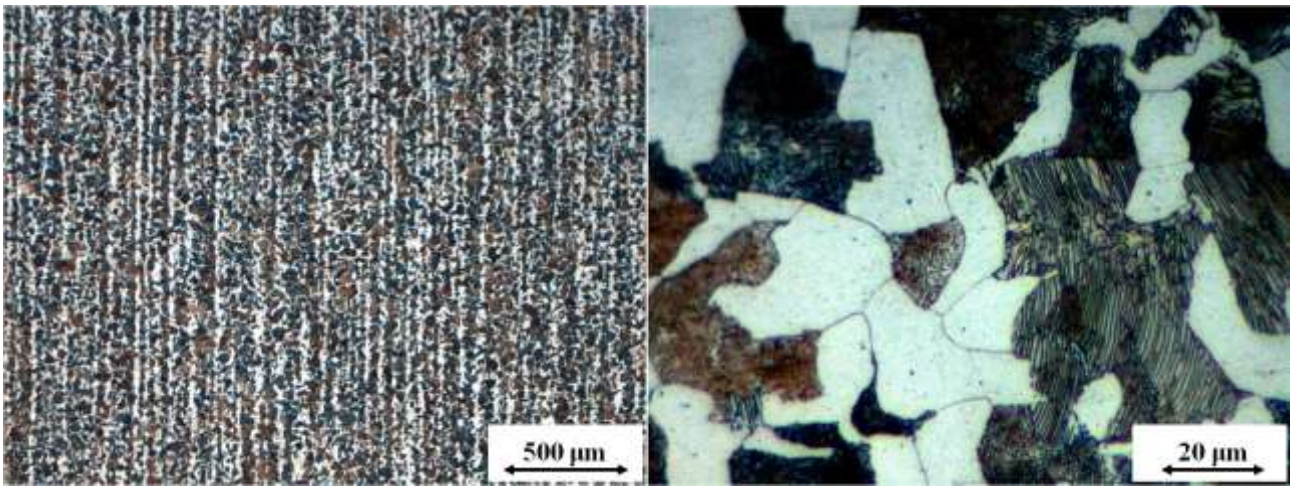

a) b)

Figure 7. The initial microstructure of the disc a) ferrite and pearlite rows b) ferrite and pearlite in higher magnification

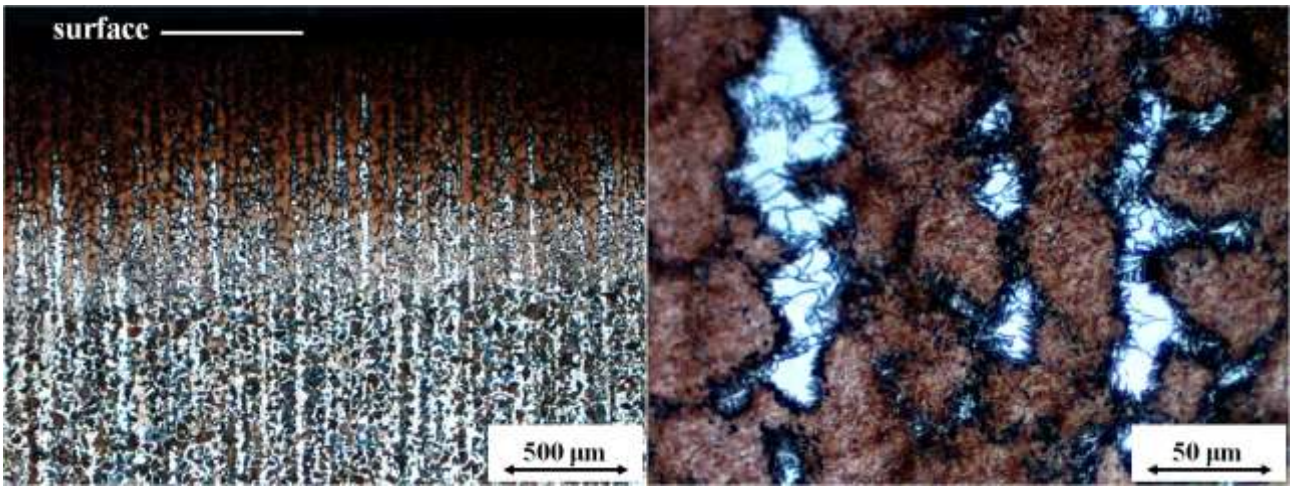

a) b)

Figure 8. Microstructure of the hardened band a) ferrite and martensite/pearlite rows b) ferrite and martensite in higher magnification

It can be seen that the final structure of rows of ferrite and martensite was obtained after the laser surface hardening treatment. It is also apparent that the amount of martensite decreases, while that of the ferrite increases as the depth increases. The depth of the hardened layer was determined by the microstructure images. Fig. 9. shows the obtained Vickers hardness profile. The depth of the hardened layer is also indicated. Vickers hardness of ~ 600 HV was observed at the surface which gradually decreases to ~ 200 HV leaving the hardened band.

Discussion

The examined hot-rolled plain carbon steel disc consisted of ferrite and pearlite forming rows as a result of rolling. The initial stress state was introduced by the sawing which resulted compressive stresses, and shear stresses being larger in the sawing direction (TD). The laser surface hardening treatment formed hardened bands within which the pearlite and ferrite were austenised then finally transformed to martensite. The pearlite transformed in a greater depth than the ferrite. It is known that the pearlite transforms to austenite at A_1 temperature, while ferrite transforms at a higher temperature, A_3. It is obvious that the heat introduced by the laser beam gradually decreased with

increasing depth. Thus, ferrite transformed only in smaller depths where A_3 was reached, while pearlite transformed in greater depths where A_1 was exceeded. The Vickers hardness gradually decreased from 600 HV to 200 HV towards the bulk. Relatively small compressive stresses, being close to the initial values formed and the shear stresses were eliminated within the hardened band. The maximal tensile stresses formed at the margins of the bands reaching values of ~ 600 MPa, where the austenised band encountered the non-transformed matrix. Iron-oxides formed on the surface of the disc and a large amount of retained austenite was found. The large volume fraction of retained austenite was probably due to the carbon diffusion from the applied graphite absorber which increased the carbon content of the surface.

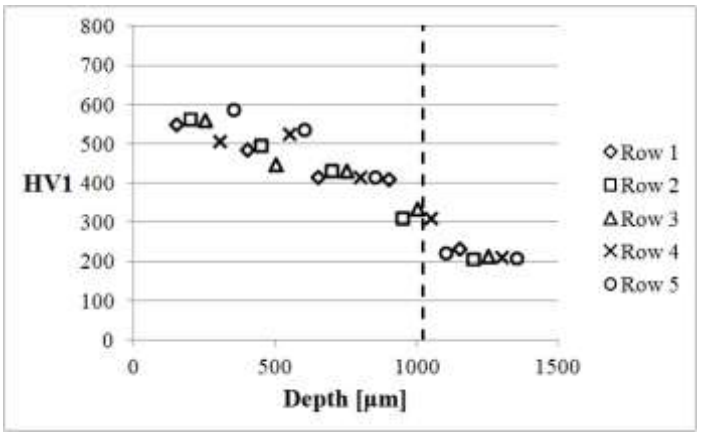

Figure 9. Vickers hardness profile

Acknowledgement

This work has been carried out as part of the TÁMOP-4.2.1.B-10/2/KONV-2010-0001 project within the framework of the New Hungarian Development Plan. The realization of this project is supported by the European Union, co-financed by the European Social Fund.

References

[1] Krauss: Principles of Heat Treatment of Steel, ASM Metals Park, Ohio 1980, pp 268
[2] G. Totten, M. Howes, T. Inoue: Handbook of Residual Stress and Deformation of Steel, ASM International, Ohio, 2002
[3] J. R. Davis, ASM Handbook of heat Treatment, ASM International, 1991, USA
[4] Valery Rudnev: Handbook of Induction Heating, Libary of Congress Cataloging – in-Publication Data, USA 2003 pp 303
[5] R. E. Haimbaugh, Practical Induction Heat Treating, ASM International, 2001
[6] J. R. Davis, Surface Hardening of Steels Understanding the Basics, ASM International, 2002
[7] C. Soriano, J. Leunda, J. Lammbarri, V. García Navas, C. Sanz, Effect of Laser Surface Hardening on the Microstructure, hardness and Residual Stresses of Austempered Ductile Iron grades, Applied Surface Science, 257 (2011) 7101-7106
[8] Y. S. Yang, S. J. Na, A Study on Residual Stresses in Laser Surface Hardening of a Medium Carbon Steel, Surface and Coating Technology, 38 (1989) 311-324
[9] G. S. Schajer, Practical Residual Stress Measurement Methods, John Wiley and Sons Ltd., 2013

Comparative corrosion study on silver coated metallic implants

M. Furko[1, a], M. Lakatos-Varsányi[1,b] C. Balázsi[1,c]

[1,] Bay Zoltan Nonprofit Ltd. for Applied Research, 1116, Budapest, Fehérvári út 130, Hungary

[a]monika.furko@bayzoltan.hu(corresponding author), [b]magda.lakatos@bayzoltan.hu, [c]csaba.balazsi@bayzoltan.hu

Keywords: silver coating, implant materials, potentiodinamic polarization measurement, antimicrobial properties

Abstract

Nano-structured silver layer was deposited by pulse current technique onto three different implant materials -TiAl6V4, CoCrMo alloy and stainless steel–that are commonly used in orthopedic surgery. The electrochemical behavior of the coatings in isotonic salt solution was investigated by potentiodynamic polarization measurements over a period of several weeks. The corrosion properties of silver coated different implant materials were compared. Degradation of silver coatings have been traced and confirmed by different methods such as scanning electron microscopy (SEM), energy dispersive spectroscopy (EDS) measurements.

1. Introduction

In orthopedic surgery the bacterial adhesion to biomedical devices surface is one of the major reason causing the inflammation and infection [1,2]. The bacteria attached to the implant surface can easily form a biofilm, which is impenetrable barrier for antibiotics. Removing bacteria being in a biofilm is impossible and the local or systemic antibiotic treatment is not effective. Staphylococci account for the majority of infections both of temporarily inserted and of permanently implanted orthopedic devices [3]. The antibacterial and antifungal effect of silver ions has been long known, and seems to provide silver the capability to inhibit biofilm formation. The Ag nanoparticles are capable of penetrating into the cell membranes and inactivate the bacteria easily by inhibiting their breeding [4]. Hence, silver is a potential and powerful antibacterial component that could be applied in biomedical engineering. Up to now, numerous results reveals that Ag implanted on the material surfaces can exhibit effective and well-antibacterial characteristics [5,7].

It is essential to incorporate minimum amount of Ag^+ ion to reduce bacterial adhesion on biomaterials as well as minimizing host tissue toxicity [8,9]. The silver coating should operate within the constraint that the silver release should not be toxic to the surrounding tissue [10].

The objective of this research is to develop nanostructured silver coatings on metallic implants as well as study and compare the corrosion behaviour of these surface modified materials. To accomplish this we execute electrochemical measurements such as potentiodynamic polarization methods in isotonic salt solution.

Polarization methods such as potentiodynamic polarization, potentio-staircase and cyclic voltammetry are often used for laboratory corrosion testing. These techniques can provide useful information regarding the corrosion mechanisms, corrosion rate and susceptibility of specific materials to corrosion in different environments. Polarization methods involve scanning the potential of the working electrode and monitoring the current which is produced as a function of time or potential [11].

2. Experimental

2.1. Preparation of silver coated implant materials

Titanium alloy (TiAl6V4), CoCrMo alloy and stainless steel discs (17 mm × 1 mm) were used as substrates. One side of each disc was roughened using a sandblasting procedure with a 180-grit aluminium oxide media. After roughening, the surfaces were ultrasonically washed in ethanol for 3 min to remove any residual aluminium oxide media and grease. The electrochemical bath was a

commercially available cyanide bath (Glanzsilberbad Elfit 73, Schlötter). Silver cyanide plating baths have long been employed and afford significant advantages from the standpoint of commercial plating processes.
The coatings were electrodeposited onto the sandblasted disc substrate using IGTV-4i/6t type pulse current generator. The electrodeposition was carried out in a two-electrode cell under normal atmospheric conditions. The anode was a silver sheet and the metallic implant disc was used as a cathode. During the deposition process the electrolyte was stirred. The morphologies of nanosilver deposits were studied by scanning electron microscopy (SEM) and the composition by energy dispersive spectroscopy (EDS).

2.2. Electrochemical tests

The potentiodynamic studies were carried out with Zahner IM6e electrochemical workstation (Zahner, Germany).The electrochemical potentiodynamic polarization tests were performed in a standard three-electrode-cell, at a potential scanning rate of 0.1 mV s^{-1}initiated at −200 mV below the open-circuit potential and the atmosphere was open to air. The working electrode was a metallic implant disc (⌀ 1.37 cm^2) with and without silver coating. Platinum net and Ag/AgCl electrode were used as counter electrode and reference electrode, respectively. The electrolyte was physiological normal saline (0.9 wt% NaCl). Three replicate tests of each group of specimens were performed. The tests were started after a steady open-circuit potential was attained (not more than±5 mV drift in 5 min). The anodic and cathodic polarization curves were obtained for each specimen and corrosion current densities and corrosion potentials of various specimens were determined from the potentiodynamic polarization curves by Tafel extrapolation methods.
The potentiodynamic polarization curves were recorded after 30 min of immersion. The corrosion current density (*i*corr) for the particular specimens was determined by extrapolating the anode and cathode Tafel curves.

3. Results and discussion

3.1. Silver deposition

Nano-crystalline silver layers were deposited onto pre-treated implant material substrates of different types by pulse-plating technique. Owing to the oxide layer on the surface of the substrate alloy; the adhesion of the silver would be very poor if a pre-treatment is not applied before plating. The appropriate surface for electroplating was sandblasted.
In our previous work [12] we had optimized the deposition parameters. The chosen pulse current parameters with the smaller grain size and highest current efficiency were as follows: t_{on}: 5ms, t_{off}: 15ms, i_p: 40mAcm^{-2}. Fig. 1 shows the SEM images on silver coated metallic implants. The thickness of deposits was about 10 μm.

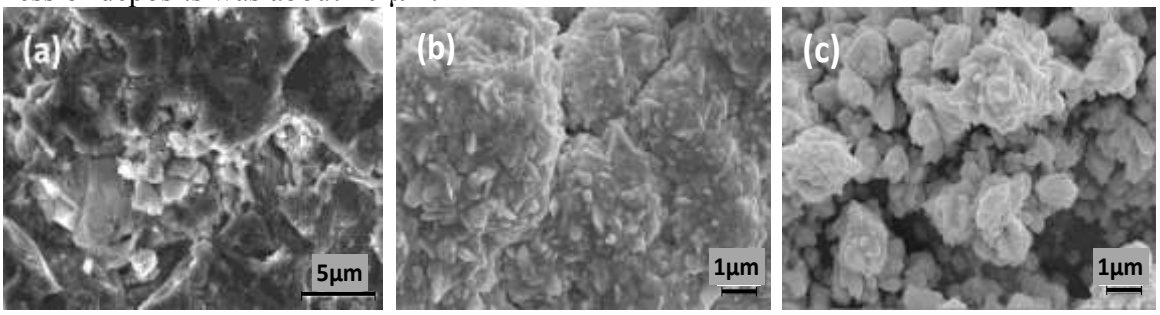

Fig. 1: SEM images on Ti substrate alloy (a) and silver coated Ti alloy after deposition (b) and after soaking in 0.9% NaCl solution for two months (c).

3.2. Electrochemical test by Tafel analysis

Potentiodynamic polarization measurements are valuable in predicting how a material will behave when exposed to a particular environment. In order to compare the susceptibility to corrosion of the silver-coated samples in relation to the bare alloy material, potentiodynamic polarization curves in isotonic physiological solution were recorded over time (Fig 2.). The polarization scan rate was 0.1 mV s^{-1}.

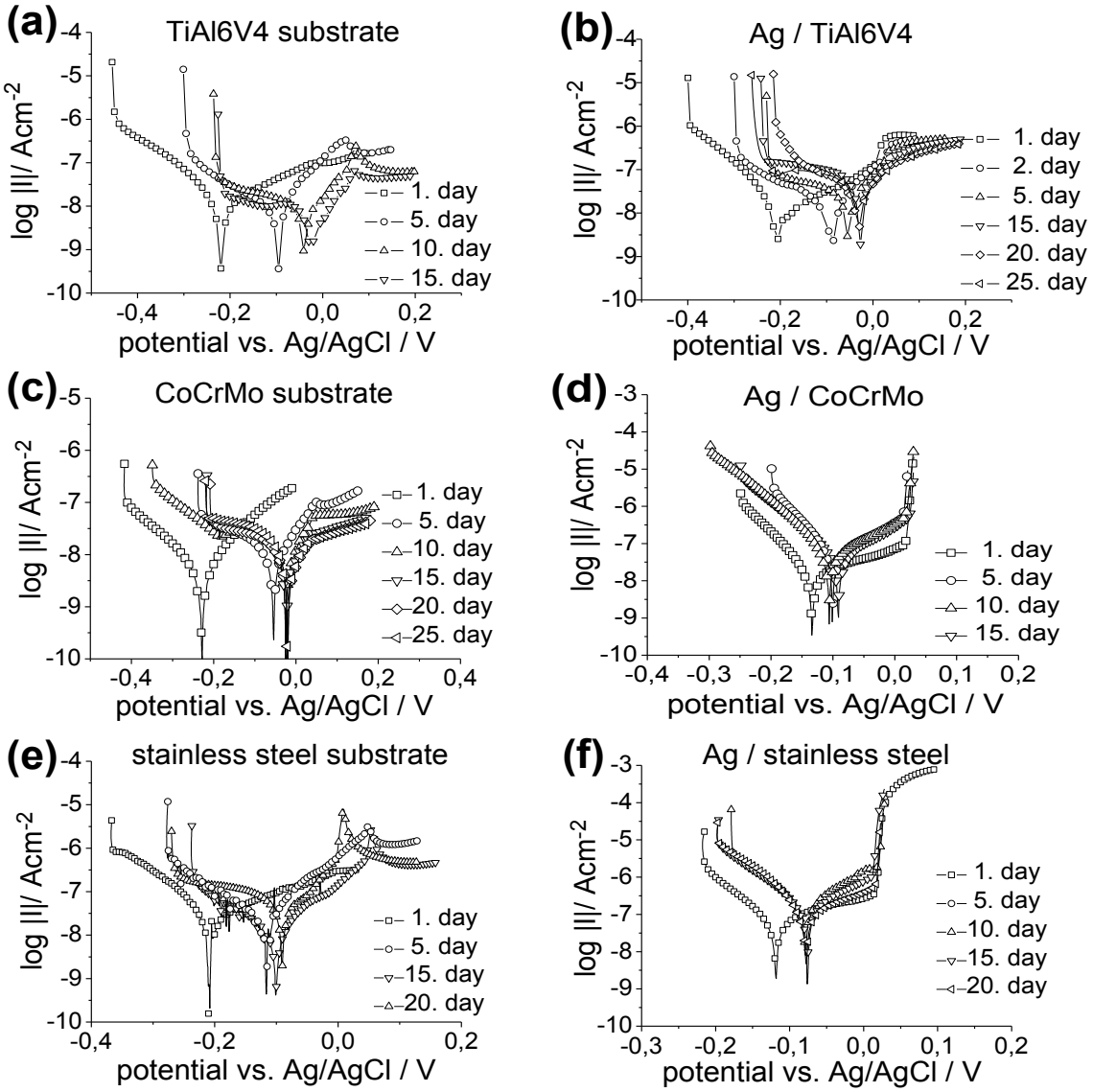

Fig. 2: Potentiodynamic measurements on uncoated (a) and silver coated TiAl6V4 alloys (b), uncoated (c) and silver coated CoCrMo alloys (d) as well as uncoated (e) and silver coated stainless steel (f)

In general, the cathodic branch of the Tafel plot shows the hydrogen evolution through a reduction process, whereas the anodic branch represents silver dissolution by oxidation.

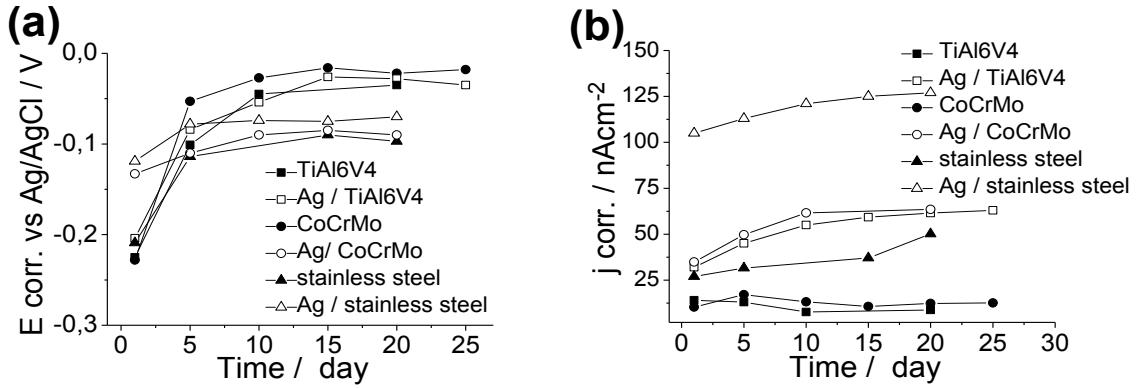

Fig. 3: Corrosion potential (a) and corrosion current (b) over time on coated and uncoated substrates.

Fig. 3 demonstrates the changes of corrosion current and potential over time. As it can be seen, in all cases there is a significant increase in corrosion potentials during the early stage immersion (~5

days), after that this increasing tendency is slowing down. The corrosion potential shifted towards more anodic values, which can be attributed to the passivation of bare implant materials and the adsorbed silver chloride precipitation on the silver coated electrode surface. To prove this assumption we have performed EDS measurements where along with the silver signal, chloride signal appears on the spectrum (see Fig. 4).

Fig. 3 (a) shows that the uncoated stainless steel possesses the lowest corrosion potentials (from -228 mV to -97 mV) while the CoCrMo substrates has the highest corrosion potential (from -209 mV to -18 mV).

The corrosion current density is representative for the degradation degree of the silver coatings. The corrosion current (i_{corr}) shows a little increasing tendency or remains constant with time elapsed in the case of silver coated implant substrates, while for bare substrates (TiAl6V4 and CoCrMo) an opposite tendency can be observed: a little decreasing in corrosion current. However, for stainless steel substrate the corrosion current slightly increases, which suggests pure stainless steel was more prone to localized corrosion due to the disruption of the protective layers.

The current densities observed for surfaces coated with silver films were higher than those observed for uncoated surfaces. According to the values of j_{corr}, the corrosion resistances of the specimens are ranked as follows: TiAl6V4<CoCrMo<stainless steel<Ag/TiAl6V4<Ag/CoCrMo<Ag/stainless steel

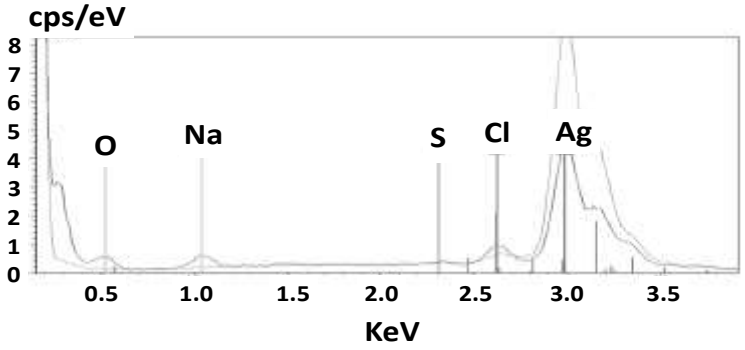

Element	series	[wt.-%]	[at.-%]
Silver	L-series	54.042	15.750
Oxygen	K-series	38.385	75.426
Sodium	K-series	4.253	5.816
Chlorine	K-series	2.645	2.345
Sulfur	K-series	0.673	0.660

Fig. 4: EDS analysis of silver coated TiAl6V4 implant material

In order to find the contact galvanic potentials and currents (bimetallic corrosion), the polarization curves on substrates and on silver coated substrates were superimposed on each other as it is shown in Fig. 5 (a-c). The intersection of cathodic polarization curve of more electropositive metal with the anodic polarization curve of more electronegative metal gives the galvanic corrosion potential and the galvanic corrosion current. The galvanic potentials are found to be –113 mV and –71.7 mV and -68.2 mV, while the galvanic current densities are 36.8 and 51.2 nA cm^{-2} and 63.8 nA for Ag/TiAl6V4, for Ag/CoCrMo and Ag/stainless steel galvanic cells, respectively.

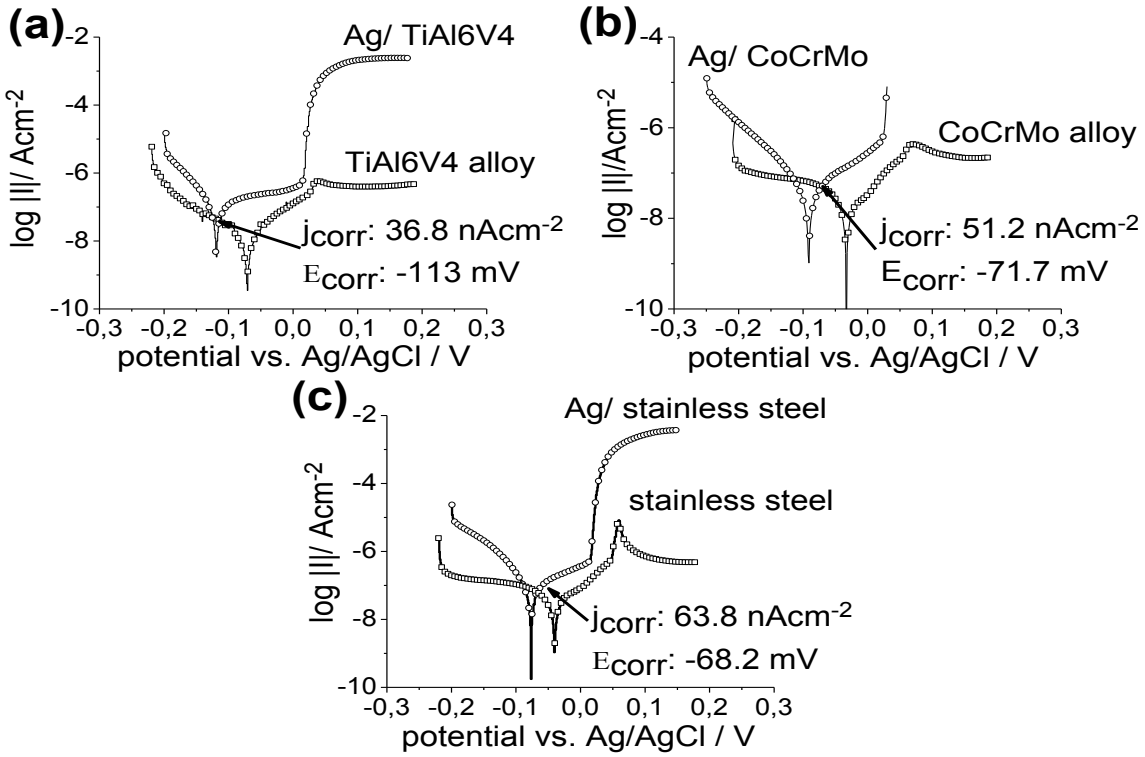

Fig. 5: Potentiodynamic curves on bare and silver coated implant materials (a) Ag/ TiAl6V4, (b) Ag/CoCrMo and (c) Ag/satinless steel galvanic systems after 10 days of immersion time.

The corrosion potential, *E*corr is defined as the potential at which the anodic and cathodic current densities have the same value. It can be seen on Fig. 5, that the corrosion potentials are more negative values for silver coated substrates, than that of uncoated substrates in all cases and the corrosion currents are shifted to higher values for substrates with silver coating after ten days of immersion in 0.9% NaCl solution.

The corrosion current as a value inversely proportional to charge transfer resistance ($R_p \sim 1/$ icorr.), so the calculated R_p values for the above mentioned galvanic systems in increasing order are as follows: Ag-stainless steel (~15.6 MΩ)<Ag-CoCrMo (~19.5 MΩ)<Ag-TiAl6V4 (~27.2 MΩ)

The corrosion rate depends on the kinetics of both anodic (oxidation) and cathodic (reduction) reactions. According to Faraday's law, there is a linear relationship between the metal dissolution rate or corrosion rate, R_m (in μm/year), and the corrosion current $i_{corr.}$:

R_m = (icorr.(mA/cm2) ×M (g)/ρ (g/cm3) × n)× 3270

where 3270 = 0.01×[1 year (in seconds)/96497.8] and 96497.8=1Faraday in Coulombs, M is the atomic weight of the metal, ρ is the density, n is the charge number which indicates the number of electrons exchanged in the dissolution reaction.

The calculated corrosion rates for these contact galvanic systems were 1.237, 1.721 and 2.128 μm/year, respectively. The Ag/stainless steel galvanic system has the highest corrosion rate, while the Ag/TiAl6V4 galvanic system exhibits the smallest corrosion rate. The corrosion relates to an increase in the oxidation rate.

4. Conclusions

This study was focused on pulse-electrodeposition of nanosilver coatings on TiAl6V4, CoCrMo and stainless steel alloys with controlled and continuous Ag^+ ion release. For antimicrobial applications of nano-silver coated implant alloys, it is necessary to sustain a continuous and long term release of silver ions.

Long-term dissolution of silver coating due to the formed galvanic cells between the silver coating and the metallic substrate was proved by potentiodynamic polarization measurements (Tafel curves). In our potentiodynamic measurements the corrosion potential is shifted to more positive

values for both nanostructured coatings and substrate materials in 0.9 % sodium chloride. The corrosion potentials significantly increase in 5 days, but after that slightly changes.
The corrosion current, which demonstrates the degradation rate of silver layer, shows an increasing tendency for all silver coated metallic implants. This tendency is more significant in about 10 days of immersion, but after that hardly changes.
The silver coatings have a worse corrosion resistance and a higher corrosion rate than that of uncoated metallic implants.
The corrosion rate calculated by potentiodynamic polarization curves obtained after 10 days from immersion in 0.9 % NaCl solution is the smallest for Ag-TiAl6V4 galvanic system (1.237 μm/year) while the highest for Ag-stainless steel galvanic system (2.128 μm/year).

Acknowledgements
The authors gratefully acknowledge the financial support of TÁMOP project. (Project code: TÁMOP 4.2.2.A11/1/KONV2012 0075)

References
[1] W.-C. Chiang, L.R. Hilbert, C. Schroll, T. Tolker-Nielsen, P. Moller: Bacterial inhibiting surfaces caused by the effects of silver release and/or electrical field, Electrochimica Acta 54 (2008) 108–115
[2] K.D. Secinti, M. Ayten, G. Kahilogullari, G. Kaygusuz, H.C. Ugur, A. Attar: Antibacterial effects of electrically activated vertebral implants, Journal of Clinical Neuroscience 15 (2008) 434–439.
[3] F. Mirzajani, A. Ghassempour, A. Aliahmadi, M.A. Esmaeili: Antibacterial effect of silver nanoparticles on Staphylococcus aureus, Research in Microbiology 162 (2011) 542-549.
[4] G.J. Zhao and S.E. Stevens: Multiple parameters for the comprehensive evaluation of the susceptibility of Escherichia coli to the silver ion, Biometals 11 (1998) 27-32.
[5] S.C.H. Kwok, W. Zhang, G.J. Wan, D.R. McKenzie, M.M.M. Bilek and Paul K. Chu: Hemocompatibility and anti-bacterial properties of silver doped diamond-like carbon prepared by pulsed filtered cathodic vacuum arc deposition, Diamond and Related Materials 16 (2007) 1353-1360.
[6] H.W. Choi , R.H. Dauskardt, S.C. Lee, K.R. Lee and K.H. Oh: Characteristic of silver doped DLC films on surface properties and protein adsorption, Diamond and Related Materials 17, (2008) 252.
[7] K.H. Liao, K.-L. Ou, H.-C. Cheng, C.-T. Lin: Effect of Silver on Antibacterial Properties of Stainless steel, Applied Surface Science 256 (2008) 3642-3646.
[8] W. Chen, Y. Liu, H.S. Courtney, Bettenga M, Agrawal CM, Bumgardner JD, et al: In vitro anti-bacterial and biological properties of magnetron co-sputtered silver-containing hydroxyapatite coating. Biomaterials 2006; 27:5512-5517.
[9] K. Jamuna-Thevi, S.A. Bakar, S. Ibrahim, N. Shahab, M.R.M.: Quantification of silver ion release, in vitro cytotoxicity and antibacterial properties of nanostuctured Ag doped TiO2 coatings on stainless steel deposited by RF magnetron sputtering, Vacuum 86 (2011) 235-241.
[10] P. DeVasConCellos, S. Bose, H. Beyenal, A. Bandyopadhyay, L. G. Zirkle: Antimicrobial particulate silver coatings on stainless steel implants for fracture management, Materials Science and Engineering C 32 (2012) 1112–1120.
[11] A.–C. Ciubotariu, L. Benea, M. Lakatos–Varsanyi, V. Dragan: Electrochemical impedance spectroscopy and corrosion behaviour of Al2O3–Ni nano composite coatings, Electrochimica Acta 53 (2008) 4557–4563.
[12] M. Lakatos-Varsányi, M. Furko, T. Pozman: Electrochemical impedance spectroscopy study on silver coated metallic implants, Electrochimica Acta 56 (2011) 7787–7795.

Electrochemical impedance spectroscopy as a prospective tool for the characterization of the intermetallic microstructure of lead free solder

Tamás Hurtony[a], Attila Bonyár, Péter Gordon

[1]Department of Electronics Technology, Budapest University of Technology and Economics

Egry József utca 18. Budapest, H-1111, Hungary

[a]hurtony@ett.bme.hu

Keywords: solder microstructure, intermetallic compound, electrochemical etching, Electrochemical Impedance Spectroscopy

Abstract. In this study the possibility to apply electrochemical impedance spectroscopy as an alternative method for the characterisation of the intermetallic microstructures of Sn-3.5Ag lead free solder samples was investigated. The aim of the study is to compare the electrochemical impedance spectra of solder samples, reflowed with different heat profiles. A quenching technique was applied in order to solidify the solder samples in cylindrical crucibles. Differences in the microstructures of the solidified alloys were achieved by changing the temperature of the quenching media. The molded and cross sectioned specimens were observed using both optical microscopy and scanning electron microscopy (SEM) combined with energy dispersive spectroscopy (EDS). The microstructure of the ingots was revealed by selective electrochemical etching. The electrochemical impedance spectrum (EIS) was measured before and also after the selective etching process. The complex impedance spectra contain information regarding the characterized microstructure. Our aim is to determine quantitative parameters which are identical to the characteristics of the microstructure.

Introduction

Due to its environmental impacts hazardous substances such as lead was banned from the consumer electronic industries. The change-over to lead-free technology was fairly challenging at the very beginning, since many properties of the initial nominees were lagging behind the commonly used tin-lead eutectic solder alloy [1-4]. These initiatives have led to the development of new lead-free solders like Sn-Cu, Sn-Ag, Sn-Zn-Bi, Sn-Ag-Bi, Sn-Bi, Sn-Ag-Cu, Sn-Ag-Zn, Sn-Zn, and Sn-In for electronic applications. All these solder alloys share Sn as a base material which is mixed with minor substances [6–7]. The Sn-Ag (SA) and Sn-Ag-Cu (SAC) alloys are considered the best substitutions of lead-containing solders in which the Sn-rich dendritic/grainy matrix is formed and eutectic mixture of a Sn-rich phase and intermetallic Ag_3Sn particles are located in the interdendritic regions. Depending on the parameters of the soldering techniques the fine microstructure composed by Sn grains and intermetallic compounds may be formed differently. Since the macroscopic properties of the solder joints are partially determined by the microstructure, its characterization is a current research topic.

Conventional metallographic observation methods like cross-sectioning only give narrow perspective into the structure of the solder joint. Our novel, previously published method, which reveals the intermetallic structure of the bulk solder by selective electrochemical etching opened new perspectives in solder joint research [8]-[10]. Due to the high level of selectivity of our deep etching method the fine structure of intermetallic compounds remain intact so it can be observed and characterized. Upon our previous investigations we found that solder microstructures, which are resulted by different technological processes – like different cooling rates – can show significant and observable differences. This leads to new ways of solder microstructure characterization [8]. The next step and our current aim is to find a quantitative method, for the characterization of different microstructures.

In this paper we investigate the possibility of applying electrochemical impedance spectroscopy (EIS) for the quantitative characterization of the revealed microstructures. EIS is very sensitive to the geometrical properties of the applied working electrodes, and was successfully utilized in the past to characterize the roughness of surfaces or to characterize the pore size and shape in case of porous electrodes. The revealed microstructure in an electrochemically etched solder sample presents a complex surface, which can be considered either rough or porous, depending on the etching time. Hence, it is safe to presume that EIS could be successfully applied to characterize different microstructures. For this purpose we compare the electrochemical impedance spectrum that has been measured after the etching process with the spectrum before etching. The complex impedance spectra contain information regarding the intermetallic microstructure.

Experimental procedure

Sample preparation. Our aim was to evaluate the feasibility of the industrial application of EIS combined with selective electrochemical etching. From this consideration a commercial, industrial grade solder alloy (ALPHA Vaculoy SAC350) was used. According to the specification of the alloy the material composition of the solder is Sn ~96.5 %, Ag 3.5 % (Cu < 0.05 %). The solder paste was heated up to 260 °C in order to separate the metallic and non-metallic phases of the paste. After solidification of the solder ingot, the major part of the still liquid flux was removed.

The solder ingots were remelted in a hot air reflow rework station and they were heated up to 260 °C again. The molten sample was merged into a defined volume of tempered Galden liquid. The IDs of the samples in this paper refer to the temperature of the quenching medium. After the solidification of the solder sample discs were cut from the ingot for further analysis. The temperature of the solder was monitored with a thermocouple sensor connected to a data logger. The solder discs were cold contacted with a measuring wire and they were molded into a two component acrylic resin. The embedded samples were grinded so that the size of their surfaces at the cross sectioning plane was approximately the same. The embedded and sectioned samples were placed in an electrochemical cell (Fig. 1) in which the measurements were performed.

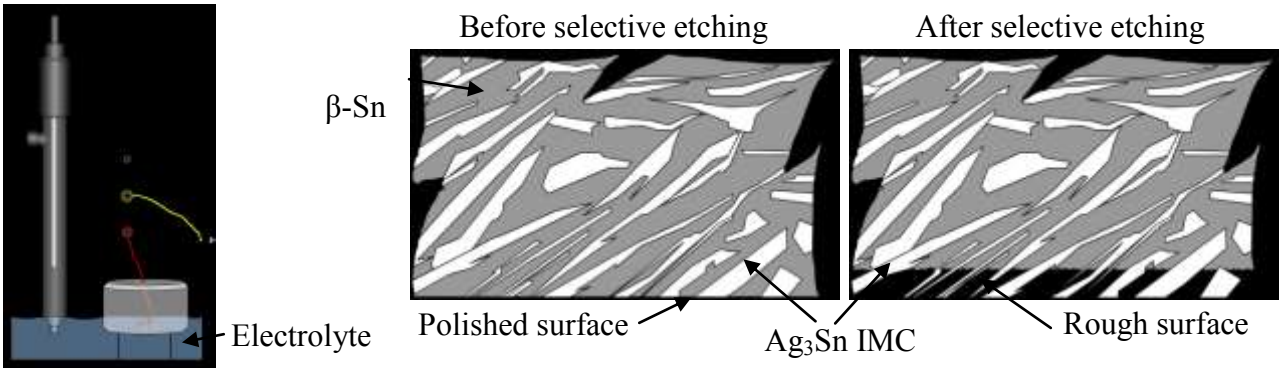

Fig. 1 The scheme of the electrochemical cell. Hg/Hg_2Cl_2 Reference electrode (RE), stainless steel Counter electrode (CE) and the solder sample as Work electrode (WE) was used during the electrochemical evaluation of the samples. Before the selective etching process the surface of the work electrode was defined by the polished flat surface. After the selective removal of tin phases the surface of the work electrode is defined by the revealed microstructure of the solder ingot.

Electrochemical preparation and measurements. The samples were elevated 12 mm from the bottom plate of the counter electrode. Once the samples were locked in the fixture they were not moved until the end of the complete measurement. Our aim was to measure only the effects caused by the changes in the work electrode surface, which is characterized best by the changes in the double layer capacitance. Thus we wanted to avoid any Faradic processes to approximate a purely capacitive electrochemical behaviour. For this purpose we applied 0.5 M NaCl solution as an electrolyte, which does not react Faradically with the sample at given DC potentials for which it is commonly used in the according scientific literature [11]-[13]. The potentiometric behaviour of such an electrochemical system was also analysed and in order to minimise the possibility of any Faradic processes -700 mV was set as the DC level of the EIS measurement. The amplitude of the AC signal was 10 mV and the frequency was alternated between 0.1 and 100 kHz. By applying the above mentioned EIS parameters charging and discharging of the double-layer capacitance is the dominant physical effect at the surface of the work electrode. The capacitance of the double-layer impedance is expected to be proportional to the total surface of the work electrode which is highly affected by the intermetallic microstructure of the lead-free solder alloy.
First the impedance spectroscopy on the polished original sectioning plane was applied and after the EIS process the electrolyte was changed to 1 (V/V) % H_2SO_4.
The β-tin phase was selectively extracted from the solder sections with electrochemical etching, which was done in a standard three-electrode cell with a Voltalab PGZ 301 potentiostat in chrono-amperometry mode. The acid basin made of stainless steel was used as counter electrode, while the section of the solder ingot itself acted as a working electrode (Fig. 1Fig). The saturated calomel reference electrode and the samples were immersed into 1 (V/V) % H_2SO_4. The bias potential was set to -350 mV. The etching time was normalized by surface of the samples and it was varying between 120-160 s.
After the removal process the electrolyte was changed again to 0.5 M NaCl, with gentle care in order not to cause any harm to the revealed fine microstructure of the sample. The EIS was repeated on the prepared surface and the before and after spectra were compared. All measurements were carried out at laboratory ambient temperature.
The microstructure of the samples were evaluated with a FEI Inspect S50 Scanning Electron Microscope. The composing elements were identified by energy dispersive spectroscopy.

Results and discussion

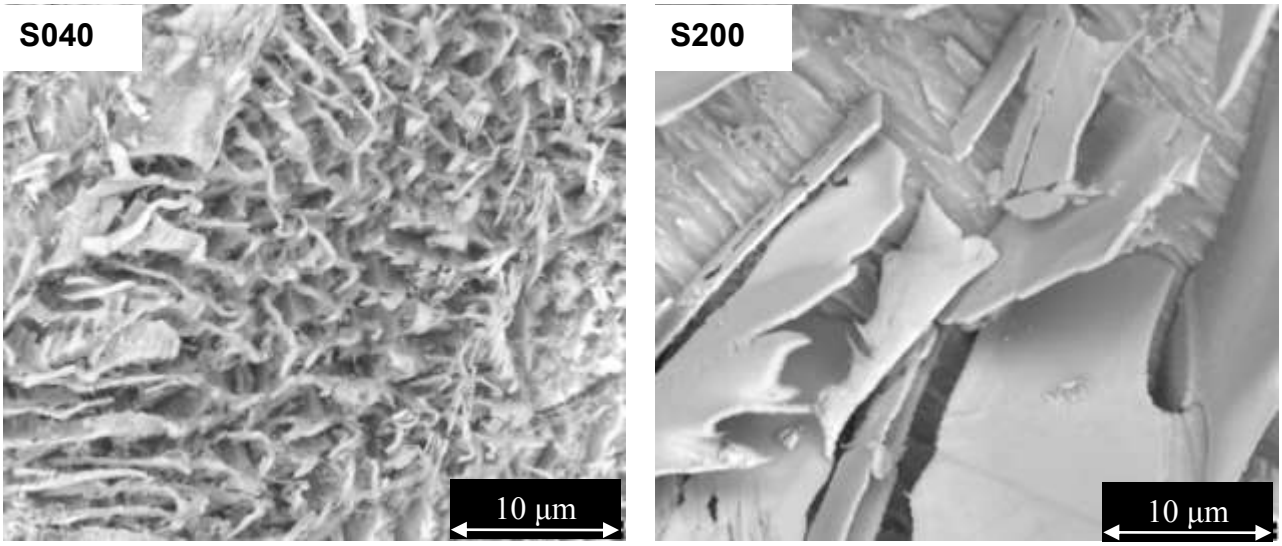

Fig. 2 SEM micrographs of selectively etched solder samples. The Ag_3Sn intermetallic morphology can either be formed as spheroid, fibre or plate-like structure. The more rapid the cooling, the finer microstructure of IMC array may form.

Morphological analysis of the microstructures was performed with SEM back scattered electron (BSE) detector because the shading effect of a secondary electron detector might cover some

structural detail. The depth of the exposure of the sample preparation during etching was optimised in order not to reveal the microstructure too deep, because the fragile IMC morphology is very sensitive to external impact. The ideal depth of etching (defined as the distance of the etching front plane and the cross sectioning plane) is 60-90 μm.

The microstructures of the solder ingots were not uniform over the total surface. As it was expected, it was always finer at the perimeter if the specimens because the outer regions of the ingot was in good thermal contact with the wall of the test tube, which was rapidly cooled by the Galden medium. Cylindrical test tubes were applied in order to ensure a cylindrical symmetric thermal distribution in the samples. Monotonic thermal gradient was evolved in axial direction, along which the microstructure was different. This is an expected side effect of the samples preparation method. It is however, considered to have minimal effect on the measurement, since the relative surface (surface divided by the perimeter in pixels) was more than 120.

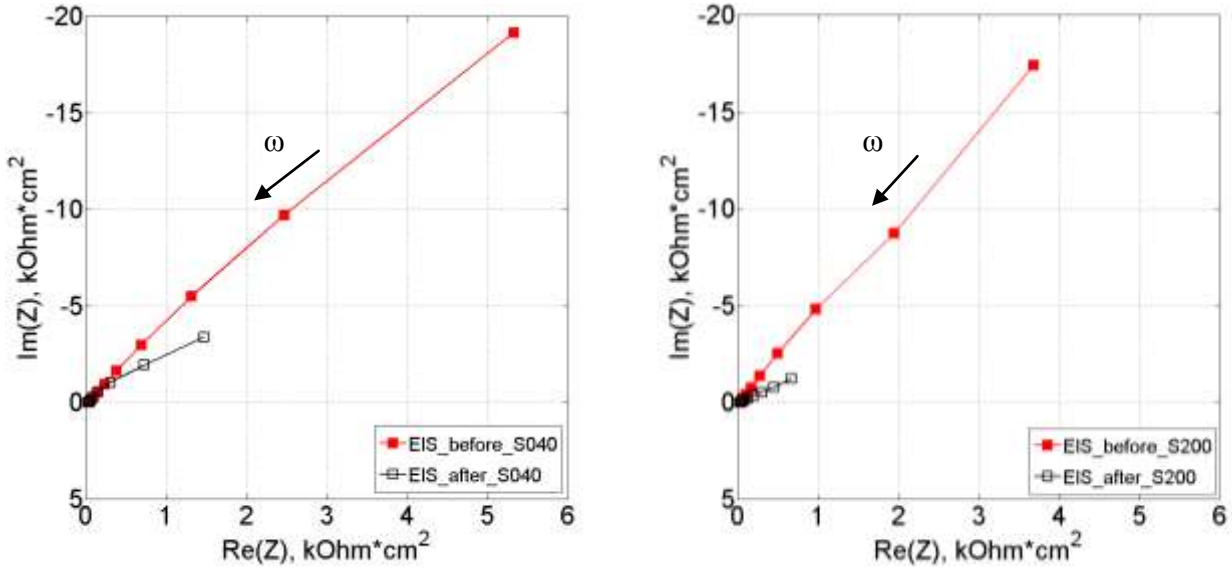

Fig. 3 EIS Nyquist plots measured before (red) and after (black) the electrochemical etching on sample S040 (left) and S200 (right)

Table 1. The parameters of the equivalent circuit of the fitted curves.

		Modell	Rs	CPE-Q	CPE-α	LoA	LoB	LoPhi
S040	B*	M2	34.6	3.44E-06	0.859	1.00E+20	-3.39E-06	-3.64
	A*	M2	35.2	1.72E-05	0.881	1.00E+20	2.44E-02	-4.79
S080	B*	M1	33.9	1.96E-05	0.714			
	A*	M2	36.0	1.05E-04	0.721	1.00E+20	6.16E-03	-4.00
S120	B*	M2	31.3	2.21E-05	0.691	1.00E+20	-1.46E-18	-4.00
	A*	M1	35.3	1.60E-04	0.694			
S160	B*	M2	35.4	3.07E-06	0.881	1.00E+20	-4.08E-07	-2.72
	A*	M2	33.6	3.13E-05	0.787	1.00E+20	5.09E-03	-4.11
S200	B*	M2	34.9	3.57E-06	0.884	1.00E+20	-8.73E-06	-3.86
	A*	M1	31.5	6.90E-05	0.670			

* B: Before etching , A: After etching

Fig. 4 The applied equivalent circuit models. M1 model assumes almost perfect capacitive behaviour, while in the case of M2 a polarisation resistance was taken into account parallel with the Constant Phase Element (CPE)

In the S040 sample the fine microstructure of the IMC array mainly composed of fibrous and grainycomponents (Fig. 2). As the cooling rate was decreased the fine structures tended to transform into plate-like structures, which is in good correlation with previously reported results [8-10].

EIS spectra were measured before and after the selective electrochemical etching on the samples. In Fig. 3 it can be seen that the obtained EIS spectra are significantly different before and after the etching process. Due to the very selective nature of the etching process the relevant change in the spectra is mainly due to the relative change in the effective surface area of the work electrode. Before etching the polished surface could be considered quite smooth, with an Ra value below 100 nm, while after revealing the microstructure the surface area is mostly determined by the surface area of the IMC in the exposed depth, which is significantly larger. As it can be seen in the EIS spectrum of Fig. 3 faster cooling rates yielded to higher electrode capacitances, which indicates larger surface areas and thus the presence of finer microstructures. However only the Nyquist plot after the etching process is not applicable to compare the microstructure to each other, since the geometry of the solder samples were intentionally different.
As it is reported in the literate the EIS spectra are usually utilized to determine the corresponding equivalent network circuit of the electrochemical system by considering the physical processes in the reaction, and fitting curves to the measured data set [8-10, 12-17]. We applied two equivalent circuit models to describe the behaviour of the work electrode (Fig 4). The M1 model assumes almost perfect capacitive behaviour, while in the case of M2 a polarisation resistance was taken into account parallel with the Constant Phase Element. The parameters of the equivalent circuits of the fitted curves are summarized in Table 1.

As it can be seen in the preliminary results in Fig. 3 and Table 1 the EIS spectra might be appropriate to characterise the fine microstructure of the exposed internal structure of solder joint as it is sensitive enough to reveal minor changes in the surface of the electrochemical cell. EIS measurement is also compatible with the sample preparation process. This technique, however, cannot be applied without being verified by a physically independent measuring technique.

Summary

In this present study we introduced a possible and general method for characterising the microstructure of lead-free solder alloy. Sn3.5Ag solder samples were reflowed and quenched in Galden liquid with different temperatures in order to generate different microstructures. The microstructure was revealed with electrochemical etching and the electrochemical impedance spectrum was measured before and after the etching process. Based on the analysis result presented above the followings were concluded:

- The microstructure is composed of fibre grain and plate-like Ag_3Sn intermetallic compounds. More intensive cooling rates result in finer microstructure. The relative occurrence of fibre and grainy type structure was higher in the samples with higher cooling rates (S040, S080).
- The Ag_3Sn intermetallic compound composed plate-like structures with lower cooling rates.
- The exposure depth of the selective etching was controlled precisely and it was set to be between 60-90 µm. The amount of extracted Sn was set to be equal in each case.
- The characteristics of the before and after EIS curves were significantly different, their absolute value between individual specimens, however, showed large variance.

References

[1] S.P. Yu, H.J. Lin, M.H. Hon, Effects of process parameters on the soldering behavior of the eutectic Sn–Zn solder on Cu substrate, J. Mater. Sci. 11 (2000) 461–471.

[2] R.A. Islam, Y.C. Chan, W. Jillek, S. Islam, Comparative study of wetting behaviour and mechanical properties (microhardness) of Sn–Zn and Sn–Pb solders, Microelectron. J. 37 (2006) 705–713.

[3] E. Çadırlı, U. Böyük, S. Engin, H. Kaya, N. Maraslı, A. Ülgen, Experimental investigation of the effect of solidification processing parameters on the rod spacings in the Sn–1.2 wt.% Cu alloy, J. Alloys Compd. 486 (2009) 199–206.

[4] L.R. Garcia, W.R. Osório, L.C. Peixoto, A. Garcia, Mechanical properties of Sn–Zn lead-free solder alloys based on the microstructure array, Mater. Charact. 61 (2010) 212–220.

[5] Yanxia Jing, Guangmin Sheng, Guoji Zhao, Influence of rapid solidification on microstructure, thermodynamic characteristic and the mechanical properties of solder/Cu joints of Sn–9Zn alloy, Materials and Design 52 (2013) 92–97

[6] Seo SK, Kang SK, Shih DY, Lee HM. An Investigation of Microstructure and Microhardness of Sn-Cu and Sn-Ag Solders as Functions of Alloy Composition and Cooling Rate, J Electron Mater 2009;38(2):257–65.

[7] Bastow E. Solder families and how they work. Adv Mater Process 2003;3:26–9.

[8] Tamás Hurtony, Attila Bonyár, Péter Gordon, Gábor Harsányi, Investigation of intermetallic compounds (IMCs) in electrochemically stripped solder joints with SEM, Microelectronics Reliability 52 (2012) 1138–1142

[9] A. Bonyár. T. Hurtony, P. Gordon, G. Harsányi „Selective electrochemical etching for the investigation of solder joint microstructures", 35th International Spring Seminar on Electronics Technology. Salzburg, Ausztria, (IEEE), o. 1-7.

[10] Tamás Hurtony, Attila Bonyár, Marco Luniak, Maik Müller, Determination of the Sn/IMC ratio in solder joints combining electrochemistry and confocal microscopy. In: Proc. of the 18th International Symposium for Design and Technology of Electronics Packages. Alba Iulia, Románia, pp. 81-84.

[11] Wislei R. Osório, Emmanuelle S. Freitas, José E. Spinelli, Amauri Garcia, Electrochemical behavior of a lead-free Sn–Cu solder alloy in NaCl solution, Volume 80, March 2014, Pages 71–81

[12] Wislei R. Osório, Leonardo R. Garcia, Leandro C. Peixoto, Amauri Garcia, Electrochemical behavior of a lead-free SnAg solder alloy affected by the microstructure array, Materials and Design 32 (2011) 4763–4772

[13] Wislei R. Osórioa,∗, José E. Spinelli b, Conrado R.M. Afonsob, Leandro C. Peixotoc, Amauri Garciac, Microstructure, corrosion behaviour and microhardness of a directionally solidified Sn–Cu solder alloy by the microstructure array, Electrochimica Acta 56 (2011) 8891– 8899

[14] F. Rosalbino, E. Angelini, G. Zanicchi, R. Carlini, R. Marazza. Electrochemical corrosion study of Sn–3Ag–3Cu solder alloy in NaCl solution Original Research Article Electrochimica Acta, Volume 54, Issue 28, 1 December 2009, Pages 7231-7235

[15] K. Al-Muhanna, K. Habib Corrosion behavior of different alloys exposed to continuous flowing seawater by electrochemical impedance spectroscopy (EIS) Original Research Article Desalination, Volume 250, Issue 1, 1 January 2010, Pages 404-407

[16] V. Moutarlier, M.P. Gigandet, B. Normand, J. Pagetti EIS characterisation of anodic films formed on 2024 aluminium alloy, in sulphuric acid containing molybdate or permanganate species Original Research Article Corrosion Science, Volume 47, Issue 4, April 2005, Pages 937-951

[17] D. Ende, W. Kessler, D. Oelkrug, R. Fuchs Characterization of chromate-phosphate conversion layers on Al-alloys by electrochemical impedance spectroscopy (EIS) and optical measurements Original Research Article Electrochimica Acta, Volume 38, Issue 17, December 1993, Pages 2577-2580

Examination of the surface phosphorus content of anodized medical grade titanium samples

Bálint Katona[1,a], Gábor Dobos[2,b], Gábor Kiss[2,c]

[1]Budapest University of Technology and Economics, Faculty of Mechanical Engineering, Department of Materials Science and Engineering. H-1111 Budapest, Bertalan L. St. 7. Hungary

[2]Budapest University of Technology and Economics, Faculty of Natural Sciences, Department of Atomic Physics. H-1111 Budapest, Budafoki St. 8. Hungary

[a]katona@eik.bme.hu, [b]dobosg@eik.bme.hu, [c]gkiss@eik.bme.hu,

Keywords: surface treatment, anodization, titanium alloy, phosphorus content, titanium-dioxide

Abstract. In case of titanium dental implants, the main goal is to create a surface where the bone cells can attach well, therefore osseointegration can occur. The chemical composition of the surface has an important role, because the surface has a direct contact with the living tissue and induces different reactions for example peri implantitis or osseointegration. In our work titanium sample made from the most commonly used dental implant material (Ti Grade 5) were investigated. The samples were treated by chemical etching in hydrogen-chloride and in phosphoric acid to remove the cut generated burr. After that the samples were anodized in phosphoric acid solution at 10 V, 20 V, 30 V or 40 V. As a result of these treatments, titanium-dioxide layers were created on the surfaces. Phosphorus (originating from the phosphoric acid bath) may also be found on the surfaces. This may promote osseointegration. The surface compositions were investigated with the aid of Secondary Ion Mass Spectrometry (SIMS). Based on these results we can conclude that anodization in phosphoric acid solution increases the phosphorus content of the surface. Approximately to the middle of the titanium-dioxide layer the phosphorus content is constant but lower with one order of magnitude than on the surface. In the deeper layers the phosphorus content continues to decrease until the base material where it significantly reduce.

Introduction

The main purpose of many types of surface treatments and surface coating methods is to modify the morphology and the properties of the surface. The type and the parameters of the applied method are depending on the desired surface properties and the base material of the sample. In case of titanium dental implants, the goal is to achieve a surface where bone cells can attach so osseointegration can occur. This is important because of the secondary stability, which acts a main role from the first week of the implantation and mainly depends on the quality of the bone attachment. Besides the properties of the implant, the health condition, sex, age, diseases and bone quality of the patient influence the osseointegration as well.

In case of implants different types of surface treatments are used to achieve the sufficient surface: sandblasting, chemical etching, electropolishing, plasma spraying, heating and remolding by laser, anodization, mechanical grinding and coatings [1-5].

Anodization. With anodization, metals can be coated by their oxides, which adhere to their surfaces. This is an electrolytic surface treatment where the sample is connected into a circuit as anode and immersed into an anodizing bath. The cathode is immersed into the bath as well and can be made of the same or different material as the work piece. The most common geometries of the cathodes are sheet form or roll. After the circuit is closed the current flowing creates hydrogen and oxygen ions in the electrolyte which migrate to the metal surfaces. The arriving oxygen ions form an oxide layer on the anode. Aside from time, the applied voltage, the composition of the anodizing bath and the material comprising the electrode/anode material, jointly determine the created layer [6-9].

In his research, Elias [10] treated discs and dental implants made of pure titanium with a range of methods. The etching bath was a mixture of nitric acid, hydrochloric acid and sulfuric acid. He found that chemically etched homogeneously rough surfaces were more biologically active in the osseointegrative sense. This facilitated the attachment of bone cells so the implants would support mechanical loading. The electrolytic solution for anodization contained calcium and phosphorus and he used micro-arc oxidation, based on previous research [11]. He found that the various treatments influenced surface morphology, therefore anodized samples needed greater torque to screw into bone than chemically etched ones.

Vanzillotta and his colleges [12] treated pure titanium samples. They used 3 different surface treatment methods to observe their effect on bioactivity. In their research they used chemically etched, chemically etched and anodized, chemically etched and heat treated samples. A mixture of HCl 18% and H_2SO_4 48% was used for etching at 55 °C whereas the etching time was 60 seconds. Before anodization and heat-treatment the same etching method was used. The anodizing bath was an 8 V/V% H_3PO_4 solution, the applied voltage was 20 V and the time was 10 minutes. The heating rate of the heat-treatment was 450 °C/hour. After this a 40 minute etching in 4 V/V% NaF solution was used. The treated samples were put into SBF (simulated body fluid) solution at 37 °C for 1, 2 or 7 days. Small globules of the calcium phosphate layer precipitated on the titanium surfaces after 7 days of soaking into SBF. The results showed that on the surface of the anodized and the heat-treated samples the Ca/P ratio after 7 days in SBF is close to the cortical bone, which is equal to 1.63. These results reinforce the possible contribution of the oxide layer to this method. Based on this result it can be concluded the phosphate ions incorporated into the oxide layer accelerate apatite formation.

Formed TiO_2 layer. Vera and his team [13] treated Ti-6Al-4V samples to determine the thickness of the formed titanium-dioxide layer and its crystal structure. For anodic oxidation they used 1M H_2SO_4 solution at room temperature and a platinum wire as cathode. Samples were oxidized for 1 minute at 10, 20, 30, 40, 50 and 60 V, respectively. The samples which were anodized at 20 and 40 V also undergone a 1 hour heat treatment at 500 °C. The samples were examined by optical microscope and with X-ray diffractometer. They found that there is a linear relation between the applied voltage and the thickness of the formed titanium-dioxide layer: t=2.4 nm/V.

Our primary goal was to observe the amount and distribution of phosphorus in the oxide layer formed by anodic oxidation as function of the applied voltage. This is an important property of any implant e.g. dental implants because the surface has a direct contact with the living tissue and induces different reactions for example peri implantitis or osseointegration.

Materials and Methods

2 mm thick samples were cut from a 15 mm diameter Grade 5 titanium rod. Besides titanium this alloy contains 6 wt% Al, 4 wt% V, < 0,25 wt% Fe, < 0,2 wt% O, and it is commonly used as dental implant base material. After the cut chemical etching was used to remove burr and surface contaminations. This treatment consisted of two steps: first the samples were etched in hydrogen-chloride for 60 minutes in an ultrasonic cleaner. Remnants of the acid were washed off by distilled water, acetone and ethanol. After drying the samples were subjected to a second chemical etching in phosphoric acid for 30 minutes. After the etching, acid remnants were washed off by the same method as before.

After cleaning, samples were affixed to nickel coated 316L austenitic stainless steel clips and anodized in an 8 V/V% phosphoric acid bath. Besides holding the samples, the clips also provided electrical contact. To avoid parasitic electrochemical reactions only the samples were immersed in the bath, the clips did not touch the surface. The cathode was a cylindrical mesh of 316L austenitic stainless steel. The applied voltages were 10 V, 20 V, 30V and 40 V. During the oxidation process we used magnetic mixing with 150 rpm to keep the anodizing solution in motion. The temperature of the anodizing bath was at 20±1 °C and the duration of the process was 1 minute. After anodization sample surfaces were cleaned by distilled water and ethanol.

The samples were analyzed by Secondary Ion Mass Spectroscopy (SIMS). By this method even trace impurities can be detected in the surface oxide layer and both the oxide thickness and the depth distribution of different elements can be established. Sample surfaces were bombarded by 3 keV Ar^+ ions from a VG Microtech EX-05 ion gun, while secondary ions were analyzed by a Baltzers QMA 140 quadrupole mass spectrometer. The ion gun was set to bombard an approximately 4.5 by 6 mm area, while the spectrometer collected ions only from a 1.5 by 2 mm area in the center to ensure good depth resolution. During the measurements the intensities of $^{1}H^{+}$, $^{12}C^{+}$, $^{16}O^{+}$, $^{23}Na^{+}$, $^{27}Al^{+}$, $^{31}P^{+}$, $^{39}K^{+}$, $^{48}Ti^{+}$, $^{51}V^{+}$ ions and $^{64}TiO^{+}$ clusters were continuously recorded. The sputtering speed of the ion gun was calibrated by sputtering through a 56 nm thick (measured by ellipsometer) SiO_2 layer.

Results

The surfaces of the anodized samples were first investigated with an Olympus SZX16 optical microscope (Fig. 1). The samples anodized at different voltages have different colors. These colors correlate with the thickness of the titanium-dioxide layer. Based on Vera's work [14] the estimated thicknesses of the oxide layers are, 24 nm at 10 V, 48 nm at 20 V, 72 nm at 30 V and 96 nm at 40 V.

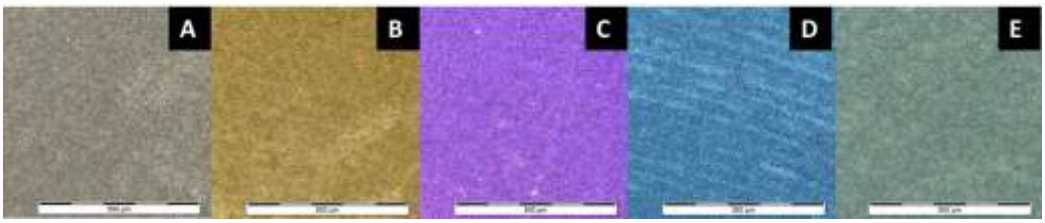

Figure 1. Optical microscope images of the etched and the anodized samples; etched (A), anodized at 10 V (B), anodized at 20 V (C), anodized at 30 V (D), anodized at 40 V (E)-, bar=500 µm

Formázott: Betűtípus: 12 pt, Nem Dőlt
Formázott: Betűtípus: Nem Dőlt
Formázott: Betűtípus: Nem Dőlt
Formázott: Betűtípus: Nem Dőlt

Hydrogen. Fig. 2 shows the intensity of the hydrogen ion signal vs. time and depth function of the different samples .As the measured hydrogen ion signals are higher in the base material than in the oxide layer it can be assumed that the solubility of hydrogen is higher in titanium than in titanium-dioxide. The abundancy of hydrogen ion on the surface can originate from surface hydroxides. The interface of the oxide layer and the base material can be located, based on the intensity of the hydrogen ion signals. Due to the roughness of the surface and inhomogenities in the oxide thickness the oxide/metal transitions on the recorded profiles are blurred, but approximate layer thicknesses may still be estimated.

Titanium. Fig. 3/A shows the intensity of the titanium ion signal in case of the different samples. Deeper in the layer $^{48}Ti^{+}$ intensities decrease. This is due to changes in oxygen concentration. The presence of oxygen promotes positive ion formation thus increasing the intensities of most ionic species. Since the base material has low oxygen content (<0.2 wt%) the intensities of most ionic species drop at the interface. In case of the etched samples, we can observe very low values because of the aforementioned phenomenon.

Titanium-oxide cluster. Fig. 3/B shows the intensity of the titanium-oxide cluster. The results are the same as for the titanium ion.

Aluminum. Fig. 3/C shows the intensity of the aluminum ion. Its behavior at the oxide/metal interface is similar to that of titanium ions, and it is also related to the decrease in oxygen concentration. It must also be noted that in case of anodized samples the intensity of $^{27}Al^{+}$ ions increases sharply in the first few minutes. As the intensity of ions related to surface contaminations (such as $^{12}C^{+}$, $^{23}Na^{+}$, $^{39}K^{+}$) drops at the same time this increase is probably related to the removal of

these contaminations. Since SIMS is a surface analytical technique even a single atomic layer of contamination may successfully cover the surface and decrease the intensities of other ions.

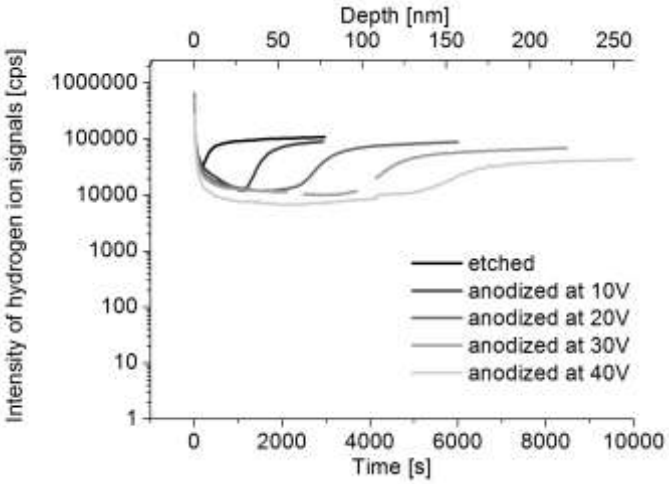

Figure 2. Hydrogen ion signals vs. time and depth measured with SIMS

Formázott: Betűtípus: Nem Dőlt, német (németországi)

Formázott: Betűtípus: Nem Dőlt, német (németországi)

Vanadium. Fig. 3/D shows us the intensity of the vanadium ion. Its behavior at the oxide/metal interface is similar to other metallic ions. On the other hand its intensity increases significantly at the surface of each anodized sample, and the duration of this increase is significantly longer than in case of aluminum ions. Therefore it cannot be explained by surface contaminations. Since no increase in oxygen concentration is observed in this depth, the only possible explanation is that the surface layers of the oxide have significantly lower vanadium content than the deeper layers. The reason of this phenomenon requires further study.

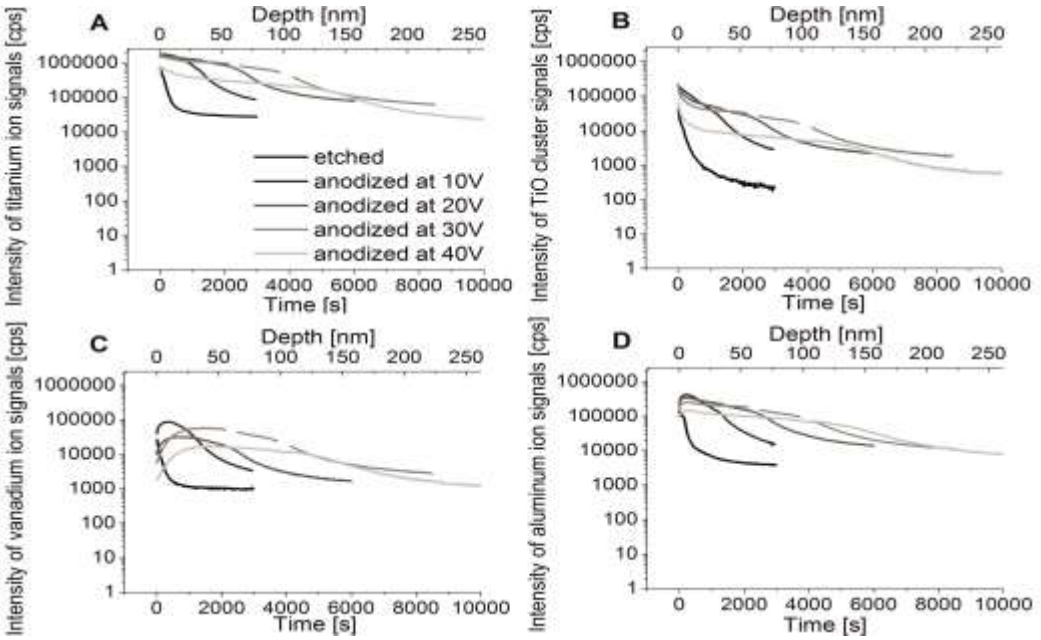

Figure 3. Titanium ion (A), the titanium-oxide cluster (B), the aluminum ion (C) and the vanadium ion (D) signals vs. time and depth measured with SIMS

Formázott: Betűtípus: Nem Dőlt

Phosphorus. Fig. 4 shows the intensity of the phosphor ion function of the time and depth. Based on these results we can conclude that the topmost 5-10 nm of each oxide layer is rich in phosphor. In deeper layers the intensity of the $^{31}P^{+}$ ion is significantly lower but it seems to be relatively constant down until approximately half the thickness of the oxide layer. At the middle of the oxide layer the amount of phosphor drops again and keeps decreasing.

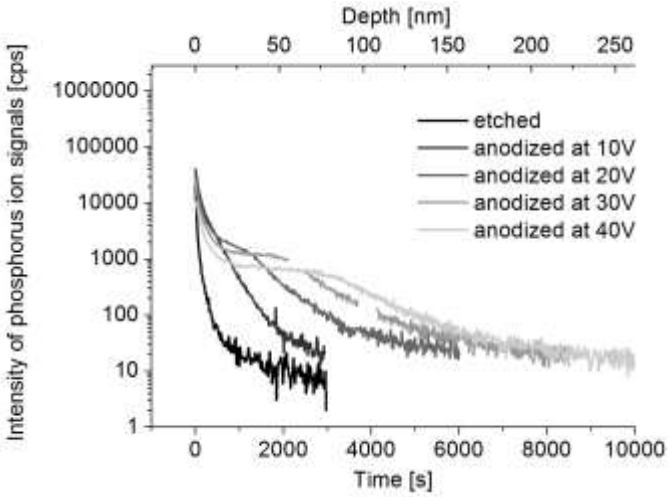

Figure 4. Phosphorus ion signals vs. time and depth measured with SIMS

Formázott: Betűtípus: Nem Dőlt

Conclusions

Based on our work we can conclude that anodization in phosphoric acid solution increases the phosphor content of the surface. Approximately to the middle of the titanium-dioxide layer the phosphorus content is constant but lower with one order of magnitude than on the surface. In the deeper layers the phosphorus content continue to decreases until the base material where significantly reduces.
This surface phosphor content may be able to facilitate osseointegration and result in appropriate secondary stability for the dental implant.

Acknowledgement

This work is connected to the scientific program of the " Development of quality-oriented and harmonized R+D+I strategy and functional model at BME" project. This project is supported by the New Hungary Development Plan (Project ID: TÁMOP-4.2.1/B-09/1/KMR-2010-0002).

References

[1] S. Bauer, P. Schmuki, K. von der Mark et al., Engineering biocompatible implant surfaces Part I: Materials and surfaces, Progress in Materials Science 58 (2013) 261–326

[2] L. Nádai, B. Katona, A. Terdik et al., Chemical etching of titanium samples, Periodica Polytechnica 57 (2013) 53-57

[3] G. Pető, A. Karacs, Z. Pászti, et al., Surface treatment of screw shaped titanium dental implants by high intensity laser pulses, Applied Surface Science 186 (2002) 7-13

[4] D. Pammer, Á. Schindler, E. Bognár, Fogászati implantátumok kémiai maratása, Műszaki Szemle 60 (2013) 29-32

[5] Á. Lengyel, E. Bognár, J. Dobránszky, The effect of stent positioning during electropolishing, 29th Danubia-Adria-Symposium on Advances in Experimental Mechanics, 32 (2012) 64-65

[6] X. Yu, Y. Li, W. Wlodarski, et al., Fabrication of nanostructured TiO2 by anodization: A comparison between electrolytes and substrates, Sensors and Actuators, 130 (2008) 25-31

[7] J. M. Macak, H. Tsuchiya, P. Schmuki: High-Aspect-Ratio TiO2 Nanotubes by Anodization of Titanium, Angewandte Chemie Internaitonal Edition, 44 (2005) 2100–2102

[8] M. Paulose, H. E. Prakasam, O. K. Varghese, et al., TiO2 Nanotube Arrays of 1000 μm Length by Anodization of Titanium Foil: Phenol Red Diffusion, The Journal of Physical Chemistry C, 111 (2007) 14992-14997

[9] G. K. Mor, O. K. Varghes, M. Paulose et al., Transparent Highly Ordered TiO2 Nanotube Arrays via Ano,zation of Titanium Thin Films. Advanced Functional Materials, 15(2005) 1291-1296

[10] C. N. Elias: Titanium dental implant surfaces, Revista Matéria, 15 (2010) 138-142

[11] L. H. Li, Y. M. Kong, K. W. Kim, et al., Improved biological performance of Ti implants due to surface modification by micro-arc oxidation, Biomaterials, 25 (2004) 2867-2875

[12] P. S. Vanzillotta, M. S. Sader, I. N. Bastos et al., Improvement of in vitro titanium bioactivity by three different surface treatments, Dental Materials 22 (2006) 275-282.

[13] M. L. Vera, M. A. Alterach, M. R. Rosenberger et al., Determination of the thickness and crystalline structure of TiO2 coatings made by anodic oxidation of Ti-6Al-4V, LNLS 2009 Activity Report (2009)

Evaluation of quenchant's cooling and hardening performance

Gábor Kerekes[1, a], Mária Kocsisné Baán[1,b] and Imre Felde[2,c]

[1]University of Miskolc, 3515 Miskolc-Egyetemváros, Hungary

[2] country University of Miskolc, 3515 Miskolc-Egyetemváros, Hungary

[3]University of Óbuda, 1034 Budapest Bécsi Str. 96b, Hungary

[a]metkg@uni-miskolc.hu, [b] m.kocsis.baan@uni-miskolc.hu, [c]felde.imre@nik.uni-obuda.hu
(corresponding author)

Keywords: quenchant characterization, aqueous polymer solution, hardening power, SmartQuench, SQIntergra

Abstract. One of the most critical parts of the heat treatment process, and usually the least controllable one, is the quenching operation. Improper selection or application of a quenching medium, or a drift in its cooling characteristics during its lifetime, may result in products that do not meet specifications and therefore give rise to large additional costs to cover e.g. straightening, rework, rejection, delayed deliveries and, sometimes, lost goodwill for the heat treater. In the case of the use of aqueous polymer solutions, the thermo-kinetic parameters characterizing the heat removal capabilities of a quenchant, are variable, in a specific interval with a complex combination of temperatures (T), concentrations (C) and agitation rates (AR). When the direction and degree of change is known, the characteristics of heat removal can be efficiently modified and predicted within given limits. The aim of the work described in this paper is to investigate how the hardening power of Houghton AquaQuench BW-T depends on the complex influence and interaction of T, C and AR.

Intorduction

The most critical part of the transformation hardening process is the quenching stage. This is when the cooling rate is determined by the distribution of required structural constituents. It is not enough to mind only the kinetics of heat removal (in the long run the cooling rate) but the thermal and structural stresses arising during the cooling to avoid unwanted deformations. It is justified, then, to use quenchants that cool the specimen faster in the region of higher temperatures – typically in interval of the pearlitic transformation – and slower above M_s for decreasing the temperature gradient in the volume. In this case, it could be available to minimize the time between the start of the martensitic transformation in the surface and in the core.

In this case, aqueous polymer solutions, provide the best possibilities considering the current quenchants that are widely used by industry. The heat removal characteristics of these i.e. the cooling performance in the three different stages of quenching is basically determined by the viscosity of the sample. The amount of heat removed is typically less in the case of using water in the first stage (the vapor blanket stage). The reason is the higher density of the solution over water and the formation of a vapor blanket at the sample surface, after the specimen has been immersed. The existence of vapor film insulating the specimen against wetting is owing to the fact that the liquid layer close to the surface is overheated and the formed vapor cannot escape from the surface. A polymerisation process starts close to the surface in a higher density solution, which results in a thin polymer layer at the surface. The heat conduction of this layer is less, than the liquid. When the

disruption of the vapor blanket starts, the heat removal rate will become more intensive, by the bubble formation mechanism. A decrease of bath temperature and increase of viscosity will decrease the intensity of nucleate boiling. In the last stage – the convection stage – the heat removal is affected by other chemical properties (e.g. solubility), not just the viscosity [1]. The behavior of the cooling media, can be characterized by several thermokinetic parameters, such as the maximum of the cooling rate, CR_{max}, temperature where the CR_{max} occurs $T(CR_{max})$, the transition temperatures between the vapour-boiling phase and boiling-converction phase, T_{cp} and T_{vp} can be affected by changing temperatures, concentrations and agitation rates. It is useful to determine the extent these thermokinetic parameters are able to change. To obtain these results it is necessary to make a systematic investigation.

Experiment

The first aim of our work was to measure the influence of the three most adjustable parameters and the behavior of the Houghton Aquaquench BW-T aqueous polymer solution. We applied the following parameter combinations to attain an accurate view concerning the evolution of the quenchant's cooling characteristics:

- *Temperature (T):* start at room temperature (~20°C), then increase 5-6°C in 5 steps to 45°C
- *Concentration (C):* 2.5%, 5%, 7.5% and 10%
- *Agitation rate (AR):* in 0 (unagitated state) then 1, 2 and 3 grade

We did not have suitable set-up to measure the flow velocity. We used the scale on agitation unit to define the agitation rate. This was changed in 10 degree increments. We used the first three degrees, as it was sufficient, from the point of measurement. It was not the aim of our investigation to describe the movement of flowing fluid, only to provide agitation under consistent conditions.

We determined the thermo-physical properties using a standardized (ISO9950) measurement method. The method is based on recording cooling curves with IVF SmartQuench equipment. The most important part of system is a specimen that has properties and dimensions that are the following:

- Geometry: cylindrical, 12.5mm diameter, 400m height
- Material: Ni-based alloy (Inconell 600)
- Thermocouple: K-type, 30mm from the lower surface in the centerline

The first step of investigation is the heating of the specimen to 850°C, and the second is to cool in a quenchant while a cooling curve is recorded. The T-t data pairs can be analyzed using the SQIntegra software and thermokinetic parameters that characterize the heat transfer during cooling. Using these parameters the hardening power (HP) can be calculated and by that, the heat removal rate of different quenchants, or quenchants with different conditions (T, C, AR), can be compared. The HP value is calculated by SQIntegra using the empirical function described below:

$$HP = 3.54 \times CR550 + 12.3 \times CR325 - 168 \quad (1)$$

when

- *CR550*: the cooling rate at 550°C (the lowest incubation time in the CCT diagram of unalloyed steels belongs to approx. 550°C)
- *CR325*: the cooling rate at 325°C (the M_s temperature of unalloyed steels belongs to approx. 325°C) [2]

The recording of the cooling curves was done for 81 parameter combinations, before the HP values were obtained. The results and conclusions are described in the next section of this paper.

Results and conclusions

It can be generally noted that the HP values decrease with higher concentrations. The HP values would result in a wide (1300 - 1800) interval when C varied between 2.5% and 10%.

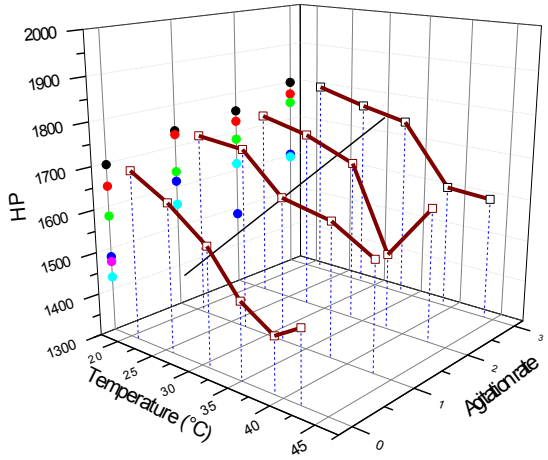

1. Figure HP values as a function of T and AR when C=2.5%

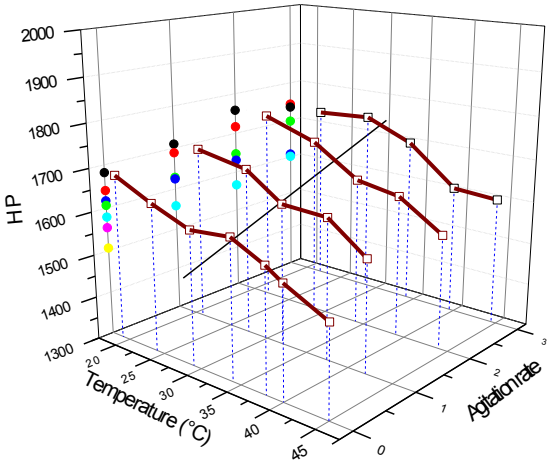

2. Figure HP values as a function of T and AR when C=5%

When we make a deeper analysis of the HP values, we can see that the rate of change is different for fixed concentrations, increasing temperatures and agitation rates.

When the concentration (C) is 2.5% and the temperature increases (actually independent of AR) hardening power decreases. But if the agitation increases then the ΔHP will be smaller. The increase of HP values is close to linear when the agitation increases and the T does not change simultaneously; the incline increases when the temperature increases. It can be also seen that the influence of higher T values a decrease in HP will occur only if the cooling media is agitated more intensively.

It can be mentioned here that when the concentration is 5%, elevated temperatures decreases, to a lesser degree, the HP values. This can be seen by the distribution of points belonging to the same AR on the XZ plane in Figure 2. The phenomenon when HP's are decreasing at a slower rate at high temperature due to higher AR is evident, but the amount of this effect is quite low compared to the case of smaller concentrations.

To explain the variation of HP values, it is necessary to analyze the change of quenchant's thermo-physical properties because these are linked with the different kinds of heat transfer methods during cooling and therefore act upon the HP values. In the following part of this section, the changing of T_{vp}, T_{cp} and CR_{max} values will be shown. The following parameters will be interpreted:

- T_{vp}: The temperature (1st critical temperature) where the rupture of vapor blanket and therefore the nucleate boiling stage starts
- T_{cp}: The temperature (2nd critical temperature) where the convection stage starts after the nucleate boiling
- CR_{max}: The maximum cooling rate during the quenching

It can be generally mentioned that the changing of T, C, and AR had a greatest effect on T_{vp}, while the T_{cp} was quite independent.

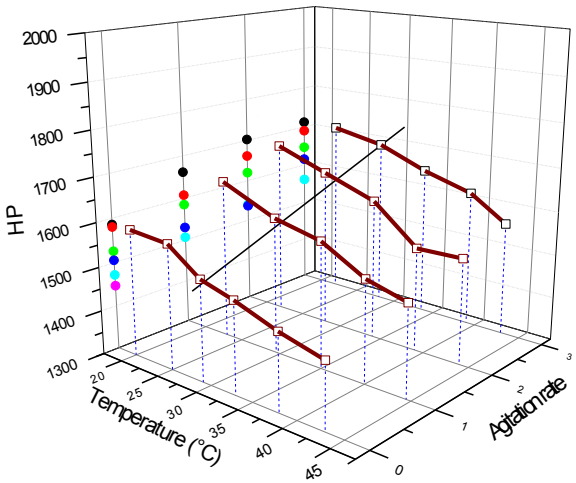

3. Figure HP values as a function of T and AR when C=7.5%

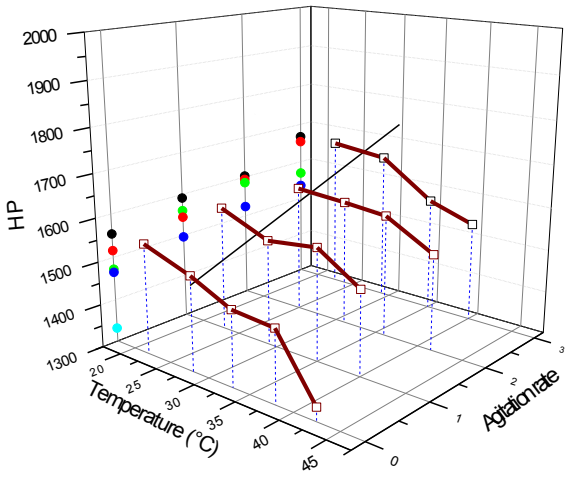

4. Figure HP values as a function of T and AR when C=10%

When the concentrations are higher (7.5% and 10%) there is a decrease of the slope of T-HP curves belonging to the same AR rate and a higher ΔHP occurs at higher temperatures.

The decreasing of the T_{vp} values at higher temperature can be explained an increase of the thickness of the vapor film, providing more thermal stability. [1] If we boosted the agitation rate this effect would disappear. The reason owing to the mechanical destruction of vapor blanket, caused by flowing quenchant, it cuts the formation of a thicker film and decrease the stability of the existing blanket.

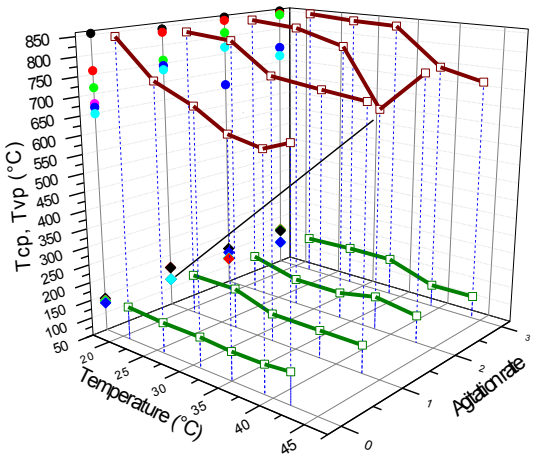

5. Figure Critical temperatures as a function of T and AR when C=2.5%

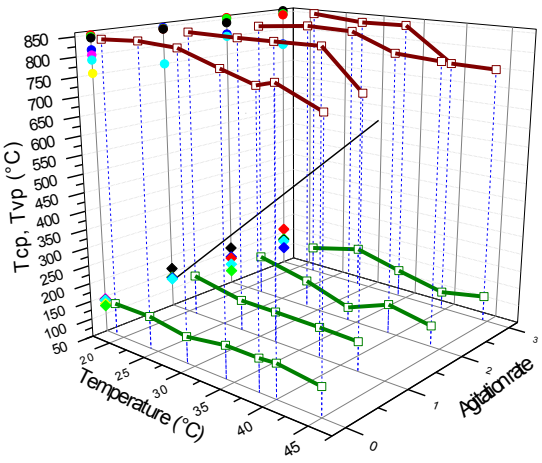

6. Figure Critical temperatures as a function of T and AR when C=5%

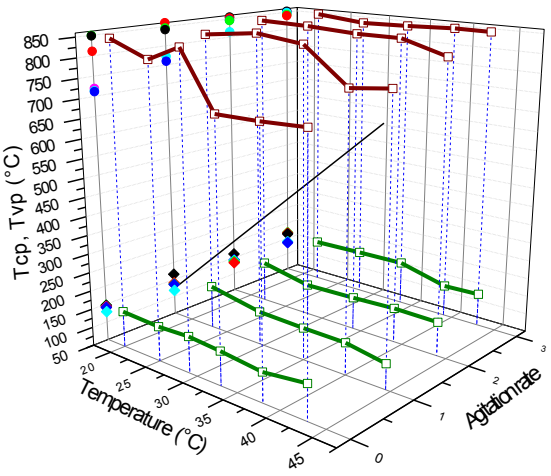

7. Figure Critical temperatures as a function of T and AR when C=7.5%

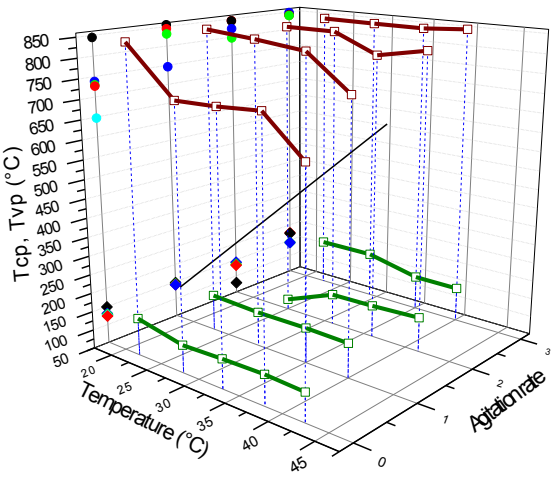

8. Figure Critical temperatures as a function of T and AR when C=10%

The high fluctuation of T_{vp} values, in the case of several measurements, can be associated with a non-uniform rupture of the vapor blanket and the kinetics of the wetting front. This fluctuation can be seen very well when C=2.5%, T=35°C and AR=2.

The maximal cooling rate was increased unequivocally by the increase of the agitation rate. This effect rose against the influence of grooving of T. The phenomenon seen in case of HP, viz water. The narrowed interval of HP values, owing to the change of concentration and agitation rate, did usually not arise.

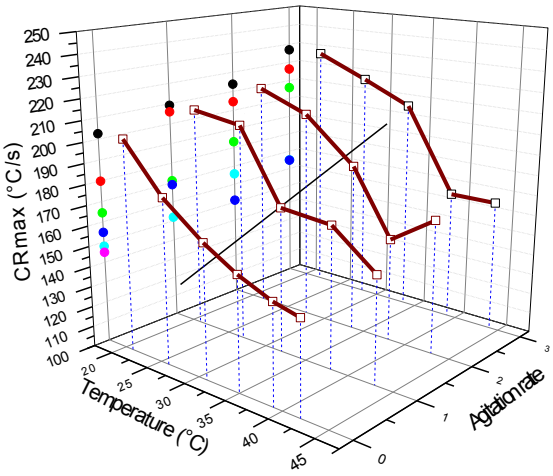

9. Figure Maximal cooling rate as a function of T and AR when C=2.5%

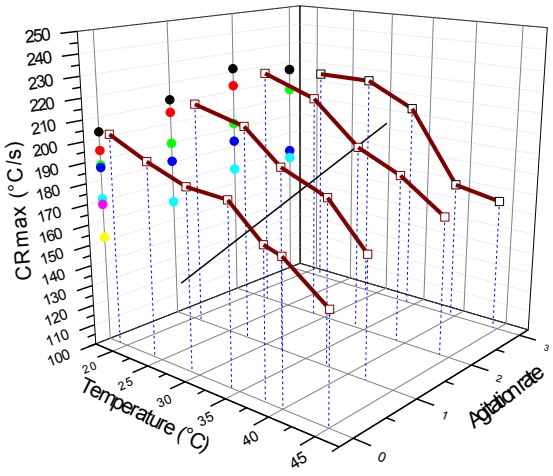

10. Figure Maximal cooling rate as a function of T and AR when C=5%

This means that the changing of parameters have not joint effect on CR_{max}, have not influence on character of variation of CR_{max} and do not shift the interval neither to higher nor to lower values.

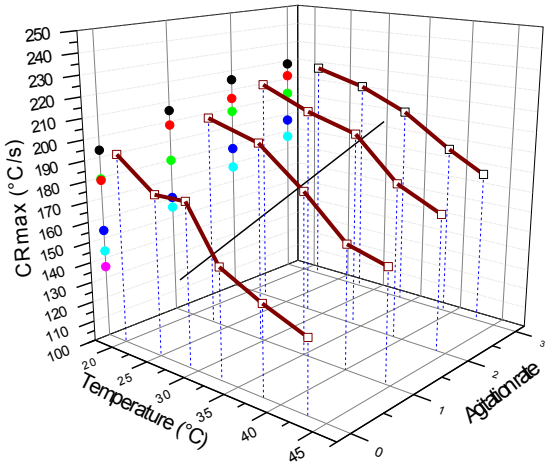

11. Figure Maximal cooling rate as a function of T and AR when C=7.5%

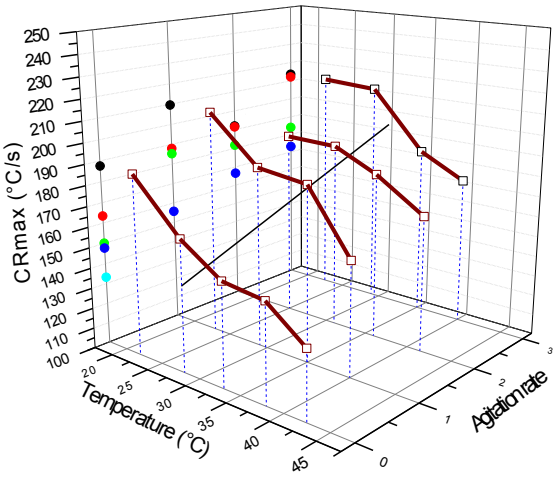

12. Figure Maximal cooling rate as a function of T and AR when C=10%

The following remarks can be made about hardening power in case of this quenchant:

- When the concentration is increasing the HP is decreasing
- The increasing of temperature, decrease HP, furthermore the rate of decline will be less when the concentration is higher
- The HP can be enhanced by increasing the AR and the rate of increasing of HP seems to be independent from the concentration
- The HP values correlate to the change of heat transfer stages described by critical temperatures, but this correlation is not independent of C and AR, because the T_{vp} depends on these parameters

Summary

The aim of this work was to determine the influence of temperature (T), concentration (C) and agitation rate (AR) on the cooling power of the Houghton Aquaquench BW-T aqueous polymer solution. This property has been qualified by HP values that should be compared to more quenchants. It was necessary to make a comprehensive investigation to determine the behavior of quenchants for different parameter combinations.

The results showed that the influence of temperature (T) is not independent from concentration (C) and the effect of agitation rate (AR) occurs independently of the other parameters for this PVP type quenchant. To prove an unambiguous independence of agitation rate, more investigations are required.

Acknowledgement

The research work presented in this paper/study/etc. was carried out as part of the TÁMOP-4.2.2.A-11/1/KONV-2012-0029 project in the framework of the New Széchenyi Plan. The realization of this project is supported by the European Union, and co-financed by the European Social Fund.

References

[1] B.Liscic, H. M. Tensi, L.C.F. Canale, G.E. Totten: Quenching Theory and Technology, CRC Press, 2010, pp. 376-383

[2] ivf Smart Quench II User's Manual, Ver. 3.1, 1st Edition, Nov. 2009, SWEREA IVF AB

Testing of power plant steel deterioration by adaptive nonlinear harmonics method (ANLH)

István Mészáros

Budapest University of Technology and Economics (BUTE)

Department of Materials Science and Engineering

Bertalan L. street 7. H-1111 Budapest, Hungary

meszaros@eik.bme.hu, jginsztler@mti.bme.hu

Keywords: Low cycle thermal fatigue, material deterioration, AC magnetic testing, adaptive testing, remnant life time estimation, NDT

Abstract.

Nowadays, there is increasing importance of the remaining life time estimation of engineering structures. In this work the thermal fatigue process induced deterioration of the three different power plant steels was investigated. The tested steels are widely used as steam pipeline base material of power plants. The applied thermal fatigue test can model the material degradation due to long term service in high temperature environment. In this paper a new high sensitivity magnetic measuring technique is presented called Adaptive Nonlinear Harmonic (ANLH) method. The sensitivity of this measurement is optimized for controlling the thermal fatigue deterioration. The presented novel measurement was developed for non-destructive testing of pipelines and pressure vessels of power plants.

Introduction

In the engineering practice a large quantity of parts are operated at high temperature. The state of power plant steels is thermodynamically metastable and the structure of these materials can change during long term service, especially at elevated temperature. In case of the real power plant overheating and steam pipelines the most important deterioration processes are the creep and a combined form of mechanical and thermal fatigue due to service temperature cycles. The typical appearance of the macroscopic deterioration of these pipelines is the longitudinal fracturing. The combined effects of creep and fatigue processes can be modelled by the separately investigated creep and thermal fatigue (TF) behaviour [1]. It is known that the microstructural effects of the two mentioned processes can be distinguished because the creep type deterioration can cause cavities along the grain boundaries [2], while the fatigue process causes the appearance of micro and later macro cracks through the grains. During the high-temperature operation the crack growth under the above mentioned complex loads can be classified as cycle- or time-dependent or a combination of the two processes. Cycle-dependent crack growth is due to fatigue and time-dependent crack growth is due to creep process or to environmental interactions. A combination of their effects is also possible [3].

Nowadays, there is increasing importance of the remaining life time estimation of engineering structures. Nowadays large number of different investigation techniques can be used for life time estimation [4-13].

Experimental

Investigated materials and samples. Three different steels were tested. All of them are commonly used traditional base materials of main steam pipelines of fossil power plants in Hungary. The tested steel grades are the followings: European grade 10CrMo9-10 (EN 10028) heat resistant martensitic steel, the Russian grades 12H1MF and 15H1MF (GOST 8732-78) low alloyed high-temperature steels. These steel grades are characterized by a good weldability with the usual welding techniques and also offer good cold and hot-forming properties. They are widely used above all for manufacturing boilers, pressure vessels and pipes transporting hot liquids and steam. The test samples were machined longitudinally from thick walled (45-50 mm) supply state main steam pipelines. The low cycle thermal fatigue samples were cylindrical with screw ending for fixation in the fatigue test machine. The diameter of the investigated middle part was 10 mm, the grain size of samples was in the range of 45-50 μm.

The low cycle thermal fatigue (sometimes called thermal shock fatigue) tests were carried out in a Gleeble 3800 thermo mechanical physical simulator produced by the Dynamic Systems Inc. The system allows us to simulate many thermal processes. The program can switch between control variables at any time and as often as required during the test. Control modes that are available include stroke displacement, force, various extensometers, true stress, true strain, engineering stress, and engineering strain.

The samples were heated up to the middle temperature of the tests (375°C) at the beginning and constant 200 MPa compressive load was applied for 10 seconds. It was followed by the activation of rigid fixation and the low cycle thermal fatigue tests were started. The temperature of the test pieces was changed periodically in the 200°C-550°C range during the tests. The temperature was kept at the maximum and the minimum for 3-3 seconds, the heating rate was 20°C/s, and the cooling time at normal air was about 46-47 seconds. The number of fatigue cycles was 0, 250, 500, 750, 1000 for each tested grades. The applied compressive stress partially relaxed at the beginning of the fatigue test and reached the stable 120 MPa level. The measured stress amplitude during thermal fatigue test was ±42 MPa.

The prepared samples including the one which suffered the highest number of cycles were at the beginning of the deterioration process. Intentionally *the thermal fatigue test was designed for testing this weakly deteriorated range because the state of power plant steels in this range well corresponds to their state in normal service conditions.* The seriously deteriorated states of thermal fatigue loaded steels were investigated in our earlier works [14, 15].

Conventional investigations

Metallography, hardness testing, traditional magnetic testing. Longitudinal and transversal metallographic images were taken from the middle part of each sample. The metallographic samples were etched in 2% Nital (5% HNO_3+ethanol). As an illustration Fig.2 demonstrates that *only minor microstructural changes can be detected* due to 1000 fatigue cycles. The grain size and shape do not changed, only the appearance of minor inclusions along grain boundaries can be observed in some samples. Voids or micro cracks are not detected in any samples.

The Vickers-hardness was measured by a Buehler-402 type hardness tester applying 1000 grams of load. As it can be seen in Fig.3 *the hardness significantly does not changed due to fatigue cycles*.

Therefore it can be stated that the thermal fatigue deterioration in the tested range does not cause significant changes in microstructure and mechanical properties. It is supposed that the dislocation and subgrain structure changed only due to the applied fatigue loading.

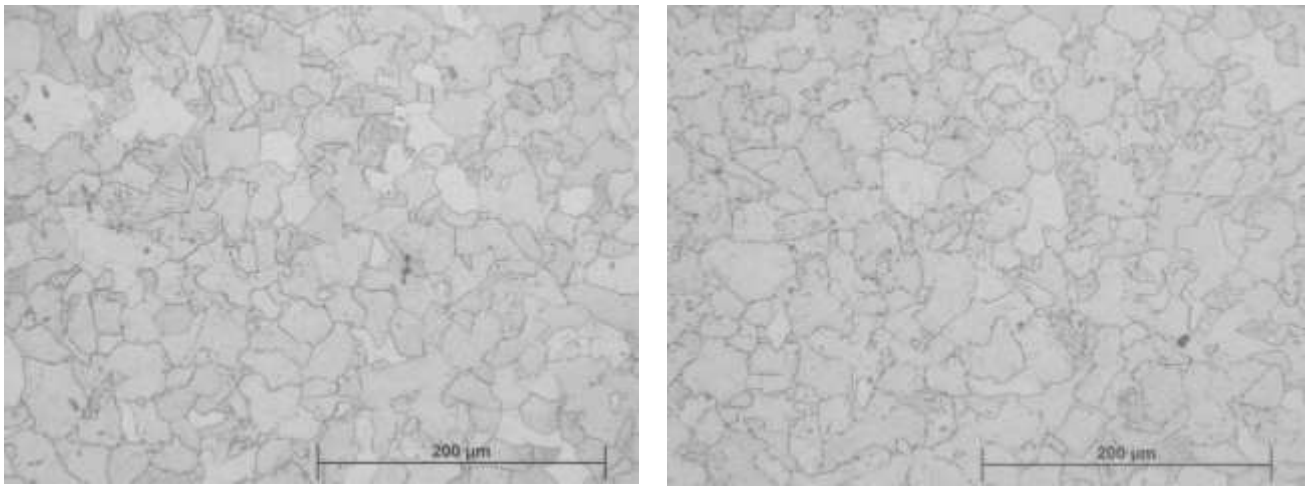

Initial condition. Thermal fatigue tested (1000 cycles).

Fig.2 Optical microscopic metallographic images of samples.

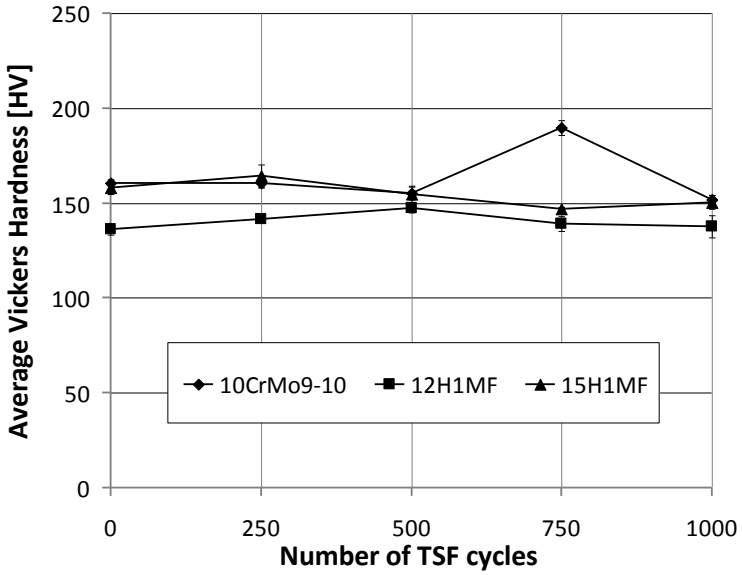

Fig.3 Vickers hardness values of the three tested series of samples vs. number of cycles.

A single sheet tester type AC magnetic tester was used for measuring the magnetization curves of each sample. The applied measuring yoke contains two symmetrical U-shaped laminated FeSi iron cores to close the magnetic circuit. The excitation current was sinusoidal produced by a digital function generator and a power amplifier, used in voltage regulated, current generator mode. The driving coil and the pick-up coil were around the middle part of the specimen. The magnetometer was under the control of a computer in which a 16 bit input-output data acquisition card accomplished the measurements. The applied maximum excitation field strength was 4000 A/m. In case of each samples 100 symmetrical minor hysteresis loops were measured.

Each minor hysteresis loops were recorded by measuring 500 points of them. The excitation magnetic field was increased in steps and there was 5 seconds delay between the steps and the data acquisition to ensure the sample's perfect magnetic accommodation, free of the effect of magnetic transients. All the magnetic measurements were carried out by using sinusoidal excitation at a frequency of 5 Hz. Because of this relatively low excitation the completed magnetic measurements could be considered as pseudo-static, the effect of eddy-current on the magnetization curves were negligibly small, well within the measuring error. The magnetometer allowed us to derive all the

practical magnetic parameters such as coercivity, remanence directly from the measured hysteresis loops.

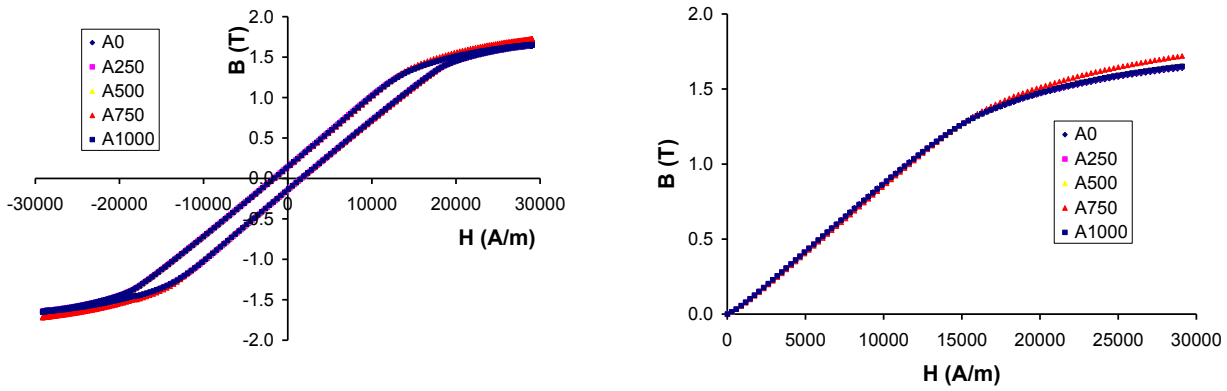

Fig.4 Hysteresis loops and normal magnetization curves of 10CrMo9-10 samples after TF testing. Curves belong to 0, 250, 500, 750 and 1000 number of cycles.

The measured saturation hysteresis loops and normal magnetization curves were not found to be sensitive to structural changes due to thermal shock loading (Fig.4). The normally used structure dependent magnetic descriptors as coercivity, remanence, initial- and maximal permeability were independent of the number of fatigue cycles. Therefore, it can be stated that microstructural changes associated with the thermal fatigue deterioration can not be detected by the traditional investigation techniques (metallography, hardness testing) including the commonly used magnetic measurements as well.

Novel magnetic testing

Adaptive nonlinear harmonic method. In a novel high sensitivity magnetic measurement based of nonlinear harmonics analysis (NLH) was developed and applied to measure magnetic properties. The basis of the NLH method is the nonlinear distortion of the tested magnetic material. If a sinusoidal magnetic field is impressed on a ferromagnetic test piece, the magnetic field that is induced into the part is shaped by the hysteresis curve of the material. Since that curve is not linear, the magnetic induction is not a single-frequency sinusoid like the excitation waveform, but rather contains higher frequencies (harmonics) of the excitation frequency. Of particular interest are the odd harmonics, specifically the 3^{rd}, 5^{th} and 7^{th}. It has been shown in previous works [16] that the spectral parameters contain more information about the material than the conventional hysteresis loop. In our nonlinear harmonic measurement system the Fourier transformation of the pick up coil signal was completed. The amplitudes and the relative phase angles of the odd harmonics are evaluated.

The Adaptive Nonlinear Harmonic (ANLH) method was developed in which the sensitivity of the NLH method was optimized. The ideal excitation level was determined for each sample to get the highest sensitivity to the structural changes caused by the thermal fatigue deterioration process. The measuring software works with different excitation levels. The applied excitation level changes the value of the magnetic field strength in equal increments in accordance with the set of the adjusted number of steps from zero level to the available maximum level and the detected magnetic values are collected to a data file. The ideal excitation amplitude was determined from the data file where the amplitude and relative phase angle (to the base harmonics) of the 3^{rd}, 5^{th}, 7^{th}., 9^{th} harmonics give the highest sensitivity, i.e. the detected properties of these harmonics are expected to give the highest difference in accordance with the specimens exposed to different level of deterioration. The amplitudes of the harmonics were found to practically independent of the level of deterioration i.e. number of fatigue cycles. *The relative phase angle of the 5^{th} and 7^{th} harmonics*

increased monotonically and significantly due to the increase of number of cycles in case of all tested steel grades. As an illustration Fig.4 shows the change of the phases in case of 10CrMo9-10 steel. Therefore the phases of 5th and 7th harmonics were found to be the especially sensitive magnetic descriptors for detecting the structural changes. The increase of the most sensitive 5th harmonics was 47%, 65% and 77 % in case of 10CrMo9-10, 15H1MF and 12H1MF respectively due to 1000 fatigue cycles (Fig.5).

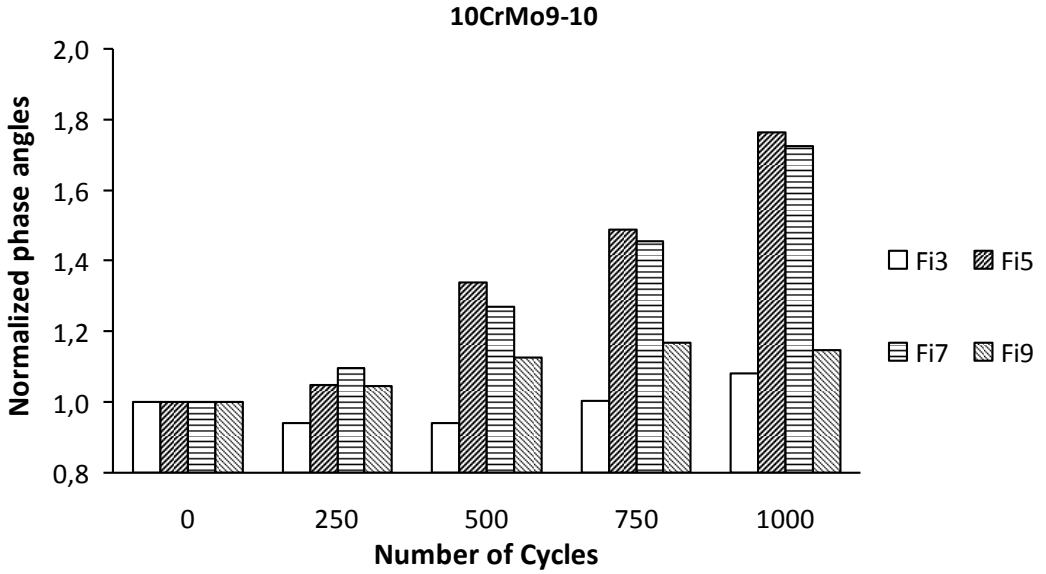

Fig.4 Normalized relative phase angles vs. number of cycles (10CrMo9-10).
Where: Fi3 means the phase of the 3rd harmonics.

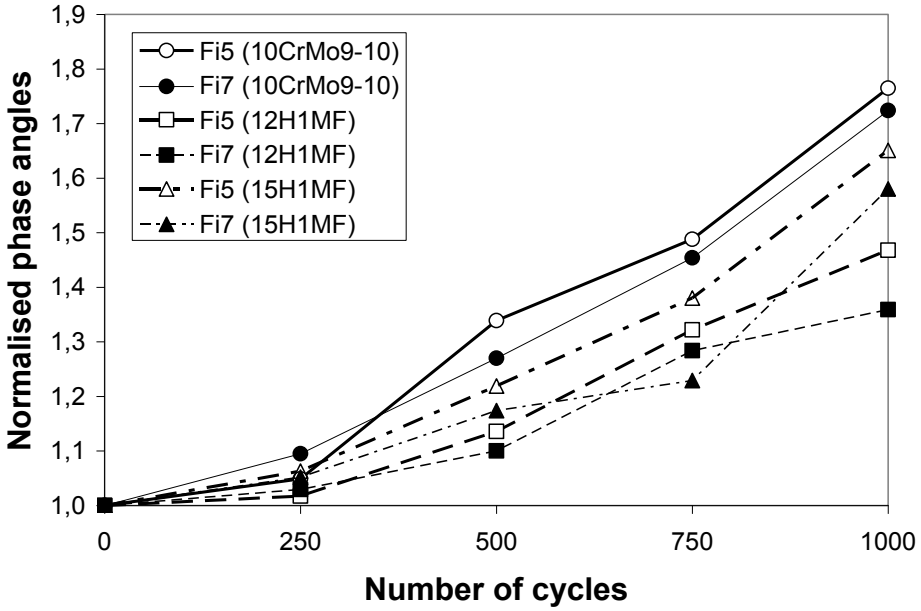

Fig.5 Normalized relative phase angles vs. number of cycles.
Where: Fi3 means the phase of the 3rd harmonics.

Summary

In the present paper we summarized our new results obtained in the field of magnetic measurement of thermal fatigue tested power plant steels. The state of power plant steels is far from being in equilibrium and this causes the changing of the structure of these materials during long term service especially at elevated temperature. The specimens exposed to thermal fatigue on the Gleeble physical simulator the detected magnetic values by the developed measuring assembly are checked with the help of metallographic and mechanical hardness tests.

A novel high sensitivity magnetic measurement technique called *Adaptive Nonlinear Harmonic testing method* was developed and introduced. In the ANLH method the applied excitation amplitude for nonlinear harmonic analysis method is optimized for gaining the highest sensitivity to the structural changes.

The relative phase angle of the 5^{th} and 7^{th} harmonics increased monotonically and significantly due to the increase of number of cycles in case of all tested steel grades. Therefore the phases of 5^{th} and 7^{th} harmonics were found to be the most sensitive magnetic descriptors for detecting the structural changes to the present microstructural changes in accordance with the deterioration process. *In case of the samples elaborated from steam pipeline material exposed to thermal fatigue the phase of the 5^{th} harmonics was found to be the optimal magnetic descriptor.*

The ANLH measurement seems to be a promising NDT tool in residual life assessment of power plant pipelines and other structural elements. These results help us to understand more deeply the microstructural changes caused by thermal fatigue process and help to develop more sensitive and accurate nondestructive investigation techniques.

Acknowledgement

This work is connected to the scientific program of the " Development of quality-oriented and harmonized R+D+I strategy and functional model at BME" project. This project is supported by the New Hungary Development Plan (Project ID: TÁMOP-4.2.1/B-09/1/KMR-2010-0002).

References

[1] J. Ginsztler, L. Dévényi: European J. of Mechanical Engineering, Vol. 36 (1991), p. 251.

[2] R.P. Skelton: High temperature fatigue: Properties and Prediction, 1987, pp 123-124

[3] J. Ginsztler, R.P. Skelton: Component reliability under creep-fatigue conditions, 1998, pp 6-7

[4] P. J. Szabó: Mat. Sci. Eng. A 387-389C (2004) p. 710.

[5] N. Mohapatra, N.R. Bandyopadhyay, et.al: J.Magn.Magn.Mater Vol. 322 (2010) p 589.

[6] S. W. Nam, S. C. Lee, J.M. Lee: Nuclear Engineering and Design, (1995) p 213.

[7] S.K. Das, A. Joarder, A. Mitra: NDT&E International Vol. 37 (2007) p 243.

[8] G. Vértesy, T. Uchimoto, I. Tomáš, T. Takagi: J.Magn.Magn.Mater. Vol. 322 (2010) p. 3117.

[9] G. Vértesy, I. Tomáš T. Uchimoto, T. Takagi: NDT & E International, Vol. 47 (2012) p. 51.

[10] J. Dobránszky – P. J. Szabó: Mat. Sci. Forum, Vol. 414-415 (2003), p. 189.

[11] G. Vertesy, A. Gasparics: Materials Science Testing and Inf. Vol. 414(4) (2004) p. 343.

[12] E. Hristoforou, K. Kosmas: International Journal of Applied Electromagnetics and Mechanics, Vol. 25 (2007) p. 287.

[13] B. Augustyniak, L. Piotrowski, et al.: IEEE Trans. Mag., Vol. 46 (2010) p. 544.

[14] I. Mészáros, J. Ginsztler: Key Engineering Materials Vols. 345-346 (2007) p. 1283.

[15] I. Mészáros, J. Ginsztler: Materials Science Forum Vols. 537-538 (2007) p. 419.

[16] I. Mészáros: Materials Science Forum Vols. 414-415 (2003) p 275.

Investigation of intermetallic phases formed in lead-free solders

Erzsébet Nagy[1,a], Anett Gyenes[2,b], Alíz Molnár[2,c], Zoltán Gácsi[2,d]

[1]MTA-ME Materials Science Research Group, University of Miskolc, Miskolc-Egyetemváros, Hungary 3515

[2]Institute of Physical Metallurgy, Metalforming and Nanotechnology, University of Miskolc Miskolc-Egyetemváros, Hungary 3515

[a]femzsofi@uni-miskolc.hu (corresponding author), [b]femanett@uni-miskolc.hu, [c]femaliz@uni-miskolc.hu [d], femtangz@uni-miskolc.hu

Keywords: lead-free solder, IMC, X-ray diffraction

Abstract. Industry should gradually replace the tin-lead solder alloys used traditionally in the soft soldering technology by lead-free soldering alloys, which raises a lot of new technological and scientific problems to be solved. The introduction and application of lead-free alloys caused a number of soldering defects not observed earlier; mechanisms of their formation are still unclear. One of such defects is whisker formation, another one is intensified formation of intermetallic phases. The appearance of undesired intermetallic phases in the soldering material spoils its mechanical properties; therefore it is particularly important that these phases do not form in electronic components. Besides, the formation of intermetallic compounds may occur in the soldering bath, thus making the soldering process difficult or even impossible.
Tin-copper-nickel and tin-silver-copper alloys are suitable for the replacement of tin-lead alloys. The components of these alloys were studied. After metallographic examination of the specimens the occurrence of intermetallic phases was determined by the XRD method. The identification of intermetallic phases was carried out by using literature data and phase diagrams.

Introduction

The basic requirement for soldering materials is that their melting temperature is lower than that of the parts being soldered to ensure proper conductivity and mechanical contact between the parts without damaging them. During soldering an intermetallic layer is formed between the solder and the surface being soldered. This brittle layer ensures good bonding between the two surfaces. If this layer is not formed, the solder joint does not appear. However, undesirable intermetallic phases may form in the solder, which can be avoided by changing the composition of the soldering alloy. In the past, lead soldering alloys proved to be most suitable; the introduction of directives on environment protection has prohibited the use of lead soldering alloys for health reasons. Sn-Cu-Ni and Sn-Ag-Cu alloys are used most frequently to replace the tin-lead solders.
According to the Sn-Cu binary phase diagram, the eutectic composition is at 0.7% m/m. In equilibrium, the η-Cu_6Sn_5 phase is formed first, then, followed an allotropic transition at 186°C, the η'-Cu_6Sn_5 phase is formed [1, 2]. The transformation from hexagonal to monoclinic lattice is accompanied by volume increase (2.15% v/v), resulting in internal mechanical stress in the solder and thereby promoting the formation of cracks. The addition of nickel to Sn-Cu solders even in small amounts (0.06% m/m) prevents the allotropic transition, thus stabilizing the hexagonal η-Cu_6Sn_5 and the $(Cu, Ni)_6Sn_5$ phases at room temperature [3, 4]. Nickel is practically insoluble in tin; however – depending on the concentration – a number of intermetallic phases can form between the two metals. At low nickel concentrations the formation of Ni_3Sn_4 (monoclinic lattice) phase is expected [8, 9]. There is no common opinion in literature on intermetallic phases formed in the Sn-Cu-Ni system [5, 6]. Since copper and nickel can replace each other in compound phases, in the case of the Sn-Cu-Ni system the formation of $(Ni, Cu)_3Sn_4$ and $(Cu, Ni)_6Sn_5$ phases is more likely than of Ni_3Sn_4 and Cu_6Sn_5 phases. Some papers specify the stoichiometry of $(Cu, Ni)_6Sn_5$ type compounds [5, 6]. According to literature, the content of nickel ranges from 0 to 29% at. in some

$(Cu, Ni)_6Sn_5$ phases. In the case of $(Ni, Cu)_3Sn_4$ compound the content of copper ranges from 0 to 8% at. [5].
In Sn-Ag alloys, eutectic is formed at 3.5% silver content, which consists of space centered tetragonal β-Sn and orthorhombic intermetallic phase ε-Ag_3Sn [1]. In the Sn-Cu system, the aforementioned eutectic is formed, which consists of β-Sn and η-Cu_6Sn_5 phases. In the Sn-Ag-Cu system, it can be assumed that at low silver and copper content both compounds are formed, thus constituting a ternary eutectic, which consists of β-Sn, Ag_3Sn and Cu_6Sn_5 phases [8].

Experimental

Three compositions of the Sn-Cu alloy were prepared (SnCu0.5, SnCu0.7 and SnCu1) and then alloyed with 0, 250, 500, 1000 and 2000 ppm nickel. The solder alloy was melted in an electrical resistance furnace at 400°C. Different amounts of Ni in the form of SnNi10 master alloy were added to the solder. After nickel addition and stirring an incubation time of 30 min was allowed to complete the dissolution of nickel. The Sn-Ag-Cu alloys contained 0.5% Cu and 1-4% Ag. The solder alloy was melted in an electrical resistance furnace at 350°C. The components for the preparation of test alloys in the form of pre-alloy (both compact material and soldering wire) were provided by GLOB-Metal Ltd. and Metalloglobus cPlc. The alloys were poured into a pre-heated (to 200°C) steel mould of metal rods with a diameter of 40 mm. The coin-shaped samples were prepared by grinding and polishing. The samples were studied by metallography and X-ray diffraction. The light microscopic images were taken by a Zeiss Axio Imager m1M optical microscope. The scanning electron microscopic studies were carried out on a Hitachi S4800 scanning electron microscope equipped with a Bruker energy-dispersive microprobe. The X-ray diffraction measurements were performed on a Phillips PW 1830 diffractometer using the copper radiation.

Results and discussion

Sn-Cu-Ni alloys. The microstructure of SnCu0.5 and SnCu0.7 nickel-free alloys contains the dendrites of β-Sn solid solution and β-Sn + Cu_6Sn_5 eutectic. The SnCu1 nickel-free alloy is fully eutectic (β-Sn + Cu_6Sn_5). In the case of SnCu0.5 alloy with up to 1000 ppm nickel content, the dendrites of β-Sn solid solution and β-Sn + $(Cu, Ni)_6Sn_5$ eutectic, while at 2000 ppm Ni content only β-Sn + $(Cu, Ni)_6Sn_5$ eutectic are observed in the microstructure. In the case of SnCu0.7 alloy, a very fine, fully eutectic structure is reached already at 1000 ppm Ni content. At 2000 ppm nickel content primary $(Cu, Ni)_6Sn_5$ intermetallic phases appear in the microstructure, which is also supported by results of EDS measurements. These microstructural differences are well visible in the SEM images presented in Fig. 1. In the case of SnCu1 alloy the initial structure is fully eutectic and does not change significantly up to 500 ppm nickel content; with 1000 ppm Ni primary intermetallic phases $(Cu, Ni)_6Sn_5$ are also visible.

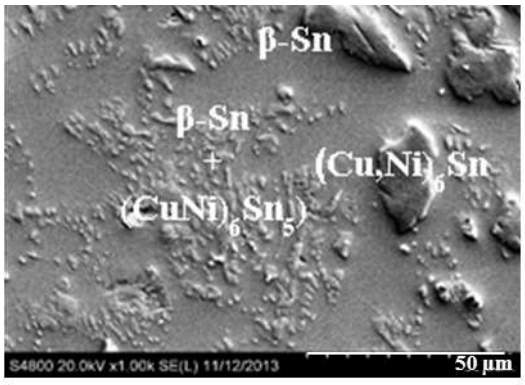

Fig. 1. SEM images of SnCu0.7Ni0.2 alloy with phases depicted

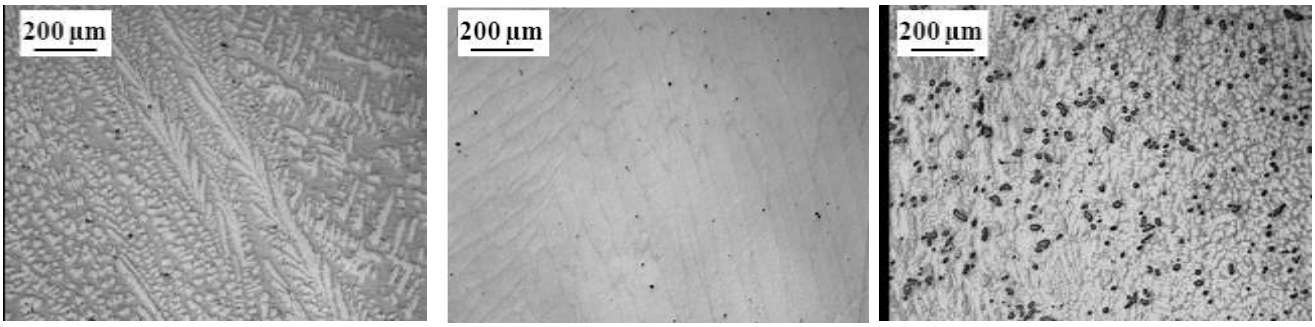

250 ppm 500 ppm 1000 ppm

Fig. 2. The microstructure of SnCu0.7 alloy with various nickel content

Increasing the nickel content of SnCu0.7 alloys the initially hypoeutectic structure (250 ppm Ni) gradually transforms into fully eutectic one (500 ppm Ni) and then, above certain nickel content (1000 ppm), into hypereutectic one (Fig. 2). The results of microstructural studies are in good agreement with the results of Ventura et al. on SnCu0.7 alloy. Examining the effect of nickel content (in the range from 0 to 1000 ppm) on the microstructure, these authors found that at 90 ppm Ni the Sn-0.7Cu alloy has a hypoeutectic structure; increasing the nickel content the eutectic structure is reached. Further increase of the nickel content causes the primary intermetallic phases to form [7].

In the XRD patterns of SnCu0.7 alloys of various nickel content the reflections of β-Sn solid solution and η-Cu_6Sn_5 intermetallic phase are visible (Fig. 3).

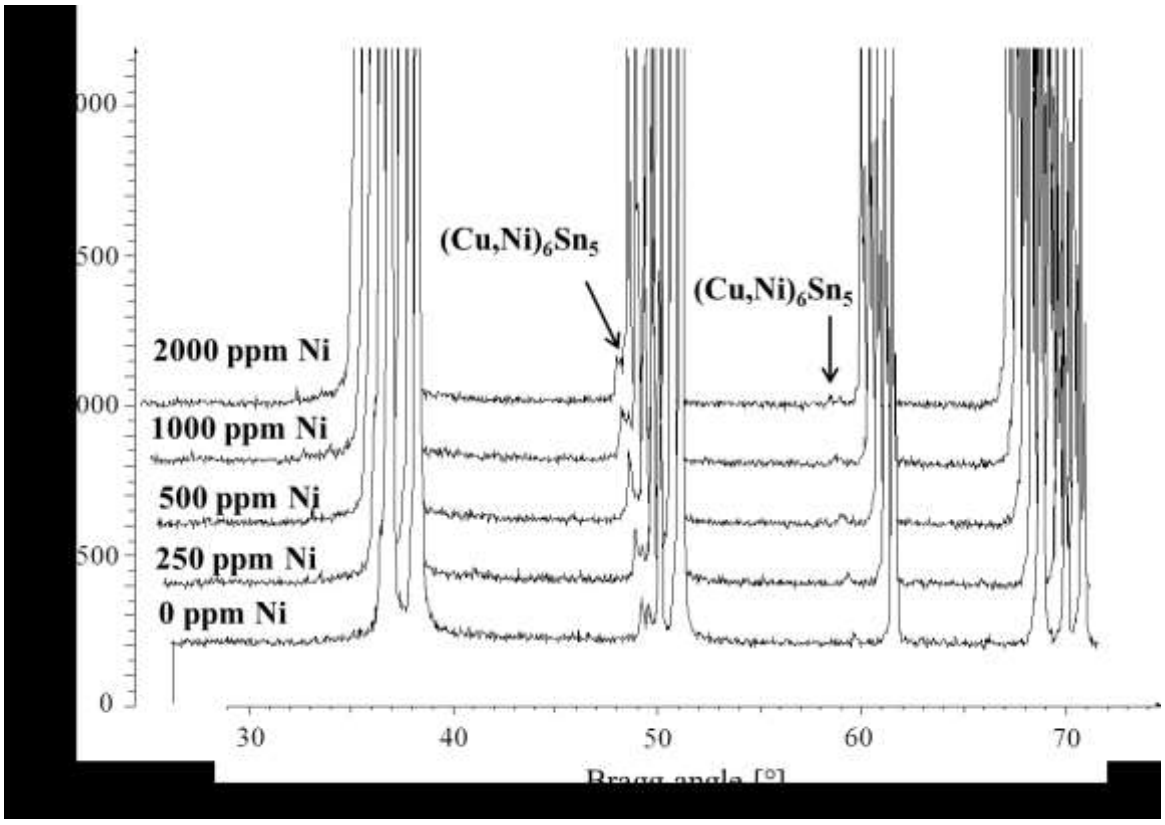

Fig. 3. XRD patterns of SnCu0.7 alloy with various nickel content

According to the phase diagram, in SnCu0.7 alloy at ambient temperature η'-Cu_6Sn_5 monoclinic phase should be present instead of η-Cu_6Sn_5 hexagonal phase. However, the addition of nickel stabilizes the η phase formed at high temperature; therefore the η → η' allotropic transition does not occur [10].

The stoichiometric composition of Cu_6Sn_5 phase may vary according to the $(Cu_{6-x}Ni_x)Sn_5$ formula. Based on the results of XRD studies, it can be concluded that the composition of the compound phase in the range of Ni content 0-0.2% varies with increasing the nickel content according to the following formula: $(Cu_{5.5-4.5-x}Ni_{0.5-1.15})Sn_5$. The lattice parameter of the compound decreases with increase of the nickel content, which is in agreement with the results found in literature [10].

Sn-Ag-Cu alloys. The microstructure of Sn-Ag-Cu alloys contains the dendrites of β-Sn solid solution and β-Sn + Ag_3Sn eutectic (Fig. 4). The copper and silver contents of the alloy are located practically within the eutectic; therefore it can be assumed that the eutectic contains Cu_6Sn_5 and Ag_3Sn phases. The microstructure of the specimen corresponds to the literature data [9].

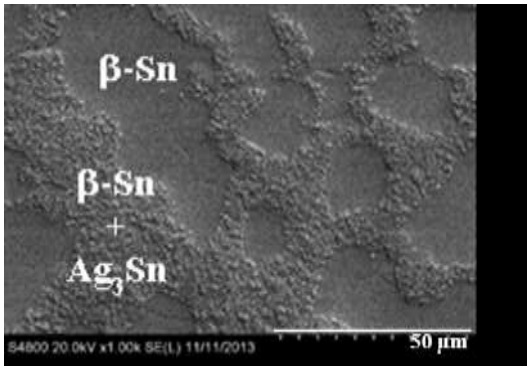

Fig. 4. SEM image of a Sn-Ag-Cu alloy containing 3% Ag

D.A. Shnawah et al. have found that the microstructure of Sn-Ag-Cu alloys is constituted by fine-grained Ag_3Sn and coarse-grained Cu_6Sn_5 intermetallic phases dispersed in the β-Sn matrix. The area of Ag_3Sn increases in line with increasing the silver content. In Sn-Ag1.0-Cu0.5 alloy traces of fine-grained Ag_3Sn along with relatively large-sized particles of primary tin are dispersed in the matrix. Primary tin particles are formed prior to the eutectic composition. In the case of SnAg2.0Cu0.5 alloy primary tin appears in cell-like arrangements, which are sometimes surrounded by fine Ag_3Sn particles. In SnAg3.0Cu0.5 alloy the Ag_3Sn compound forms a network around the primary tin; the particle size of primary tin is significantly smaller. In SnAg4.0Cu0.5 alloy the Ag_3Sn particles are well dispersed in the eutectic [9].
In the case of Sn-Ag-Cu alloys the eutectic content increases with increase of the silver content up to 3%. The microstructure of the alloy containing 4% silver is different: the higher silver content results in the formation of a large number of Ag_3Sn particles and small-sized primary tin (Fig. 5) [10].

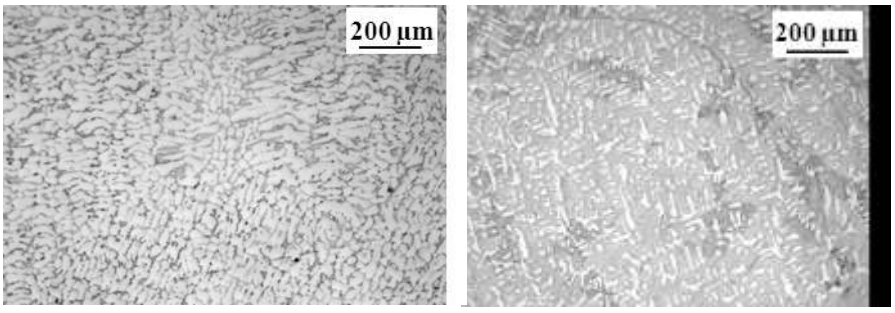

SnAg1Cu0.5 SnAg4Cu0.5

Fig. 5. Light microscopic images of Sn-Ag-Cu alloys

The XRD patterns of Sn-Ag-Cu alloys of various silver content are shown in Fig. 6.

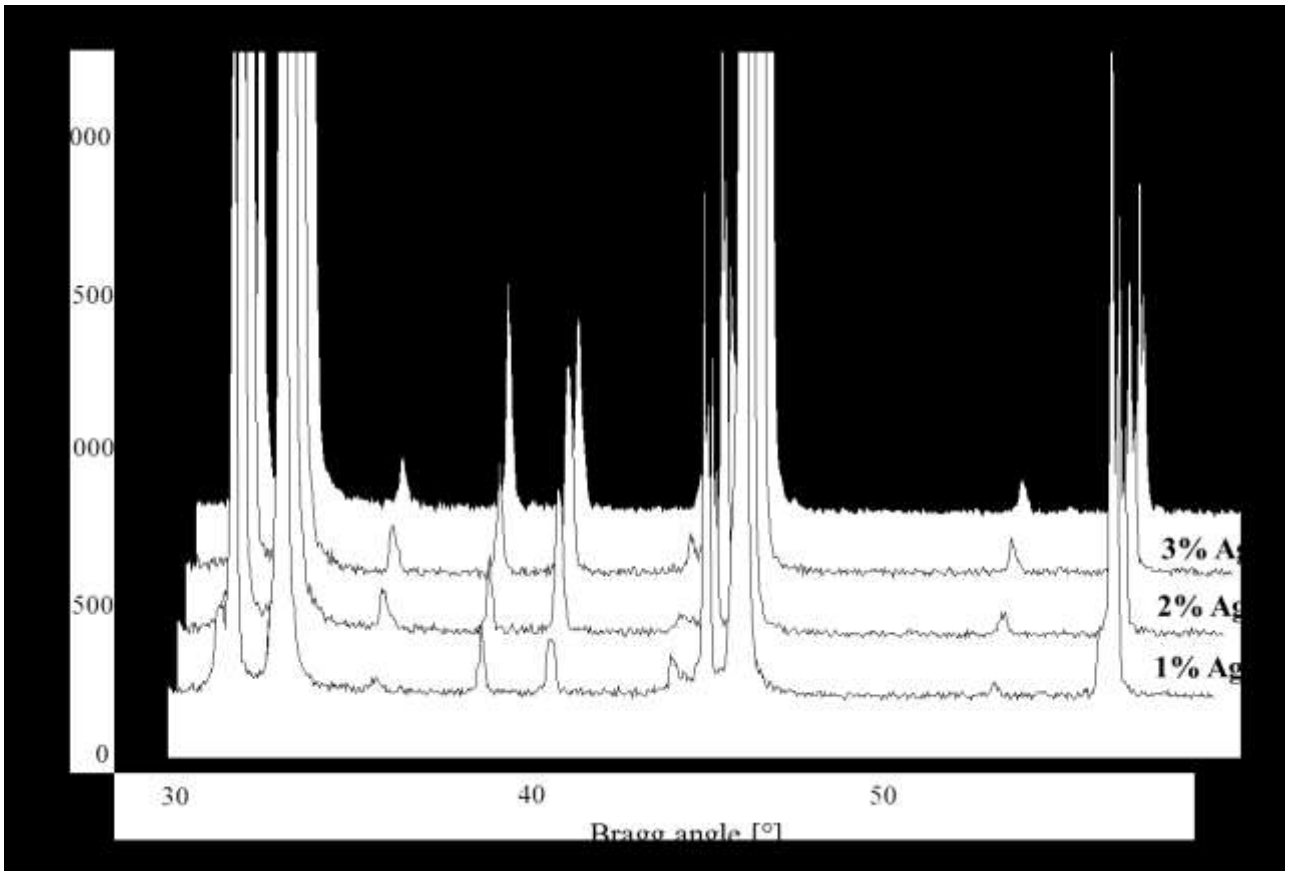

Fig. 6. XRD patterns of Sn-Ag-Cu alloys

The reflections of β-tin solid solution and Ag_3Sn intermetallic phase are identified in the XRD patterns.

Summary

In the case of Sn-Cu alloys, the nickel content resulting in the eutectic microstructure has been determined for the given copper content. In Sn-Cu alloys, the $\eta \rightarrow \eta'$ allotropic transition does not take place due to the stabilizing effect of nickel. The composition of Cu_6Sn_5 intermetallic phase varies with increase of the nickel content (in the range 0-0.2% Ni) according to the following formula: $(Cu_{5.5-4.5-x}Ni_{0.5-1.15})Sn_5$. The lattice parameter of the compound phase decreases with increase of the nickel content.
In the case of Sn-Ag-Cu alloys one of the phases (Ag_3Sn intermetallic compound) constituting the eutectic has been identified. It has been established that increasing the silver content results in an increase of the eutectic quantity.

AcknowledgementThis research was supported by the European Union and the State of Hungary, co-financed by the European Social Fund in the framework of TÁMOP 4.2.4. A/2-11-1-2012-0001 'National Excellence Program'. This research is related to the project TÁMOP-4.2.2. A-11/1/KONV-2012-0019 "Development of environmentally safe solders for automotive industry from primary and secondary resources based on materials science considerations" carried out at the University of Miskolc.

References

[1] ASM Handbook, Volume 3: Alloy phase diagrams, ASM International, 1992.

[2] Kattner, U.R.: Phase diagrams for Lead-free solder alloys, Journal of The Minerals, Metals & Materials Society, 54, 2002, p. 45-51.
[3] Nogita, K.: Stabilisation of Cu_6Sn_5 by Ni in Sn-0.7Cu-0,05Ni lead-free solder alloys, Intermetallics, 18, 2010, p. 145-149.
[4] Nogita, K.; Nishimura, T.: Nickel stabilized hexagonal $(Cu,Ni)_6Sn_5$ in Sn-Cu-Ni lead-free solder alloys, Scripta Materialia, 59, 2008, p. 191-194.
[5] Gourlay, C.M.; Nogita, K.; Read, J.; Dahle, A.K.: Intermetallic formation and fluidity in Sn-rich Sn-Cu-Ni alloys, Journal of Electronic Materials, 39, 1, 2010, p. 56-69.
[6] Snugovsky, L.; Snugovsky, P.; Perovic, D.D.; Rutter, J.W.: Phase equilibria in Sn rich corner of Cu-Ni-Sn system, Materials Science and Technology, 22, 8, 2006, p. 899-902.
[7] Ventura, T.; Terzi, S.; Rappaz, M.; Dahle, A.K.: Effects of Ni addition, trace elements and solidification kinetics on microstructure formation in Sn-0.7Cu solder, Acta Materialia, 59, 2011, p. 4197-4206.
[8] http://www.metallurgy.nist.gov/phase/solder/agcusn.html
[9] D.A. Shnawah, M.F.M. Sabri and I. A. Badruddin, A review on thermal cycling and drop impact reliability of SAC solder joint in portable electronic products, Microelectronics Reliability 52, 2012, p. 90
[10] K. Nogita, D. Mu, S.D Mcdonald, J. Read, Y.Q. Wu: Effect of Ni on phase stability and thermal expansion of $Cu_{6-x}Ni_xSn_5$ (X=0, 0.5, 1, 1.5 and 2), Intermetallics 26, 2012, pp 78-85.

Determination of the guidewire's visibility

Liza Pelyhe[1,2,a], Eszter Bognár[1,2,b]

[1]Budapest University of Technology and Economics, Department of Materials Science and Engineering, H-1111 Budapest, Bertalan Lajos u. 7. Hungary

[2]MTA-BME Research Group for Composite Science and Technology, H-1111 Budapest, Műegyetem rkp. 3. Hungary

[a]liza@eik.bme.hu, [b]eszter@eik.bme.hu

Keywords: guidewire, radiodetectability, visibility

Abstract. The purpose of our research was the development of a new algorithm to the objective quantification of guidewire's visibility; which is suitable for the classification and comparison of different guidewires, according to this property. The guidewire is a flexible medical device, over which the catheter or the dilator is lead into the vascular system to assist the insertion and position of these devices. During the insertion and the removal of guidewire the movement of distal end is monitored under fluoroscopy. At the beginning of our experiments two algorithms were developed and applied: the first one investigated the total distal end, while the second one investigated two parts of the distal end. Both algorithms were tested on ten guidewires made of same brand and material, so their relative visibility (the visibility of guidewire's investigated part compared the background) were determined by both method. The average relative visibility was 19.8%±3.0% in case of algorithm for total distal end, and it was 21.5%±2.9% in case of algorithm for two part of distal end. The coefficient of variation was calculated in case of both algorithms, thus characterized by their reliability. Both coefficient of variation were low (0.15 and 0.13), so the algorithms were considered to be reliable. The two algorithm were no significant different ($p=0.15$), therefore the investigation of the total distal end might be replaced by the investigation of two parts.

Introduction

Worldwide, including Hungary, cardiovascular diseases are the leading causes of death [1,2]. One of their treatments is the angioplasty. This is a minimal-invasive procedure to open the narrowed, occluded vessels [3-5]. During this procedure fluoroscopy is used to follow-up the devices, since the radiodetectability, visibility of these devices is highly important [6-11].

One of the angioplasty's important devices is the guidewire, over which the catheter or the dilator is lead into the stenosis, thereby facilitating their insertion and position in the vessels. The distal part of guidewire is introduced into the body and first passes through the stenosis; the proximal end remains outside the body [6,7,9].

Like all intravascular catheter introducer (except dilators), the guidewire too shall be radiodetectable according to standard that apply to it (ISO 11070:1998). This standard for guidewire does not contain measurement method to the investigation and quantification of the guidewire's visibility [9].

To determine radiopacity, the ASTM F640 - 12 standard contains standard test methods but only in general, so their accurate description is not specified [12].

Our aim was to develop a new algorithm to objective quantify the guidewire's visibility based on ASTM F640 - 12 standard and our earlier research [12,13], which is suitable for the objective classification and comparison of this property for the available guidewires.

Algorithm for determining visibility

First of all it was necessary to define which part of the guidewire should be investigated, how large should be the investigated part of the sample. This had to be adapted to straight or pre-formed guidewires. Since the distal end reaches first the stenosis and then passes through, the visibility of

the distal end was determined. In case of straight guidewire, the total distal end was investigated (Fig. 1), which was 20±2 mm long in our case. In case of pre-formed guidewire two shorter part of the distal end was investigated. In our study we checked that the investigation of the total distal end might be replaced by two shorter part's analysis, by apply both methods on all guidewire. The two shorter parts denoted the first and last 6 mm of the distal end (Fig. 2) and their mean was used during the quantification.

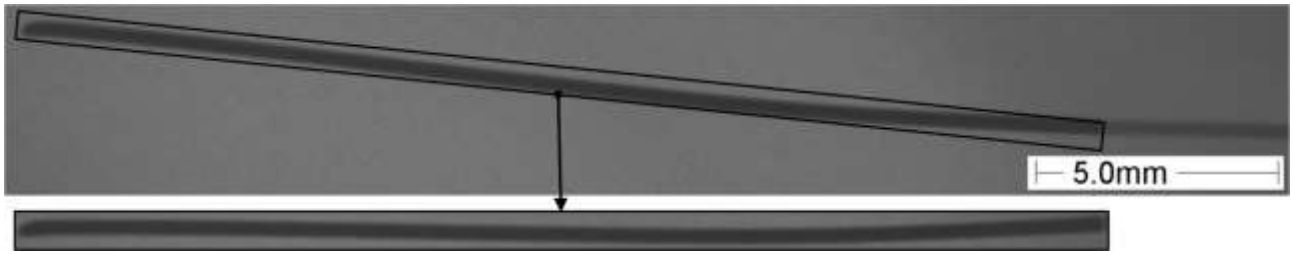

Figure 1: The investigated sample part in case of total distal end's investigation

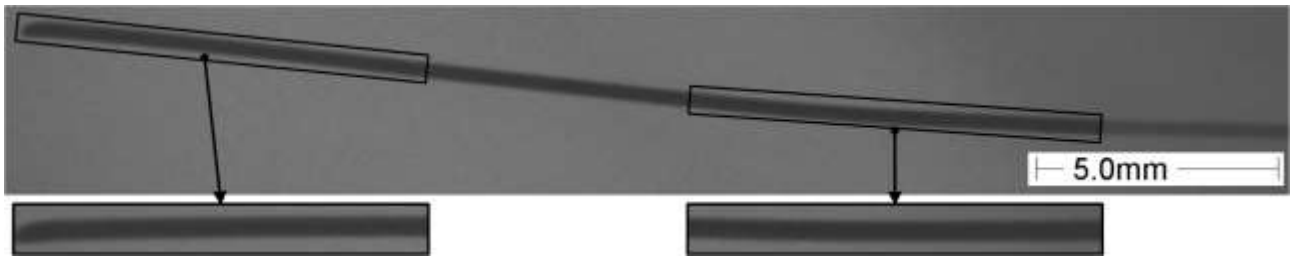

Figure 2: The investigated sample part in case of two part's investigation

To the determination of visibility first of all X-ray images were made from the distal end of guidewire by a Dage XiDAT XD6600 X-ray Inspection System. The settings were set in accordance with hospital practice, i.e. the accelerating voltage was between 90-110 kV, the cathode power was between 0.90-1.20 W and the average frame rate was 32 frame per second. The pixel intensity of the background and the guidewire's investigated part were determined on the X-ray image by image processing software, developed and written by our research group. Than by the same software, the pixel intensity differences were determined between the background and the investigated part. Gy. Ring introduces the software's operating principles and the determination of the compared image sizes [13].

The result of the image processing software is the relative visibility, which gives the visibility of guidewire's investigated part compared to background on a scale of 0 to 100%. The better guidewire appear, this value get higher. If this value is zero, the guidewire blends into the background that is invisible.

The guidewire can be characterised by the relative visibility of investigated part in case of the total distal end's investigation, and by the average relative visibility of investigated parts in case of two sample parts (Fig. 3).

The two algorithms were tested on ten guidewires made of same brand and linear elastic Nitinol core. The mean and the standard deviation of 10-10 measures were calculated, then the both algorithms' coefficient of variation was determined (the percentage ratio of standard deviation to the mean). The coefficient of variation may add values between 0.0-1.0 and the algorithm's reliability may be characterised by it. The lower this value the more reliable the developed algorithm.

We checked that the investigation of total distal end might be replaced by the average of the two investigated parts. For this the two algorithms were compared by Mann-Whitney U test. It is a nonparametric t-test, which is suitable to compare two independent samples. Our samples have non-normal distribution and it was used instead of the t-test do to the greater efficiency. If $p<0.05$, then the two algorithm are significantly different, i.e. one may not be used instead of the other. If $p>0.05$, then the investigation of the total distal end may be replaced by the average of the two investigated

parts. The reliability was determined by the coefficient of variation (relative standard deviation), which is the ratio of the standard deviation and the average. Under 0.1 it indicate the homogeneity of the sample. The coefficient of variation indicate moderate heterogeneity between 0.1 and 0.3 (according to some literature between 0.1 and 0.2), and extremely variability over 0.3. Under 0.3 this value is acceptable.

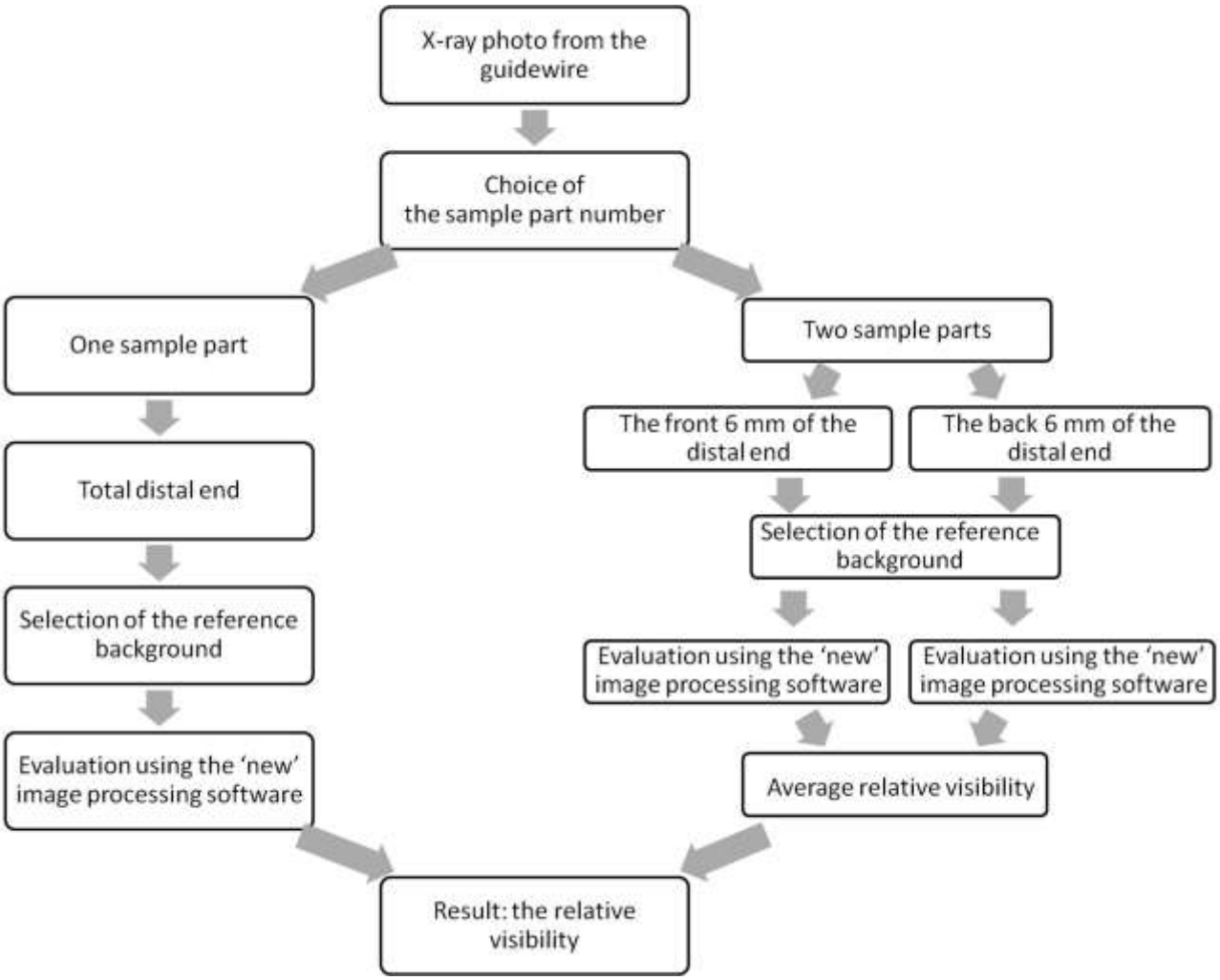

Figure 3: Algorithm for determination the visibility of guidewire's distal end in case of one or two sample part

Testing of the developed algorithms

Fig. 4 shows the calculated relative visibility of the ten measured samples for both algorithms. At first sight, the two algorithms' results were different from each other (Fig. 4, Fig. 5), but by applying the Mann-Whitney U test, it revealed, that there were no significant difference between them ($p=0.15$).

The coefficient of variation was 0.15 in case of algorithm for total distal end, and it was 0.13 in case of algorithm for two part's investigation, therefore both algorithms work reliably.

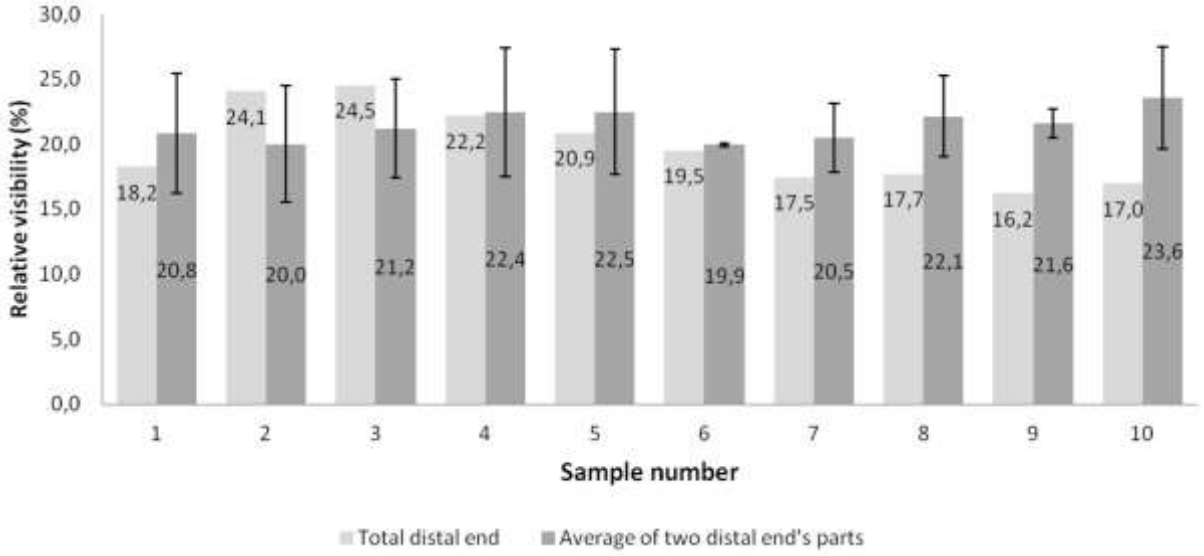

Figure 4: The relative visibility of the distal end according to the two developed algorithms

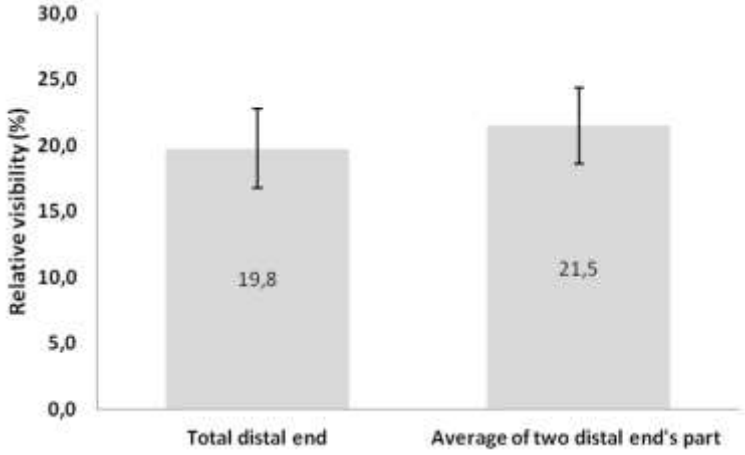

Figure 5: The average relative visibility of the distal end according to the two developed algorithms

Conclusion

In our article two algorithms were presented which are suitable to the objective quantification of guidewire's visibility.

One of the two developed algorithms was useful in case of the total distal end's investigation and the other in case of two part's investigation. Both algorithms considered reliable according to the coefficient of variation, therefore both are suitable in future research.

The relative visibility's values obtained by two algorithms were not differing significantly; therefore the algorithm for two part's investigation might be used instead of the total distal end's investigation.

Based on this statement, one can see, that succeeded to develop an algorithm to quantify the relative visibility of the guidewire's distal end, so they can be classified and were comparable on the basis of these properties.

Acknowledgement

This work is connected to the scientific program of the "Development of quality-oriented and harmonized R+D+I strategy and functional model at BME" project. This project is supported by the New Hungary Development Plan (Project ID: TÁMOP-4.2.1/B-09/1/KMR-2010-0002).

References

[1] Information on http://who.int/mediacentre/factsheets/fs310/en/index2.html 09.01.2014.

[2] Information on http://www.ksh.hu/docs/hun/xstadat/xstadat_hosszu/h_wdsd001c.html 09.01.2014.

[3] OECD, Health at a Glance: Europe 2012, OECD Publishing, Paris, 2012.

[4] S. Baum, M.J. Pentecost, Abrams' Angiography, Lippincott Williams & Wilkins, Philadelphia, 2006.

[5] Information on http://www.accessdata.fda.gov/cdrh_docs/pdf11/P110040d.pdf 09.01.2014.

[6] R.A. Morgan, E. Walser, Handbook of Angioplasty and Stenting Procedures, Springer-Verlag, London, 2010.

[7] M.J. Kern, The Interventional Cardiac Catheterization Handbook, Elsevier Health Sciences, Philadelphia, 2012.

[8] ISO, Intravascular catheters - Sterile and single-use catheters - Part 1: General requirements, ISO 10555-1:2013, International Organization for Standardization, 2013.

[9] ISO, Sterile, single-use intravascular catheter introducers, ISO 11070:1998, International Organization for Standardization, 1998.

[10] ISO, Cardiovascular implants - Endovascular devices - Part 1: Endovascular prostheses, ISO 25539-1:2009 2, International Organization for Standardization, 2009.

[11] ISO, Cardiovascular implants - Endovascular devices - Part 2: Vascular stents, ISO 25539-2:2013, International Organization for Standardization, 2013.

[12] ASTM International, Standard Test Methods for Determining Radiopacity for Medical Use, ASTM F640 - 12, American Society for Testing and Materials, 2012.

[13] Gy. Ring, Pre-clinical evaluation of coronary stents and other endoprotheses. Ph.D. dissertation, Dept. of Materials Science and Engineering, BME, Budapest, Hungary, 2011.

Laboratory-scale simulation of acid pickling of steel sheets with an instrument modeling the production line

László Péter[1,a], Orsolya Sánta[2], Ottó Szabados[3], Balázs Verő[2]

1: MTA Wigner Research Centre for Physics,
1121 Budapest, Konkoly-Thege út 29-33, Hungary

2: College of Dunaújváros, 2400 Dunaújváros, Táncsics Mihály utca 1/A, Hungary

3: Association of the Hungarian Steel Industry, 1373 Budapest, Pf. 548., Hungary

a: Corresponding author. Email: peter.laszlo@wigner.mta.hu

Keywords: hydrochloric acid pickling, steel sheet, simulation device, scale removal, overpickling

Abstract. A fully automated laboratory-scale workstation has been constructed for simulating industrial acid pickling processes of steel sheet products. The device built comprises 4 liquid tanks that can be heated up to 80 ^{o}C and an arbitrary immersion program can be performed with the sheets to be tested by varying the immersion time and the motion velocity in each tank. The weight loss has been measured for both hot-rolled and cold-rolled specimens as a function of all variable parameters. The weight loss associated with the removal of the oxide layer could be established. The average oxide-related loss was 58 g·m^{-2} and 2 g·m^{-2} for hot-rolled and cold-rolled samples, respectively. It was found that the immersion time is the decisive parameter in the weigh loss measured, while the motion velocity and the temperature of the sample treatment are of secondary importance.

Introduction

The regulation of composition, casting conditions, rolling rate and temperature and annealing treatment provides the desired mechanical properties of steel sheet products. Before the final step of manufacturing, the surface properties also have to be adjusted to comply with the required purity. This is especially important for hot-dip zinc coating, galvanizing, enameling, passivating and painting; i.e., for essentially all surface-related procedures.

The major way of the removal of the oxide formed in air during the high-temperature processing of steel sheet products is acidic pickling. This method involves the drawing of the unrolled sheet through tanks containing pickling liquors of successively increasing acid concentrations in a counterflow system, then washing the sheets and re-rolling them under surface-preserving conditions (application of protecting lubricants). The pickling liquors used for carbon steels nowadays are almost exclusively of the hydrochloric acid type. After the complete removal of the oxide, the base metal can also be dissolved, and this process is often termed as overpickling. The latter process is to be reduced by the addition of inhibitors to the pickling liquors that decelerate the dissolution of the free metal in acids.

The list of the appropriate descaling conditions includes the rolling rate, the residence time of the sheet in the acid, the pickling liquor temperature and the inhibitor concentration. Since there is no way to perform any test at the production plant, the above mentioned parameters should be determined preferably at the laboratory scale. The construction of a full device for this pickling test has the following advantages: (i) The bath properties (i.e., both the number of the tanks and the concentration of each bath) of the industrial plant can be strictly followed; (ii) Bath temperatures can be set to real values without jeopardizing the lab environment; (iii) Large sets of specimens can be tested in an automated mode with little specific loss of the pickling acid; (iv) Inhibitor efficiency can be tested with a little amount of chemical by using the actual steel quality; (v) The motion velocity and the residence time can be adjusted independently of each other, unlike under industrial conditions where these parameters are connected with the tank length; (vi) Impact of the pickling liquor of each tank can be determined separately.

The scientific literature of the research related to the pickling process is mostly constrained to the characterization of some inhibitors and their adsorption process [1-2]. The determination of both the pickling rate and the overpickling rate appears only exceptionally [3]. The typical experimental conditions include a single solution only that contains an acid but no dissolved metal salts are present, unlike in a real pickling system. The construction of a complete device simulating a multiple immersion process has not been described yet to the best knowledge of the authors.
In the sections below the descaling simulator built by our team will be shortly described. The first weight loss measurements will be presented together with the evaluation of the results.

Experimental

Construction of the descaling dimulator. The simulator is a free-standing box of 1 meter length, 1 meter width and 2 meter height. The device is divided horizontally into 3 sections (see Figure 1.a). The bottom section of the device is the location of all motor units and the tanks that are used for the transfer of the pickling liquors. The medium level of the simulator includes 4 tanks that contain the pickling liquors and rinsing liquids during the device operation. The samples are immersed into these tanks during the pickling test. Samples can be attached to the holder at this level through the window in the front side. The center of the tanks and the sample changing position are accessible with a 72^{o} rotation around the central axis of the device. The upper section of the simulator provides the space for raising the sample holder above the tank level and to make it possible to rotate the central axis to reach the desired tank with the sample holder. The tanks are open only for the short time of the position change of the sample holder. The motion velocity of the samples is controlled with a variable-speed rotor system within the tanks that is also responsible for stirring the liquids. The degrees of freedom for the sample motion are represented with arrows of various color in Figs. 1,a and 1,b.

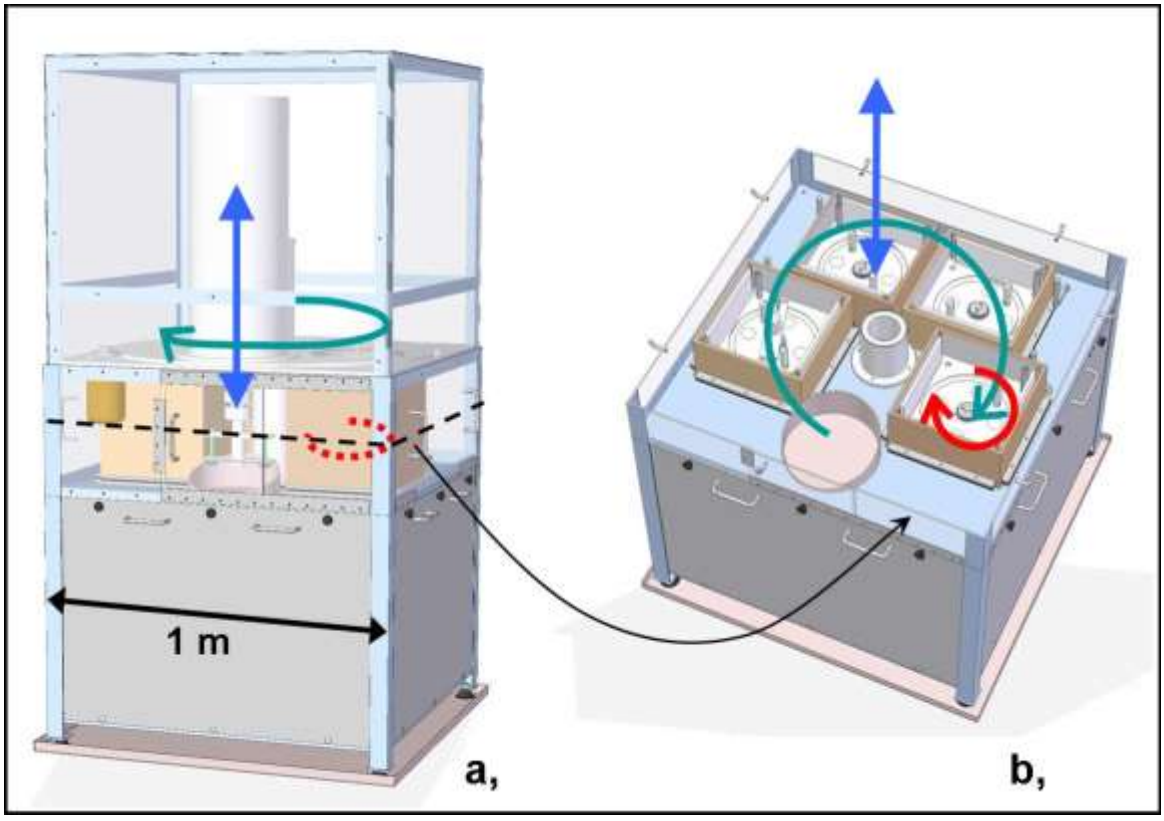

Figure 1. – The descaling simulation device with the front view (a) and the cross-sectional view at the tank level (b). Arrows show the sample motion modes according the three degrees of freedom.

All parts of the simulator that contact the pickling acid are made of highly resistant fluoropolymers. The content of the tanks are heated by using coated immersion heaters. The level of the liquids is continuously monitored. The emission-free operation of the system is provided with a sucking ventilator at the top of the simulator. The part of the electrical regulation is comprised into a separate stand next to the device. All setup and control options are accessible via a touch screen interface, and the device operation is controlled with a PLC that runs a custom-made program.

Materials and chemicals. Hot-rolled and cold-rolled steel sheets were cut to 40 mm x 70 mm specimens. The quality of the samples was conformal to the DC01AL, S235JRG, S355MC, ST24 or DD11 quality (typical chemical composition in %: C < 0.12, Si = 0.5, Mn = 0.5-1.5, P < 0.04, N < 0.009, Cr = 0.4-0.8, Cu = 0.25-0.55)
All pickling weight loss data refer to the average of 2 or 3 independent experiments. Pickling acid was mostly obtained from the production line of DUNAFERR with the following average concentrations: c(HCl) = 45, 110 and 175 g/l, $c(Fe^{2+})$ = 125, 60 and 9 g/l in tanks # 1, 2 and 3, respectively.
Sample motion rate. Since the relative motion rate of the steel sheet and the pickling acid in the industrial tank is not known, the following approximation was applied: The flow of the liquid was assumed to be laminar. Hence, the following equation served to calculate the equivalent motion rate in the simulation device: $v_{PR}/d_{PR}=v_{SIM}/d_{SIM}$, where v is the velocity of the sample as compared to the wall of the tank, and d is the distance from the wall. The indices, PR and SIM refer to the production line and the simulator, respectively. Therefore, the velocity gradient (that is the key parameter in the convective mass transport) is roughly identical in industrial and laboratory conditions.

Results and discussion

The weight loss of both hot-rolled and cold-rolled samples has been studied as a function of the following technical parameters: a, residence time of the samples in all the three tanks; b, motion rate of the samples in the pickling acid; c, temperature of the baths; d, application of some selected tanks only instead of the sequential immersion into all tanks. Below, the general features of the weigh loss functions are highlighted. Then, the discussion of the results is given for the two steel qualities separately, following the above mentioned order of the parameters varied for both sample types.
General features of the weight loss functions. The weigh loss was usually measured as a residence time in the tanks. When such data are displayed, all measurement could be elucidated with the same scheme, as shown in Figure 2. Namely, the weigh loss increase linearly with the residence time. When the trend obtained from the experimental data is extrapolated to zero residence time, the intercept with the ordinate yielded a positive value. This value is attributed to the weight loss due to the dissolution of the oxide layer (scale) from the sample surface. This concept is verified by the comparison of the typical weigh loss extrapolated to zero residence time for cold-rolled and hot-rolled samples where the oxide layer thickness is different. The linear increase of the weight loss can be explained as the evidence of the overpickling; i.e., the unwanted dissolution of the metal in the acid.

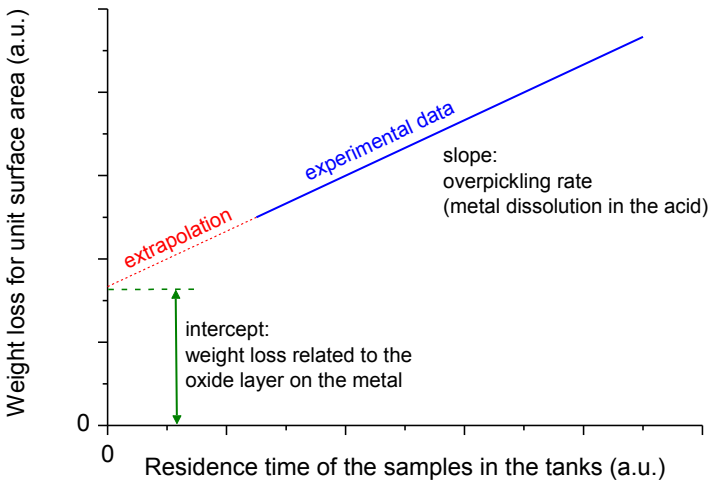

Figure 2. – General features of the weight loss vs. residence time curves (schematic explanation)

Results for the hot-rolled samples. Figure 3 shows the weight loss of the hot-rolled samples as a function of both the residence time and the motion rate. For this sample series, no difference can be established due to the variation of the sample motion rate. The weight loss extrapolated to zero residence time was about 58 $g \cdot m^{-2}$ in both cases. The main difference caused by the difference in the inhibition level of the two experiment series was the slope of the weight loss vs. residence time function. Where the inhibitor was not present, the dissolution of the steel specimens in the highly acidic media was faster (1.33 $g \cdot m^{-2} \cdot s^{-1}$) than in the industrial pickling liquor containing inhibitors (0.44 $g \cdot m^{-2} \cdot s^{-1}$).

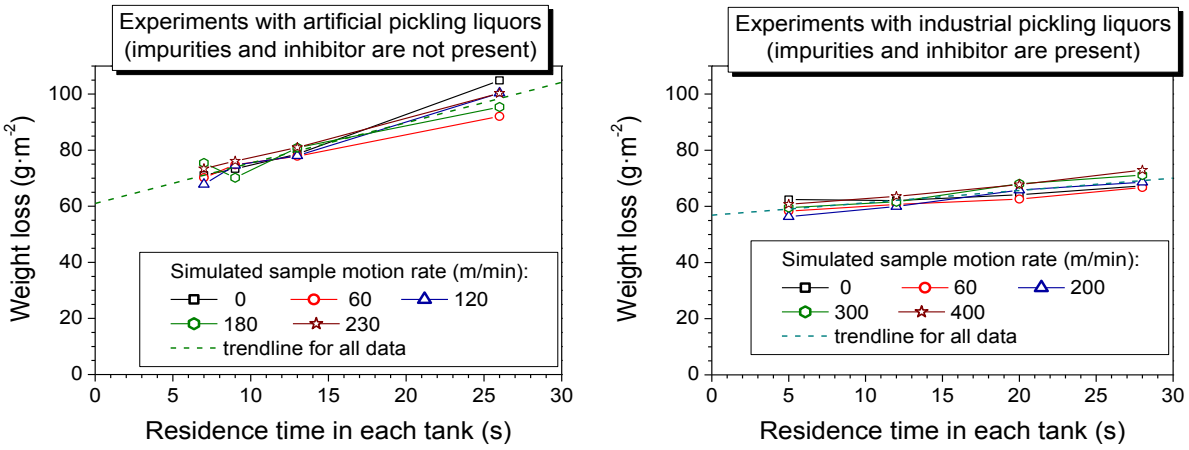

Figure 3. – Weight loss data measured for hot-rolled samples in artificial pickling liquors (without any inhibitor or impurity; left) and with industrial pickling liquors (containing inhibitor and all typical impurities of the production line; right). Temperature: 80 °C.

The impact of the sample motion rate could not be identified in any of the experiment series performed with the hot-rolled samples. It is believed that the fairly large weight loss and its fluctuation from one sample to another hides the manifestation of the impact of the stirring conditions.

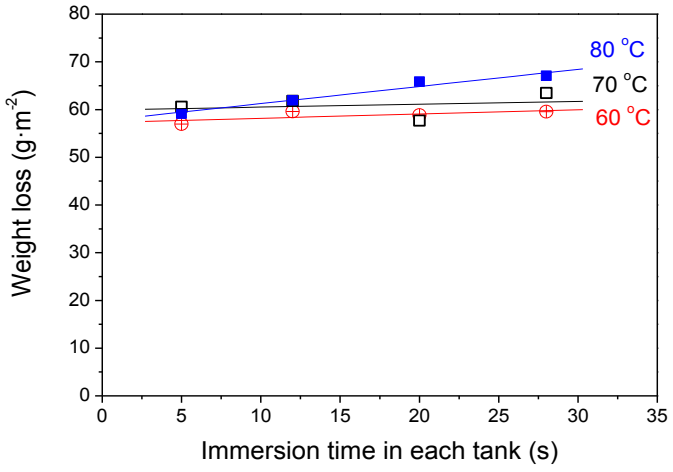

Figure 4. – Weight loss data for hot-rolled samples as a function of the descaling temperature

The impact of the temperature of the pickling liquors on the weight loss of the hot-rolled samples is depicted in Figure 4. The effect of the acid temperature seems to be somewhat uncertain, since the data are a bit scattered. For either of the temperatures applied, the data trend is essentially the same, and the weight loss extrapolated to zero residence time is equal to that derived from the other measurements within the experimental error. The expectation that the overpickling rate increases with temperature is fulfilled since the slope of the lines obtained increases with temperature.

Results for the cold-rolled samples. Figure 5 shows the weight loss data for cold-rolled samples as a function of both the residence time in ach tank and the motion rate. As compared to the data obtained for hot-rolled samples, the main difference is that the weight loss extrapolated to zero residence time is much smaller. Depending on the actual sample quality, the oxide-related loss varied between 9 and 2 $g \cdot m^{-2}$ (the latter being the typical value for many sample series). This difference is natural, regarding that at lower rolling temperature, the oxide formation rate is much more moderate as opposed to the hot-rolling conditions.

In the absence of any inhibitor (when the overpickling rate is rather high) the weight loss of the sample was independent of the sample motion rate. Interestingly, when the inhibitor was present and the weight loss extrapolated to zero residence time was small enough, the overpickling rate was a function of the sample motion rate. The higher sample motion rate was applied, the faster overpickling process was observed. However, independently of the overpickling rate, the weight loss extrapolated to zero residence time was the same.

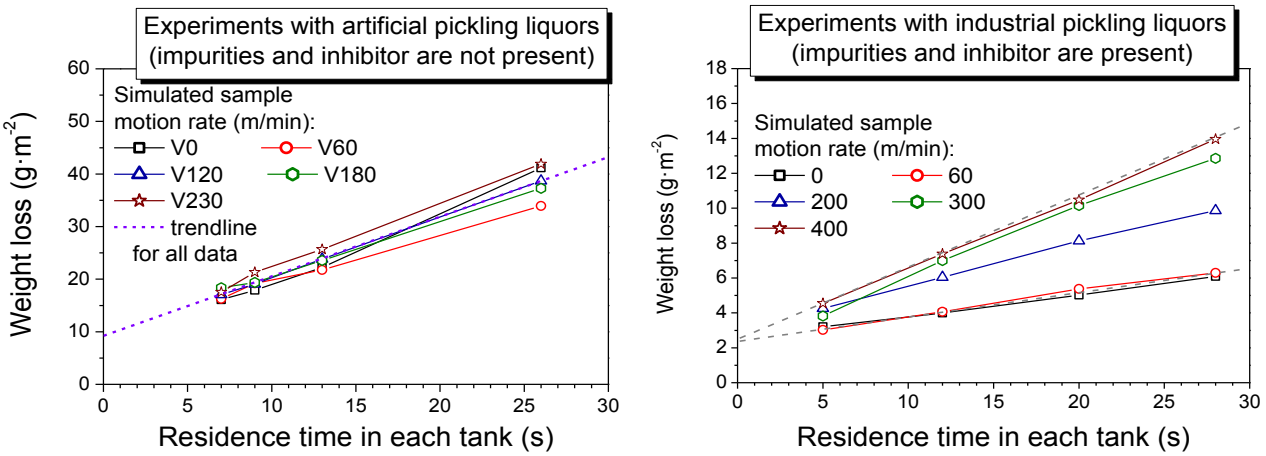

Figure 5. – Weight loss data measured for cold-rolled samples in artificial pickling liquors (without any inhibitor or impurity; left) and with industrial pickling liquors (containing inhibitor and all typical impurities of the production line; right). Temperature: 80 °C.

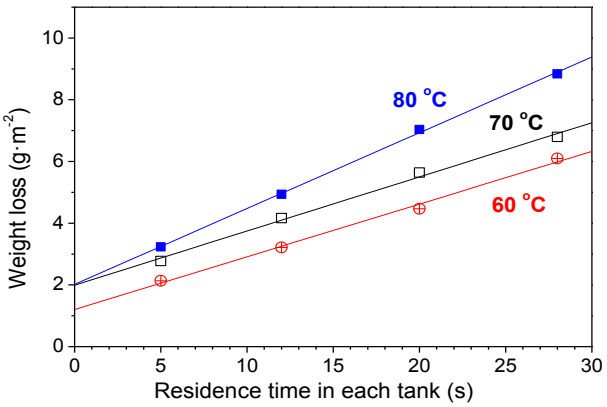

Figure 6. – Weight loss data for cold-rolled samples as a function of the descaling temperature

The low descaling loss of the cold-rolled samples made it possible to highlight subtle effects that remained hidden for the hot-rolled samples where the experimental error of the fairly high weight loss did not enable us to detect fine differences. Beside the impact of the dependence of the overpickling rate as a function of the motion rate, another example is the temperature dependence of the weigh loss function. This is clearly shown in Figure 6. The weight loss measured show a clear trend for all temperature values applied and for all residence times. The higher the temperature, the higher the weight loss under otherwise identical conditions. Also, the overpickling rate increases with temperature, which is in accord with the expectations.

The descaling simulator made it possible to study all pickling conditions independently of each other. Taking this advantage of the simulation device, an experiment was performed in which the samples were immersed in a various number of tanks, while rinsing was always applied at the end of the pickling test. The results are shown in Figure 7. It is apparent that the immersion into any of the acid tanks leads to a weight loss roughly equivalent to the weight loss extrapolated to zero residence time when all the three tanks are used (c.f. data in Fig. 5 or Fig. 6). This means that the weight loss after immersing into a single tank reaches the value attributed to the loss related to the oxide layer, and any further treatment has a contribution to the overpickling loss only. When two or three tanks are used for pickling, it can be seen that the weight loss is an approximately linear function of the number or acid tanks used. This is because in both the second and third tank the loss is caused by the same process; i.e., by the dissolution of the metal.

Data shown in Fig. 7 are in a strong agreement with the measurements presented in Fig. 6. In both measurement series, the impact of the descaling temperature could be resolved finely, and the overpickling rate increase with temperature. However, a slight anomaly can be seen in Fig. 7. Upon the immersion into a single tank, the least weight loss was obtained in Tank 3 where the acid concentration is the highest. This anomaly can be attributed to the construction of the descaling simulator device. When the sample is transferred from Tank 1 to Tank 4 (i.e., from the most dilute acid to the rinsing tank), the transfer time is larger than for the path Tank 3 to Tank 4, while the reactions at the surface could not be stopped. Hence, the apparent decrease of the weight loss from Tank 1 to Tank 3 when a single tank is used only is a technical artifact.

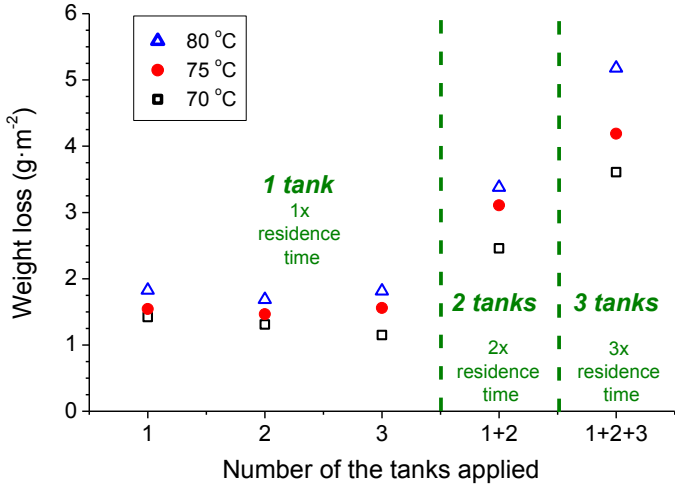

Figure 7. – Weight loss data for cold-rolled samples treated in selected tanks. The samples were rinsed in each experiment in Tank 4 after pickling them in either 1, 2 or all the 3 tanks. Residence time: 9 s, simulated motion rate: 160 m/min

Conclusion

A laboratory-size descaling workstation has been constructed and tested. The simulation device allows one to immerse small steel sheets consecutively in the pickling liquors of at most 80 °C for an arbitrarily selected immersion time and by rotating them. The rotation rate can be set so as to be equivalent with the strip passing rate under industrial condition. The independent tuning of all pickling parameters made it possible to separate the impact of all parameters. While the immersion time is of primary importance, the motion rate and the acid temperature has a minor effect on the weight loss. The weight loss extrapolated to zero time is essentially the same for a particular sample type, regardless of the conditions of the descaling process. The scale-related weight loss is an order of magnitude larger for hot-rolled samples than for cold-rolled samples, in accord with the kinetics of the thermal oxide formation.

Acknowledgement

The construction of the descaling simulation device was funded by Grant # TIOP-1.3.1. The experimental work is supported by the TÁMOP-4.2.2.A-11/1/KONV-2012-0027 project. The project is co-financed by the European Union and the European Social Fund.

References

[1] B. Tang, D.N. Li, F.L. Fu, Y.C. Xu, G.J. Yu, J.Y. Zhang, A Strategy for Cleaner Pickling: Effect, Mechanism and Evaluation Method of a Complex-Inhibitor in Hydrochloric Acid Medium, Industr. Eng. Chem. Res. 51 (2012) 2615-2621.

[2] M.N. El-Haddad, K.M. Elattar, Role of novel oxazocine derivative as corrosion inhibitor for 304 stainless steel in acidic chloride pickling solution, Res. Chem. Intermed. 39 (2013) 3135-3149.

[3] M.J. Cornu, A. Koltsov, S. Nicolas, L. Colom, M. Dossot, Behaviour of tetramine inhibitors during pickling of hot rolled steels, Appl. Surf. Sci. 293 (2014) 24-36.

The properties of welded joints made by 6082-T6 aluminium alloy and their behaviour under cyclic loading conditions

D. Pósalaky[1, a], J. Lukács[1,b]

[1]Institute of Materials Science and Technology,
Faculty of Mechanical Engineering and Informatics, University of Miskolc,
H-3515 Miskolc-Egyetemváros, Hungary

[a]metpdora@uni-miskolc.hu, [b]metluk@uni-miskolc.hu

Keywords: 6082-T6 aluminium alloy, welding, physical simulation, fatigue crack growth (FCG), high cycle fatigue (HCF).

Abstract. The magnitude of different aluminium alloys, especially the ones with higher strength, are increasing in the structural engineering, not just the usual applications (like the aerospace industry) but more likely in the automotive industry. There are more assumptions of the effective use of aluminium; we should highlight two important factors, the technological and the applicability criterions. The technological criterion is the joining of structural elements, frequently with welding thus the technological criterion ultimately is the weldability. The assumption of applicability comes from the loading capability of these structures, which is typically cyclic loading so the key issue from the point of view of applicability is the resistance to fatigue. This article represents physical simulation and fatigue test results both on the base material and on the welded joints.

Introduction

The importance of aluminium alloys. The reason of the increasing consumption of aluminium alloys is due to its characteristic properties. The attributes of pure aluminium are: low density, good heat and electric conductivity, good ductility and formability, but low strength. However, the strength and the toughness of aluminium can be raised by alloying and heat treatment as high as the properties of steel, also increasing the corrosion resistance. The flexibility, the strength and light weight are some of the qualities that make the aluminium alloys attractive in so many different applications (e.g. aerospace industry, packaging). On the other hand the aluminium alloys can be recycled under very positive conditions [1, 2].
The 6082-T6 aluminium alloy is one of the 6xxx series, it has two main alloying elements, magnesium and silicon – both of them increase the strength of the alloy, and as a solid solution it can be heat-treated, i.e. artificially aged. The usual properties of this alloy are shown in the Table 1.

Table 1. Chemical composition and mechanical properties of the investigated 6082-T6 alloy.

Chemical composition [weight%]							
Si	Fe	Cu	Mn	Mg	Cr	Zn	Ti
1,1	0,19	0,02	0,46	0,6	0,08	0,03	0,03
Mechanical properties							
R_m [MPa]		$R_{p0,2}$ [MPa]		A [%]		HB [–]	
305		266		22		97	

These aluminium alloys are significant in the automotive industry because of their high strength and toughness, very good formability and the light weight.

Proper welding technologies. The aluminium alloys can be welded by fusion welding and pressure welding technologies too. But the high heat conductivity, thermal expansion and the low melting point (*650 °C*) beside the aluminium-oxide's high melting point (*2050 °C*) makes difficult to prepare an appropriate welding technology.

We applied MIG (metal inert gas) and CW TIG (cold wire tungsten inert gas) fusion welding processes and FSW (friction stir welding) pressure welding technologies to compare the load bearing capacity of the welded joints made by different technologies. The characteristic differences among the technologies and the similarities are shown in the Table 2 [3].

Table 2. Comparison of the welding technologies.

Features	Method		
	MIG	**CW TIG**	**FSW**
Consumable	✓	✓/×	×
Shielding gas	✓	✓	×
Local liquefaction	✓	✓	×
Energy source	electric arc	electric arc	mechanical
Oxide decomposition	cathode sputtering, chemical cautery	cathode sputtering, chemical cautery	unnecessary
Porosity	occur	occur	×
Spatter	occur	occur	×
Health hazard	arc light, flue	arc light, flue, radioactive ThO_2	×

Welding problems [4]. The first major problem during the welding process is the extremely high melting point of the surface oxide film compared to the melting point of the base material. That means the base metal is already melted while the oxide is still in solid state, however in this case producing welded joints is impossible. Therefore the oxide must be removed from the base metal's surface before the welding process. There are more ways to eliminate the surface oxide film, e.g. chemical deoxidizing, mechanical thinning and cathode sputtering.

In the welded joints of aluminium alloys the hazard of hot cracking (solidification, liquation cracking) and cold cracking is high because of the attributes of aluminium (high heat conductivity and heat expansion). The hot cracking results of the deformation of the aluminium during the solidification and the cold cracking originates from the hydrogen caused porosity. If the deformation of the welded material is greater than its deformation capacity then hot cracks supervene (Fig. 1).

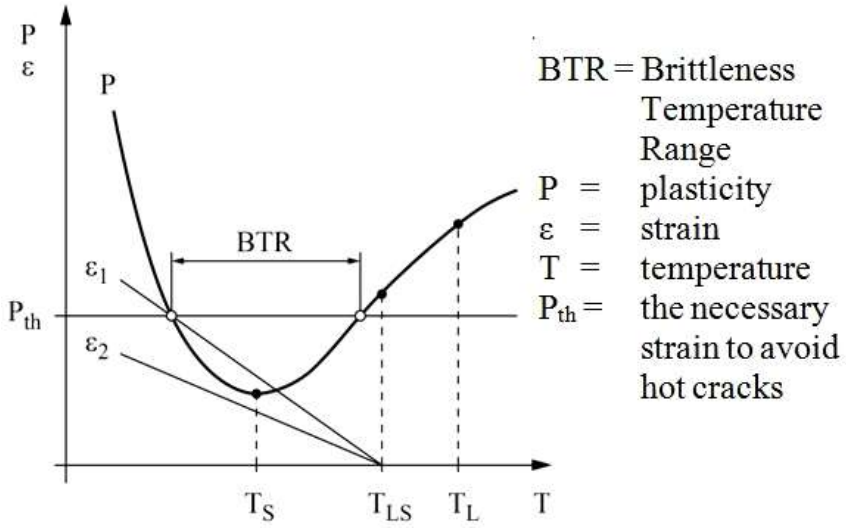

Fig. 1. Strain theory.

Objectives of the research work. Due to the development in material science, there are more and more high strength alloys, the application of which extends rapidly. High strength aluminium alloys have particularly great importance in automotive industry, since beside improved strength and toughness not only are they easier to be formed, they are significantly lighter than alloyed steels. The combination of these properties is beneficial not only for the manufacturers, but can result in savings during operation for the consumers.

However, the group of these alloys faces engineers with significant challenges regarding the development of suitable manufacturing processes, since aluminium has numerous properties those make processing more difficult. The goal of this research is to unfold aforementioned problems during welding, and to provide basic data for designers through the material research explained hereinafter. Therefore physical simulations and various fatigue tests have to be performed:

- nil strength temperature (NST) determination,
- fatigue crack growth (FCG) tests,
- and high cycle fatigue (HCF) tests.

More tests were needed to quantify the hot crack sensitivity, and to refine the basic design data:

- hot ductility tests: on heating, on cooling both,
- more fatigue tests (FCG and HCF) on welded joints made by different technologies.

Examinations

Nil strength tests. The aim of this test is to determine that temperature at which on the grain boundaries are segregating without any tensile load. The NST test helps to quantify the liquation and solidification cracking or even hot cracking [5]. The test can be performed on the Gleeble 3500 thermo-mechanical simulator, which is able to accomplish *10000 °C/sec* heating/cooling rate, displacement rate as fast as *1000 mm/sec*, *100 mm* displacement and can also provide *100 kN* static load (in tension and in compression) [6]. The test requires specific specimen, which has a diameter of *6 mm* and is *80 mm* long.

The examination constituted of the following steps:

- preparative steps: preparing an appropriate specimen (*Ø6x80mm*), bonding the thermo elements one by one to the specimen on the centre using resistance welding, affix the thermocouple with cement fondue in case of aluminium specimens;
- the starting steps of the test program: loading the specimen with a moderate tensile load to eliminate the possible compressive stresses arising in the material and baking the cement fondue, establishing vacuum atmosphere in the test cell;
- main test process: heating till rupture.

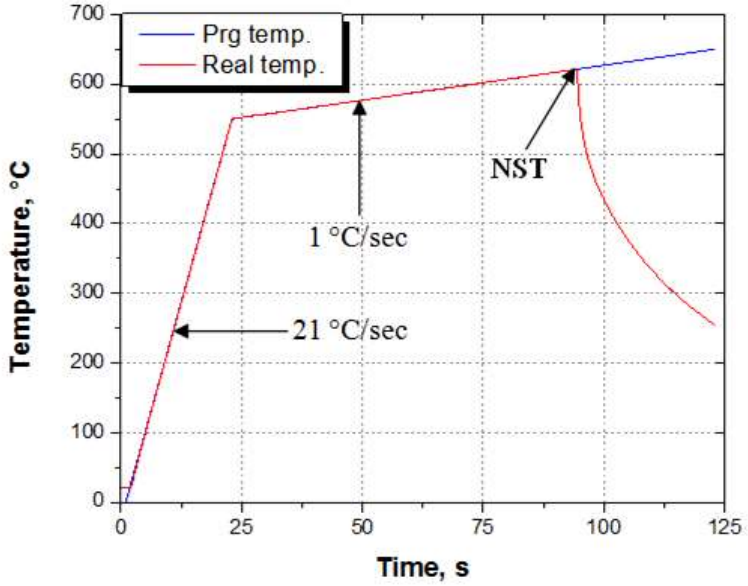

Fig. 2. The record of 6-BM-NST-12 specimen.

Specimen ID	NST [°C]
6-BM-NST-01	612
6-BM-NST-02	627
6-BM-NST-03	623
6-BM-NST-04	621
6-BM-NST-05	605
6-BM-NST-07	608
6-BM-NST-08	612
6-BM-NST-10	623
6-BM-NST-11	616
6-BM-NST-12	617
Average	**616,6**
Standard deviation	**7,15**
Coefficient of standard deviation	**1,16 %**

Table 3. Test results.

During the main process, at first the heating starts with high heating rate, but near to the probable nil strength temperature, the heating rate decreases to allow the determination of the correct NST. Fig. 2 shows one test data as an example, and Table 3 summarizes the test results of all the specimens.

Fatigue crack growth tests. Fig. 3 shows the specimen geometry for the FCG examination. The examinations were performed with tensile stress, $R = 0,1$ stress ratio, sinusoidal loading wave form, the loading frequency was $f = 20$ *Hz* at the two-thirds of crack growth, and it was $f = 5$ *Hz* at the last third. The propagating crack length was registered with compliance method, at room temperature and on laboratory air, using MTS type electro-hydraulic testing equipment.

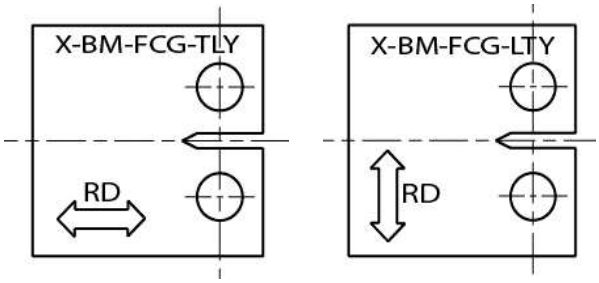

Fig. 3. Specimen geometry for FCG tests.

Seven point incremental polynomial method was used to evaluate the fatigue crack growth data, constants (C and n) of the Paris-Erdogan relationship [7] were calculated. Fig. 4 shows the kinetic diagrams based on the results of the FCG examinations, which were performed on the 6082-T6 base material. The Paris-Erdogan constants determined from the kinetic diagrams and the correlation indexes are shown in Table 4.

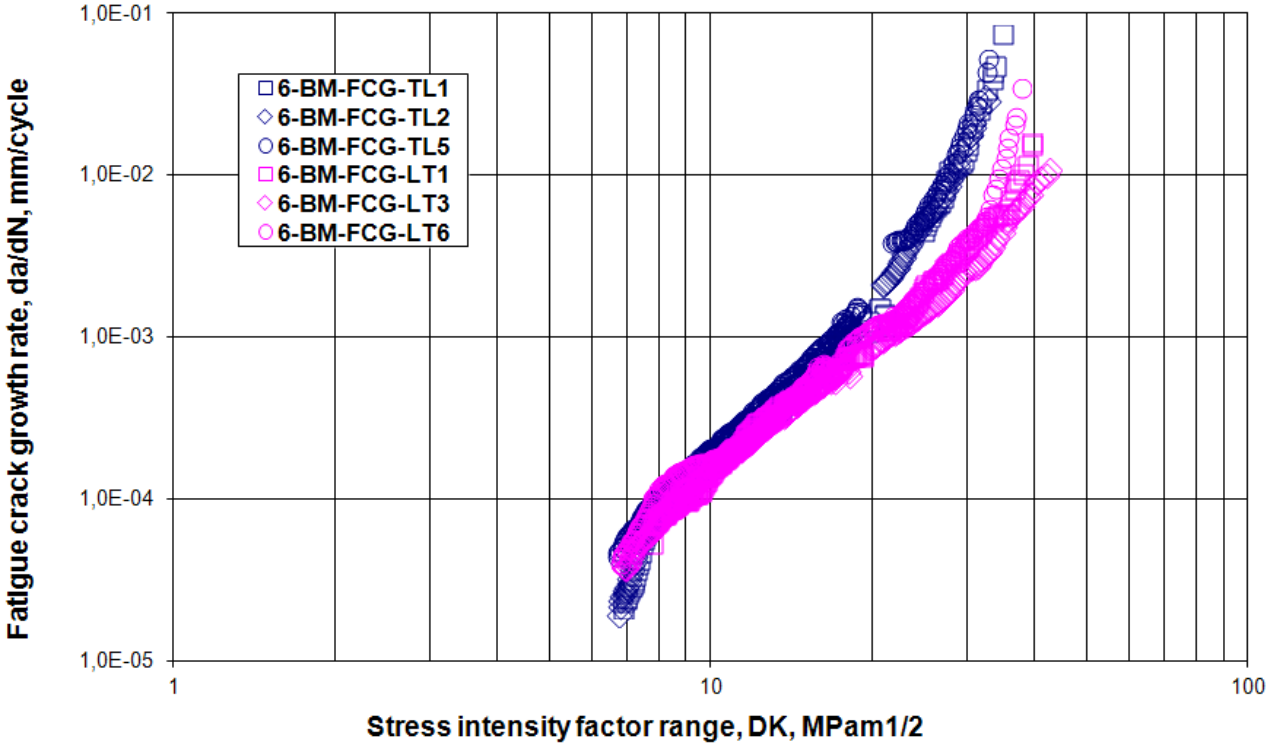

Fig. 4. FCG test results on the 6082-T6 base material.

Table 4. The Paris-Erdogan constants (C and n) and the correlation indexes.

Specimen ID	*C*	*n*	Correlation index
	[MPam1/2 and mm/cycle]		
6-BM-FCG-TL1	1,522E-07	3,011	0,9991
6-BM-FCG-TL2	9,022E-08	3,287	0,9966
6-BM-FCG-TL5	1,013E-07	3,298	0,9941
6-BM-FCG-LT1	1,913E-07	2,875	0,9979
6-BM-FCG-LT3	3,312E-07	2,629	0,9981
6-BM-FCG-LT6	3,738E-07	2,676	0,9952

High cycle fatigue test. Flat specimen geometry was applied for HCF tests (Fig. 5), the specimens were cut out from the FSW joints. The substance of FSW is that as a result of the friction generated heat the base materials along the weld path will be transformed into a plastic state without melting [8]. The FSW joints were made with a special designed tool on a conventional milling machine. The welding parameters were the following: rotation v_r=*400 rpm,* welding rate v_w=*100 mm/min,* dip shoulder diameter *16 mm,* dip angle *2°* [9].
HCF tests were executed under the same circumstances as FCG tests (*R = 0,1* stress ratio, sinusoidal loading wave form, room temperature, laboratory air, MTS type electro-hydraulic testing equipment). The loading frequency was different, it was *f = 30 Hz* during the whole examination.

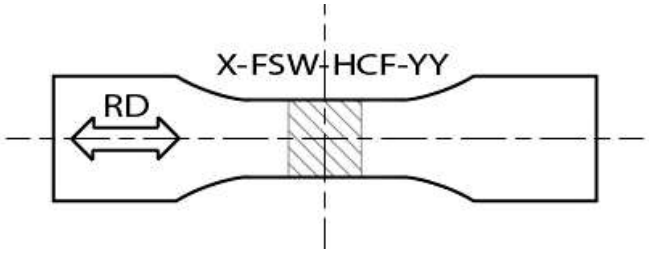

Fig. 5. HCF test required specimen geometry, welded part at the centre.

Staircase method [10] was applied to evaluate the HCF results, the S-N curve - based on the measured data - and the comparative test results (measured data without S-N curve) are shown in Fig. 6.

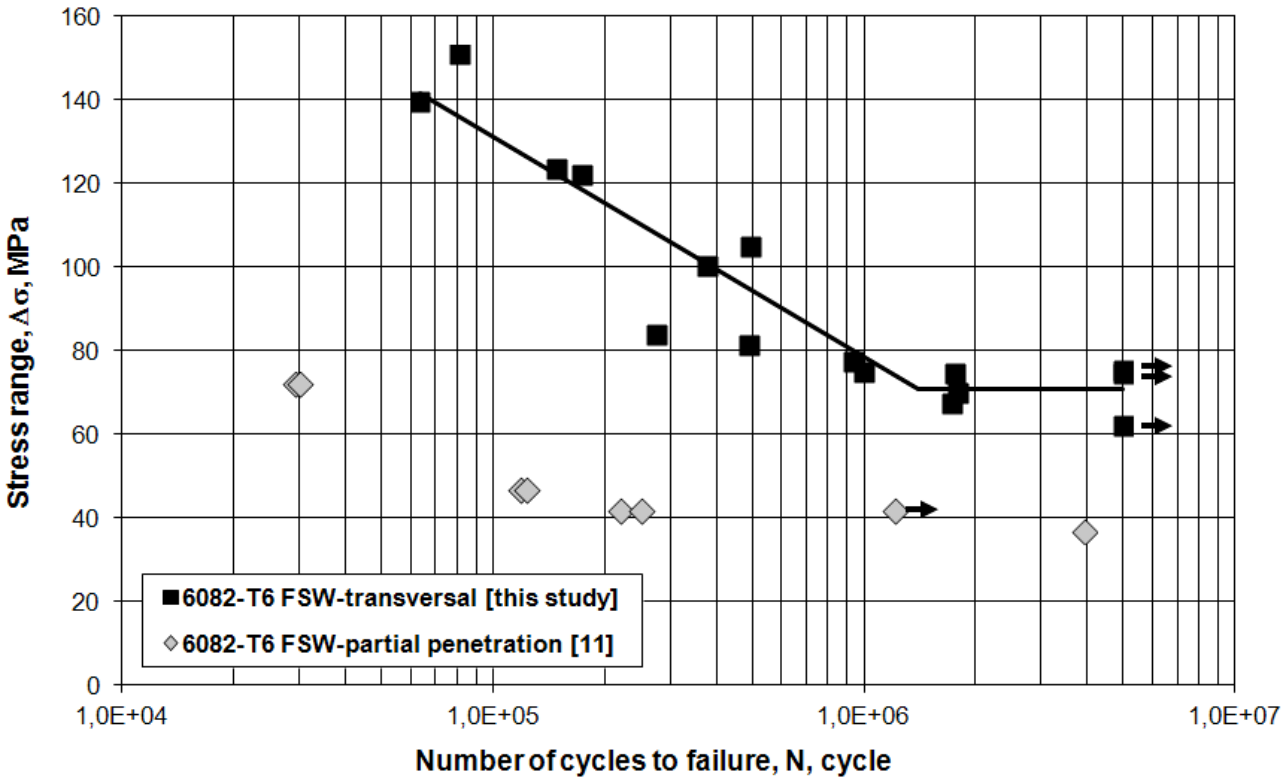

Fig. 6. HCF test results on the FSW joints.

Summary

High strength steel and aluminium alloys play a dominant role in nowadays applications. Although a significant percentage of the alloys used in automotive industry were iron based until today, in recent years the usage of aluminium increased. This can be observed in key branches of the industry such as the automotive industry. In favour of aluminium usage based on its good corrosion resistance, good conductivity, and the high strength that characterizes modern alloys. The significant weight advantage to be gained by using aluminium alloys is an important aspect not only

during the manufacturing process, but it has advantages for the consumers as well (For example, in the automotive industry weight loss result fuel saving.) However, this „new" group of materials faces engineers with great challenges in the aspects of design, manufacture and operation.
The objectives of the research as a consequence are complex. On one hand, the development of welding technologies suitable to make welded joints with adequate and aggregate properties.. On other hand cyclic stress resistance has to be determined as the emphasized property.
Based on the results of our first examinations, the following conclusions can be drawn.

- It can be determined from the nil strength temperature (NST) tests performed on the base material, and the NST of the 6082-T6 aluminium alloy is *617°C*.
- The fatigue crack growth (FCG) resistance of the material is significantly different in T-L and L-T orientations.
- The high cycle fatigue (HFC) resistance of the joints made by friction stir welding can be considered appropriate.
- In order to determine the hot crack sensitivity of the material, further hot tension tests are necessary; furthermore the selection of proper welding technologies is also subject to further comparative studies with welded joints made by other technologies.

Acknowledgements

The research work presented in this paper was carried out as part of the TÁMOP-4.2.2/A-11/1-KONV-2012-0029 project in the framework of the New Hungarian Development Plan. The realization of this project is supported by the European Union, and co-financed by the European Social Fund.

References

[1] Aluminium: http://www.hydro.com/

[2] Aluminium: http://www.world-aluminium.org

[3] M. Wihsbeck, Welding aluminium wagon body parts of the high-speed trains with robots, Hegesztéstechnika 4/2013. XXIV, 57-59. (In Hungarian.)

[4] C. Kammer, Aluminium handbook, 1st edition, ASTM Intl, 1999.

[5] L. Kuzsella, J. Lukács and K. Szűcs, Physical simulation tests on S960QL HSLA steel, Gép 11/2012. LWIII, 37-42. (In Hungarian.)

[6] Attributes of Gleeble 3500: http://gleeble.com/index.php/products/gleeble-3500

[7] P. Paris and F. Erdogan, A critical analysis of crack propagation laws, Journal of Basic Engineering, Transactions of the ASME (1963) 528-534.

[8] Friction Stir Welding: http://www.twi.co.uk/technologies/welding-coating-and-material-processing/friction-stir-welding/

[9] Á. Meilinger and I. Török, Influence of technological parameters at friction stir welding, Gép 11/2012. LWIII, 29-32. (In Hungarian.)

[10] H. Nakazawa and S. Kodama, Statistical S-N testing method with 14 specimens: JSME standard method for determination of S-N curves, in: T. Tanaka, S. Nishijima, M. Ichukawa (Eds.), Statistical Research on Fatigue and Fracture. Current Japanese Materials Research, Vol. 2. Elsevier Applied Science, London-New York, 1987. pp. 59-69.

[11] M. Ericsson, Fatigue strength of friction stir welded joints in aluminium. Doctoral Thesis. Department of Materials Science and Engineering, Royal Institute of Technology, Stockholm, 2005.

Observed phenomena during the development of an adhesion test for coated medical devices

Torda László SÉLLEY[1,a], Anna KERTÉSZ[1], Eszter BOGNÁR[1,2]

[1]Department of Materials Science and Engineering, Faculty of Mechanical Engineering, Budapest University of Technology and Economics, Bertalan Lajos utca 7, 1111 Budapest, Hungary

[2]MTA–BME Research Group for Composite Science and Technology, Műegyetem rkp. 3, 1111 Budapest, Hungary

[a]selley.torda@gmail.com

Keywords: adhesion, biocompatible polymer, biocompatible metal, coating, PUR, PLGA, stainless steel

Abstract

Devices used in the field of medical technology require high biocompatibility. Medical devices that are made from stainless steel have good biocompatible properties, but polymer coatings can radically improve it. One of the most important quality of the coating is adhesion, and this was our rationale for developing a polymer adhesion testing protocol. In our research, two biocompatible polymers were compared, polyurethane (PUR) and poly-(DL-lactic-co-glycolic acid) (PDLG). Surface-treated stainless steel sheets were used as carrier for polymer layers. The adhesive properties of different layers were compared. Adhesion of the coatings was characterised by concentration of coating solution and surface roughness of the carriers, and some phenomena were observed.

Introduction

In the field of medical technology coatings are widely applied. Implants, surgical instruments and other medical devices can be provided with coatings [1]. Coatings and especially the polymer coatings can improve some surface properties such as biocompatibility [2]. Polymer coatings generally improve the bio – and haemocompatibility, as well as the coated material's corrosion-resistance. Polymer coatings other advantage is that they are also able to store and release active agents such as drugs. Another important property is the carrier-coating interaction, the adhesion. The coatings we applied are thin films with a micro-meter scale thickness [3]. There is a wide variety of existing adhesion measurements, like bending, capitation, impact test, etc [4,5]. Scratch tests and AFM for adhesion testing are used for measuring thin layer/carrier interaction like polymer coatings [5,6,7]. Some of these tests are not appropriate for our coating, and some of them like scratch tests are impractical and slow, especially if we want to examine layers we are developing ourselves. In this paper we test the adhesion of two kinds of polymers using a method we developed [8]. We show the phenomena which was observed during the development of the adhesion test. For a carrier we chose stainless steel, a commonly used raw material in biomedical devices. Stainless steel type 304 is used where high corrosion resistance, good formability, strength, manufacturing precision, reliability and hygiene are of particular importance [9].

The first polymer we tested as a coating was PUR. PUR is increasingly used as a coating in medical devices. Polyurethanes offer very high flexibility, high strength and proven impact resistance [10].

The other polymer we tested was PDLG. It has been successful as a biodegradable polymer because it undergoes hydrolysis in the body to produce the original monomers, lactic acid and glycolic acid. These two monomers are easily broken down in the body without toxic effects, so this polymer is also biocompatible [11,12].

Dip-coating were applied to create the layers. This is one of the commonest and easiest techniques for producing a continuous layer [13]. We created a polymer layer on a surface-treated 304 type

stainless steel carrier and compared the properties of different coatings. Adhesion of the coatings were characterised by concentration of coating solution and carrier surface roughness.

Methods

Carrier sheets. During our examinations 0.3×10×50 mm 304 type stainless steel sheets were used as coating carriers. Sheets were prepared by laser cutter type LASAG KLS 246-FC with Nd:YAG laser source. Sheets were surface-treated to improve and set to the proper value their surface properties.

Surface treatment. Laser cutting causes burr and damages the surface so first the sheets were etched to remove the unwanted inherent. Hydrochloric acid (36 wt %), nitric acid (65 wt %) and water in a 3:1:9 mixture was used as an etching solution. Sheets were etched in the mixture for 60 minutes in an ultrasonic cleaning vat. After etching sheets were electropolished in order to improve surface properties and to reduce roughness. Phosphoric acid (85 wt %) sulphuric acid (98 wt %) and water in a 3:6:1 mixture with 20 g/L glycerol was used as the electrolyte. For electropolishing we applied 0.01 A/mm^2 current density at room temperature (~25 °C) for 180, 210, and 240 seconds.

Surface roughness. The surface roughness of the surface-treated stainless steel sheets were measured. Based on preliminary tests we aimed to observe the connection of surface roughness to adhesion in both kinds of polymer. A Talysurf CLI 2000 scanning-topography measurement instrument was used to determine the surface-treated sheets' surface roughness. Needle speed was 50 μm / second, geometry of the needle was 90°. A 4 to 4.75 mm area was examined on every 3-3 sample.

Applied polymers. During our experiments we used two types of biocompatible polymers. The applied PUR composition was methylene diphenyl 2, 4'-diisocyanate (MDI), methylene diphenyl 4, 4'-diisocyanate butanediol, polytetrahydrofuran [14]. It is a non–biodegradable polymer, T_g = 40 ° C.

We applied PURAC PURASORB PDLG 5010 DL-lactic acid / glycolic acid 50:50 copolymer (PDLG). It is a biocompatible and biodegradable polymer, ρ = 1.24 kg/L density, IV = 1.04 dL/g inherent viscosity, MW = 104 kDa molecular weight, T_g = 42 °C.

Creating the coating. 1, 2, and 3 wt% concentration solutions were made from the polymers. PDLG was dissolved in acetone, and PUR was dissolved in tetrahydrofuran. Stainless steel sheets were put into the solutions for 3 seconds then they were removed from the solutions at a speed of 5 mm per second. We created one-layer coatings at room temperature.

Adhesion test. Each freshly coated sample was stacked to overlap part of another same-size steel sheet. Pairs of parallel sheets in flat-face contact were left to dry for one day in a constant air steam. Stuck-together samples were then pulled in opposite directions within the carrier-sheet plane (Fig. 1). The contact area was 100 mm^2.

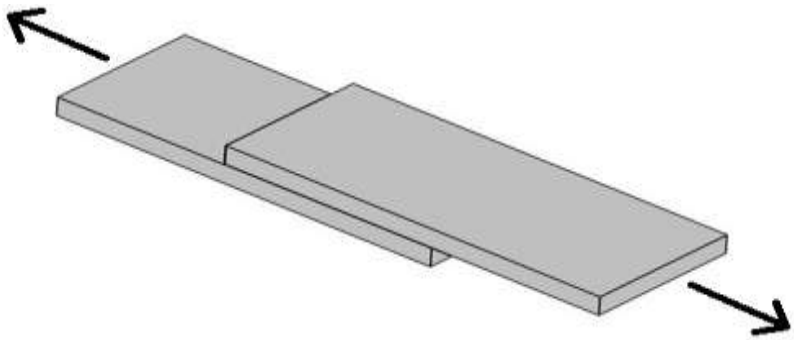

Fig. 1. Schematic figure of each two-sheet sample as left to dry. Same-size surface-treated steel sheets were flat-face stacked like this after coating. In later tests we pulled the sheets in the two directions shown here by arrows

During the separation by sliding, force (N) was measured as a function of displacement (mm). Motion was set at 4 mm per minute in every case. From the maximum values we got from experiments we deduced the relationship between the coating and the stainless steel sheet carrier. An Instron type 5965 tensile machine was used.

Results

We measured the surface roughness of the carriers, and the adhesion of polymer coatings from different solutions on various surface-treated carriers.

Surface roughness. Sheet surface texture was compared to time of electropolishing. No other parameters varied. Average surface roughness (R_a) reduced with increased electropolishing time. Higher roughness peaks are broken down by this surface treatment. Rough surfaces can adhere better. Table 1 shows average surface roughness (R_a).

Electropolishing time (sec)	180	210	240
R_a (μm)	0.106 ± 0.033	0.091 ± 0.008	0.089 ± 0.031

Table 1. Treated stainless steel sheets' surface roughness. More time spent electropolishing gave a smoother surface

Adhesion of coating. All the coating types were tested three times with this method. Fig. 2 shows a typical tensile diagram similar to that for other samples. From these kinds of diagrams we took the maximums. Averages of each three measurement were counted. Averages were divided the appropriate contacted areas. Adhesion was characterized with a unified comparable unit (N/mm^2).

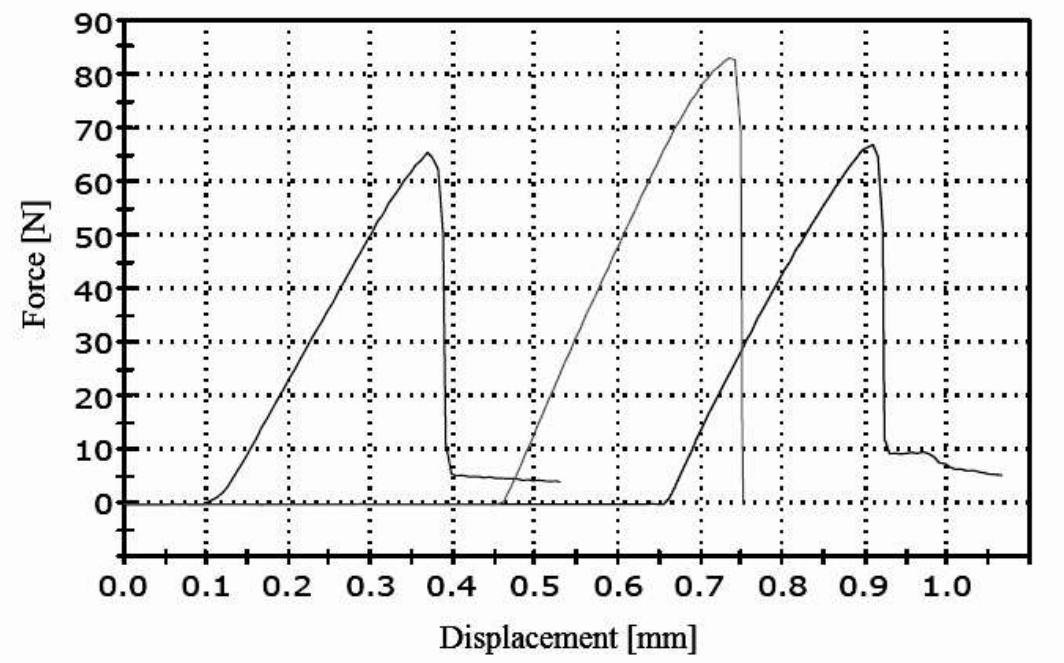

Fig. 2. One sample's three adhesion test

Based on our previous experiments, we expected adhesion to worsen with increased electropolishing time. This statement was true in one case, the 1 wt% PDLG solution coatings (Fig. 3). So in coatings made from less polymer the determining factor is steel-sheet surface roughness after electropolishing and before polymer coating. Higher average roughness provides better adhesion.

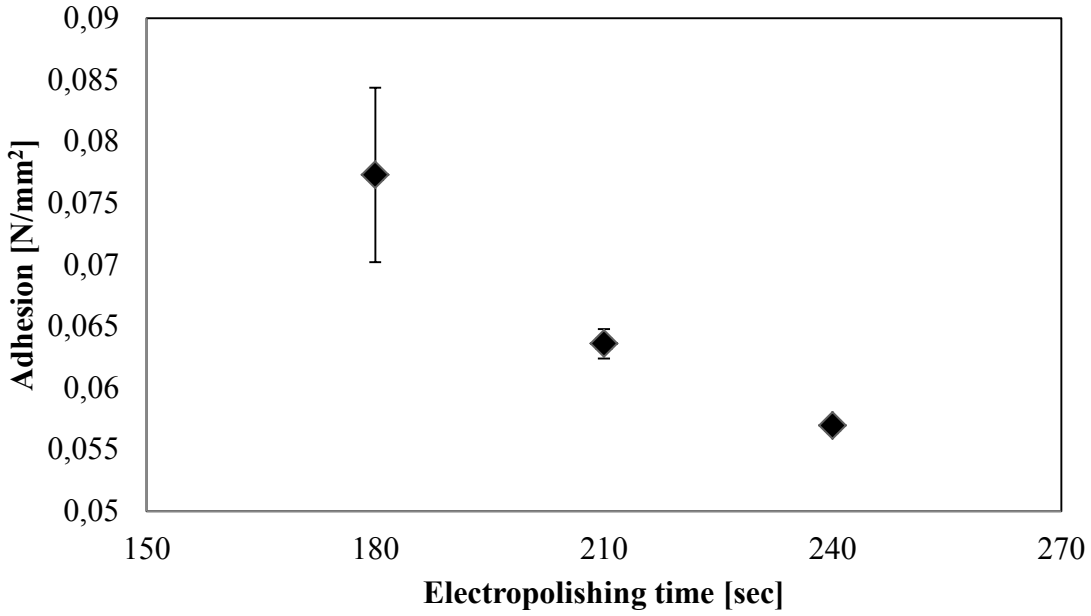

Fig. 3. Adhesion test results for the coating made from 1 wt% PDLG, area in contact 100 mm^2. The smoother surface created by electropolishing caused weaker adhesion

In case of higher polymer solution the carriers surface does not affect the adhesion as we can see on Fig. 4. In our test the key factor is the polymer solution concentration and the coating material. Increasing polymer solution concentrations increased adhesion. With more continuous coating polymer-metal interaction become stronger. It can be observed in both polymers, PDLG and PUR. Fig. 4 shows that under the same conditions, PUR has better adhesion than PDLG.

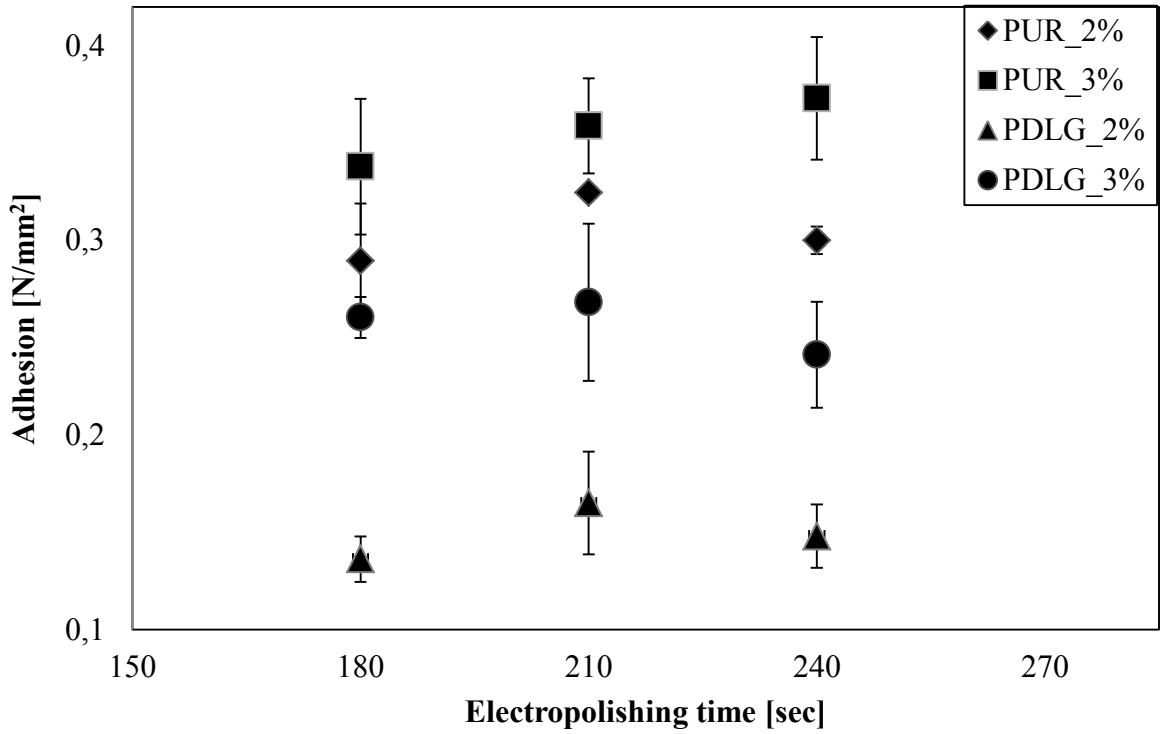

Fig. 4. Comparing PUR and PDLG coating adhesion to electropolishing time. Contact area was 100 mm^2, PUR had better adhesion than PDLG

Conclusion

The developed systematic method to examine coating layers' strength of adhesion is appropriate for our research. We can use it to classify and compare future coatings.
During our experiments we observed the carrier-coating interaction in particular the carrier's surface, the polymer solution concentration and the coating material.
Furthermore we conclude that from the two studied polymers, the PUR has better adhesion in all circumstances on surface-treated stainless steel 304 type carrier.

References

[1] H.F. Hildebrand, N. Blanchemain et al, Surface coatings for biological activation and functionalization of medical devices, Surface and Coatings Technology. EMRS 2005 Symposium K — Protective Coatings and Thin Films: 2005 May 31 – June 3: Strasbourg(FR) (2006) 200 (22–23) 6318–6324.

[2] G. Mani, M. D. Feldman, et al, Coronary stents: A materials perspective, Biomaterials 28 (2007) 1689-1710.

[3] H. W. Fang, K. Y. Li, et al, Dip coating assisted polylactic acid deposition on steel surface: Film thickness affected by drag force and gravity, Material Letters (2008) 62 (21-22) 3739-3741.

[4] H. Ollendorf, D. Schneider, A comparative study of adhesion test methods for hard coatings, Surface and Coatings Technology (1999) 113 (1-2) 86-102.

[5] M. El-Shabasí, Perspective of adhesion of thin films, Electrical Engineering and Computer Science, (1981) 25-2 123-134.

[6] E. V. Cortés, M. A. Lorenzo, et al, Adhesion Testing of Epoxy Coating, Texas Department of Transportation, 1998 Sept.

[7] C. S. Litteken, R. H. Dauskardt, Adhesion of polymer thin-films and patterned lines, International Journal of Fracture (2003) 119/120 475-485.

[8] T. L. Sélley, A. Terdik, E. Bognár, Biológiailag lebomló polimerbevonatok tapadásának vizsgálata (Investigation of biodegradable polymer coatings' adhesion test), Fiatal Műszakiak Tudományos Ülésszaka XVIII 2013 March 21–22 Kolozsvár (RO).

[9] T. Newson, Stainless Steel – A Family of Medical Device Materials, Business Briefing: Medical Device Manufacturing & Technology (2002) London (UK).

[10] R. W. Smith, New Developments and Trends in Medical-grade Adhesives, Medical Device Manufacturing & Technology (2004) London (UK).

[11] Y. Onuki, U. Bhardwaj, M. P. F. Papadimitrakopoulos, D. J. Burgess, A Review of the Biocompatibility of Implantable Devices: Current Challenges to Overcome Foreign Body Response, J Diabetes Sci Technol. (2008) November 2 (6) 1003–1015.

[12] J. M. Anderson, M. S. Shive, Biodegradation and biocompatibility of PLA and PLGA microspheres, Advanced Drug Delivery Reviews (1997) 28 5–24.

[13] A. Raval, A. Choubey, H. Kotadia, et al, Novel Biodegradable Polymeric Matrix Coated Cardiovascular Stent For Controlled Drug Delivery, Trends Biomater. Artif. Organs (2007) 2 101-110.

[14] D. Fejős, P. Sütő, K. Molnár, B. Pukánszky, PU/PBT keverékek vizsgálata esetleges orvosi alkalmazásra, (Examination of PU / PBT blends for possible medical applications), Műanyag és Gumi (2011) 48 (12) 446-449.

Acknowledgements

This work is connected to the scientific programme of the "Development of quality-oriented and harmonized R+D+I strategy and functional model at BME" project. This project is supported by the New Hungary Development Plan (Project ID: TÁMOP-4.2.1/B-09/1/KMR-2010-0002).
The work reported in the paper has been developed in the framework of the project „Talent care and cultivation in the scientific workshops of BME" project. This project is supported by the grant TÁMOP-4.2.2.B-10/1--2010-0009.
Many thanks go to Esther Kooijman at PURAC, who provided the PDLG and Kinga Molnár, who provided the PUR we used.

Investigation of typical bonding faults of plated Al sheets developed during rolling

Gábor Szabó [a], Valéria Mertinger [b]

Institute of Physical Metallurgy, Metal Forming & Nanotechnology, University of Miskolc, H-3515, Egyetemváros, Miskolc, Hungary

[a]szabogabor@uni-miskolc.hu (corresponding author), [b]femvali@uni-miskolc.hu

Keywords: sandwich sheet rolling, aluminum-plating technology, rolling, hot rolling, welding by rolling, pressure welding, plated by rolling, plating with mechanical press, bonding fault, bond development, AlMn1Si0.8, AlSi10, experimental duo mill.

Abstract. In this study the typical bonding faults of three layer-plated aluminum sheets are investigated. The bonding was performed between AlMn1Si0.8 and AlSi10 alloys using hot rolling (a VON ROLL experimental duo mill). The experimental temperatures were 460, 480 and 500 °C. T-peel test provided a good description about the quality of bonding. Structure analysis was also performed by light microscopy to detect typical bonding faults. The aim of this investigation is to produce some typical bonding faults and find the cause of formation. The influence of the rolling temperature and surface roughness on the bonding was also analyzed. Rolling schedule and the role of first pass on the development of perfect bonding were experimentally determined.

Introduction

Aluminum plating technology is used worldwide, not only in the automotive industry but also in household items. The essence of the technology is that a layer with a certain property is plated with another layer with different properties. The understanding of the bond development is highly important, because these sheets have high added value. In previous studies it was determined that plating technology by rolling can weld sheets that normally cannot be welded by means of conventional technologies. Roll welding is a type of pressure welding, where bond develops through plastic deformation [1-6]. The goodness of bond development depends on the deformations. Bonding does not occur until the deformation reaches a threshold value [1-3, 6]. Once deformation reaches a threshold value, the goodness of bonding dynamically increases until it attains the basic material tensile strength [1-2, 6-7]. This threshold value varies from material to material [1-2, 4]. Bond development is influenced by surface roughness and surface preparations [1-2, 4-5, 8]. In a previous study a numerical value of bonding goodness was investigated [9]. The aim of our study is to illustrate several bonding faults and to analyze the influence of surface roughness, surface preparations, rolling temperature and deformation rates. T-peel test can provide numerical values about bonding goodness. This fact was mentioned in a previous study [9].

Experimental procedure

Several sandwich sheets of three layers were produced. The core alloy was AlMn1Si0.8 and the liner alloy was AlSi10 on both sides, performed on a VON ROLL experimental duo mill in the Institute of Physical Metallurgy, Metal Forming and Nanotechnology at the University of Miskolc. The sandwich structures were assembled in a symmetric fashion. The thickness of the liners amounted to 10 percent that of the core alloy on both sides. Table 1 lists the geometrical parameters of the liners and core alloys.

Type of layers	Length, mm	Width, mm	Thickness, mm
Core	200	50	25.0
Liners	195	50	2.5

Table 1. – Geometrical parameters of sheets

Full rolling experiments and one pass rolling experiments were performed. Table 2 presents the full rolling schedule and parameters. In the first 7 passes of rolling small deformation occurred, at a rolling speed of 5 m/sec. These parameters were chosen to have an optimum bond development performance. During further rolling, rolling speed and deformation per pass were increased. In a previous study the cause of bond development was tested. If the bond development does not occur in the first few passes nor will it during further rolling.

Pass	Inbound sheet height (meas.), mm	Reduction, mm	Rolling speed, m/min	Sheet temp. after pass, °C	Outbound sheet height (calc.), mm	Reheating time, min
1	30.0	0.4	5.2	480	29.6	15
2	29.7	0.4	5.2	475	29.3	15
3	29.3	0.4	5.2	472	28.9	15
4	28.9	0.4	5.2	470	28.5	10
5	28.5	0.4	5.2	465	28.1	8
6	28.2	0.5	5.2	-	27.7	-
7	27.8	0.5	7.5	438	27.3	8
8	27.4	0.6	7.5	-	26.8	-
9	26.9	0.8	7.5	434	26.1	7
10	26.2	1	11.2	-	25.2	-
11	25.3	1	11.2	416	24.3	6
12	24.4	1	11.2	-	23.4	-
13	23.5	1	11.2	398	22.0	6
14	22.1	1.5	11.2	-	20.6	-
15	20.7	1.5	11.2	388	19.3	6
16	19.3	1.5	11.2	-	17.8	-
17	17.9	1.5	11.2	354	16.4	6
18	16.5	1.5	11.2	-	15	-
19	15	1.5	11.2	331	13.5	-
20	13.6	1.5	11.2	-	12.1	-
21	12.2	1.5	11.2	-	10.7	-
22	10.7	1.5	11.2	-	9.2	-
23	9.2	1.5	11.2	-	8.2	-
24	8.2	1	11.2	-	7.2	-
25	7.2	1	11.2	-	6.2	-

Table 2. – Rolling schedule and parameters of full rolling experiments

The plated sheet rolling experiments were performed at three different temperatures, namely 460, 480 and 500 °C. The furnace temperature was set 20 °C higher than the experimental temperatures. Until the 5th pass the sandwich structures were reheated after each pass. After the 6thpass, reheating was carried out after every 2 passes.

Surface quality effect was also tested during single pass (first pass) rolling experiments. Surface roughness of the contacting layers in the sandwich was increased by wire brush in some cases and cleanness of surface was modified by removing the grease. The parameters of rolling were identical. Another single pass experiment series were performed to investigate the bond development in the first pass. The degree of reduction was modified in the pass while the rolling speed and the

temperature were identical, 5 m/min and 500 °C respectively. The individual strains of the three layers (upper, lower side liner and core) in the longitudinal direction were measured and compared.

Fig.1. VON ROLL experimental duo mill during plated sheet rolling

Results and conclusions

Three series of experiments were performed to investigate the reproducibility of the tests, and 5 samples were tested in each case to produce an average value. To validate the quality of bonding a "probability bonding confirmation" value was introduced. If the bonding was perfect the value rich 100%, otherwise it is 0 %. If partial bonding was built the value vas calculated on based of T-peel test. If the measured load during the T-peel test constantly reached the threshold value (necessary load to tear of the perfect bond), the probability of bond development was 100. If this load only partly reached the threshold value, the probability was calculated between 0 and 100. These values were then added up. This amount was divided by the value of maximal probability of bond development.

Fig. 2 shows that the probability of bond development, was calculated from T-peel load strongly depends on the temperature. Fig. 3 illustrates the effect of surface quality on the bond development in function of temperature. The presence of lubricant contaminant (grease) always has bad effect on bonding while effect of surface roughness shows an opposite action. The temperature is higher the roughness effect is stronger. It suggests increasing the rolling temperature, but the diffusion developed between some layers, caused by temperature increase, has a drawback on the final product as the disappearing interface caused by diffusion of layers leads to the increase in the corrosion potential. Keeping this fact in mind, the temperature of plated sheet rolling was not higher than 500 °C. So to determine the optimal rolling temperature is very important to rich the best situation for bonding and keep the perfect value of the final product behavior.

Fig .4-Fig. 5 show the optical microscope images about the surface of layers after the T-peel test. Typical bonding faults are observed. Fig. 4.a shows a core layer with roughened surface, after the liners were removed. Partly bonded layer is visible; at the imperfect bounded parts the toolmarks are remained. The rolling temperature was 460 °C. The formations of these faults can be minimized by raising rolling temperature. Fig. 4.b shows the same core layer after performing the rolling at a temperature of 500 °C. It is clearly visible that the toolmarks have disappeared. Fig. 5 shows the liner layer. The bright parts indicate the perfect bonding while the dark parts show the free surface with oxide layers.

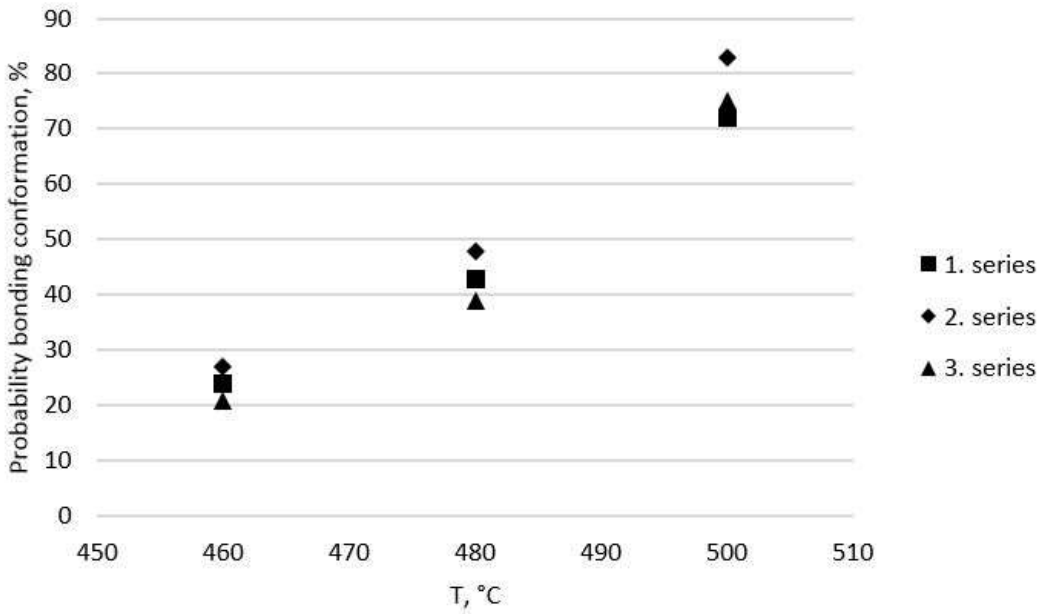

Fig. 2. Probability of bond development vs. rolling temperature

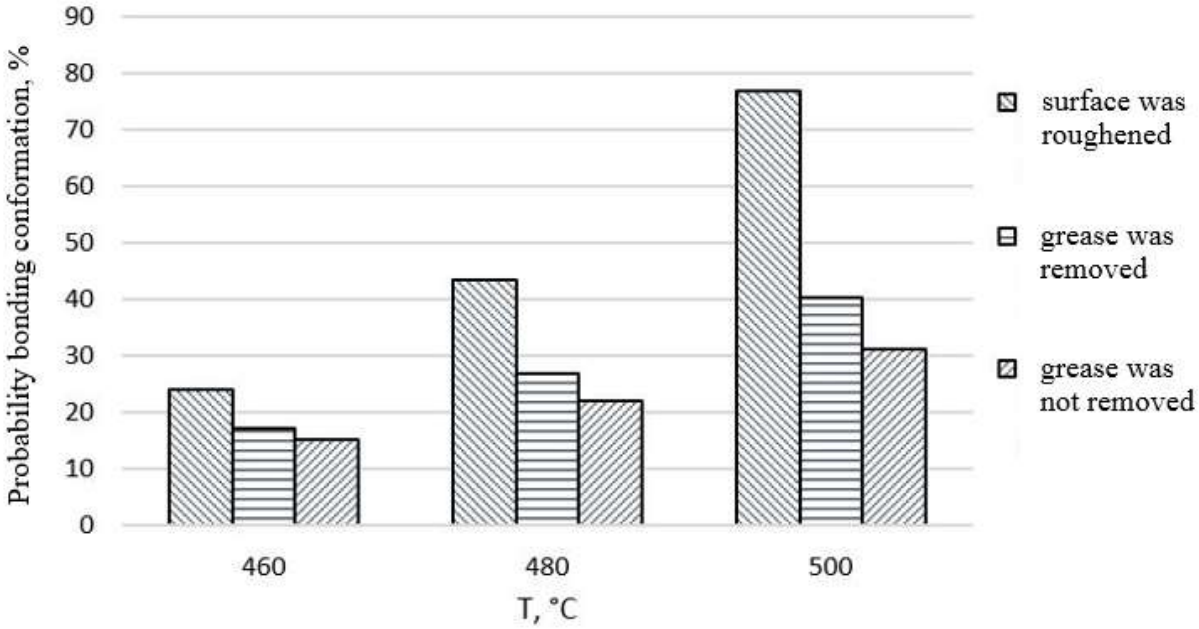

Fig. 3. Probability of bond development vs. surface quality and rolling temperature

It can be established that the most typical bonding faults are generated by improper rolling temperature. Improperly roughened and prepared surface also cause faults. The probability of bond development decreases if the initial surface is smooth.

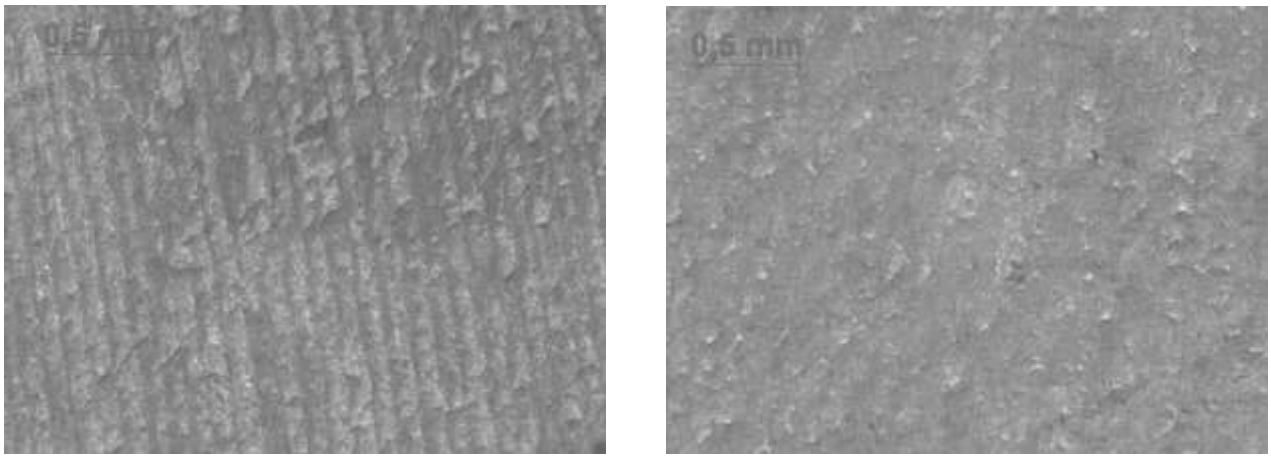

a. partly bonded b. bonded

Fig.4. Surface of core layer after T-peel test (a. T=460 °C; b. T=500 °C)

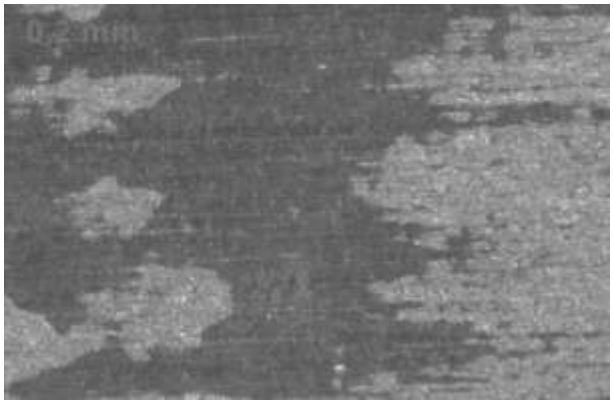

Fig. 5. Surface of liner layer after T-peel test

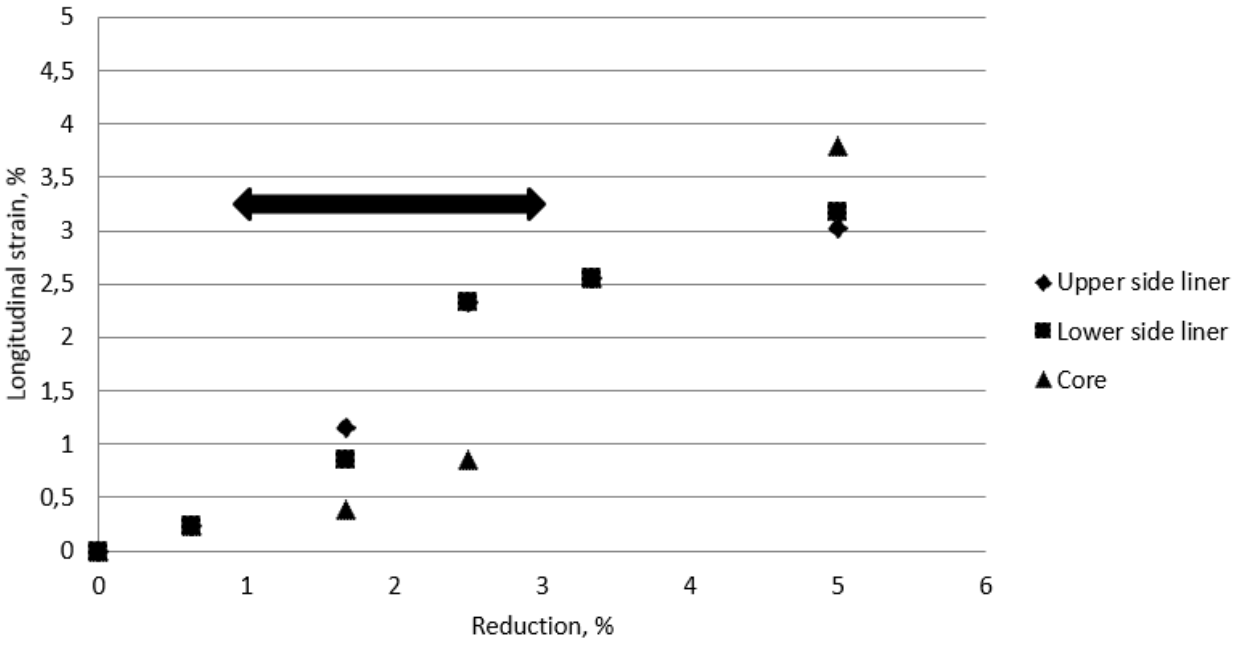

Fig. 6 – Longitudinal strain of layers in function of reduction in the first pass

Fig. 6 shows the individual longitudinal deformation of core and liners layers in function of reduction after single pass rolling. It is clear that the individual strains of the different layers are different if the degree of reduction is increased in the first pass. If the longitudinal deformation of liner layer is larger than that of the core layer, the probability of bond development is the highest.

Once the bond development is complete the longitudinal deformation of layers is the same. The black arrow shows the ideal interval of reduction which guarantees the perfect bonding in these geometrical dimensions. If the reduction was smaller the bonding could not develop. If the reduction is exceeded the ideal value the bonding formed but it was ripped in the subsequent pass of rolling.
The rolling schedule should be created by considering these results. In the first passes the longitudinal deformation of liners needs to be longer than that of the core layer. After the bond development is complete, the longitudinal deformations of core and liner layers need to be identical. Only after these steps are performed, the reduction can dynamically increase.

Summary

In this study the typical bonding faults of plated aluminum sheets made of three layers were investigated. The bonding was performed between AlMn1Si0.8 and AlSi10 alloys using hot rolling. Several bonding faults and possible causes of these faults were illustrated. It was determined that the typical bonding faults are a result of the improper rolling temperature. Additionally, the smooth surface also retards the development of bonding. Rolling schedule, to get perfect bonding and the function of ideal first pass on the development of bonding were experimentally determined.

Acknowledgements

The research work presented in this paper is based on the results achieved within the TÁMOP-4.2.1.B-10/2/KONV-2010-0001 project and carried out as part of the TÁMOP-4.2.2.A-11/1/KONV-2012-0019 project in the framework of the New Széchenyi Plan. The realization of this project is supported by the European Union and co-financed by the European Social Fund.

References

[1] Bay N. Cold welding, Part I, Characteristic, bonding mechanisms, bond strength. Met Construct (1986) 369–372.

[2] Eizadjou M., Danesh Manesh H., Janghorban K., Mechanism of warm and cold roll bonding of aluminum alloy strips, Materials and Design (2009) 4156–4161

[3] Zhang W., Bay N., Cold welding-theoretical modeling of weld formation. Weld J (1997) 417–420.

[4] Wright P. K., Snow D. A., Tay C. K., Interfacial conditions and bond strength in cold pressure welding by rolling. Met Technol (1978) 24–31.

[5] Wu H. Y., Lee S., Wang J. Y., Solid state bonding of iron-base alloy, steel-brass and aluminum alloy. J Mater Process Technol (1998) 173–179.

[6] Danesh Manesh H., Karimi Taheri A., Study of mechanisms of cold roll welding of aluminum alloy to steel strip. J Mater Sci Technol (2004) 1064–1068.

[7] Danesh Manesh H., Karimi Taheri A., An investigation of deformation behavior and bonding strength of bimetal strip during rolling. Mech Mater (2005) 531–542.

[8] Zhang W., Bay N., Cold welding-experimental investigation of the surface preparation methods. Weld J (1997) 326–330.

[9] Szabó G., Mertinger V., Technological investigation of plated aluminium sheets. Materials Science Forum Vol. 729 (2013) pp 482-486.

Investigation of the common modification effect of strontium and antimony on the structure in case of Al-Si alloy

Monika TOKÁR[1,a], György FEGYVERNEKI[1], Valéria MERTINGER[2,b]

[1,2]University of Miskolc, Metallurgical and Foundry Engineering Institute, 3515 Miskolc-Egyetemváros, HUNGARY

[2]University of Miskolc, Physical Metallurgy, Metalforming and Nanotechnology Institute, 3515 Miskolc-Egyetemváros, HUNGARY

[a] monika.tokar@uni-miskolc.hu, [b] femvali@uni-miskolc.hu

Keywords: Silicon modification, Strontium, Antimony, Image analysis

Abstract: In the course of our investigations, AlSi8Cu3 foundry alloy was alloyed in different strontium and antimony concentrations. The mechanical properties of structure developed during the given cooling conditions as well as the effect of strontium and antimony on the modification of eutectic Si were investigated by a computer image analysis and by using a scanning electron microscope. Samples with a wall-thickness of 8 mm cast in the course of the experiment-series were used for our investigations. A part of our long-term research work is described in our present paper.

1. Introduction

The „modification" has a significant improving effect on the strength properties of cast products; during this process, the eutectic Si is refined by adding a foundry alloy into the melt and by this the development of coarse Si-crystals is prevented [1,2]. Since the patent was issued by Aladár Pacz [3] in which the author describes that the morphology of eutectic Si can be modified , more different theories concerning the possible mechanism of action of strontium have been published attracting a lot of research workers' attention. The two most established growth models of eutectic modification from coarse plate-like into fine fibrous Si morphology are i) restricted growth of the''twin plane re-entrant edge'' (TPRE) mechanism based on {111} twinning and involving <112> directions [4] and ii)''impurity induced twinning'' that can be explained by the adsorption of impurity atoms on{111} close packed planes which promotes {111} twinning by displacing a {111} monolayer growth step to an alternative stacking sequence [5,6]. The impurities in the Al-Si foundry alloy have a serious effect on the extent of modification and as a consequence the quality of cast products is significantly influenced by them. The effect of impurities is not well-known in case of the secondary alloys made of scraps used for making cast products in a greater and greater extent. In the course of our investigations, the cross-effect of antimony as an impurity element and of the strontium as a modification element was investigated in case of an AlSi8Cu3 foundry alloy. Cast-product-series with different wall-thickness (6 mm, 8 mm, 12 mm, 25 mm) and with different antimony- and strontium concentrations were cast in laboratory circumstances. In our present paper, the detailed evaluation of cast-product-part with a wall-thickness of 8 mm is described. The planned concentration-ranges were between 5-300 ppm of strontium and 40-340 ppm of antimony. Tensile rods (diameter: 6 mm) were made of the cast sample for the tensile tests. The mechanical properties of the investigated samples were determined by using an Instron 5982 electromechanical tension tester with a strain rate of 0.004 mm/mm/s and the structure was investigated by means of a Zeiss EVOMA 10 type electron microscope (SEM) equipped with an EDAX system.

2. Experimental work

For experimental casting, we used standard AlSi8Cu3 (226.10) alloy ingots, their chemical compositions are given in Table 1. We used AlSr10 (Al-10wt.%Sr wire) and AlSb10 (Al-10wt.%Sb, ingots) master alloys. Inductively coupled plasma (ICP) technique was used to determine the chemical compositions of the alloys.

Table 1 Chemical compositions of the AlSi8Cu3 aluminium alloys used in our experiments

Elements	Si	Cu	Mg	Ti	Sr	Sb	Fe	Mn	Pb	Sn	Ni
wt.%	8.85	2.53	0.30	0.10	0.0005	0.0040	0.51	0.35	0.05	0.01	0.049

The AlSi8Cu3 alloy ingots were melted in an electric resistance furnace, the melting and alloying temperature was 775±5°C. The melts were cleaned by using Coverlux 0021 drossing flux. The planned strontium and antimony alloying matrix of the 4 experimental series can be seen in Table 2. The antimony was added to the melt at the beginning of the 4 casting processes, and in every experimental series, the strontium concentration was increased from 5 to 300 ppm in 4 steps. After the addition of every modifying element (Sb, Sr), the melt was held at a constant temperature for 15 minutes.

Table 2 The planned strontium and antimony alloying matrix of the experiment

Casting series	**Strontium (ppm)**	**Antimony (ppm)**			
1.	5 (base alloy)	40	140	240	340
2.	100				
3.	200				
4.	300				

The extent of modification was determined by using the Cprob quantitative computer image analyzing program [7]. The evaluation was performed on the basis of the method described by Djurdjevic et al. [8] by using the AFS standard by digitizing 6 levels of modification. The median of the database of the entire measured perimeter was determined in each image on the basis of the perimeter of objects. The level of modification was determined for each image on the basis of the value of median by using Table 3.

By using a ZEISS type optical microscope, 15 photos were taken of the structure of each alloy of Sr-Sb combination (magnification x500) by us and the values of perimeter of Si-particles were measured in each image by means of the computer image-analyzing program. At last, the modification level of sample having a given Sr-Sb concentration was obtained by averaging the 15 modification levels of the 15 images.

Table 3 The modification levels (ML) and median values of perimeter of eutectic silicon [8]

Modification level (ML)	**Perimeter (μm)**
1 - Unmodified	96.5
2 - Lamellar	31.2
3 - Partial modified	24.6
4 - Non-lamellar	9.3
5 - Modified	8.1
6 - Very fine modified	3.2

3. Results

3.1. Tensile rods

In case of an alloy of a given strontium- and antimony combination, 6 tensile test pieces were loaded to fracture. The average values of tensile strength and strain as a function of the strontium- and antimony concentrations are shown in Figures 1-2 in case of a wall-thickness of 8 mm.

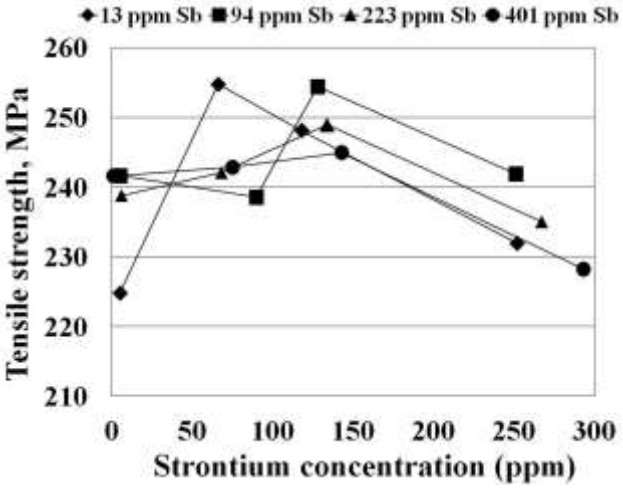

Fig.1 The average value of tensile strength as a function of the strontium and antimony concentrations in case of a wall- thickness of 8mm

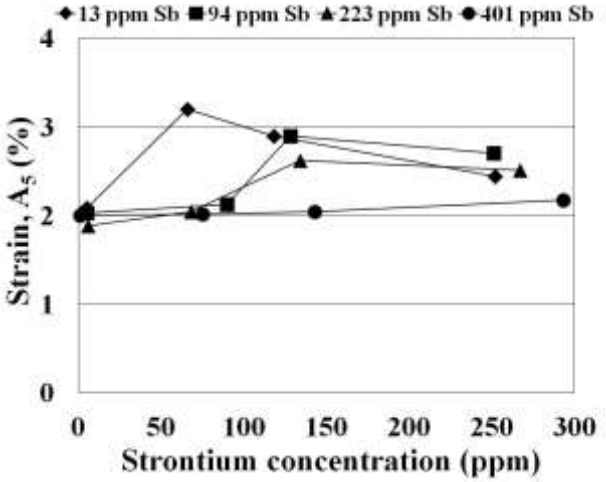

Fig.2 The average values of strain as a function of the strontium and antimony concentrations in case of a wall-thickness of 8 mm

The images of structure of tensile rods having the highest and lowest values of tensile strength belonging to a given combination of strontium- and antimony series are demonstrated in Fig. 3. It can be seen that in case of the samples having the highest and lowest values of tensile strength, the unmodified eutectic Si-structure is the characteristic structure in case of 401 ppm of antimony and 131 ppm of strontium moreover 401 ppm of antimony and 266 ppm of strontium combinations. In case of the tensile rods having the lowest value of tensile strength, the unmodified structure appears even in case of 223 ppm of antimony and 75 ppm of strontium combinations as well.

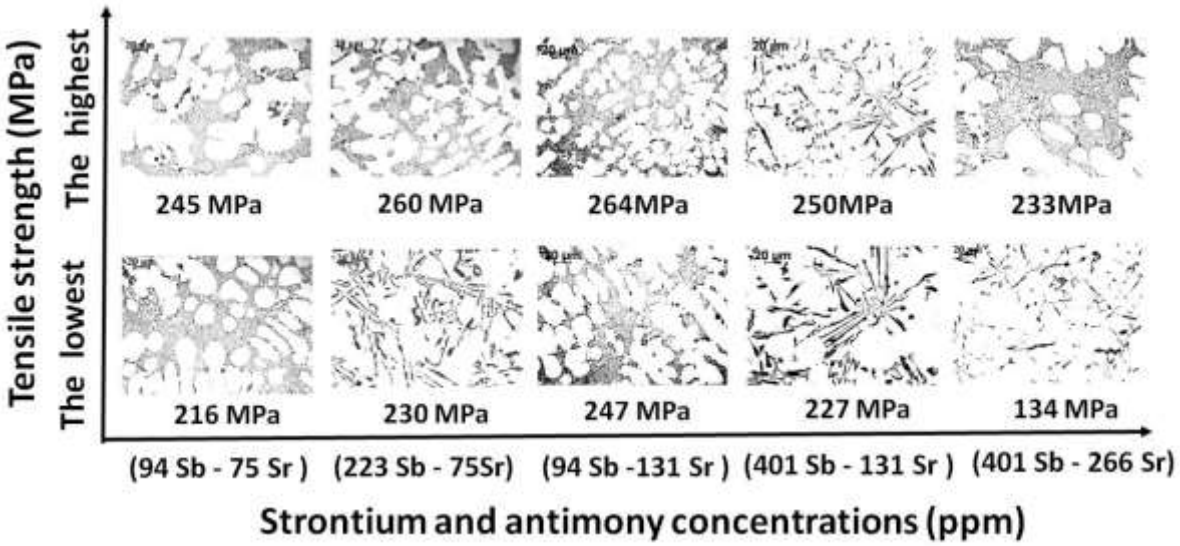

Fig.3 The structure-images of the sections of tensile rods made of the sample-parts with a wall-thickness of 8 mm in case of different values of Sr-Sb concentrations

3.2. Scanning electron microscope

The compound-phases containing both antimony and strontium appearing in the structure were identified in case of each tensile rod with strontium- and antimony combination by means of a scanning electron microscopy investigation. The compound-phases identified on the tensile rods containing 131 ppm of strontium and 94 ppm of antimony of the tensile-rod series having lower tensile strength can be seen in Fig. 4 a-b.

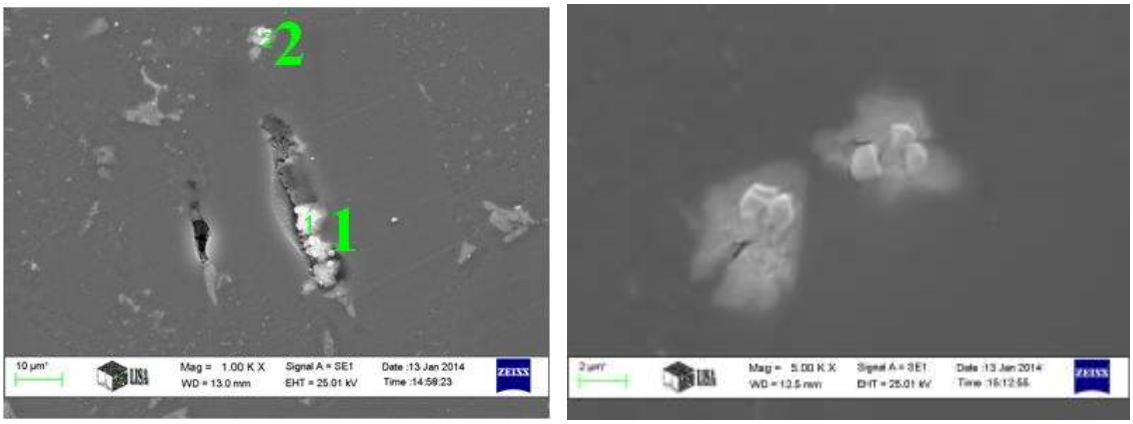

Figs. 4 a-b Compound-phases of Sr-Sb concentrations identified in the SEM images of section of tensile rod made of sample-parts of a wall-thickness of 8 mm

Table 4 Results of the EDS analysis for Figs. 4.a-b

Elements (wt.%)	Al	Sr	Sb	Si	Cu	Mg	Mn	Fe	Bi	Ni
No. 1	40.69	**17.48**	**25.38**	6.65	1.28	3.41	0.14	0.29	4.35	0.33
No. 2	36.01	**11.45**	**33.22**	8.93	1.42	1.45	0.39	0.41	6.11	0.61

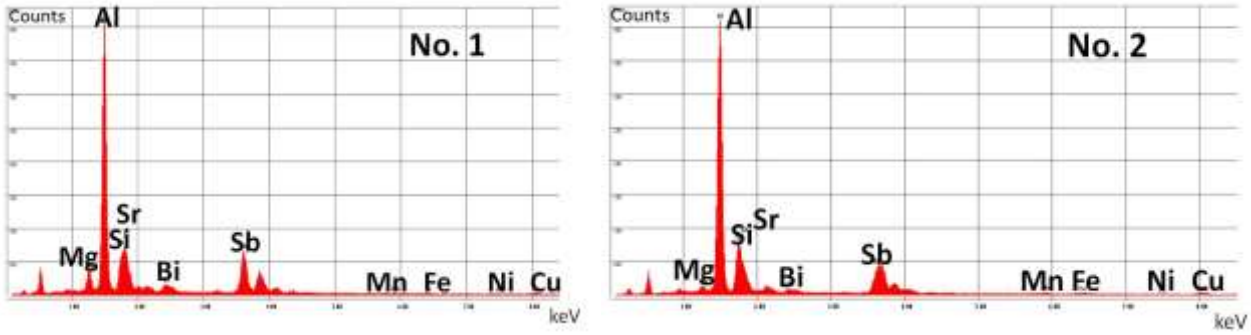

Figs. 5 a-b EDS analysis for Fig. 4a No. 1 (a) and for No. 2 (b)

The compound-phases identified in the tensile rod with 266 ppm strontium- and 401 ppm of antimony-content of the tensile-rod series of a lower value of tensile strength can be seen in Figures 6 a-b.

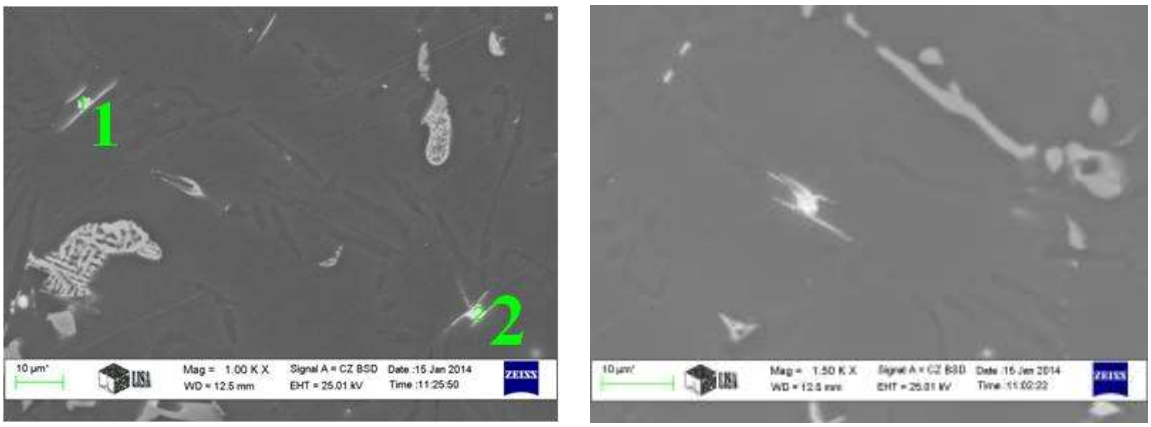

Figs. 6. a-b Compound-phases of Sr-Sb concentration identified in the SEM images of sections of tensile rod made of the sample-parts of a wall thickness of 8 mm

Table 5 Results of the EDS analysis for Figs. 5a-b

Elements (wt.%)	Al	Sr	Sb	Si	Cu	Mg	Mn	Fe	Bi	Ni
No. 1	61.52	**1.42**	**17.38**	17.06	1.16	0.40	0.26	0.33	0.20	0.28
No. 2	38.43	**1.40**	**48.50**	8.57	0.99	0.49	0.33	0.37	0.67	0.26

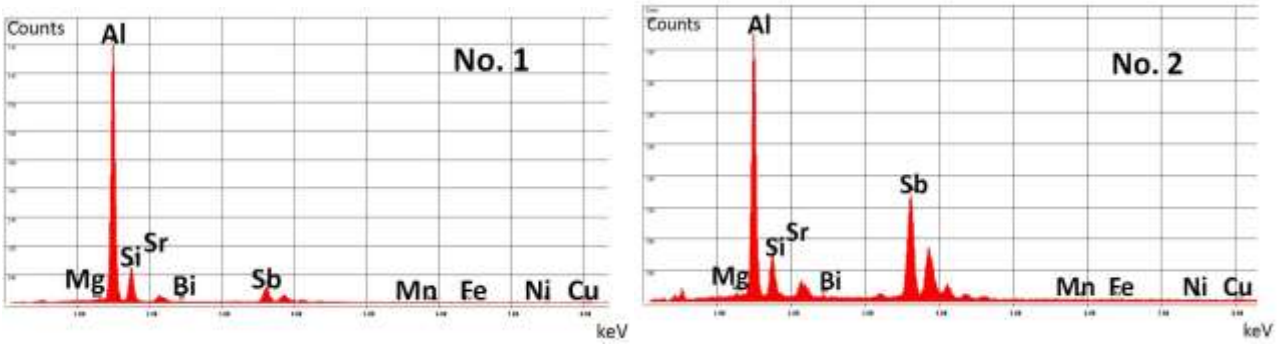

Figs. 7 a-b EDS analysis for Fig. 6a No. 1 (a) and for No. 2 (b)

3.3. Quantitative image analysis

Table 6 shows alloys containing different modification levels of Sr and Sb determined on the basis of the count above. These data can be seen in Fig. 8 as a function of the Sr and Sb content.

Table 6 Modification levels determined by computer image analysis as a function of the measured strontium and antimony concentration (wall-thickness: 8 mm)

ML	**Sr (ppm)**			
Sb (ppm)	1.0 *(13;5)*	5.0 *(11;66)*	5.0 *(14;118)*	5.1 *(12;252)*
	1.0 *(84;5)*	5.0 *(92;90)*	5.1 *(99;128)*	5.0 *(99;251)*
	1.0 *(232;6)*	1.0 *(217;68)*	5.0 *(224;134)*	5.0 *(220;267)*
	1.0 *(403;1)*	1.0 *(395;75)*	1.0 *(399;143)*	5.0 *(408;293)*

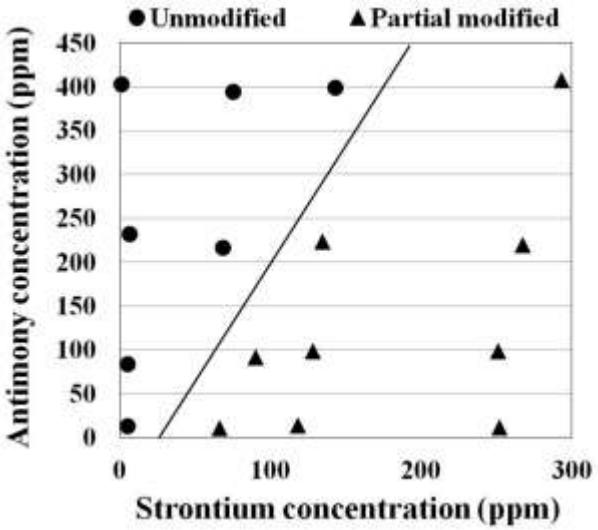

Fig. 8 Modification levels determined by computer image analysis as a function of the measured strontium and antimony concentration (wall-thickness: 8 mm)

Conclusion

The goal of our research is to show experimentally the correlation effect of antimony and strontium on the modification level in the cast aluminium alloys. So, series of alloys containing strontium between 5 and 300 ppm and antimony between 40 and 340 ppm were prepared.
On the basis of the mechanical- and structural results of tensile rods, it can be stated that the values of tensile strength and strain can decrease in case if the strontium- and antimony-concentrations are increased above a certain level (above about 300 ppm). Compound-phases containing strontium- and antimony were identified by means of the scanning electron microscope investigation; these compound phases were found in addition to the eutectic Si-particles and compound phases containing Fe. The compound phases were found near the porosities and along the cracks as well but the mechanism resulting in the development of these defects shall be investigated in the future. By means of the computer image analysis, the modification level was stated in case of given strontium- and antimony concentrations. It was proven that the concentration of strontium necessary for the modification shall be increased in case if the concentration of antimony increases (Fig. 8).

Acknowledgement

This research was realized in the frames of TÁMOP 4.2.4. A/2-11-1-2012-0001 „National Excellence Program – Elaborating and operating an inland student and researcher personal support system convergence program" The project was subsidized by the European Union and co-financed by the European Social Fund.

References

[1] A.K.Dahle, K.Nogita, S.D.McDonald, C.Dinnis, L.Luc: Eutectic modification and microstructure development in Al-Si alloys, Materials Science and Engineering, A413-414(2005)243-248
[2] N.Fatahalla, M.Hazif, M.Abdulkhalek: Effect of microstructure on the mechanical properties and fracture of commercial hypoeutectis Al-Si alloy modified with Na, Sb and Sr, Journal of Materials Science, 34(1999)3555-3564
[3] J.G.Kaufman, E.L.Rooy: Aluminium alloy castings properties, processes and applications, ASM International, ISBN: 0-87170-803-5, 2005.
[4] M.G. Day, A. Hellawell: The microstructure and crystallography of aluminium-silicon eutectic alloys, Proceedings of the Royal Society A 305 (1968) 473–491.
[5] S.Z. Lu, A. Hellawell: The mechanism of silicon modification in aluminum-silicon alloys: impurity induced twinning, Metallurgical and Materials Transactions A-Physical Metallurgy and MaterialsScience 18(1987) 1721–1733.
[6] M.Timpel, N.Wanderka, R.Schlesiger, T.Yamamoto, T.Isheim, G.Schmitz: Sr-Al-Si co-segregated regions in eutectic Si-phase of Sr-modified, Ultramicroscopy, 132(2013)216-221
[7] Z.Gácsi: The application of digital image processing for materials science, Materials Science Forum, Vol. 414-415, pp.213-220., 2003.
[8] M.Djurdjevic, H.Jiang, J.Sokolowski: On-line prediction of aluminium-silicon eutectic modification level using thermal analysis, Materials Characterization - Elsevier, 46(2001)31-38

CSI vs. Reality

Péter Tóth

Hungarian Institute for Forensic Sciences

H-1903 Budapest, P. O. Box 314/4, Hungary

morf@orfk.police.hu

Keywords: crime, forensic science, accident

Abstract. Nowadays forensic sciences try to keep up with criminality. Unfortunately despite this criminality continues to grow. Armed robbery, murder have become rife, yet the number of other crimes does not seem to decrease.

The employees in the Institute for Forensic Sciences meet a wide range of crimes and have to deploy the available arsenal of modern natural sciences to solve the problems. In addition to the special optical microscopes we have at our disposal an infrared spectroscope with microscope, a Raman spectroscope, a scanning electron microscope, etc. But above all these the most important weapon in criminal investigation is the expertise of the skilled specialists.

In the popular TV-crime series we witness exciting investigations, forensic operations, etc. However these do not have much to do with reality. In this presentation a series of interesting „domestic" cases of real forensic examinations will be discussed. Thereby you'll get an insight into the everyday life of the modern forensic sciences.

In films the specialists are versatile superheroes: members of commando units, first class investigators and experts in all kinds of specialities. In reality: experts are specialists in natural sciences and in criminal sciences.

In films they do a lot of idiotic things e.g.: the specialist wipes the hand of a person suspected of something with a DNA sample holder, sprays it with a magic material, and the verdict is ready: Guilty! In reality we apply useful methods. In Hungary the forensic experts have no investigative powers per se. We deal with natural sciences; the investigation is the task of the police.

The common parts are: the similar cases. Criminalized societies are almost the same on every continent.

The most efficient way to present this forensic work is by reviewing some real, interesting cases from our archives.

Case studies

Hunting accident #1

The hunting had just ended. On the field a man began to flay a downed animal. Six nouveau riche hunters remained in their ambush, failed to empty their rifles. Unexpectedly a boar ran between them and the man on the field. All six hunters began to shoot at the boar, and all of them hit the beast. Unfortunately one of the bullets which penetrated the boar struck the man who was skinning the previously shot animal. But whose bullet was it? The surgically removed lead bullet was so badly damaged that the experts of classical ballistics could not determine its origin. So we had to compare the material of this particular bullet to the bullets remaining in the magazines of the six hunters.

The method was X-ray fluorescent spectroscopy inside the scanning electron microscope. Lead for bullets is alloyed with a little antimony (Sb), sometimes with a little tin (Sn) to set the hardness of the bullet. In our case we found the same alloy concentrations in only one type of ammunition among the six hunters (Fig. 1.). The others had different alloys (Fig. 2.). So we could determine the hunter whose bullet hit the man.

In Hungary this case had an unfortunate legal consequence: the hunter could keep his gun license. One year later he shot a young woman dead in place of a wild pig.

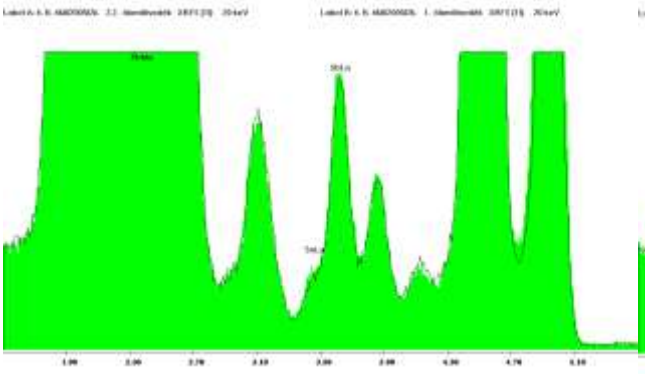

Fig. 1.

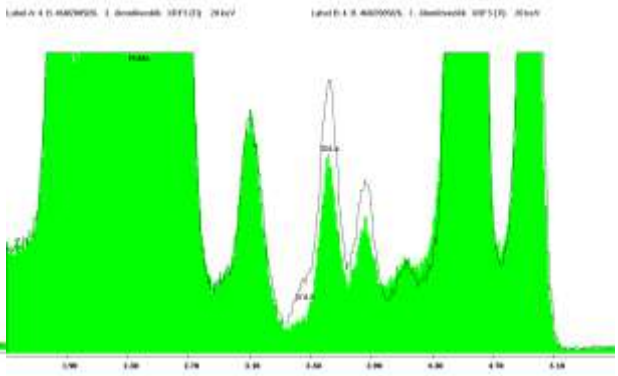

Fig. 2.

Comparative XRF spectra of lead alloy bullets

Hunting accident #2

A stupid master of hounds marked the firing line on the field for two high stands directly towards each other. The distance between them was about 300 meters. Wild animals crossed the field between the ambushes and the hunters shot at them. The animals stayed alive, but one of the hunters was hit by a bullet and died. The incriminated rifle was powerful, but the bullet removed from the body was hardly deformed (Fig. 3.). The ballistics expert diagnosed that the bullet had been fired from that rifle (Fig. 4.). How could it happen? The bullet should have been strongly deformed if it reached him directly or after penetrating an animal.

Fig. 3. The hardly deformed bullet

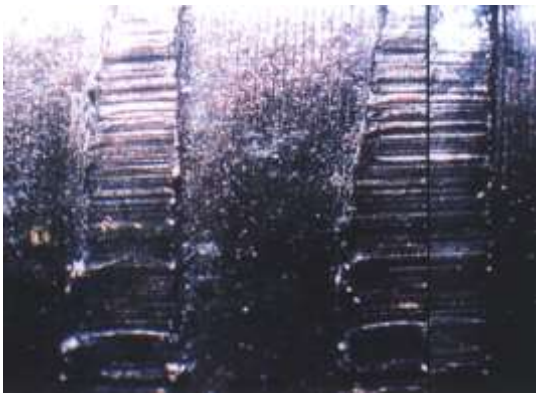

Fig. 4. Comparative photo of the incriminated and the sample bullets

At the scene of the event we determined that there were deep ruts caused by a tractor wheel between the two high stands. At the time of the accident there was water in them. According to witness statements the animals crossed the field near these ruts. Could the bullet ricochet on the water surface?

We performed a series of experiments at an abandoned lake. Most of the bullets shot at shallow angles ricocheted from the surface of the lake, and the trajectories of some of them corresponded to the incriminated bullet. So the accident happened as follows: the bullet missed the animals, ricocheted on the water in the wheel ruts thereby losing a lot of kinetic energy, and hit the body of the hunter who was in the other high stand.

Traffic accident

A parliamentary representative was speeding at night on the motorway, at the same time phoning and sending several SMS from his mobile. His car went off the road and landed in the 5-meter deep road ditch. A lorry driver reported it to the police because he saw the car disappear from view. The representative did not use his seat belt, flew out through the right hand side window and died.

Police chiefs wanted to know how the body could fall out through the opposite side to where the steering wheel was, so the case landed in our Institute. We found some smeared plastic on the trousers of the deceased person, which was similar to the material of the right hand side window frame, except that the smeared plastic did not contain silicate while the window frame did. How could that be?

The answer came from the examinations in the field of scanning electron microscopy. The image of the window frame plastic showed that quite big silicate particles are suspended in the organic plastic (Fig. 5.). When the thermoplastic smears on fabric the material removes only the top few micrometers, so the big silicate particles remain in the substrate. That way we could reconstruct the event: The car left the motorway and flew for one second, causing weightlessness inside. Since the driver had not used the seatbelt, he moved out of the seat, and in the moment of landing the airbag hit him out through the right hand side window. Had he used the seatbelt he would have escaped with a broken leg. The lesson: high rank does not exempt anybody from the laws of physics.

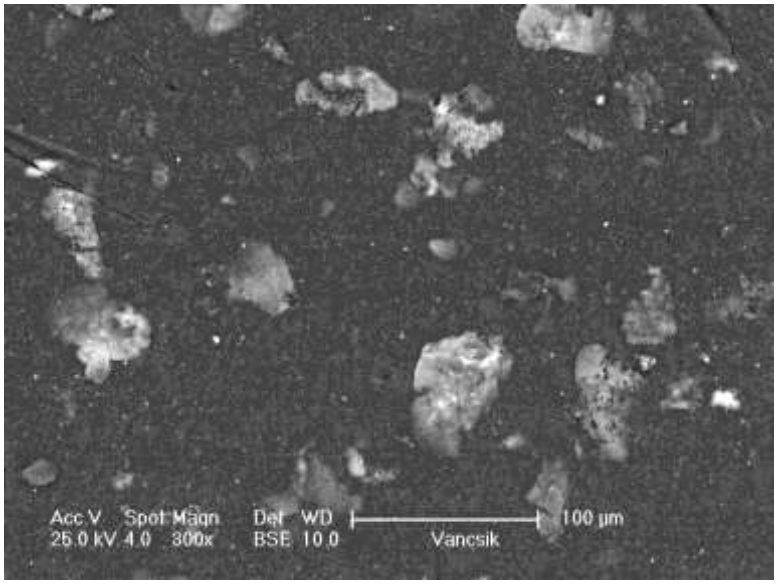

Fig. 5. The SEM image of the frame

Proof of burglary by paint fragments

A gang went by car to the chosen location to commit a night-time burglary. Near to the location they switched the car-lights off so as not to be conspicuous, and promptly ran into a fire hydrant. Some carpaint fragments remained on the surface of the hydrant. We were able to compare them to the paint of the car impounded by the police.

The preparation is the following: the pertinent paint fragments are embedded in resin block (Fig. 6.) and sliced in a microtom with a special plan-concave glass knife. These slices can be taken on normal or on special split glass slides (Fig. 7. and 8.).

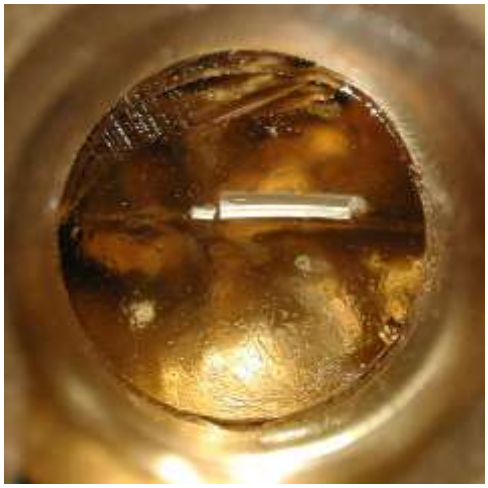

Fig. 6. Resin block

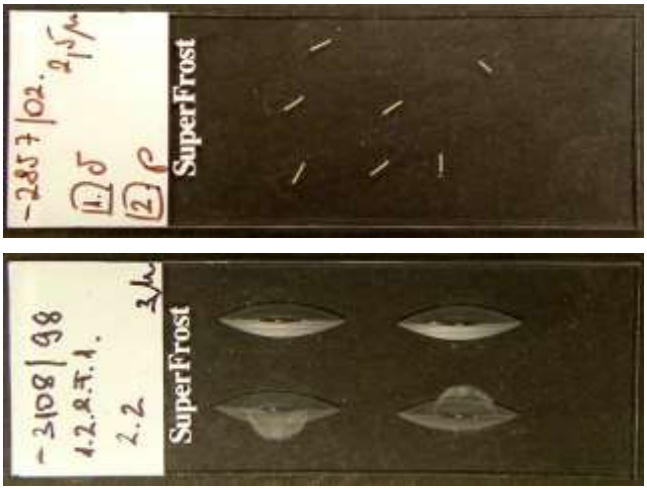

Fig. 7. & 8. Slices on glass slides

In this particular case we found fragments of multilayered paint coat from the car on the hydrant (Fig. 9.). So it was sure that this car had been present there on the night in question.

from car from hydrant

Fig. 9. Polarizing microscopical image of paint fragments

Magn.: 160×

Guerillas

An extremist group could not wait for the next parliamentary election, and wanted to blow up the car of a politician. The technical method was the following: two strong magnetic pucks were glued on the packaged bomb, and this was put onto the chassis. The plan fizzled out, so

the terrorists wanted to remove the bomb. They tried, the bomb was removed, but the magnets were so strong that they remained on the chassis. The police found the magnets.

During a search at the suspect's house police found similar magnetic pucks (Fig. 10.).

Fig. 10. A nickel coated magnetic puck

The pucks removed from the chassis had the same geometrical features and nickel coating. The crystal structures of them were equal (Fig. 11. and 12.) and element compositions were special and also equal (Fig. 13. and. 14.). These magnets contain not only neodymium but praseodymium as well. So this composition was unique. Furthermore on the magnets from the chassis we found some traces of epoxy resin identified by the FTIR method. The conclusion was that these magnetic pucks came from the same source, and something had been glued onto them.

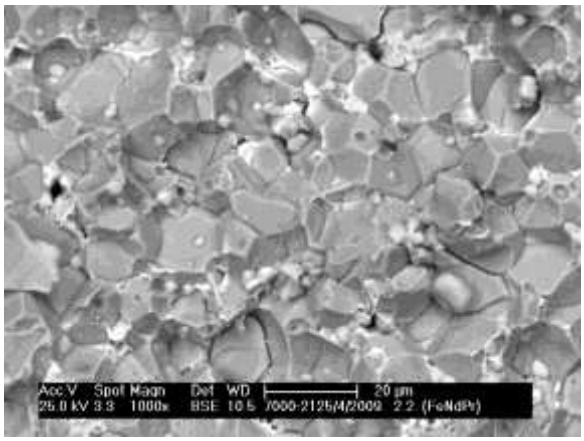

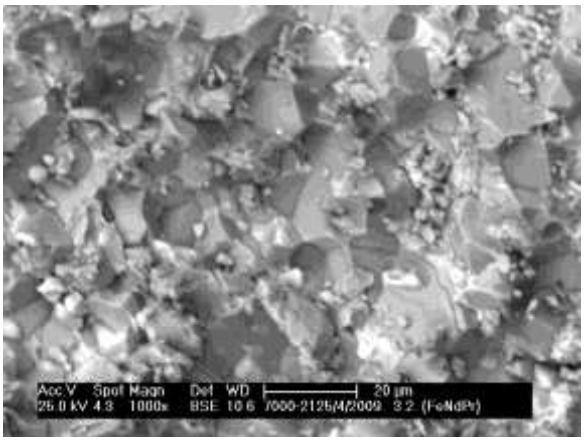

Fig. 11. & 12. SEM images of crystal structures of magnets

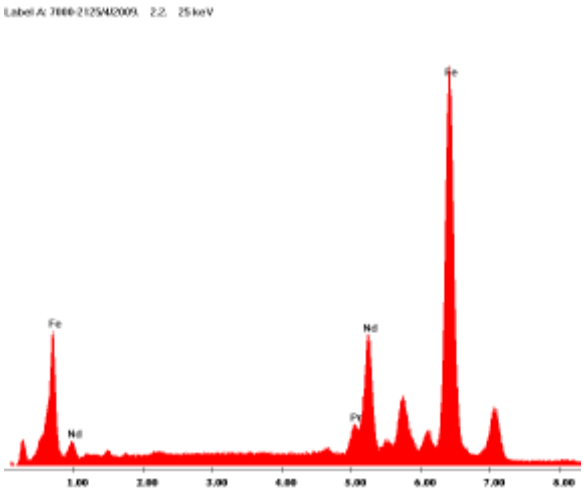

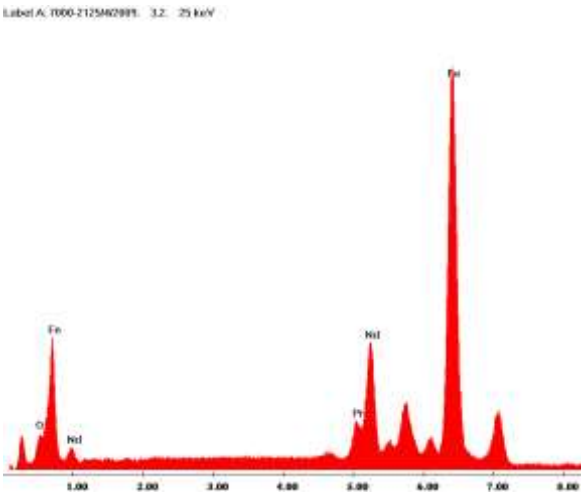

Fig. 13.& 14. Similar EDS spectra of magnets

Electric fire in a nuclear power plant

In the cable channel of the nuclear power plant fire broke out, and the reactor block was stopped. It was very important to determine the source of the fire. The origin was probably electrical, but they had to know which cable had malfunctioned. On site we collected a lot of parts of cables. Most of them were steel armored aluminum cables, but at the bottom of the truss there were some copper cables without steel armor. On these cables we found a lot of parts that had been flash melted by short-circuiting (Fig. 15. and 16.).

Fig. 15. & 16. Melted parts on copper cables

We examined all the flashes. After the special preparation process the microscopic image of the crystal structure shows whether the short-circuit arose before the fire or was only the result of the fire (e.g. insulation burned down). Most of the flashes had after-fire macrocrystalline structures (Fig. 17.). One of them had microcrystalline structure showing the source of fire (Fig. 19.).

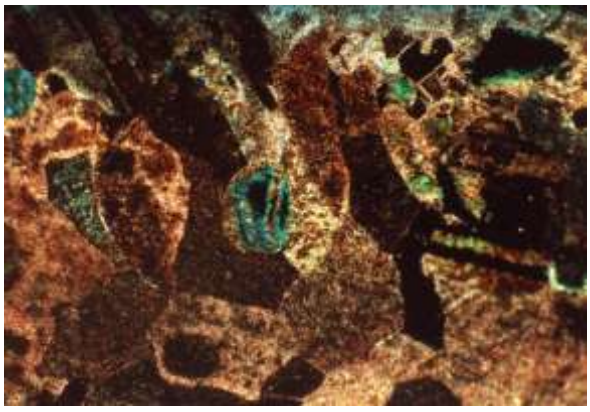

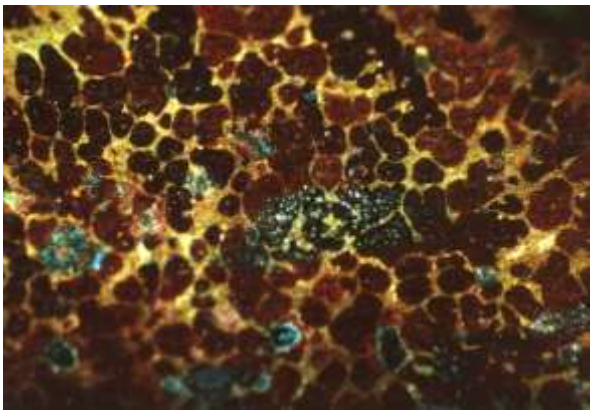

Fig. 17. & 18. Macrocrystalline and microcrocrystalline structure under polarizing microscope. Magn.: 100×

In this way it could be determined which cable was defective.

Final conclusion

The experts of forensic sciences should be polymaths. It is impossible, but we have to aspire to this. Different types of cases require multifarious scientific and technical methods. Irrespective of this, the criminal inquest must remain the responsibility of the criminal investigators.

Determing the Viscosity of Rarely Examined Glasses

Gabriella, Zsoldos[1,2, a], István, Kocserha[2,3] and András, Szegedi[2,3]

[1]Zerlux Hungary Ltd, Hungary, H-2100, Godollo, Pattantyus Abraham str. 10

[2] Unversitas Scientiarum Szegediensis, Faculty of Sceince and Informatics, Department of Mineralogy, Geochemsitry and Petrology, Hungary, H-6722, Szeged, Egyetem str. 2.

[3] University of Miskolc, Faculty of Materialsciences, Institute of Ceramics and Polymer Engineering, Hungary, H3515, Miskolc-Egyetemvaros

[a]femzsgab@uni-miskolc.hu

Keywords: viscosity, silica glass,

Abstract. High energy explosions and irradiation may cause that the minerals and mineraloids form glassy phase on the earth surface. We would like to determine the mechanical properties of these glassy materials. To achieve this and manufacture samples we need to measure the main technological property, the viscosity.

Introduction

For glass melts the main technological parameter is the viscosity of the liquid itself, the technology could be planned and optimised, knowing the exact viscosity. The viscosity is greatly dependent on the temperature, this relation resulted in the widely accepted Vogel–Fulcher–Tammann Equation(Eq1): [1,2]

$$\log(\eta)=A+B/(T-To) \quad (1)$$

where η: viscosity (Pas),

T: temperature (°C),

A, B, T_0: constant.

After determining the viscosity –temperature curve, the viscosity fixpoints can be selected.

Table 1: The Viscosity fixpoints[2]

log10[viscosity in ...]		Description
Pas	Poise	
1	2	Melting Point (glass melt homogenization and fining)
3	4	Working Point (pressing, blowing, gob forming)
4	5	Flow Point
6.6	7.6	Littleton Softening Point (Glass deformes under its own weight)
8-10	9-11	Dilatometric Softing Point T_d, depending on load
10.5	11.5	Deformation Point
11-12.3	12-13.3	Glass Transition Temperature T_g
12	13	Annealing Point (Stress is relieved within a few minutes.)
13.5	14.5	Strain Point (Stress is relieved within several hours.)

There are a lot of methods to determine the viscosity e.g. calculating the viscosity from the chemical glass composition using Fluegel's method, another possibility is measurement of the viscosity fixpoints.

Professor Fluegel collected in an online database more than 2200 composition-viscosity data.[2] His model takes in account the viscosity changes due to phase separation, changes in composition due to evaporation and other composition effects (borosilicate anomaly, the effect of alkalines). [1,2]

The calculator based on Fluegel's model can be accessed at http://glassproperties.com/viscosity/.

Determining a rarely examined glass viscosity

Using Fluegel's model we have examined silicate glasses made from mineral composition representative to specific areas of Hungary. It gave us the viscosity curves for compositions of interest.

Table 2: Composition of ANT samples

	ANT 2007	ANT 2003	ANT 2004
Mineral	**Glass composition (m/m%)**		
Na_2O	2.05	1.49	1.58
MgO	0.20	3.68	3.24
Al_2O_3	12.71	8.96	9.62
SiO_2	74.95	60.14	57.27
P_2O_5	0.07	0.13	0.11
SO_3	-	0.08	0.09
K_2O	6.02	1.66	1.97
CaO	0.47	7.84	10.41
TiO_2	-	0.50	0.44
MnO	-	0.06	0.07
Fe_2O_3	1.76	2.71	3.37
SrO			0.03
Rb_2O	0.03	-	-
ZrO_2	0.02	-	-
LOI	1.71	12.72	11.78
Σ	99.98	99.99	99.98

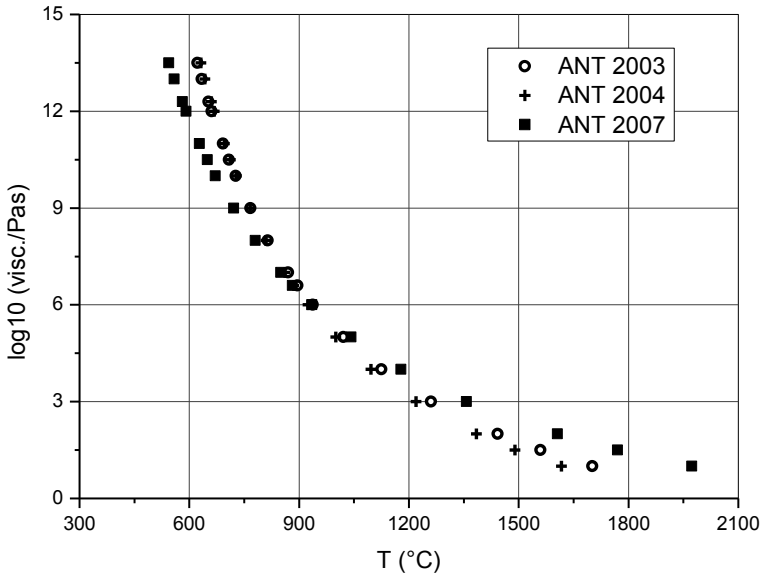

Figure 1. Temperature-viscosity curves determined by Fluegel's model

Viscosity results from measurements

To determine viscosity thought measurement multiple methods can be used: parallel-plate viscometry, ball penetration viscometry, fiber elongation viscometry, uétasonic measurements, heating microscopy. [1,4]

The heating microscope is set up by combining a controlled temperature tube furnace (up to 1500°C), a microscope with digital camera and recording and evaluation software. During heating the software registers the geometry changes of the sample. From the records the viscosity can be determined by the following equation (Eq2):

$$\mathbf{d(\Delta \boldsymbol{L}/\boldsymbol{L_0})} = \mathbf{(3}\gamma\nu/8\eta(T)r_{min})\mathrm{d}t \qquad (2)$$

Where: L_0 is the original length of the sample, ΔL is the change in size after t time of heating, $\eta(T)$ is the shear viscosity as a function of temperature, γ is the surface energy between the glass and air, r_{min} is the minimum particle size (radius), ν is the volume ratio of particles with r_{min}.

Measurements were carried out *Camar Elettronica* heating microscope.

Fig. 2 shows the schematics of the used instrument: (1) frame, (2) light source, (3) tube furnace, (4) high resolution CCD camera, (5) sample holder, (6) sample, (7) control and registering unit (computer with control and image evaluation software).

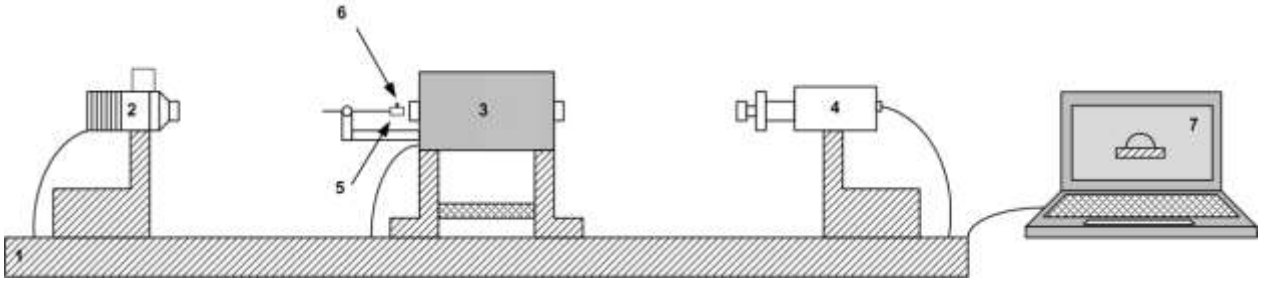

Figure 2. Schematics of Camar Elettronica heating microscope

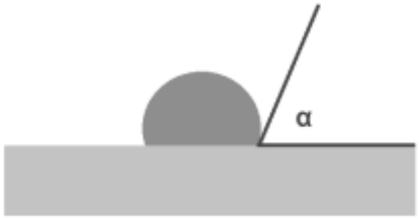

Figure 3. Image recorded by the instrument

Fig 3 shows a typical image recorded by the instrument, which can be used to determine the wetting angle by measuring the (α) supplementary angle, the height (L) and the width (w) of the sample at given temperature.

The wetting angle can be use to determine the γ surface energy.

Our results are demonstrated trough sample ANT 2007.

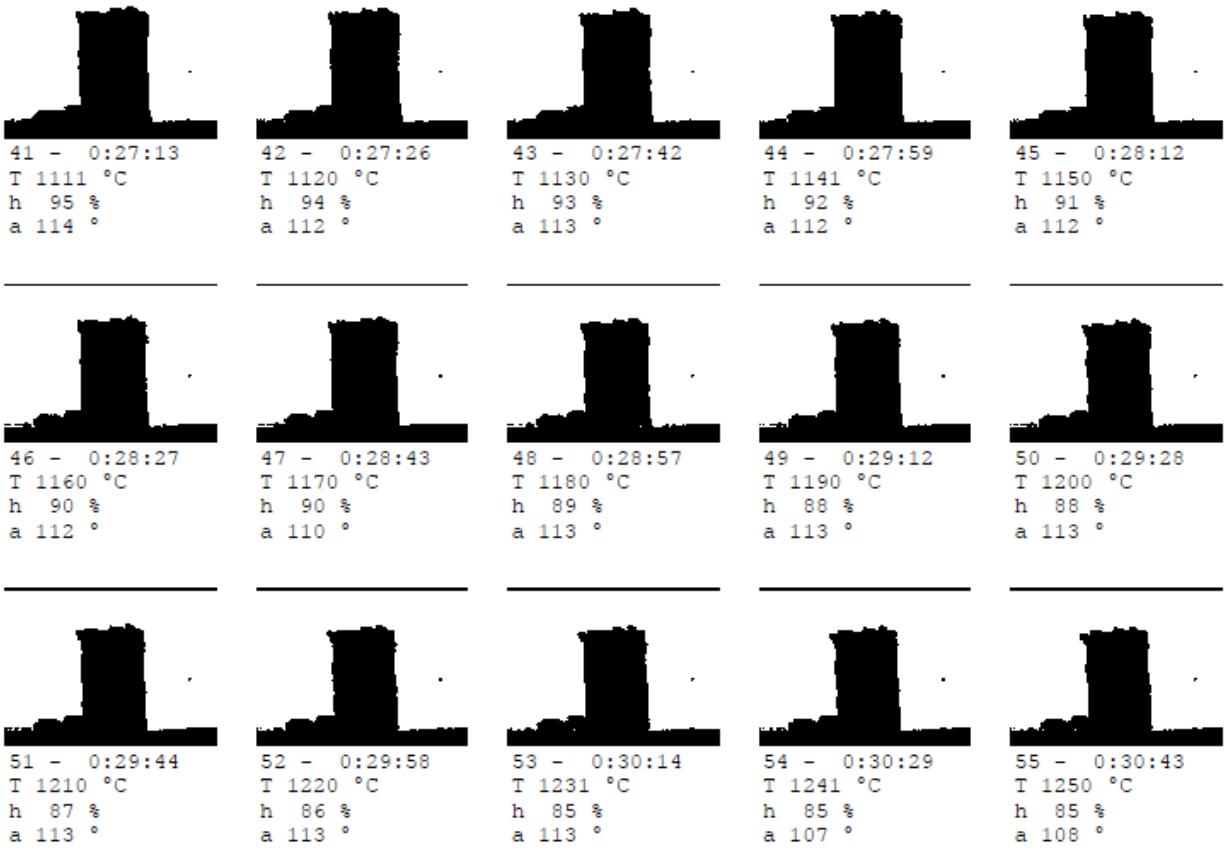

Figure 4. Heating microscope measurement of sample ANT 2007

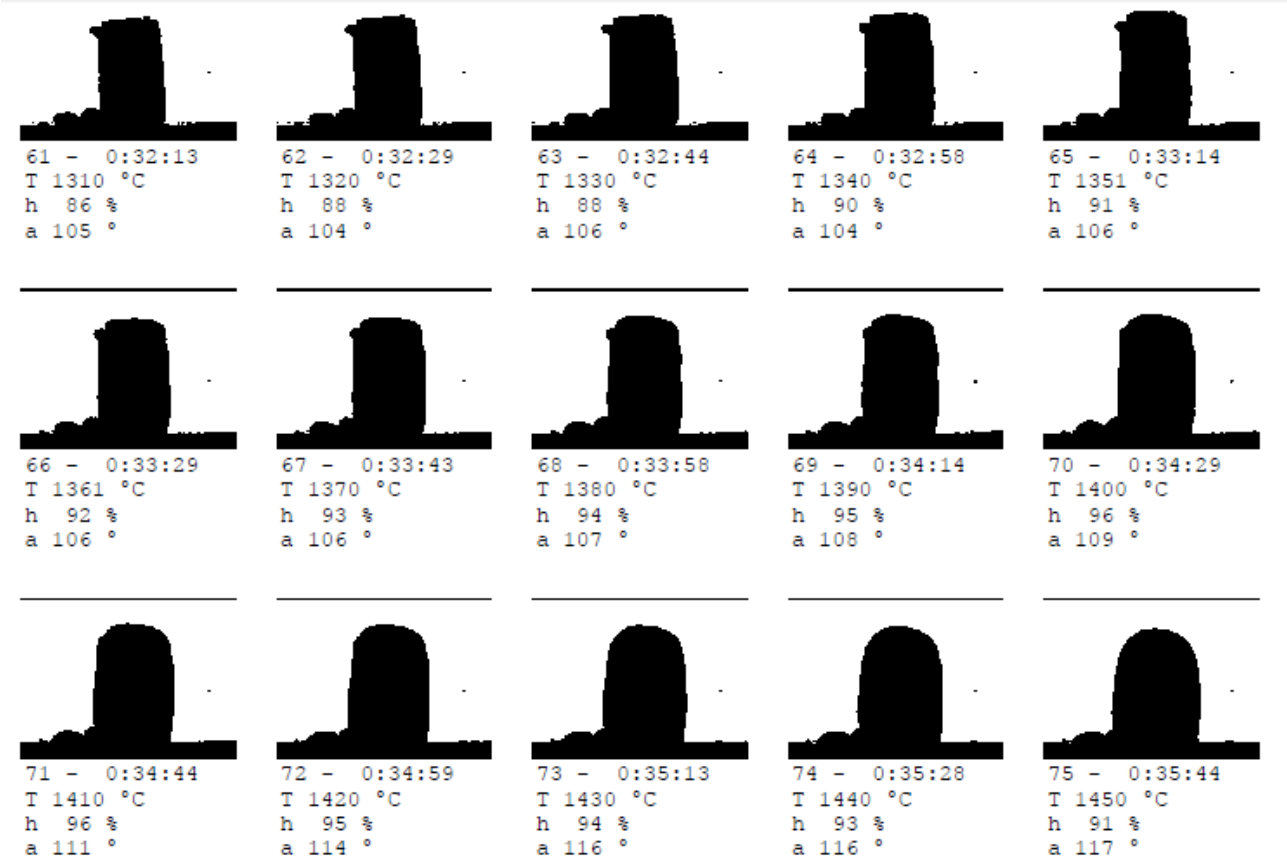

Figure 4. Heating microscope measurement of sample ANT 2007

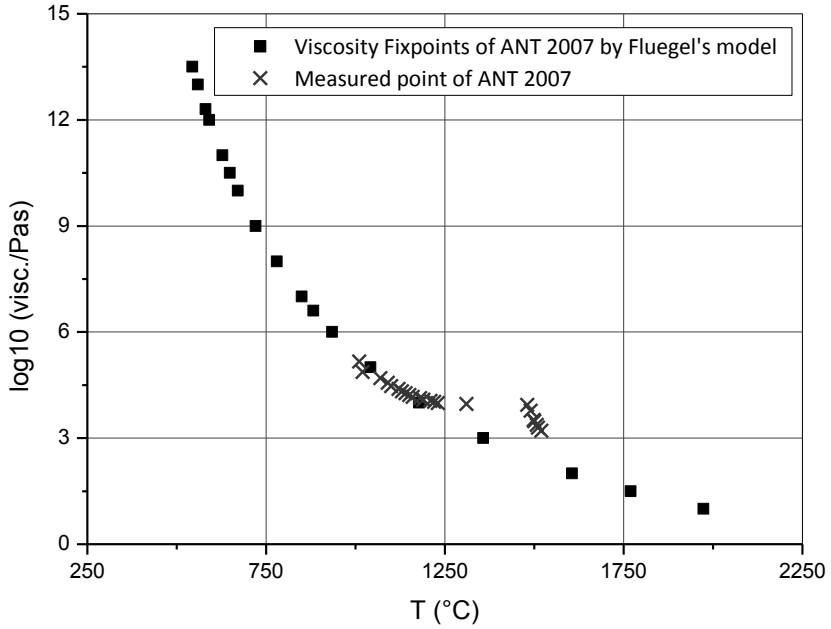

Figure 5. Comparison of the model and measured data of ANT 2007

Fig. 4. shows the outline the sample ANT 2007 as function of temperature. The height of the sample decreases until 1250°C indicating the decrease of viscosity, after 1250°C the height of the sample starts to increase slightly (the edges are getting rounded off), which is most probably caused by the formation of some gaseous side products. This will also cause a discrepancy on Fig. 5. between the measured and calculated viscosity curves. After the viscosity decreases further at about 1430°C, the two curves start to close again. At this temperature the viscosity of the glass lowers enough so the gasses can escape, thus as the height starts to decrease again. Above this temperature the whole shapes gets rounded, starts to form a droplet.

Summary

Fluegel's model was used to determine the viscosity curves of specific Hungarian mineral based glasses. Experiments using heating microscope were carried out to compare theoretical data to practical results. On sample ANT 2007 we have found good agreements between theory and practice, significant differences only show up were gaseous side products affect the measurement.

Acknowledgement

This work has been carried out as part of the GOP-1.1.1-11-2012-0335 project. The realization of this project is supported by the European Union, co-financed by the European Social Fund.

References

[1] A. Fluegel: Glass viscosity calculation based on a global statistical modelling approach. Glass Technology: European Journal of Glass Science and Technology A, February 2007, 48 (1), pp. 13-30
[2] Information on http://glassproperties.com/viscosity/Glass-Viscosity-Fixpoints.htm,
[3] Szemán József: A viszkozitás szerepe az üveggyártásban, Építőanyag 58. évf. 2006. 1. szám
[4] C. Lara et al. / Solid State Ionics 170 (2004) 201–208